SUBCRITICAL TRANSISTION TO TURBULENCE
IN TAYLOR-COUETTE FLOW

A Thesis
Presented to
The Academic Faculty

by

Daniel Borrero Echeverry

In Partial Fulfillment
of the Requirements for the Degree
Doctor of Philosophy in Physics

Georgia Institute of Technology
December 2014

SUBCRITICAL TRANSISTION TO TURBULENCE
IN TAYLOR-COUETTE FLOW

Approved by:

Professor Michael F. Schatz, Advisor
School of Physics
Georgia Institute of Technology

Dean Paul M. Goldbart
College of Sciences
Georgia Institute of Technology

Professor Kurt Wiesenfeld
School of Physics
Georgia Institute of Technology

Professor Alberto Fernández-Nieves
School of Physics
Georgia Institute of Technology

Professor Donald R. Webster
School of Civil and Environmental
Engineering
Georgia Institute of Technology

Date Approved: 11 August 2014

Para mis papás, Guillermo y Magdalena, que un día, hace muchos años, me dejaron hacer chispas...

ACKNOWLEDGEMENTS

The work presented here would not have been possible without the support of many people. First, and foremost, I would like to thank my advisor, Mike Schatz, without whose patience and optimism this work would have never come to be. Mike was always a great sounding board for ideas and somehow managed to find the funds to try out any crazy idea that I came up with, always egging me on with a cheeful, "Onward and upward!" Mike was a constant source of support through the ups and downs of research and was incredibly generous with providing me with many opportunities for professional development. Mike's passion for teaching has also been a great inspiration.

Predrag Cvitanović has been a persistence presence, always pushing me and the rest of the Center for Nonlinear Science to dream big and attack the hard problems. Ever quotable, his dry sense of humor is always good for a chuckle. Roman Grigoriev has been the ying to Predrag's yang. Ever patient and willing to answer even the most basic questions, Roman has a methodical, grounded approach that has allowed me to make connections between the abstract mathematics of dynamical systems theory and my experiments. Kurt Wiesenfeld was a great teacher and working with him to study the synchronization of coupled nonlinear oscillators was a great pleasure. Minami Yoda is probably the most careful experimentalist that I know and has always been a source of practical advice on all things experimental. Sam Raben helped plan and carry out some of the experiments reported in Chapters 4 and 5.

A great institution not only has great faculty but also great staff. Sam Mize of the College of Sciences Machine Shop and Dennis Brown, Dennis Denney, and Jeff Wilkie of GTRI Machine Services helped with the fabrication of various mechanical parts. Without them, various broken taps, bent parts, and seized bearings would probably be permanent parts of the Schatz lab Taylor-Couette apparatus. Lee Strickland, Stephen Lester, and Jeff Sullivan kept our computers up and running and were of great help fixing things whenever I

decided that I had "hacking skills". Darryl Warsham, Vicki Speights, and Mary Helen Hayes were always incredibly helpful whenever I needed help with purchasing and understanding whenever I inevitably lost receipts during conferences. Lori Federico, Felicia Goolsby, Ashley Jeter, and Malu Mbungi somehow always managed to keep things running smoothly as us physicists knocked it down around them and were always willing and able to help with a smile.

Naturally, I would have never even made it to Tech without the support of my family. My parents, Guillermo and Magdalena, instilled in me a love of tinkering and mathematics, respectively. My uncle Alberto was always good for a quick call about bearings or shaft seals. My brother Felipe, with his boundless love of bugs, is an inspiration in curiosity and I cannot wait to see where his scientific adventures take him. My grandparents, Gonzalo and Mary, have always been my biggest cheerleaders and nothing makes me happier than seeing their faces light up with each of my successes.

I would also like to acknowledge my friends throughout grad school, who without knowing it, made my time in Atlanta one of the best in my life. Joaquin Ospina took me up the day I drove in from Austin and has been my go-to guy for anything, always willing to put me up in his house, feed the cat, borrow his car, etc, expecting nothing in return. Bill Knouse, Lee Miller, and Erin McGrath kept us sane through the first year of classes, always planning some kind of escapade for Friday nights. Adam Perkins joined the Schatz lab at the same time as I did and was always willing to listen to and exchange ideas about getting our experiments up and running. This would have never happened without the careful tutelage of Hüseyin Kurtuldu and Vivek Sharma. Alex Wiener, Chris Malec, and Domenico Lippolis always made for interesting discussion over coffee. Radford Mitchell kept things interesting on the third floor of Howey with stories of his various misadventures. It has been a great pleasure to mentor Bala Suri and Jeff Tithof as they evolved from doe-eyed first-year grad students into the Terrible Tag Team of 2D Turbulence. John Bell, Judy Bowers, Todd and Alice Ziegler, Mike Terwilliger, and Katie Hall peridiocally dragged me out of the lab and into the great outdoors. A little sun was always a welcome pick me up. Danny Caballero has been a great friend and partner in crime dating back to the Austin days with whom I

share a love of punk rock, comic books, and all things Affleck. Ed Greco was always up for a quick (or not so quick) lunch and became a great friend, who always had a new bit of new trivia to share. Alex and Ed, along with Paul Goldbart, deserve a special thanks for their careful reading and helpful comments on earlier drafts of this dissertation.

Finally, I would like to thank Sarah Neal, who supported me when research stagnated and I was unbearable to be around, put up with the late nights when I had to take "just one more data run", and talked me down whenever the "That's it! I'm dropping out!" bug came around. I am forever grateful for her love and confidence in my ability to succeed and look forward to our new life together in the Pacific Northwest.

TABLE OF CONTENTS

LIST OF TABLES

LIST OF FIGURES

xiv

SUMMARY

Turbulence is ubiquitous in naturally-occurring and man-made flows. Despite its importance in scientific and engineering applications, the transition from smooth laminar flow to disorganized turbulent flow is poorly understood. In some cases, the transition can be understood in the context of linear stability theory, which predicts when the underlying laminar solution will become unstable as a parameter is varied. For a large class of flows, however, this approach fails spectacularly, with theory predicting that the laminar flow is stable but experiments and simulations showing the emergence of spatiotemporal complexity.

In this dissertation, the direct or *subcritical* transition to turbulence in Taylor-Couette flow (i.e., the flow between independently rotating co-axial cylinders) is studied experimentally. Chapter 1 discusses different scenarios for the transition to turbulence and recent advances in understanding the subcritical transition within the framework of dynamical systems theory. Chapter 2 presents a comprehensive review of earlier investigations of linearly stable Taylor-Couette flow. Chapter 3 presents the first systematic study of long-lived super-transients in Taylor-Couette flow with the aim of determining the correct dynamical model for turbulent dynamics in the transitional regime. Chapter 4 presents the results of experiments regarding the stability of Taylor-Couette flow to finite-amplitude perturbations in the form of injection/suction of fluid from the test section. Chapter 5 presents numerical investigations of axisymmetric laminar states with realistic boundary conditions. Chapter 6 discusses in detail the implementation of time-resolved tomographic particle image velocimetry (PIV) in the Taylor-Couette geometry and presents preliminary tomographic PIV measurements of the growth of turbulent spots from finite-amplitude perturbations. The main results are summarized in Chapter 7.

CHAPTER I

INTRODUCTION

Turbulent flows are ubiquitous in science and engineering. From the naturally occurring flows like ocean currents and the flow in blood vessels to man-made flows such of the wakes behind airplanes and automobiles, turbulence is all around us. Turbulence occurs when the inertial forces in a flow are sufficiently strong to overcome the smoothing effects of viscosity ν. The relative importance of these two effects is usually captured by a dimensionless quantity called the *Reynolds number Re*. When Re is small, viscous forces dominate and the resulting flow is laminar, meaning that adjacent fluid layers slide past each other and the flow is regular and smooth. For sufficiently high values of Re, inertia dominates and the laminar flow is replaced by a series of chaotic eddies and vortices that fluctuate erratically at a variety of spatial and temporal scales. One of the great outstanding problems in classical physics is deriving a general theory that can predict when a particular flow will be turbulent.

1.1 The Transition to Turbulence

For a large class of fluid flows, the transition to turbulence can be explained by studying the stability of the laminar solution to infinitesimal perturbations using linear stability theory. This allows one to predict when the laminar solution becomes unstable so that the flow transitions to a new, more complex flow pattern [2–5]. These patterns typically bifurcate from the laminar solution and correspond to spatial or temporal modulations of the laminar state. As the control parameter is increased, these patterns grow in amplitude and eventually become unstable themselves, giving way to other flow states. The complexity of these states becomes progressively higher, eventually resulting in turbulence. Flows that follow this route to turbulence are said to undergo a *supercritical* transition.

A famous example of a system that undergoes a *supercritical* transition to turbulence is Rayleigh-Bénard convection. This is the flow that occurs when a temperature gradient is applied across a thin layer of fluid under the action of gravity. For small thermal gradients,
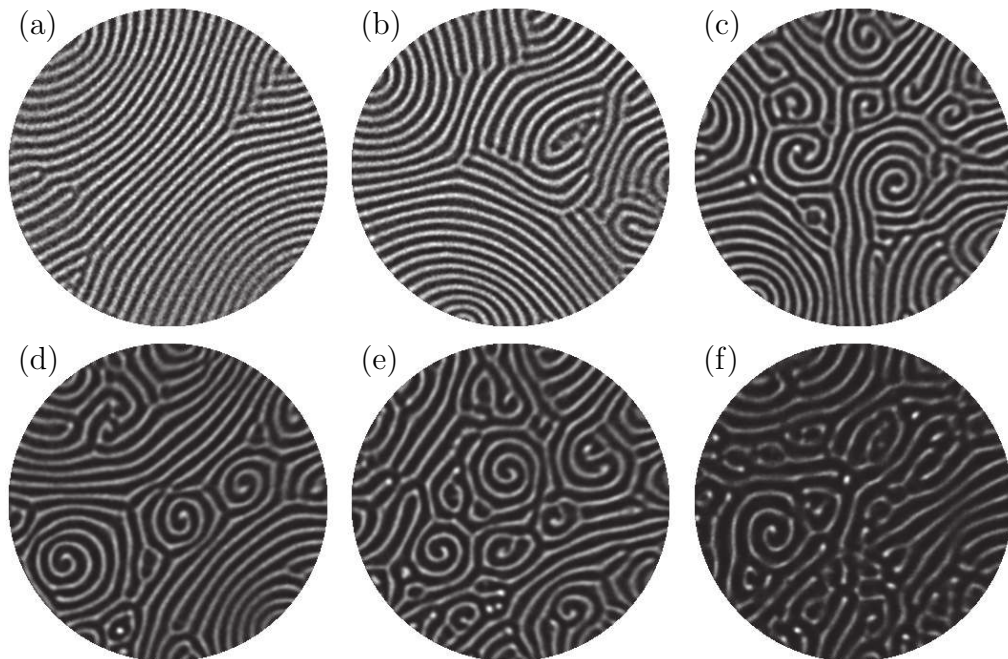
Figure 1.1: Shadowgraph images of Rayleigh-Bénard convection show hot upwelling and cold downwelling flows as dark and bright regions, respectively. As the temperature gradient is increased beyond a critical value (a)-(f) the spatiotemporal complexity of the flow gradually increases. Adapted from H. Kurtuldu, "New Methods of Characterizing Spatio-temporal patterns in Laboratory Experiments," Ph.D. dissertation, School of Physics, Georgia Institute of Technology, Atlanta, Georgia, 2010 [7].

heat transport is purely conductive. If the temperature gradient is sufficiently large, however, buoyancy effects become dominant and the flow undergoes a transition to a simple convective state with uniform convection rolls [5]. Increasing the temperature gradient further causes the flow to undergo a series of transitions to states of increasing spatiotemporal complexity and eventually leads to turbulence (see Figure 1.1). The study of transition in Rayleigh-Bénard convection and other flows that undergo supercritical transitions has been instrumental in the development of the theories of pattern formation and nonlinear dynamics of extended systems [5, 6].

Another class of flows exists for which the transition to turbulence is very different. For these flows, linear stability analysis predicts that the laminar solution is stable up to some critical Reynolds number Re_c. However, experiments show that these flows become
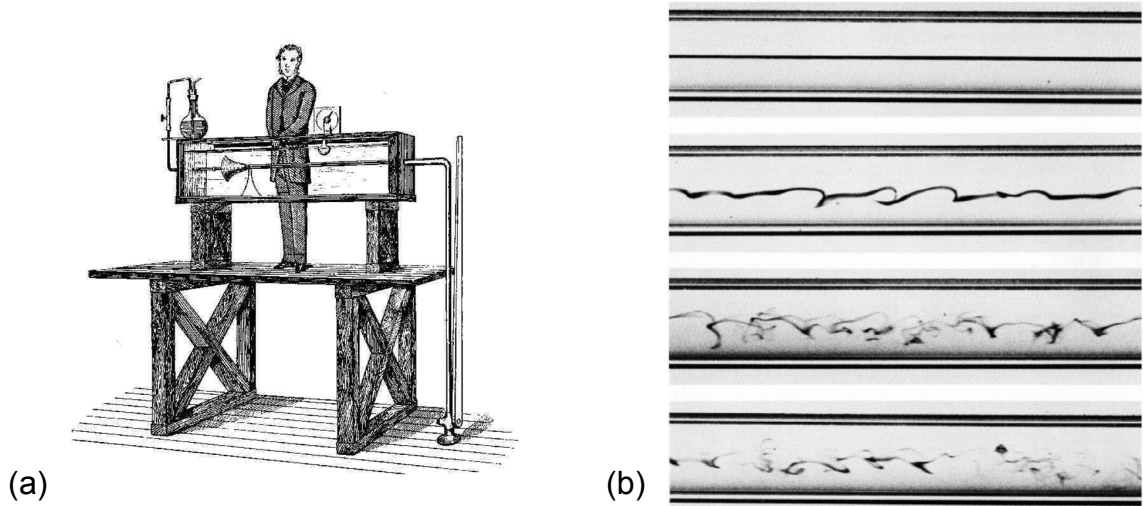
Figure 1.2: (a) The subcritical nature of the transition to turbulence in pipe flow was first observed in the pioneering experiments of Osborne Reynolds. Reynolds noticed that as the dimensionless control parameter $Re = Ud/\nu$ increased beyond a certain value, a filament of dye injected along its center line suddenly became incoherent and disorganized. For pipe flow, the U is the mean flow rate in the pipe and d is the pipe diameter. (b) A modern realization of Reynolds's experiment shows the sudden onset of disorder with increasing Reynolds number (top to bottom). (a) is adapted from O. Reynolds, *Papers on Mechanical and Physical Subjects, Vol. II* p. 71, 1901 Cambridge, UK: Cambridge University Press. Copyright 1901 by Cambridge University Press. (b) is adapted from M. Van Dyke, *An Album of Fluid Motion*, p. 61, 1982, Stanford, California: Parabolic Press. Copyright 1982 by Milton Van Dyke.

turbulent at Reynolds numbers significantly lower than Re_c.[1] Furthermore, as the flow transitions to turbulence, it does not visit a series of progressively more complex flow patterns as in the supercritical transition scenario but instead bypasses these and makes a direct transition to a state with a high degree of spatiotemporal complexity. Flows that follow this route to turbulence are said to undergo a *subcritical* transition to turbulence. Subcritical transitions are much less well understood than supercritical transitions and have been the subject of much recent work [8–11]. Examples of flows that undergo a subcritical transition to turbulence include the pressure-driven flow in a cylindrical pipe (see Figure 1.2) and the shear-driven flow between two parallel plates [10], which is known as plane Couette flow.

---

[1]For many canonical shear flows, including pipe flow and plane Couette flow, linear stability theory predicts that the laminar flow is stable for *all* Reynolds numbers (i.e., $Re_c \to \infty$).

1.2 Taylor-Couette Flow

Most flows become turbulent via either the supercritical route or the subcritical one only. One important exception is the flow in the gap between concentric rotating cylinders (see Figure 1.3). Known as Taylor-Couette flow after the seminal contributions of G.I. Taylor and M. Couette, this flow is most famous for its role in the development of hydrodynamic stability theory and for the wide variety of flow regimes that it can exhibit depending on the rotation rates and relative sizes of the two cylinders.

The Taylor-Couette geometry is specified by the radius of the inner cylinder r_i, the radius of the outer cylinder r_o, and the height of the fluid column between them H. The inner cylinder rotates with angular velocity ω_i and the outer one rotates with angular velocity ω_o. Dimensional analysis shows that four nondimensional parameters are sufficient to characterize the system. One choice of control parameters that has been historically popular with experimentalists (and which will be used throughout most of this work) is to define two Reynolds numbers and two geometric parameters as follows:

$$
\begin{aligned}
Re_i &= \frac{r_i \, \omega_i \, d}{\nu}, \\
Re_o &= \frac{r_o \, \omega_o \, d}{\nu}, \\
\eta &= \frac{r_i}{r_o}, \text{ and } \Gamma = \frac{H}{d},
\end{aligned}
\tag{1}
$$

where $d = r_o - r_i$ and ν is the kinematic viscosity of the fluid. This choice is convenient because for a fixed geometry it nondimensionalizes the problem in terms of the readily accessible boundary conditions. The inner cylinder Reynolds number Re_i corresponds to the nondimensional linear velocity of the inner cylinder surface. Similarly, the outer cylinder Reynolds number Re_o corresponds to the nondimensional linear velocity of the outer cylinder wall. The geometrical parameters η and Γ capture the curvature and spanwise aspect ratio of the flow, respectively.[2] More recently, Dubrulle et al. have suggested that (Re_i, Re_o, η) should be replaced with an alternative set of parameters (Re_s, R_ω, R_c). These parameters are based on dynamical considerations and separate the effects of shear and

---

[2]η also sets streamwise aspect ratio Γ_θ. For example, if Γ_θ is defined in terms of ratio of the mean circumference to the gap between between the cylinders, then $\Gamma_\theta = \pi \, (r_o + r_i)/(r_o - r_i) = \pi \, (1 + \eta)/(1 - \eta)$.
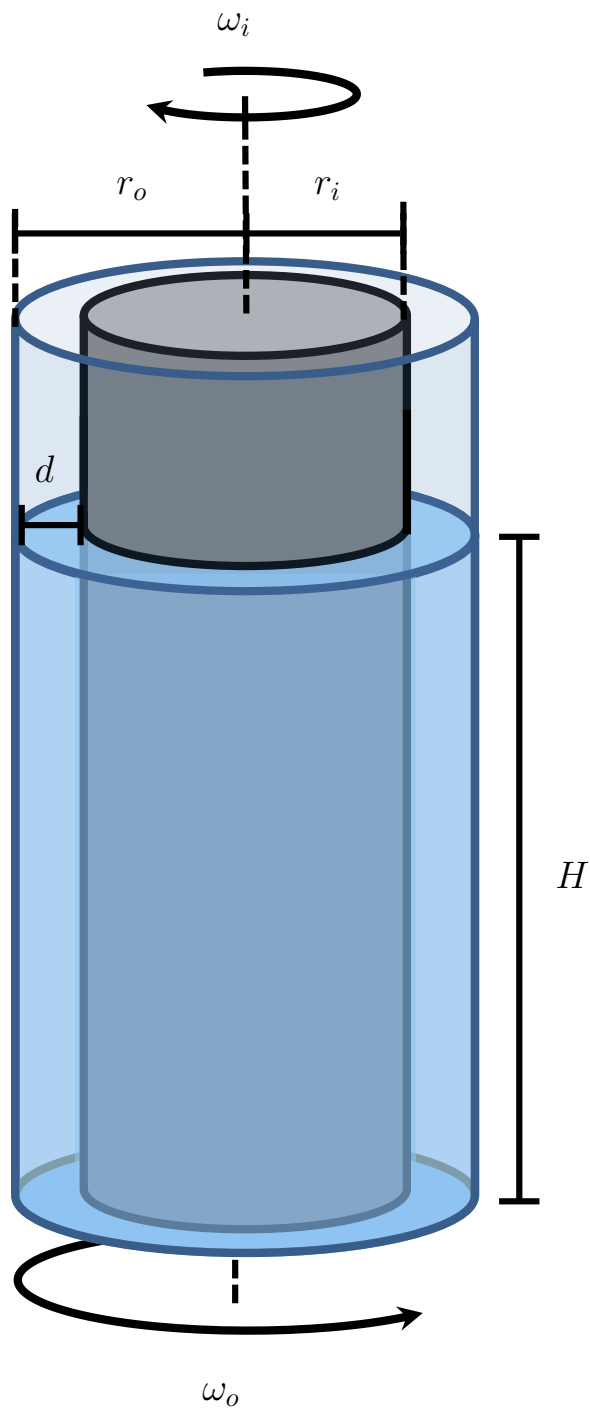
Figure 1.3: Studied by researchers going as far back as Newton, the flow of the fluid between two coaxial rotating cylinders has come to be known as Taylor-Couette flow in honor of seminal contributions by Maurice Couette and Geoffrey Ingram Taylor.

rotation, allowing the direct comparison of flow regimes in Taylor-Couette flow with those in other rotating shear flows [12]. The definition of these parameters and their use will be discussed in Section 3.5.5 as part of the analysis of the lifetimes of turbulent transients in weakly co-/counter-rotating Taylor-Couette flows.

For low rotation rates, fluid elements in Taylor-Couette flows simply follow circular paths as would be expected from symmetry considerations. This featureless flow is called *circular Couette flow*. However, if the inner cylinder rotation rate exceeds a certain critical value, the flow undergoes a bifurcation that breaks the axial symmetry and results in a stack of axisymmetric, toroidal vortices known as *Taylor vortices*. As the rotation rate of the inner cylinder is increased further, the Taylor vortices become unstable themselves, giving way to a series of progressively more complicated states famously described by Coles [14] and by Andereck, Liu, and Swinney [13]. The plethora of possible flow states is illustrated in Figure 1.4. This supercritical transition to turbulence is analogous with transition in Rayleigh-Bénard convection.[3] Experimental and theoretical studies of these two systems have played a fundamental role in showing the validity of abstract mathematical ideas from dynamical systems theory in real-world physical systems.

Although Taylor-Couette flow is most famous for its supercritical transition to turbulence, it can also make the transition following a subcritical route. When outer cylinder rotation dominates (a notion that will be made more specific in Chapter 2), linear stability analysis predicts that the flow will be stable to infinitesimal perturbations for all Re_o [16]. However, linear stability does not preclude the growth of perturbations of *finite amplitude*. If Re_o is sufficiently large, finite-amplitude perturbations can grow. Instead of leading to a series of increasingly more complex states, these instabilities lead directly to highly complex states typically featuring spatiotemporal intermittency, as shown in Figure 1.5.

---

[3]The analogy between the supercritical transition to turbulence in Taylor-Couette flow and the transition to turbulence in Rayleigh-Bénard convection is more than qualitative. It turns out that in certain regimes the two problems can be mapped onto each other mathematically. For more details, see the paper by Prigent et al. [15].

(a)

(b)
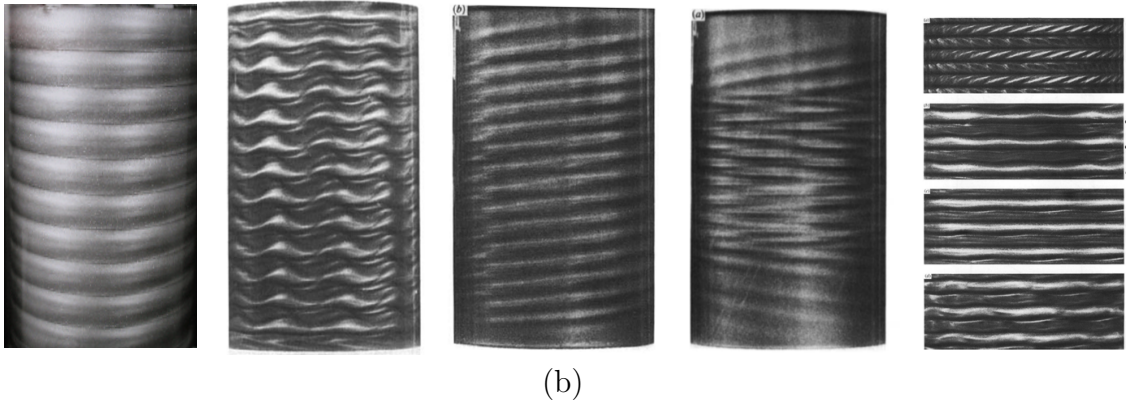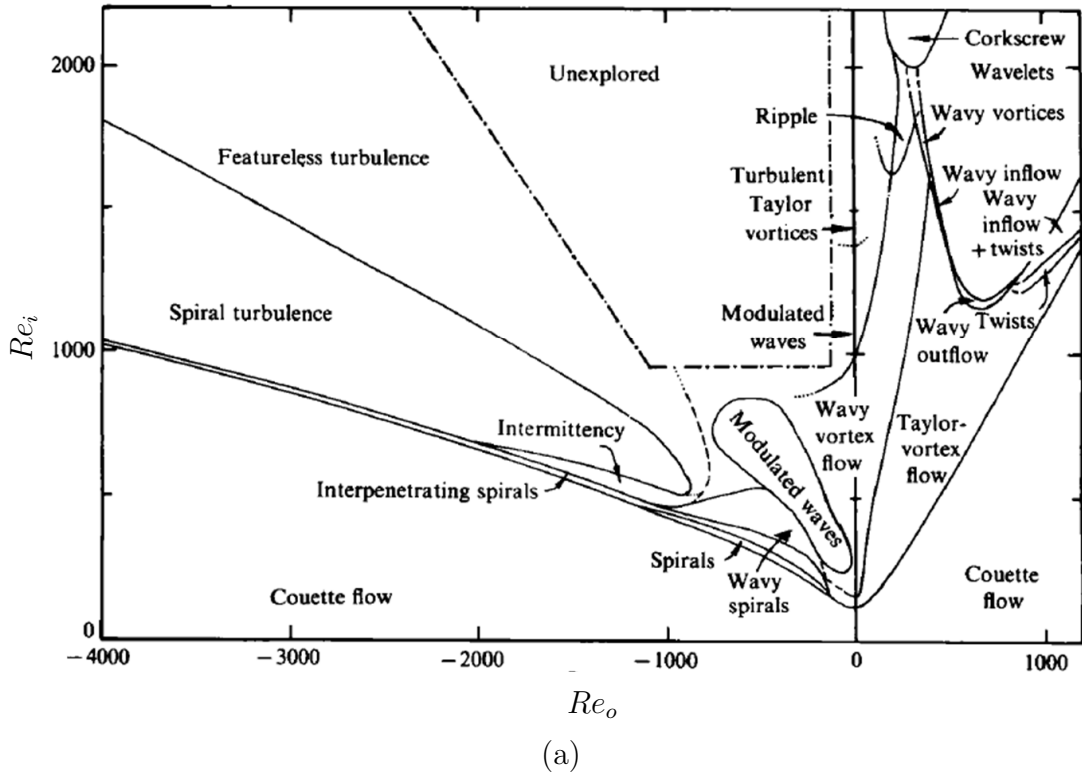
Figure 1.4: (a) Andereck, Liu, and Swinney showed that, like Rayleigh-Bénard convection, Taylor-Couette flow undergoes a series of bifurcations as the driving parameters Re_i and Re_o are varied [13]. These bifurcations are driven by instabilities that arise when fast moving fluid near the inner cylinder overcomes viscous damping forces and gets centrifuged outward. (b) Kalliroscope visualizations of various flow regimes. Adapted from C.D. Andereck et al., "Flow regimes in a circular Couette system with independently rotating cylinders," J. Fluid Mech., p. 155, 1986, Cambridge, UK: Cambridge University Press. Copyright 1986 by Cambridge University Press.

(a)

(b)

(c)

(d)

(e)

(f)
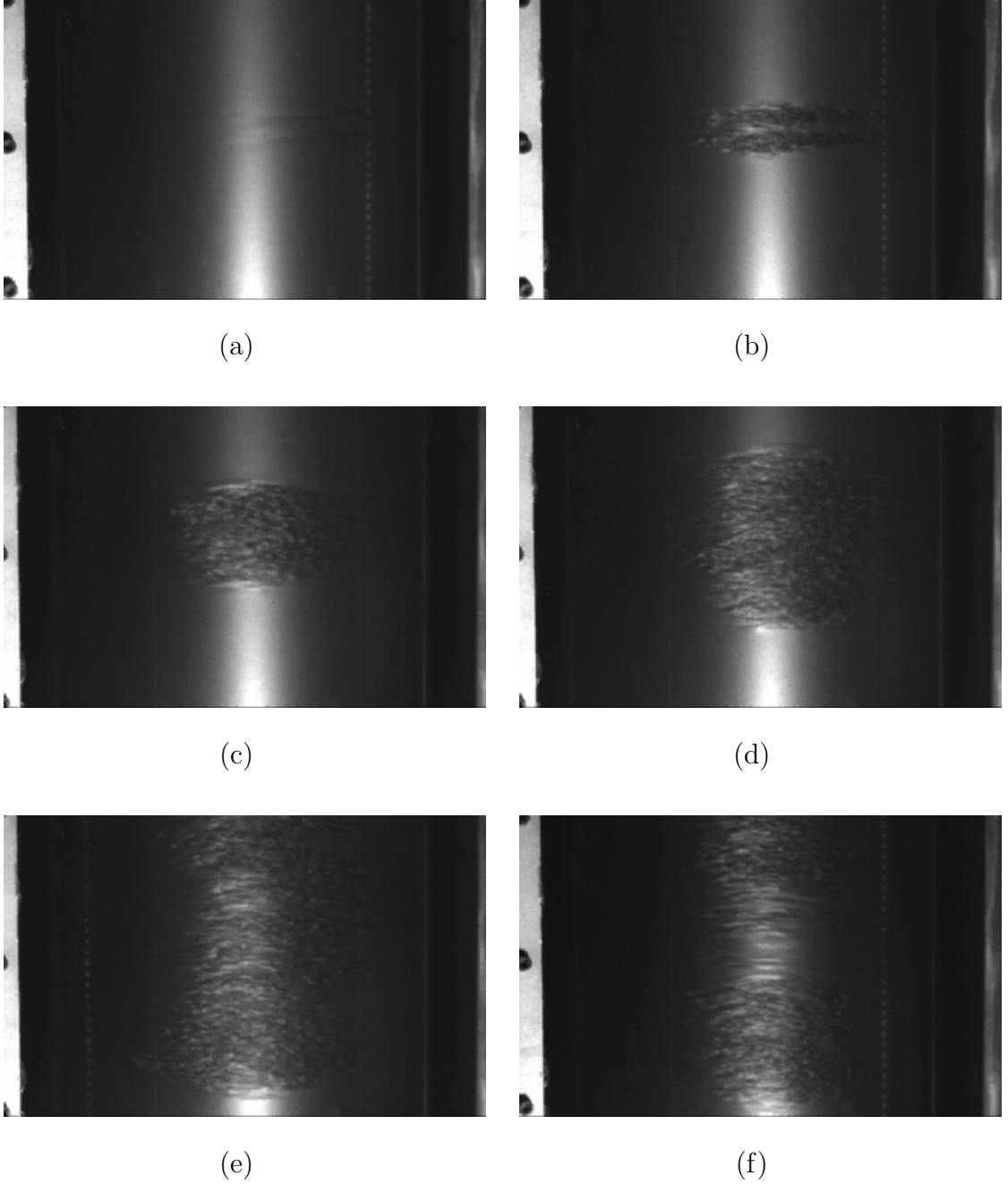
Figure 1.5: When the flow is dominated by the rotation of the outer cylinder, Taylor-Couette flow is stable to infinitesimal perturbations. However, if a perturbation of finite amplitude is applied to the flow, it can grow, bypassing the pattern-forming bifurcations of flows dominated by inner cylinder rotation, and go directly to turbulence. (a) Taylor-Couette flow is perturbed by a small injection of fluid, barely visible here as two horizontal stripes. (b)-(e) The perturbation grows and forms a patch of turbulence. (g) Subcritical transitions, such as this one, are often characterized by spatiotemporal intermittency and the coexistence of laminar and turbulent domains. This sequence of images was taken at $Re_o = 3000$ with the inner cylinder fixed. The radius ratio η was 0.905 and the aspect ratio Γ was 40.

1.3   Transitional Turbulence from the Dynamical Systems Point of View

When dealing with turbulence, the primary weapon in the fluid dynamicist's arsenal has long been the statistical approach pioneered by Reynolds, Taylor, Prandtl, von Kárman, and Kolmogorov.[4] In this framework, turbulence is viewed as a stochastic process where the velocity field fluctuates randomly about a mean flow. Starting from empirically motivated models for the fluctuations, the statistical approach has proven quite successful in describing the mean behavior of turbulent flows at very high Reynolds numbers [17]. This success, however, does not carry over to moderate Reynolds numbers. Significant challenges remain, including the central problem of linking the observed stochastic fluctuations to the deterministic Navier-Stokes equations that govern the flow. As put by Eberhard Hopf in 1948 [19], "The ultimate goal... must be a rational theory of statistical hydrodynamics where... properties of turbulent flow can be mathematically deduced from the fundamental equations of hydromechanics."

In his paper, Hopf laid out a research program by which such a theory might be arrived at. He proposed that solutions of the Navier-Stokes equations could be thought of as existing in an infinite dimensional state space, where each velocity field corresponds to a point. Within this infinite space of all conceivable velocity fields, Hopf conjectured that there is finite-dimensional manifold corresponding to flows that are actually permissible by the Navier-Stokes equations. This manifold is called the *inertial manifold* and its dimensionality is governed by the effects of viscosity. At low Re, viscosity damps out fluctuations and smooths out spatial gradients, collapsing the inertial manifold to a single point that corresponds to the laminar flow. At higher Re, inertia becomes dominant and the space of allowable flows grows, increasing the complexity of the inertial manifold. In this view, turbulence arises as the flow visits different regions of the inertial manifold. Unfortunately, Hopf was unable to pursue his proposed research program due to the limited computational power available in 1948, leading him to lament, "The great mathematical difficulties of these important problems are well known and at present the way to a successful attack on them

---

[4]The statistical theory of turbulence is reviewed in the classic book by Tennekes and Lumley [17] and more recently in the book by Pope [18].
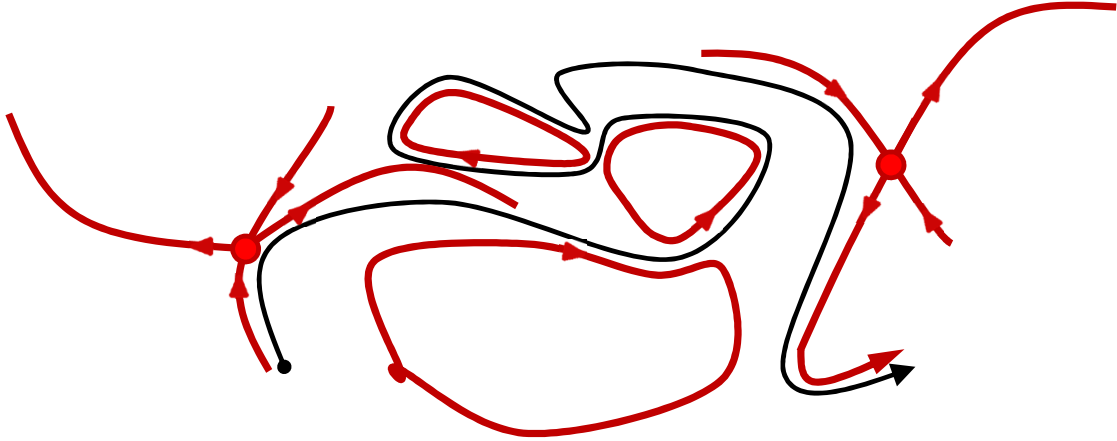
Figure 1.6: In the dynamical systems picture of turbulence, a turbulent flow corresponds to a trajectory (black line)in a high-dimensional state space. The trajectory is guided by hyperbolic dynamical objects called *exact coherent structures* (ECS) and their stable and unstable manifolds (shown in red). When in the neighborhood of a particular ECS, the turbulent flow exhibits dynamics that are qualitatively similar to those of the ECS and has similar physical properties such as energy dissipation. Because the inertial manifold is compact, a trajectory will visit the neighborhood of a given ECS many times, leading to the close recurrences observed empirically in turbulent flows. The amount of time that a trajectory spends near a particular ECS is determined by the ECS's stability. This means that the time-average of any quantity of interest over a trajectory can be approximated by an average of that same quantity calculated for the ECS's whose neighborhoods the trajectory visits, weighted by the amount of time that the trajectory spends in each neighborhood. This procedure is formalized within the framework of periodic orbit theory [20, 21].

seems hopelessly barred."

The exponential growth in computing power of the last decade has made it possible to revisit Hopf's dynamical theory of turbulence. Drawing on advances in the study of low-dimensional nonlinear systems, a dynamical picture of turbulence has begun to emerge.[5] Central to this picture is the idea of recurrent patterns. As a turbulent trajectory evolves on the inertial manifold, it often revisits the same neighborhoods in state space, showing qualitatively similar, although never exactly repeating, spatial and temporal features characteristic of that neighborhood. The trajectories themselves are guided by a set of solutions

---

[5]Some of the early successes of this research program are reviewed in the books by Holmes et al. [22] and by Bohr et al. [23]. More recent advances are reviewed in the papers by Eckhardt et al. [9, 10] and by Gibson, Halcrow, and Cvitanović [24], in the online tutorial by Gibson and Cvitanović [25], in the review by Kawahara, Uhlmann and van Veen [26], and in the proceedings of the IUTAM Symposium on the Laminar-Turbulent Transition and Finite Amplitude Solutions [8].

of the Navier-Stokes equations called *exact coherent structures* and their stable and unstable manifolds [24], as shown schematically in Figure 1.6. Although never observed directly in experiments, these weakly unstable hyperbolic objects correspond to stationary states (fixed points), periodic orbits, traveling waves and other coherent structures [10]. Calculating these solutions numerically is now feasible [24, 27–30] and efforts are underway to use them to calculate dynamical averages within the framework of periodic orbit theory [31, 32].

While this program has made great strides in the last decade, most of this progress has been limited to numerical studies. Two important exceptions are experimental papers by Hof et al. in 2004 [33] and by de Lozar et al. in 2012 [34]. The former study reported the first experimental evidence of the existence of unstable traveling wave solutions in pipe flow. The latter study went one step further by using experimental data as a seed for a numerical search that yielded exact coherent structures embedded in the so-called *edge state* that separates the laminar solution from turbulent dynamics in state space. Beyond these two studies, experimental evidence for the existence and relevance of exact coherent structures in laboratory flows is scarce.

Experimental investigations of Taylor-Couette flow have a long history of informing dynamical systems research and have provided key insights in the development of the theory of bifurcations, chaos, and pattern formation [5, 6, 35]. Interestingly, however, Taylor-Couette flows have largely been excluded from the push to develop a dynamical theory of turbulence along the lines described above. This may be in part because the field has been mostly the realm of theorists and numericists, who have eschewed the complications introduced by flow curvature and rotation and concentrated mostly on pipe and plane Couette flows. In this dissertation, the viewpoint is taken that even though Taylor-Couette flow may introduce additional complexity, it opens the possibility of high-precision experimental studies of the subcritical transition that are not practical in other simple shear flows. In certain flow regimes, Taylor-Couette flow shares many of the features observed in transitional shear flows and serves to complement existing studies in other geometries.

The rest of this dissertation is organized as follows: Chapter 2 presents a comprehensive review of the literature concerning the subcritical transition to turbulence in Taylor-Couette

flows. Emphasis is given to experimental investigations of linearly stable regimes where the inner cylinder is at rest. Chapter 3 presents the first systematic study of long-lived super-transients in Taylor-Couette flow with the aim of determining the correct dynamical model for turbulent dynamics in the transitional regime. Part of this work was previously reported in D. Borrero-Echeverry et al., *Phys. Rev. E* **81**, 025301(R), 2010. That work is discussed in more detail and additional unpublished results regarding the effects of system size, boundary conditions, and inner cylinder rotation on transient lifetimes are reported. Chapter 4 presents the results of experiments regarding the stability of Taylor-Couette flow to finite-amplitude perturbations in the form of injection/suction of fluid from the test section. Critical thresholds for transition are reported and their scaling with Reynolds numbers is discussed. Chapter 5 presents the results of axisymmetric simulations of laminar Taylor-Couette flows that can be used to calibrate tomographic particle image velocimetry (PIV) measurements. Chapter 6 discusses in detail the implementation of time-resolved tomographic PIV in Taylor-Couette flow and presents preliminary measurements of the growth of a turbulent spot from a finite-amplitude perturbation, as well as measurements of some basic laminar flows. This technique allows the measurement of three-dimensional velocity fields in a volume and holds great promise in elucidating the complex dynamics of turbulence at moderate Re. Chapter 7 provides a summary of the main results from the earlier chapters.

The main document is supplemented with a series of appendices. Appendix A provides tables of the data gathered in the experiments of Chapter 3. Appendix B contains a series of Matlab codes used in this work, including details pertaining to computer control of various hardware. Appendix C contains mechanical drawings for parts of the experimental apparatus that were constructed as part of this research. Appendix D contains mechanical drawings for a new inner cylinder that allows for the injection/withdrawal of fluid to/from the test section as a source of finite-amplitude perturbations. Appendix E contains mechanical drawings for the three-dimensional calibration target developed for the tomographic PIV measurements. Appendix F provides technical details of the distributed computing cluster that was assembled for the processing of tomographic PIV data.

CHAPTER II

HISTORICAL INVESTIGATIONS OF THE SUBCRITICAL TRANSITION TO TURBULENCE IN TAYLOR-COUETTE FLOW

"Those were the days when plumbers were plumbers..."

— Predrag Cvitanović

The history of Taylor-Couette flow is a long and storied one. The literature concerning pattern forming bifurcations driven by inner cylinder rotation and their role in the supercritical transition to turbulence is extensive (see, e.g., the book by Koschmieder [5], the bibliography compiled by Tagg [36], the review articles by Tagg [35, 36] and by Di Prima and Swinney [37], and the expansive study by Andereck et al. [13]). The literature, however, is much sparser regarding flows where outer cylinder rotation dominates and the transition to turbulence is subcritical. These sources are scattered in the literature and no comprehensive review of them exists. For this reason, an attempt has been made here to review as much of the prior work in this regime as possible. Emphasis is given to experimental investigations of transitional flows where the inner cylinder is at rest or of weakly counter-rotating subcritical flows.

2.1 The Early Years: Newton, Coulomb, and Stokes, 1687-1848

The first theoretical discussion of the flow between concentric cylinders is attributed to Newton in 1687, who in Section IX of Book II of the *Principia* discussed the laminar flow that occurs when the two cylinders co-rotate such that "the times of their revolutions be as their semidiameters" (i.e., the linear velocity of the walls for both the cylinders is the same) [38]. Newton incorrectly arrived at the conclusion that in this case, the velocity profile is constant (independent of radial position), an error that would stand uncorrected for 161 years.

The first experimental investigation of the flow between concentric cylinders is attributed
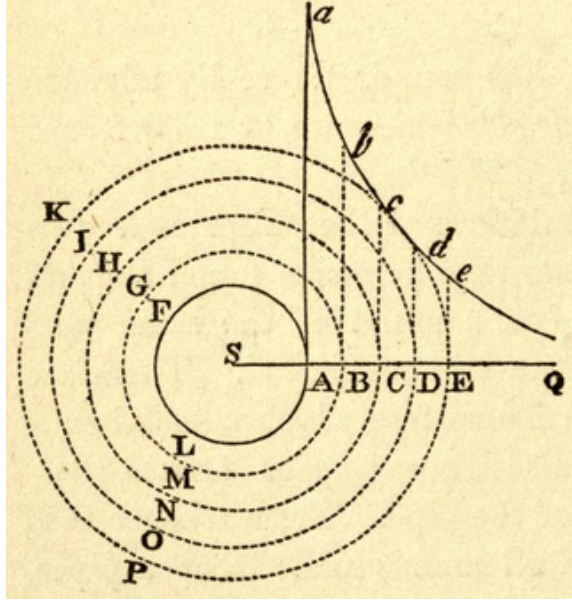
Figure 2.1: Newton's illustration of the flow due to a rotating cylinder in an infinite fluid. By realizing that a stream surface could be be replaced by a solid wall moving with the same velocity, Newton made the first, if incorrect, prediction of the laminar flow between rotating cylinders. Adapted from I. Newton, *Philosophiæ Naturalis Principia Mathematica*, (trans. Andrew Motte), 1846, New York, NY: Daniel Adee.

to Marcel Coulomb, who in 1794, constructed the earliest recorded concentric cylinder apparatus in an attempt to measure "liquid friction" [39]. Coulomb's apparatus was driven by the energy stored in the torsion of a wire from which the inner cylinder was suspended. Coulomb's apparatus was not very successful as a rheometer and he continued his work using other techniques that were in vogue at the time. It would not be until the 1880s when electrical motors allowed researchers to carefully regulate the rotation rates in their apparatus that the use of concentric cylinders as rheometers became popular [40].

In 1848, George G. Stokes discovered Newton's mistake and derived the correct expression for the laminar flow between arbitrarily rotating infinite concentric cylinders [41]. He showed that the azimuthal velocity v_θ as a function of the radial position r is given by

$$v_\theta(r) = Ar + \frac{B}{r}, \tag{2}$$

where

$$A = -\omega_i \frac{\eta^2 - \mu}{1 - \eta^2} \text{ and } B = \omega_i r_i{}^2 \frac{1 - \mu}{1 - \eta^2}, \tag{3}$$

r_i and r_o are the radii of the inner and outer cylinders, respectively, ω_i and ω_o are their angular frequencies of rotation, $\mu = \omega_o/\omega_i$, and $\eta = r_i/r_o$. The axial and radial components of velocity v_z and v_r are zero. Today, this flow is known as circular Couette flow. Stokes went on to suggest that observing such flows would help determine the appropriate boundary conditions at solid walls, which were still under debate at the time. He also predicted that flows dominated by inner cylinder rotation would be centrifugally unstable, meaning that fast moving fluid near the inner cylinder would get centrifuged outward, and that this would lead to turbulence [41].

2.2 The Experimentalists: Couette and Mallock, 1880-1900

The final two decades of the 19$^\text{th}$ century saw a great number of researchers turning their attention to the study of flows between concentric cylinders. In 1881, Max Margules derived a formula that allowed the measurement of fluid viscosity by measuring the torque exerted by the fluid on one of the cylinders in a Taylor-Couette configuration as the other was rotated at constant speed [42]. This inspired a variety of experimentalists to construct concentric cylinder apparatus starting with John Perry. Perry appears to have built a Taylor-Couette apparatus as early as 1882, but his work was not published until 1893 [43] and was largely ignored [44].[1] Working independently in Paris and Cambridge, Maurice Couette and Arnulph Mallock conducted experiments in apparatus driven by electric motors publishing their initial results in 1888.

Mallock's 1888 paper is mostly concerned with measurements of the viscosity of water, which he measured by rotating the outer cylinder and measuring the torque on the inner [45]. In this paper, Mallock notes the presence of a secondary flow due to the finite size of his apparatus. He also notes that these effects are minimized when the ratio of the length of the cylinders to the gap between cylinders is large. Now known as Ekman cells, these secondary flows are driven by deviations from the ideal infinite cylinders considered by Stokes [13, 46]. Although such finite-size effects have been shown to play an important role in determining the dynamics of centrifugally unstable Taylor-Couette flows (see Ref. [47] for examples),

---

[1]Perry's device was more akin to a modern-day "double cup" rheometer in design than to a typical Taylor-Couette apparatus.

their role in the subcritical transition to turbulence is still a subject of debate [48–55].

In 1896, Lord Kelvin presented to the Royal Society a follow-up paper by Mallock where Mallock discussed the effect of inner vs. outer cylinder rotation and system size on his viscosity measurements, as well as his efforts to minimize end wall effects [56]. In it, Mallock reported that if the inner cylinder is rotated "the motion of the fluid was eddying and unstable, even at very low velocities" and therefore not suitable for viscosity measurements. As noted by Donnelly, the lowest rotation rate for the inner cylinder used by Mallock exceeded the critical rotation rate for the emergence of Taylor rolls, leading Mallock to arrive at the incorrect conclusion that Taylor-Couette flows with inner cylinder rotation are always unstable [42]. Mallock also reported that when he rotated the outer cylinder instead, the torques measured with his apparatus increased linearly with rotation speed (as predicted by Margules for circular Couette flow) until, at some critical speed, the torque readings began to fluctuate erratically. At even higher rotation rates, the torque readings stabilized again and were observed to vary smoothly with increasing cylinder rotation rate. However, the readings no longer scaled linearly with rotational speed of the cylinder. Mallock also noticed that if the system was set to a rotation rate just below the critical one, where the torque measurements became erratic, any small perturbation of the system would cause the torque readings to fluctuate wildly before the torque readings stabilized to the value measured before the perturbation. These episodes lasted for extended periods of time and had "irregular" durations. Mallock noted that they were also correlated with the appearance of "small dimples and elevations" on the free surface of the water.

Across the English Channel, Couette was conducting his own experiments in the laboratory of Gabriel Lippmann at the Sorbonne [57]. Couette presented his preliminary results in a series of notes to the French Academy of Science in 1888 [57]. In these notes and his 1890 doctoral thesis, Couette described a series of experiments in which he measured the viscosities of water and air using a concentric cylinder apparatus of his own design in which the

outer cylinder was driven by an electric motor. It appears that Couette realized that capillary viscometers would provide more accurate viscosity measurements[2], but was fascinated by his observations of rotating flows. Couette made a concerted effort to verify the validity of the equations for the motion of liquids proposed by Navier in 1823[3] and carefully studied the relevance of the no-slip boundary condition [40]. The no-slip boundary condition states that, at a solid boundary, the relative velocity between the fluid and the boundary vanishes. Although now generally accepted as the appropriate boundary condition in most settings, the no-slip boundary condition was still under scrutiny in Couette's time. Like Mallock, Couette realized that the boundary conditions at the ends of his cylinders would affect his measurements and designed a system of guard rings to help mitigate these effects.

(a) **(b)**
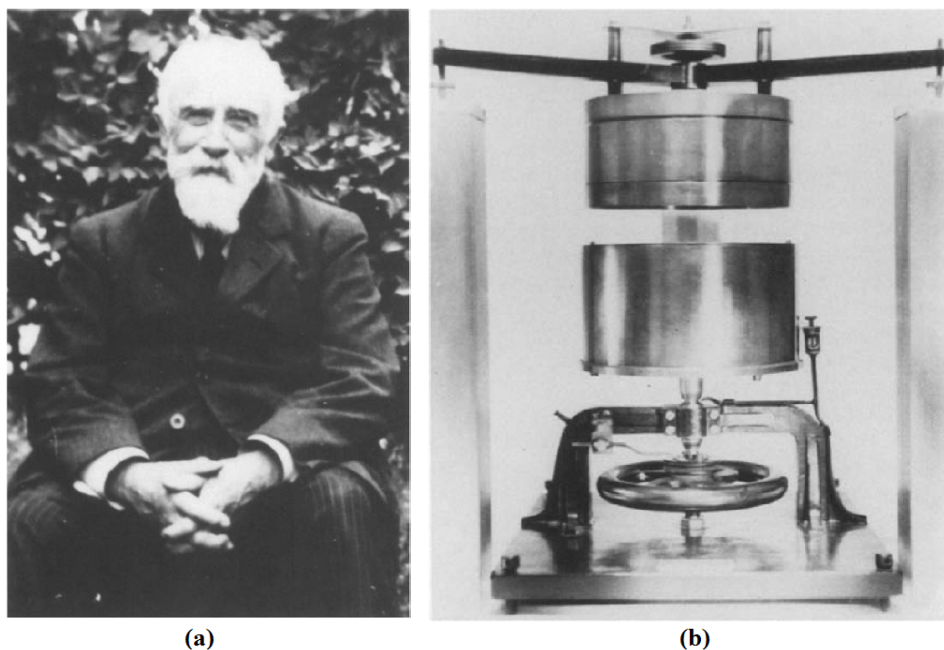
Figure 2.2: (a) Maurice Couette performed extensive studies of the flow between rotating concentric cylinders. (b) His original experimental apparatus was rediscovered in a storeroom at the Catholic University of the West in 1990. Adapted from J.M. Piau, M. Bremond, J.M. Couette, and M. Piau, "Maurice Couette, one of the founders of rheology," *Rheologica Acta* **33**, p. 357-368, 1994. Copyright 1994 by Springer Berlin Heidelberg.

---

[2]Couette also performed careful studies on the flow of liquids through small pipes and made important contributions to the development of capillary tube rheometers. Couette's many contributions to rheology are highlighted in the biography by Piau et al. [57] and in the reviews by Dontula [44] and Piau and Piau [40].

[3]Together with Stokes's equations for viscous flow, these equations are now known as the Navier-Stokes equations.

Couette's torque measurements showed the same general trends as Mallock's. At low rotation rates the torques scaled linearly with rotation rate, becoming erratic at intermediate rotation rates, and finally scaling nonlinearly with rotation rate at high rotation rates. Couette interpreted this as evidence of the existence of two forms of fluid motion: one given "exactly and not approximately by simplest integrals of the Navier equation" and one which was not [42,57]. Couette also made substantial theoretical contributions, performing detailed calculations of fluid flows near the walls of slowly oscillating bodies. He also analyzed the effects that non-concentricity of the cylinders would have on his measurements and developed a theory to compensate for them [57]. Unfortunately, Couette's work on rotating flows was not continued after he left the Sorbonne and his apparatus lay "unused in a store-room, unknown to most people" [57] at the Catholic University of Angers (now the Catholic University of the West) where he taught for the rest of his career. It was not until 1990 that it was discovered and refurbished by Michel Brémond and Maurice Dubois and displayed at the university's exhibition of historic scientific instruments [57], Figure 2.2.

2.3 Linear Stability: Rayleigh and Taylor, 1916-1923

The hydrodynamics literature concerning the flow between concentric cylinders is rather sparse during the three decades following the experiments of Couette and Mallock [58].[4] One important exception is Lord Rayleigh's 1917 paper "On the Dynamics of Revolving Fluids" [61]. Motivated by meteorological considerations, Rayleigh derived a general criterion for the stability of rotating, *inviscid* flows. Rayleigh's argument proceed as follows:[5] A rotating fluid in equilibrium will flow in such a way that the centrifugal force is balanced by the radial pressure gradient, i.e. $\partial p/\partial r = \rho v(r)^2/r$. Suppose that a fluid element originally at $r = r_1$ is moved outward to a new radial position r_2. The flow will be stable if the fluid element experiences a restoring force that tends to move it back toward its original position. For an incompressible fluid this requires that $v(r_2)^2/r_2 > v(r_1)^2/r_1$ for all $r_2 > r_1$. Mathematically, this can be expressed in terms of the angular velocities ($\omega = v/r$) as:

---

[4]Some references exist in the rheology literature during this period. For some representative examples, see the papers by Drew [59] and Gurney [60].
[5]A formal proof is given by Chandrasekhar in Ref. [3].

$$\frac{d(rv)^2}{dr} = \frac{d}{dr}\left(r^2\omega\right)^2 > 0. \tag{4}$$

Rayleigh applied this criterion to the inviscid flow between concentric cylinders and arrived at the conclusion that such flows are always unstable when the inner cylinder rotates and the outer cylinder is stationary and always stable when the outer cylinder rotates and the inner cylinder is stationary. The more general case can be evaluated by inserting the velocity profile derived by Stokes (Eq. 2) into Eq. 4, resulting in the constraint that when

$$\frac{\omega_o}{\omega_i} > \left(\frac{r_i}{r_o}\right)^2 \tag{5}$$

the flow is stable, as summarized in Figure 2.3. Here it can be seen that the Taylor-Couette flow of an inviscid fluid will be unstable for all counter-rotating flows or whenever the ratio of the angular velocity of the outer cylinder to that of the inner cylinder is less than the square of the radius ratio. It is important to note that by construction Rayleigh's criterion only predicts the stability of rotating *inviscid* flows to *axisymmetric* perturbations, meaning that other instability mechanisms are possible.
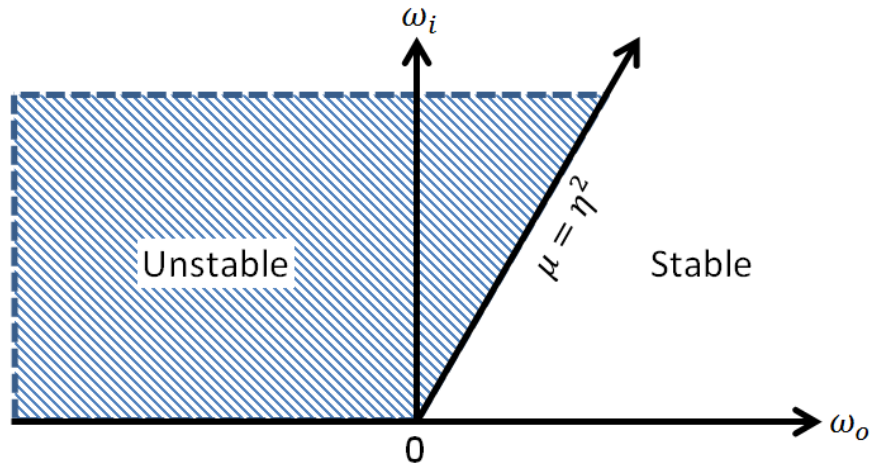
Figure 2.3: Rayleigh's stability criterion for inviscid Taylor-Couette flow. Adapted from *Bénard Cells and Taylor Vortices* by E.L. Koschmieder, 1993, Cambridge, UK: Cambridge University Press. Copyright 1993 by Cambridge University Press.

In 1921 G.I. Taylor, inspired by the theoretical work of Lord Rayleigh and others, began work on a concentric cylinder apparatus [62]. Noting that Couette and Mallock's data dealt almost exclusively with flow configurations were the inner cylinder was held fixed

and were, therefore, not adequate to fully examine the validity of Rayleigh's result, Taylor constructed an apparatus where both cylinders could be rotated independently. The results of Taylor's experiments were reported in his seminal 1923 paper "Stability of a Viscous Liquid Contained Between Two Rotating Cylinders" [2]. In this paper, Taylor successfully applied linear stability theory to the *viscous* flow between concentric cylinders and was able to calculate the critical condition for instability in terms of the rotation rates of the cylinders, their radii, and the fluid viscosity in the narrow gap approximation, i.e. as the radius ratio $\eta \to 1$.[6] Taylor concluded that viscosity played a stabilizing role in some flows that would otherwise be unstable according to Rayleigh's criterion (Eq. 5). Taylor predicted that flows where the outer cylinder rotation dominates (i.e., when the cylinders co-rotate and the angular velocity of the outer cylinder is greater than that of the inner cylinder, so that $\mu > +1$, or when the inner cylinder is held fixed, so that $\mu = \pm\infty$) should be linearly stable at all rotation rates and derived more detailed stability criteria for general co- and counter-rotating flows. Taylor's results are summarized in Figure 2.4.
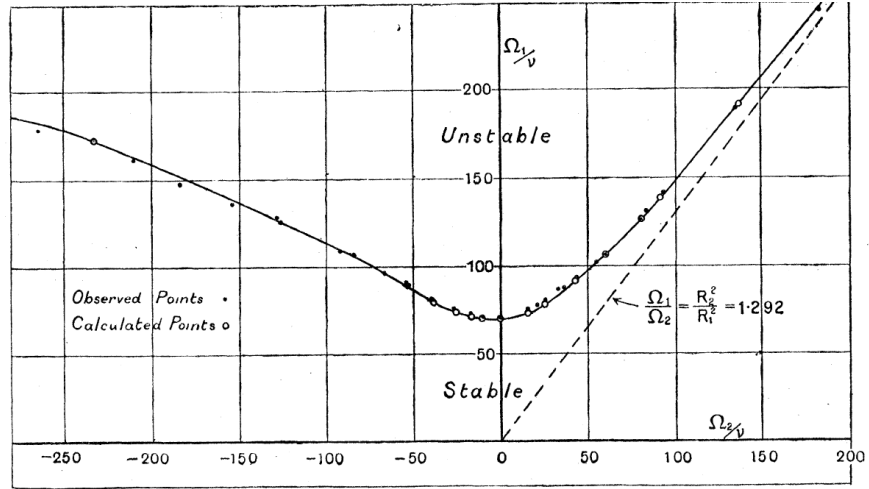
Figure 2.4: Stability diagram for Taylor-Couette flow from Taylor's 1923 paper. Open circles correspond to the theoretically predicted stability boundary. Closed circles correspond to the experimentally observed stability boundary. Adapted from G.I Taylor, "Stability of a Viscous Liquid Contained between Two Rotating Cylinders", *Phil. Trans. R. Soc. Lond. A* **223**, p. 339, 1923. Copyright 1923 by Royal Society Publishing.

---

[6]A more general, modern treatment of this analysis can be found in Chadrasekhar's 1961 book *Hydrodynamic and Hydromagnetic Stability* [3].

Taylor verified his theoretical predictions for stability and for the structure of the super-critical flow fields in a series of flow visualization experiments using dye injections. Before discussing his experimental results, Taylor critiques Mallock's observations on the stability of Taylor-Couette flows and attributes them to deficiencies in Mallock's apparatus. In particular, he criticizes the small aspect ratio of Mallock's apparatus. The aspect ratio Γ of a Taylor-Couette apparatus is defined as the ratio of the height of the cylinders H to the width of the gap $d = r_o - r_i$. Mallock's experiments were conducted at Γ between $\sim$ 8 and 20. Taylor also pointed out that in Mallock's experiments the inner cylinder hung from a torsion wire, which allowed for it to move off-axis. Taylor addressed these issues by mounting both cylinders rigidly on bearings and using a tall test section with $\Gamma \sim 90$. Taylor's experimental results showed an excellent agreement with his theoretical predictions. For flows where $\mu > +1$,[7] where outer cylinder rotation dominates, Taylor wrote that "the motion was completely stable even at the maximum speed of which the apparatus was capable" in contradiction to Mallock's result [2]. Taylor's experiments were confirmed in a 1928 paper by J.W. Lewis, who used aluminum powder suspended in the fluid to visualize the flow [63]. A refinement of this technique by Schultz-Grunow and Heim in the 1950s would prove to be instrumental in the study of Taylor-Couette flows (see Section 2.6).

2.4   The Beginnings of Velocimetry: Taylor and Wendt 1933-1936

For the remainder of the 1920s and into the early 1930s, Taylor turned his attention to a variety of other problems in mechanics. In the mid-1930s he returned to the problem of concentric cylinders. In a 1935 paper, Taylor reported Pitot tube measurements of the velocity profile in the gap between a fixed outer cylinder and a rotating inner cylinder [64] at large Reynolds numbers. This was followed the next year by a two-part paper titled "Fluid Friction Between Rotating Cylinders".

In the first part, Taylor reported a series of measurements of the torque on one cylinder due to the rotation of the other for a variety of radius ratios and Reynolds numbers [65]. For the case where the outer cylinder rotated and the inner cylinder was fixed, Taylor observed

---

[7]Taylor's results regarding flows where inner cylinder rotation dominates are reviewed in chapter 11 of the Koschmieder's book [5].
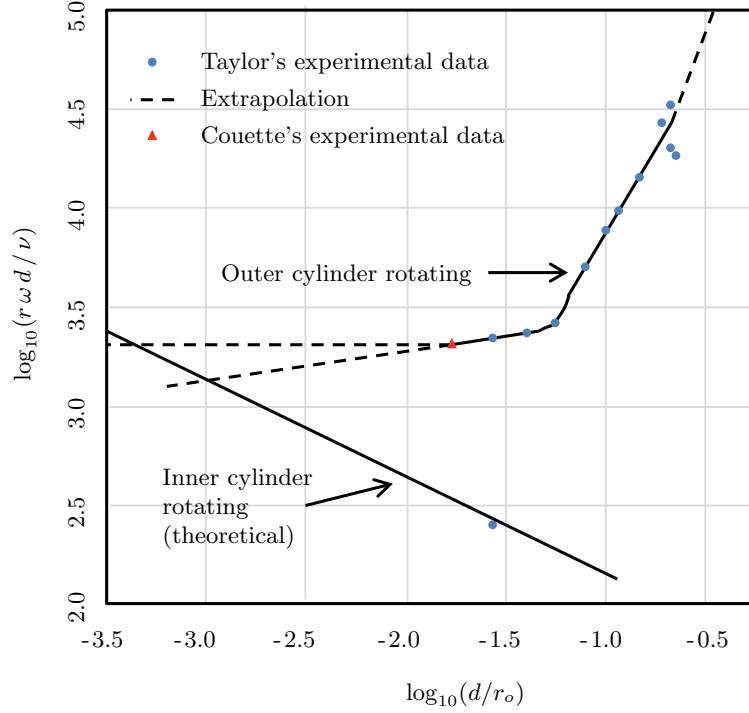
Figure 2.5: Stability boundary for flows driven by the rotation of only one cylinder as a function of normalized gap $d/r_o = 1-\eta$. Taylor's experiments showed that as the radius ratio is decreased below $\eta \sim 0.95$, the Reynolds number where transition occurs spontaneously grows very quickly for flows driven by the outer cylinder. For smaller gaps, the dependence on gap width is much weaker. At the same time, the critical Reynolds number for linear instability increases as the gap becomes smaller. If both curves are extrapolated to $\eta \to 1$, a crossover is observed between $\eta = 0.999$ and $\eta = 0.99955$. Taylor predicted that beyond this point nonlinear instability mechanisms would dominate and direct transition should be observed. Adapted from G.I Taylor, "Fluid Friction Between Rotating Cylinders I – Torque Measurements", *Proc. R. Soc. A* **157**, p. 546-564, 1936. Copyright 1936 by Royal Society Publishing.

(as did Couette and Mallock before him) that as the rotation rate of the outer cylinder was increased the torque scaled as predicted for circular Couette flow (Eq. 2) up to some critical Reynolds number Re_c above which the flow became turbulent and the scaling broke down.[8] He also noted that in between the laminar and turbulent regimes there existed a range of Reynolds numbers for which steady flow could be achieved if the system was prepared with sufficient care, but where "a slight disturbance, such as that produced by a slight rotation of the inner cylinder in the opposite direction of that of the outer one" would

---

[8]It is interesting to note that in his 1923 paper Taylor dismisses Mallock's results even though Taylor's apparatus at the time was not able to reach the Reynolds numbers where Mallock reported observing a transition to turbulence.

"make the flow permanently turbulent". Taylor noticed that if he extrapolated his data on the dependence of Re_c on radius ratio to the limit of $\eta \to 1$ there would come a point when the critical Reynolds number for flows with only the outer cylinder rotating would be lower than the critical Reynolds number for linear instability for flows with only the inner cylinder rotating (see Figure 2.5). He conjectured that at this radius ratio (somewhere between 0.999 and 0.99955) the nonlinear mechanisms that drive the transition to turbulence in flows dominated by outer cylinder rotation would take over and direct transition would be the norm. Following this reasoning, he estimated that the critical Reynolds number for spontaneous transition in plane Couette flow would fall between 315 and 500,[9] which is in good agreement with modern experiments [67].

The second part of Taylor's 1936 paper describes Pitot tube measurements of the velocity profile of a Taylor-Couette flow where the outer cylinder rotates and the inner cylinder is fixed [68]. Taylor reports that even at high Reynolds numbers these flows can sustain significant velocity gradients across the gap, unlike flows where the inner cylinder rotates and the outer is fixed. He also reports that the velocity profile is similar to that predicted by Eq. 2, but that the velocity near the inner cylinder is greater than predicted. He attributes this to the end effects, which tend to push fast moving fluid inwards at the midplane when the end caps are attached to the outer cylinder. Toward the end of this paper, Taylor mentions an earlier paper by Wendt that describes similar measurements, but concludes that quantitative comparison between the experiments is not possible due to the small aspect ratio of Wendt's apparatus.

Fritz Wendt was a doctoral student of Prandtl at Georg-August-Universität Göttingen [69]. In 1933, he published a paper in the German journal *Ingenieur-Archiv* titled "Turbulent Flows Between Two Rotating Coaxial Cylinders" in which he described the main results of his doctoral dissertation [70]. Wendt's paper was the first to study flows far from the regime discussed by Taylor in 1923 [5]. In it, he reported the first measurements of the

---

[9]The Reynolds number for plane Couette flow is conventionally defined in terms of half the gap between planes and half the velocity of one plane relative to the other. Reynolds numbers for Taylor-Couette flow are traditionally defined in terms of the full gap and the speed of the wall. Therefore, the Reynolds numbers for plane Couette flow are a factor of four smaller than those for Taylor-Couette flow with only one cylinder rotating. Additional corrections for curvature are given by Prigent et al. in Ref. [66].

23

velocity and pressure distributions inside the gap, as well as measurements of the torque transferred between the cylinders for a range of aspect and radius ratios. Unlike previous researchers, who concentrated on configurations where only one cylinder rotated, Wendt acquired data for a variety of co- and counter-rotating flows.

Wendt's data showed that even in cases where Taylor's 1923 theory predicted the Couette profile to be stable, a sudden increase in the measured torques occurred at sufficiently large Reynolds numbers and that this transition was hysteretic. Wendt's also studied the effect of varying end conditions on the torque measurements, attaching the bottom end cap of his apparatus to either the inner cylinder or the outer cylinder, or a "split-ring" configuration, where the inner half of the bottom end cap rotated with the inner cylinder and the outer half rotated with the outer cylinder (his experiment had a free surface at the top of the gap). He found that the different end conditions changed the critical rotation rate by about 10%. Wendt's measurements would remain the sole source of experimental velocimetry in counter/co-rotating Taylor-Couette flow at high $Re \sim \mathcal{O}\left(10^5\right)$ until the advent of laser Doppler velocimetry (LDV) in the late 1970s.[10] Wendt also noted that the measured torques depended strongly on the end conditions when the aspect ratio was small.

2.5 Experiments in Liquid Helium II: Hollis-Hallett and Heikkila, 1953-1958

The theory of linear stability successfully employed by Taylor in 1923 continued to advance throughout the 1930s and 1940s, but, as Coles described it in 1965, "experimental work on transition in Couette flow... moved at a somewhat slower pace" with most experiments covering "the same limited ground explored in the earliest work" [14]. The early 1950s brought a series of new experiments on the flow of liquid helium II in Taylor-Couette geometries. While the focus of this dissertation is on the subcritical transition to turbulence in Taylor-Couette flows of viscous fluids, the substantially different phenomenology of Taylor-Couette

---

[10]While Wendt's 1933 paper is widely cited, it is not clear what happened to Wendt himself after he left Prandtl's group. A search of English and German language academic databases found no further publications in his name. The only other mention of Wendt in the literature is in an appendix of a biography of Johann Nikuradse by Hager and Liiv, which contains documents regarding Nikuradse's dismissal from Göttingen in 1934 [71]. These mention that Wendt became an Assistant Professor at the Clausthal University of Technology and was accused by Nikuradse of stealing some of Nikuradse's research papers, but later absolved.

flows of liquid helium, which has a normal viscous component and a superfluid component at temperatures below 2.1768 K, is quite interesting so it is briefly reviewed here.

In 1953, A.C. Hollis-Hallett realized that a Couette viscometer provided a way to measure the absolute viscosity of the normal component of liquid helium II [72]. Taking into account that Rayleigh's criterion dictates that inner cylinder rotation would destabilize the superfluid component, he designed the viscometer so that the outer cylinder rotated and the torque (due to the normal component) would be measured on the inner cylinder. To his surprise, Hollis-Hallett discovered that the measured torques were larger than expected and did not scale linearly with increased outer cylinder rotation rate. He was unable to explain these results but discounted the possibility of flow instability given that the Reynolds numbers for his experiments ($Re_o \sim \mathcal{O}(75)$) were significantly lower than the critical Reynolds numbers reported by Wendt and Taylor ($Re_c \sim \mathcal{O}(10^4)$) [65,70]. Instead, he speculated the possibility that an "interaction between the superfluid component and the boundary walls" might lead to a "new type of frictional force" that would lead to an increased torque.

Hollis-Hallett and W.J. Heikkila revisited the Taylor-Couette problem in a 1955, adapting Hollis-Hallet's viscometer to operate at very low rotation speeds [73], which allowed them to study flows with Reynolds numbers of $\mathcal{O}(1)$. Heikkila and Hollis-Hallett were able to observe a regime where the measured torques behaved as predicted for Couette flow. This suggested a transition in the flow structure for which they measured a critical Reynolds number of ~ 51 at 2 K. The relevant instability mechanism would not be fully explained until 1988 by C.F. Barenghi and C.A. Jones [74]. Barenghi and Jones studied the stability of liquid helium II in the Taylor-Couette geometry using the two-fluid Hall-Vinen-Bekharevich-Khalatnikov (HVBK) model [75–77]. They found that even in Rayleigh-stable flows, the interplay between the rotation of the outer cylinder and the elasticity of the superfluid vortex lines makes the superfluid component unstable to *non-axisymmetric* perturbations. So-called "mutual friction" then couples the unstable superfluid component to the stable normal component destabilizing it and leading to an increase in the measured torques. Barengui and Jones' theory also successfully explained the pioneering 1959 observations of Donnelly [78] that the linear instability of both the superfluid and viscous

components was delayed by mutual friction in experiments where only the inner cylinder rotated, i.e., the critical Reynolds number increased from 128 (as predicted for viscous fluids) to 202 in helium II.[11] Taken together, the experiments of Hollis-Hallett and Heikkila and Donnelly lead to the surprising conclusion that Taylor-Couette flow of helium II is more unstable when only the outer cylinder is rotating than when only the inner cylinder rotating [79]! It should also be noted that Hollis-Hallett and Heikkila's experiments studying the stability of Taylor-Couette flows of helium II with only the outer cylinder rotating have never been repeated [79].

2.6   Two Extremes: Bagnold and Schulz-Grunow, 1954-1959

In 1954 R.A. Bagnold published what would become one of the founding papers of the field of particle-laden flows [80]. In it, he derived a theory describing the relationship between the shear and normal stresses exerted on a wall by a liquid laden with large (as opposed to molecular) particles. He tested his theory in a series of experiments in which he used a specially designed Couette rheometer to measure the shear and normal forces on the inner cylinder as he sheared a suspension of neutrally buoyant particles by rotating the outer cylinder. As opposed to earlier experiments, which used torsion fibers, Bagnold's apparatus used a calibrated spring to measure the torque on the inner cylinder. The surface of the inner cylinder was made of flexible rubber sheet and its interior was sealed off from the surrounding air. Air was only allowed to escape via a small tube connected to a manometer. By monitoring the changes in pressure inside of the cylinder, Bagnold was able to extract the normal forces exerted by the particle suspension on the inner cylinder.

As a limiting case, Bagnold performed experiments using pure water at Reynolds numbers between 8000 and 33000. He measured a quadratic dependence of the shear stresses on shear rate for all the Re that he studied, indicating that the flow was turbulent. Earlier experiments by Taylor and Wendt using similar radius ratios had shown Taylor-Couette flow to be stable up to Re up to ~ 18000, which leads to the conclusion that Bagnold's rubber sheet design probably suffered from significant perturbations [52,81]. It is probably for this

---

[11]Donnelly's result was predicted in a theoretical paper by Chandrasekhar and Donnelly in 1957, but their theory did not make a prediction for flows with the outer cylinder rotating and the inner cylinder fixed.

reason that Bagnold's experiments are not typically discussed in the hydrodynamic stability literature. However, they provide a reminder that the construction of the apparatus can significantly affect the stability of the flow.

Five years later, in 1959, F. Schulz-Grunow of RWTH Aachen University would publish a paper titled "On the Stability of Couette Flow". In it, Schultz-Grunow used linear stability analysis to study the stability of Taylor-Couette flow with the outer cylinder rotating and the inner cylinder at rest. He predicted that such flows should be linearly stable at all Re_o for all gap sizes, extending Taylor's result for narrow gaps from 1923. Schultz-Grunow tested his theory in a series of carefully controlled flow visualization experiments. His apparatus was constructed with stringent tolerances and he was able to establish stable axisymmetric flows at Reynolds numbers an order of magnitude higher than earlier experiments. He also went on to show that if he purposely misaligned his apparatus so that the cylinders were not coaxial or if he used inner cylinders that were not perfectly round,[12] his system would undergo transition at Reynolds numbers similar to those observed by Couette, Mallock, Taylor, and Wendt. Schultz-Grunow also reported that when the system became turbulent, this usually started near the ends of the cylinders.

In order to visualize the flow, Schultz-Grunow employed a technique that he developed in 1956 with H. Heim [82]. This technique consists of suspending aluminum flakes in the fluid. Because of their shape the flakes align themselves preferentially in the flow, affecting the optical properties of the fluid. Schultz-Grunow and Heim used this technique to capture the first photographs states that later would become known as wavy Taylor vortices and turbulent Taylor vortices. Interestingly, neither Schulz-Grunow nor Heim investigated these flows further. Their technique, however, would become the flow visualization method of choice for studying supercritical Taylor-Couette flows and be used in hundreds of papers [5].[13]

---

[12]Schultz-Grunow used inner cylinders with elliptical (m=2), square (m=4), and hexagonal (m=6) cross-sections.

[13]The aluminum powder technique was not invented by Schultz-Grunow and Heim and dates back at least to Bénard, who used it in 1900 to visualize the boundaries of convection cells [83]. Aluminum powder was also used to generate streaklines in studies of Taylor-Couette flow by Terada and Hattori in 1926 [84], Lewis in 1928 [63], and Hagerty in 1947 [85]. However, Schultz-Grunow and Heim appear to be the first to have used aluminum flakes in high concentration to visualize Taylor-Couette flow.

2.7 The Catastrophic Transition and Spiral Turbulence: Coles and Van Atta, 1955-1966

In 1955, while Schultz-Grunow and Heim were conducting their experiments at Aachen, Donald Coles at Caltech was beginning what would become a monumental, decade-long study of flow transitions in Taylor-Couette flows. The results of this study were reported in his 1965 paper "Transition in circular Couette flow" [14]. Coles's study was originally inspired by the lack of experimental data on the transition to turbulence in the absence of the Taylor instability. His initial experiments were carried out in a large apparatus and used air as the working fluid. The apparatus was equipped with hot wire anemometers, which could be translated across the gap and provided point measurements of the flow velocity. Coles performed detailed hot wire measurements for cases where one cylinder rotated and the other was at rest, as well as cases where both cylinders rotated. When inner cylinder rotation dominated (i.e. above the linear stability boundary shown in Figure 2.4), Coles found that turbulence was preceded by velocity signals with discrete frequency spectra. These spectra grew more complex as the rotation rate was increased, with the discrete spectrum eventually giving way to broadband noise.[14] Subsequent flow visualization experiments in a smaller apparatus, using a variation of the technique developed by Schultz-Grunow and Heim [82], would shed a light on the source of these measurements. Coles reported that the transition to turbulence dominated by centrifugal instability was governed by the emergence of a series

---

[14]While Coles never published his hot wire spectra, his qualitative description of their evolution for increasing inner cylinder rotation rates suggest that he observed but did not recognize that he had evidence rejecting Landau's famous scenario for the transition to turbulence. In 1944 Landau proposed that turbulence arises after a large number of successive bifurcations with each bifurcation introducing new temporal frequencies into the flow until turbulence is reached [86]. Under this scenario, the measured spectra would have progressively more and more peaks as the Reynolds number was increased. Coles reported that he observed spectra that were at first discrete (with increases in Reynolds number adding only a few new frequencies and their harmonics), but that after a few bifurcations the peaks began to broaden and lose intensity until the spectrum was dominated by broadband noise. It turns out that this is exactly the behavior that would be observed in a nonlinear system making the transition to chaos in the scenario proposed by Ruelle and Takens in 1971 [87, 88]. Ruelle and Takens showed mathematically that if "a system undergoes three Hopf bifurcations, starting from a stationary solution, as a parameter is varied, then it is likely that the system possesses a strange attractor with sensitivity to initial conditions after the third bifurcation" [89]. Effectively, this means that spectra will show an increasing number of frequencies for the first three or four bifurcations but after that the broadband spectrum of chaotic dynamics will dominate. Gollub and Swinney showed the inadequacy of the Landau model and that turbulence exhibits the hallmarks of deterministic chaos by careful quantitative analysis of the spectral features of laser Doppler velocimetry time-series of Taylor-Couette flow which showed qualitatively similar features to the hot wire measurements described by Coles [90].

of progressively more complicated patterns, which were reflected by the hot wire spectra. He called this route to turbulence "transition by spectral evolution".

Although some of the patterns he reported were observed by earlier researchers [82], Coles was the first to study supercritical Taylor-Couette flows in depth. Much to his surprise, he discovered that the equilibrium state reached by any given experiment depended very sensitively on experimental protocol. His extensive study showed that for a given Re_i above the linear stability boundary as many as 26 states with differing azimuthal and axial wave numbers could be observed. These states are now collectively known as *wavy Taylor vortices* and (along with other supercritical flow regimes of Taylor-Couette flow) have been the subject of intense study in the decades since Coles's pioneering work. For a comprehensive review, the reader is referred to the book by Koschmieder [5].

For counter-rotating flow regimes dominated by outer cylinder rotation, Coles observed drastically different behavior. His hot wire measurements showed "patterns of alternating laminar and turbulent flow" [14]. In some regimes, these fluctuations were irregular but in other regimes they seemed to alternate at roughly half the frequency of the outer cylinder. The latter were the first observations of so-called *spiral turbulence*, which is discussed below. The intermittent turbulent episodes "appeared with almost explosive suddenness" out of purely laminar flow as the outer cylinder was slowly accelerated and showed considerable hysteresis. Coles called this transition "catastrophic", noting that the resulting states were characterized by spatiotemporal intermittency with coexisting laminar and turbulent domains separated by well-defined interfaces.[15]

Coles determined that there were two qualitatively different regimes. The first occurred when the inner cylinder was slowly accelerated for fixed Re_o below ~ 2700 but above ~ 570. In this case, the linear instability was observed to occur first in the form of laminar spirals. As shown in Figure 2.6 the boundary for catastrophic transition in this regime is just above the Taylor boundary. At slightly higher values of Re_i, the spirals were observed to grow

---

[15]Some of Coles's early work seems to have been done with a Masters student called Haruo Oguro who graduated from Caltech in 1957. Oguro appears to have later obtained a doctoral degree and joined the faculty at Tokai University in Japan. Attempts were made to obtain his thesis, which was titled "Catastrophic transition and spiral turbulence in circular Couette flow", but these attempts were unsuccessful.
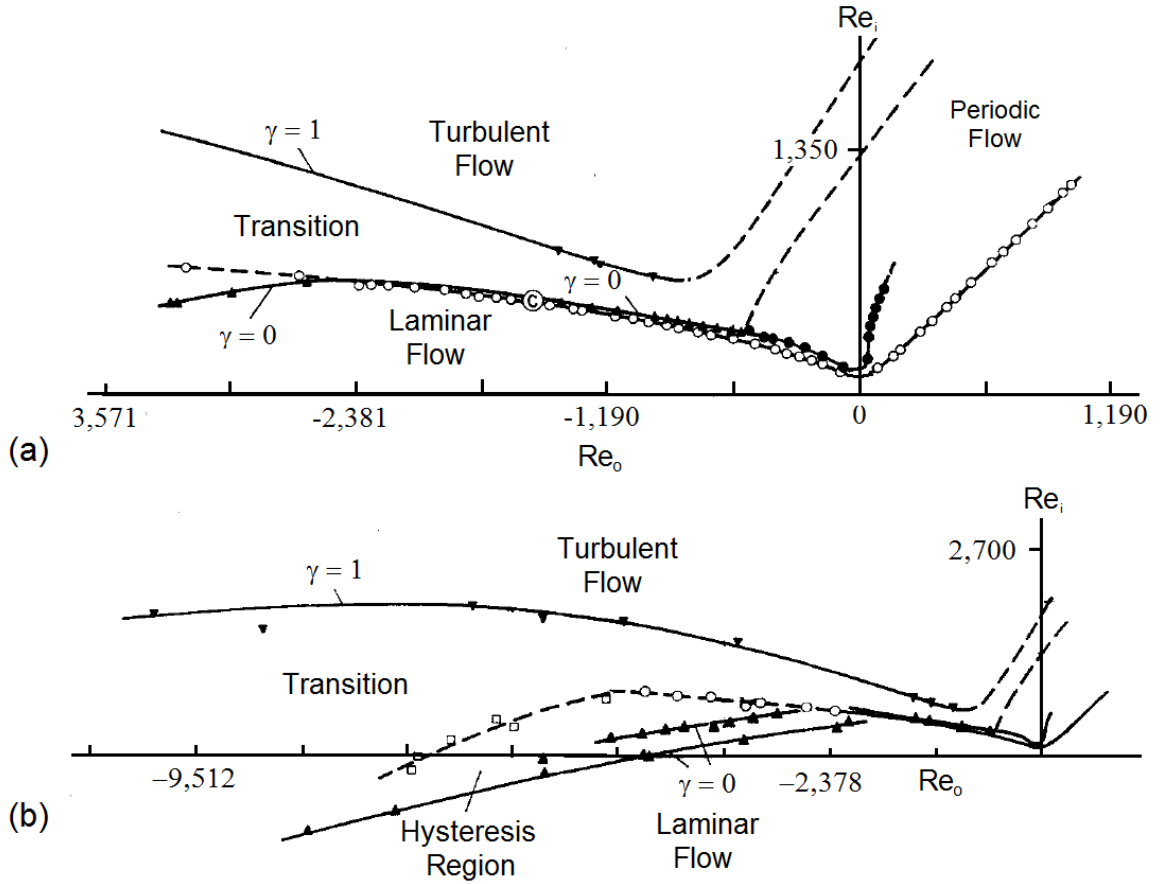
Figure 2.6: Coles's phase diagram for catastrophic transition. (a) For $-570 < Re_o < 0$, the flow undergoes a transition to wavy Taylor vortices as Re_i is increased beyond the curve marked by •. For $\sim -2700 < Re_o < -570$, the catastrophic transition boundary (▲) lies above the Taylor boundary (∘), so the transition is such that the linear instability mechanism provides a perturbation in the form of laminar spirals, which trigger turbulence. This eventually decays leaving behind laminar flow that is linearly unstable, leading to the formation of new spirals and restarting the process. As Re_i is increased further the turbulent fraction γ increases until eventually the flow becomes fully turbulent (▼) (b) For $Re_o < -2700$ the catastrophic transition boundary drops below the linear stability boundary. This creates a region (bounded below by ▲ and above by □ and ∘) in which Couette flow is stable if left to itself, but which becomes turbulent if subjected to sufficiently large external perturbations. Once turbulent, the flow will remain so until the system is brought back across the transition boundary ($\gamma = 0$). Above the line marked with □, perturbations inherent to the apparatus are sufficient to trip the flow so turbulence is always observed. However, like in the hysteretic region, the flow is characterized by coexisting laminar and turbulent domains, sometimes in the form of spiral turbulence. Note: The Reynolds numbers in Coles's original figure are based on cylinder radii. Here the numbers have been recalculated in terms of the gap width. Adapted from D. Coles, "Transition in circular Couette flow", *J. Fluid Mech.* **21**, p. 390, 1965. Copyright 1965 by Cambridge University Press.

and then break down into small turbulent patches at random locations within the flow. The patches persisted for a short time but then broke down, leaving behind laminar flow, which in turn became unstable to the formation of spirals starting the whole process again. This regime is now known as the intermittency regime (INT in the nomenclature of Andereck et al. [13]). As Re_i was increased further, the turbulent episodes became more frequent and the *turbulence fraction*, (i.e., the fraction of the flow that was turbulent) increased until the flow became fully turbulent.

For even larger Re_o, Coles found a second regime where finite-amplitude perturbations triggered the transition to turbulence, even in the absence of linear instability. Once tripped, turbulence persisted indefinitely and only disappeared if the system was run well below the transition boundary for some time. Coles did not report how long these states were observed or how long the system had to run below the transition boundary before the flow relaminarized. At sufficiently large values of Re_o, the transition could be spontaneously triggered by imperfections in the apparatus or end effects. In this regime the transitional flows were characterized by well-defined turbulent and laminar domains. Although these could take on a variety of configurations, one commonly observed pattern consisted of a single band of turbulence that spiraled around the apparatus like the pattern on a barbershop pole. Coles reported that the spiral pattern rotated at the mean angular velocity of the cylinders, so that the fluid near the walls would have to alternate quite suddenly between laminar and turbulent flow. This suggested the existence not only of a front where laminar flow became turbulent, but a also sharp interface where the flow relaminarized. The nature of these fronts is not well understood and has been the object recent study [91].

Coles's 1965 paper would be followed the next year by two papers in the Journal of Fluid Mechanics. The first paper was co-authored by Coles's doctoral student Charles Van Atta. In it they describe hot wire measurements of circular Couette flow with the inner cylinder fixed and the outer cylinder and end walls rotating together at high Reynolds number [46]. Their data showed that the secondary flow induced by the finite aspect ratio of their apparatus, while small, could result in significant deviations from the ideal velocity profile (Eq. 2), as shown in Figure 2.7. The second paper, authored by Van Atta [92],
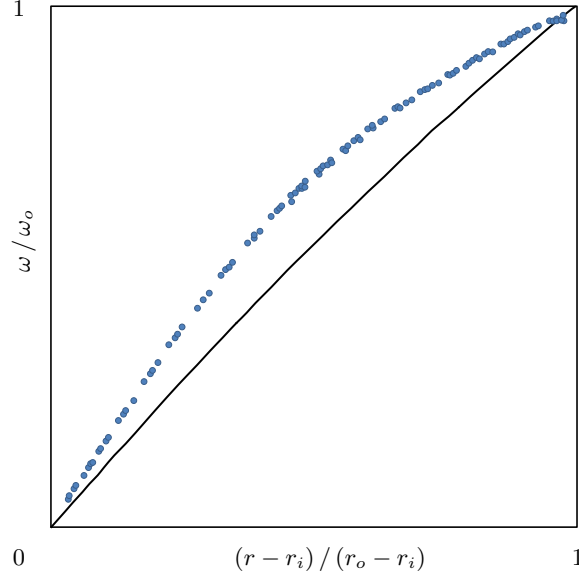
Figure 2.7: Coles and Van Atta's hot wire measurements (●) show that even though the radial and axial velocity components in Couette flow are small at $Re_o = 6000$, they lead to significant deviations from the Couette profile (solid line). Their apparatus had a radius ratio of $\eta = 0.89$ and an aspect ratio of $\Gamma = 27.35$, similar to the apparatus used in the experiments described in Chapter 3. Adapted from D. Coles and C. Van Atta, "Measured distortion of a laminar circular Couette flow by end effects", *J. Fluid Mech.* **25**, p. 513, 1966. Copyright 1966 by Cambridge University Press.

describes a series of exploratory measurements of spiral turbulence.

The boundary for catastrophic transition measured by Van Atta is qualitatively similar to the one established by Coles using flow visualization, but was systematically shifted to higher Re_o. Van Atta attributed this to the fact that the smaller apparatus used a split-ring configuration for the end caps, while the large apparatus used end caps that rotated with the outer cylinder. Van Atta also noted that unlike in the supercritical case, where the final state of fluid depends strongly on the protocol used to reach it, transitional states (characterized by their turbulent fraction or by the velocity of the turbulent laminar interfaces) appeared to be unique and independent of the protocol used to obtain them. He also noted that as long as the flow was below the Taylor stability boundary, the turbulent patches appeared to rotate at roughly the mean angular velocity of the two cylinders. By traversing his hot wire probes through the flow, Van Atta was also able to measure the structure of the turbulent domain (see Figure 2.8), noting that for flows dominated by outer cylinder rotation, the leading edge of the turbulent patches was near the outer cylinder and the trailing edge was

near the inner one. Van Atta also noted that spiral turbulence was more frequent at larger aspect ratios and that spirals of either handedness were equally likely.[16]
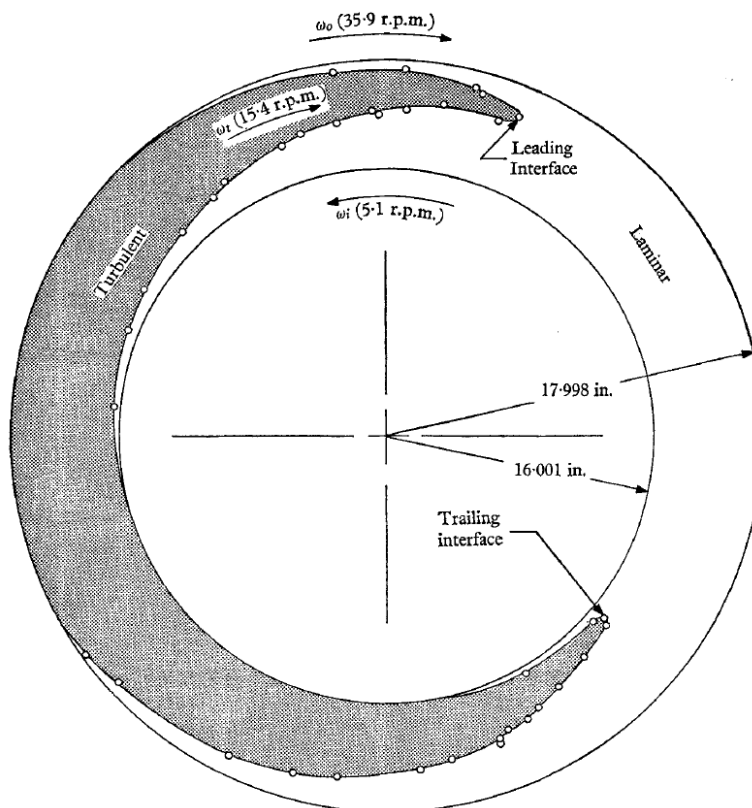
Figure 2.8: Van Atta measured the shape of the laminar/turbulent interfaces in spiral turbulence by traversing hot wire anemometers through the flow. He found that the leading edge of the turbulent band traveled close to the outer cylinder and the trailing edge traveled close to the inner cylinder. Overall the turbulent patch traveled at approximately the mean angular velocity of the two cylinders. Adapted from C. Van Atta, "Exploratory measurements in spiral turbulence", *J. Fluid Mech.* **25**, p. 495-512, 1966. Copyright 1966 by Cambridge University Press.

2.8 Modern Investigations of Subcritical Taylor-Couette flow

2.8.1 Nonlinear Stability Analysis

The rich phenomenology of Taylor-Couette flows discovered by Coles and Van Atta would spur a whirlwind of activity in the 1970s. The majority of this work concentrated on experimental, theoretical, and eventually numerical investigations of supercritical bifurcations in

---

[16]Additional details about the turbulent domains and their interfaces with the laminar flow were reported in follow-up papers by Coles in 1966 [93] and 1967 [94].

flows dominated by centrifugal effects. The subcritical regime, however, received fairly limited attention. One important exception is the work of D.D. Joseph and his collaborators between 1970 and 1971. Building on the earlier work of Serrin [95], Joseph and Munson used the Reynolds-Orr energy method to study the stability of Couette flow to arbitrary finite-amplitude perturbations [96]. This approach allowed them to predict the existence of a window of absolute stability, shown in Figure 2.9, where finite-amplitude perturbations could not grow. Joseph and Hung considered the special case of axisymmetric perturbations [97], which allowed them to increase the size of the stability window to finite-amplitude perturbations up to a specific size. The approach taken by Joseph and his collaborators cannot predict stability boundaries in the way that linear stability does, since it considers all possible arbitrary perturbations including ones that are not hydrodynamically allowed. However, flow regimes that are predicted to be stable for all perturbations are naturally also stable to all hydrodynamically realizable ones. This means means that the energy method provides a lower bound for stability instead of a criterion for instability. A detailed discussion of energy stability criteria for Taylor-Couette flow can be found in Ref. [16].
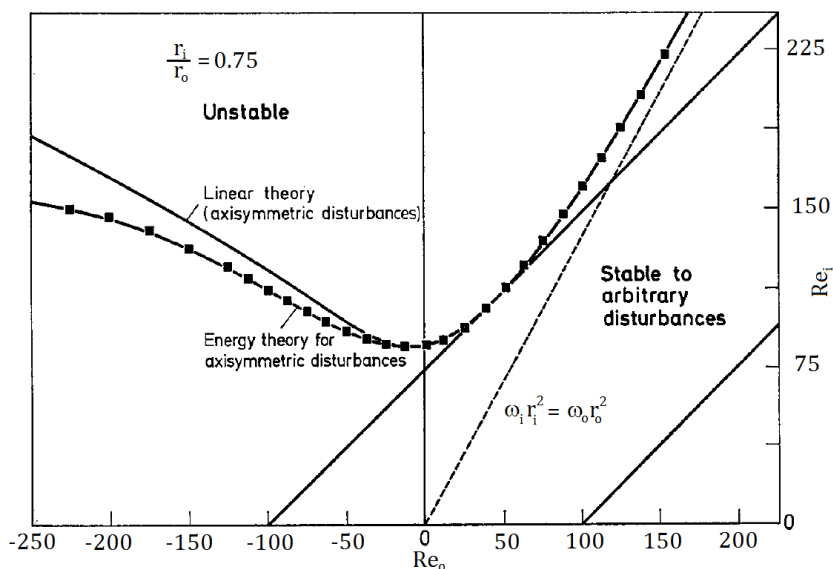
Figure 2.9: The nonlinear stability analysis of Joseph and Hung predicts a window of stability to arbitrary perturbations. Adapted from D.D. Joseph and W. Hung, "Contributions to the Nonlinear Theory of Stability of Viscous Flow in Pipes and Between Rotating Cylinders", *Arch. Rat. Mech. Anal.* **4**, p. 1-22, 1971. Copyright 1971 by Springer.

Since the pioneering work of Joseph and his collaborators in the 1970s, several attempts have been made at finding criteria for nonlinear stability for Taylor-Couette flow. In 1995, Levinski and Cohen made a theoretical prediction that there should be flow regimes where the fluid impulse of finite size vortical disturbances would grow in external shear flows [98]. In 1999, Malkiel, Levinski, and Cohen extended this theory to Taylor-Couette flow and tested it in a series of experiments where they perturbed the flow using concurrent injection and suction of fluid from ports on the inner cylinder wall [99]. They observed that large enough perturbations led to the periodic shedding of hairpin vortices from the inner cylinder wall, in agreement with their theoretical predictions.

In 2005 Garaud and Ogilvie proposed a physically motivated closure for the Reynolds averaged Navier-Stokes equations [100]. Applying this model to Taylor-Couette flow allowed them to predict regimes of linear stability, as well as regimes where finite-amplitude perturbations might grow. As shown in Figure 2.10, their model predicts subcritical instability in co-rotating as well as counter-rotating flows in regimes that are qualitatively similar to those where Richard observed turbulence in experiments [101].

2.8.2 Predictions of Nonlinear Stability Thresholds from Historical Data

One approach that has proven popular with the astrophysics community has been to use the experimental data of Couette, Taylor, and Wendt on the subcritical transition to derive phenomenological models of the transition. This approach was introduced by Zeldovich [102] in 1981, who determined that, in the narrow gap limit, the critical Reynolds number for transition scales with the square of $d/\bar{r}$, where $\bar{r}$ is average radius of the two cylinders. An explanation for this scaling was proposed by Dubrulle in 1993 [103]. Richard and Zahn [104] took a similar approach to Zeldovich and found that the stability boundary for the historical data of Taylor [65] and Wendt [70] for large gap flows ($\eta > 0.95$) was well captured by a critical Reynolds number based on the gradient of angular velocity $Re^* = (\bar{r}^3/\nu)(|\omega_o - \omega_i|/d)$ of 6×10^5.

Dubrulle et al. [12] generalized Zeldovich's approach and performed a meta-analysis of the historical data, along with new data from the thesis of D. Richard [101] and Tillmark
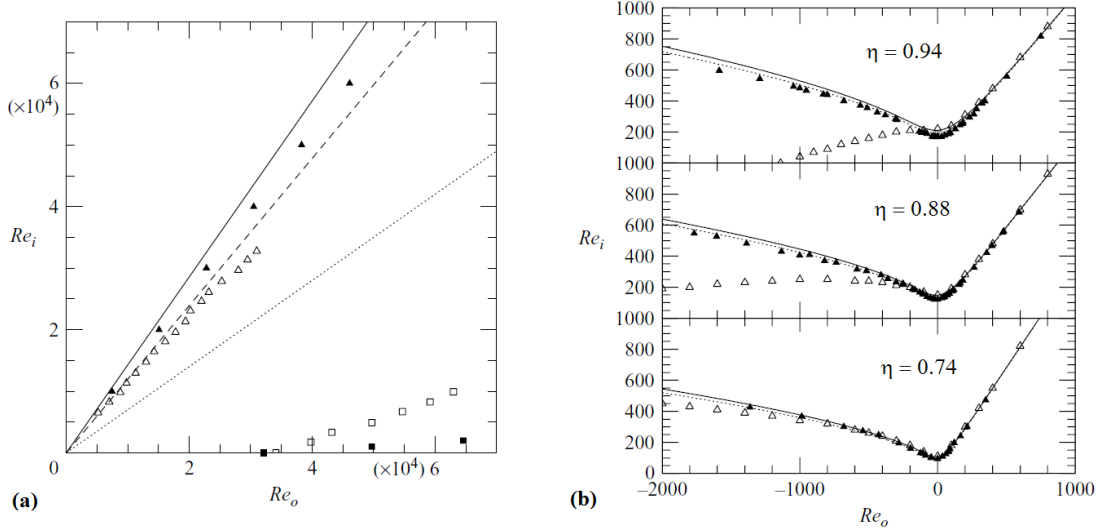
Figure 2.10: Garaud and Ogilvie's model predicts that there are regimes of Taylor-Couette flow where finite-amplitude perturbations can grow. (a) For co-rotating flows, their model (closed symbols) is in qualitative agreement with the experimental observations of Richard [101] (open symbols). (b) For counter-rotating flows, their model predicts that nonlinear instability (open symbols) is possible below the linear stability boundary (closed symbols). Adapted from P. Garaud and G.I. Ogilvie, "A model for the nonlinear dynamics of turbulent shear flows," *J. Fluid Mech.* **530**, pp. 145-176, 2005. Copyright 2005 by Cambridge University Press.

and Alfredsson's data for rotating plane Couette flow [105]. They arrived at an empirical expression for the subcritical stability boundary for Taylor-Couette flow for both co-rotating and counter-rotating flow, capturing its dependence on both Reynolds number and radius ratio. They also concluded that using different boundary conditions (end caps rotating with the inner/outer cylinder or split end rings) only changed the critical Reynolds number for subcritical instability by about 10%. They also discussed the effects of additional forces on the flow, concluding that both magnetic forces and vertical stratification can destabilize subcritical flows by exciting linear instability mechanisms. Using the historical torque data, Dubrulle et al. derived a turbulent viscosity model that, when used in models of astrophysical disks, predicted angular momentum transfer rates in good agreement with astronomical observations.

2.8.3 Spiral Turbulence

After the pioneering work of Coles and Van Atta, the subcritical regime was first revisited by Andereck, Liu, and Swinney in 1986 [13]. In this expansive study, Andereck et al. studied the boundaries separating both supercritical and subcritical flow regimes of Taylor-Couette flows. They found that for $Re_o > -4500$,[17] the turbulent spirals appeared to rotate at approximately the same rate as the outer cylinder, in contrast with Van Atta's observations at larger Re_o, which showed the spirals rotating at the mean speed of the two cylinders. Andereck et al. also discovered a stable state in which two spirals of opposite helicities coexisted, with one in the upper half of the gap and the other in the bottom. The two spirals joined at the midplane to form a V-shaped pattern. The same year, Yamada and Imao published the results of experiments in the spiral turbulence regime, reporting the existence of new spiral turbulence states with two spirals [106]. They also conducted hot wire measurements of the flow in the gap, confirming earlier results by Van Atta [92]. Both groups observed that spiral turbulence was hysteretic and that, once initiated, could be sustained, even below the linear stability boundary.

Spiral turbulence has since been studied by several authors. Hegseth et al. studied the axial variation in the pitch and the width of the turbulent spiral in a system with varying aspect ratios and end conditions [107]. They were able to explain the variation they observed within the framework of phase dynamics theory. The coexistence of turbulent and laminar domains in spiral turbulence was explained by Hayot and Pomeau using a quintic Ginzburg-Landau equation in 1994 [108]. The dynamics of spiral turbulence were next addressed in experiments by Litschke and Roesner in 1998, who studied how varying end conditions affect the formation of turbulent bands [109]. They noted that although experiments with the end caps rotating with the outer cylinder tended to lead to turbulent spirals, experiments with the end caps rotating with the inner one usually led to the V-shaped turbulent pattern observed by Andereck et al. They also studied the effects of gap width and found that the

---

[17]The rotation direction of the inner cylinder is conventionally taken to be positive. Negative values of Re_o mean that the outer cylinder is rotating in the direction opposite to the rotation direction of the inner cylinder.

onset of turbulence was shifted to higher Re for larger gaps.

More recent studies have focused on the transitional intermittency regime (INT) between the supercritical interpenetrating spiral regime (IPS) and spiral turbulence (SPT), which is characterized by sporadic bursts of turbulence. Originally noted by Coles [14] and by Andereck et al. [13] as a precursor to spiral turbulence, this regime was first studied in detail in the Masters thesis of F. Hamill [110] in 1995 and by Colovas and Andereck [111] in 1997. Colovas and Andereck measured the size distribution of laminar domains as a function of the inner cylinder rotation rate and found that the increase in turbulent fraction abruptly slowed at the onset of spiral turbulence. The mechanism behind cyclic turbulent bursting was elucidated in numerical simulations by Coughlin and Marcus, who discovered that the linearly unstable inner layer was itself unstable to a secondary instability [112]. As this mode grew, it acted as a finite-amplitude perturbation to the outer layer. Goharzadeh and Mutabazi [113] performed additional experimental characterization of the intermittency regime in 2001 and studied its role as a precursor to spiral turbulence.

In 2002, Prigent and Dauchot discovered that the turbulent spots observed in small aspect ratio plane Couette experiments [67, 114, 115] organized into alternating stripes of laminar and turbulent flow in a large aspect ratio plane Couette flow experiment [116]. These oblique bands were found to be analogous to spiral turbulence in a very large aspect ratio apparatus ($\Gamma = 442$) with a small gap ($\eta = 0.983$) [117]. The analogy between plane Couette flow and Taylor-Couette flow in the limit of large Γ and η had earlier been discussed by Faisst and Eckhardt [118], who found that in this limit the linear instability of circular Couette flow moves to Re larger than those observed for subcritical instability. Prigent and Dauchot found that for large aspect ratios, spiral turbulence takes the form of a periodic pattern of helical laminar and turbulent bands. Prigent and Dauchot explained their observations of the onset of spiral turbulence in terms of coupled amplitude equations with additive noise. This work was expanded in a 2003 paper by Prigent et al. [66], who concluded that the observed patterns were the result of a supercritical long-wavelength instability of fully turbulent shear flow. Additional evidence for this scenario was presented by Prigent and Dauchot in 2005 [119]. Direct numerical simulations of turbulent stripes

in plane Couette flow have been conducted by Barkley and Tuckerman [120], who used the insight gained from them to develop a low order model to explain the wavelengths and tilt angles observed in experiments [121]. More recently, the dynamics of turbulent stripes have been studied numerically by Tuckerman and Barkley [91], who found that the turbulent stripe regime can be subdivided into four different subregimes with distinctive characteristics.

The first fully-resolved direct numerical simulations (DNS) of spiral turbulence were performed by Alvaro Meseguer's group at the Universitat Politècnica de Catalunya in 2009 [122]. They found that spiral turbulence originates from the detachment of vortex filaments from the inner cylinder wall. These are advected by the rotation of the inner cylinder and eventually break down leading to turbulence. For low outer cylinder rotation rates (Re_o= -1200), they found that the transition from spiral turbulence could not be sustained as the inner cylinder is slowed down, yielding to interpenetrating spirals before full relaminarization occurred. For higher outer cylinder rotation rates (Re_o= -3000), spiral turbulence could be sustained well into the linearly stable regime and relaminarization was directly back to circular Couette flow.

Additional simulations of spiral turbulence have been carried out by S. Dong and his collaborators at Purdue University [123,124]. They confirmed the experimental observations of Coles and Van Atta [92–94] that in spiral turbulence, the turbulent intensity is greater in the middle of the gap. They also confirmed that the leading edge of the turbulent spiral is located near the outer cylinder, while the trailing edge is near the inner one. A similar asymmetry was found in the axial components of velocity, where the mean flow in the turbulent region was observed to go toward one end near the outer cylinder and toward the other near the inner one [123]. They also noted that the turbulence in the turbulent bands of spiral turbulence is composed of "small-scale azimuthally elongated vortices" [124] and that the laminar domains are not completely "void of vortices."
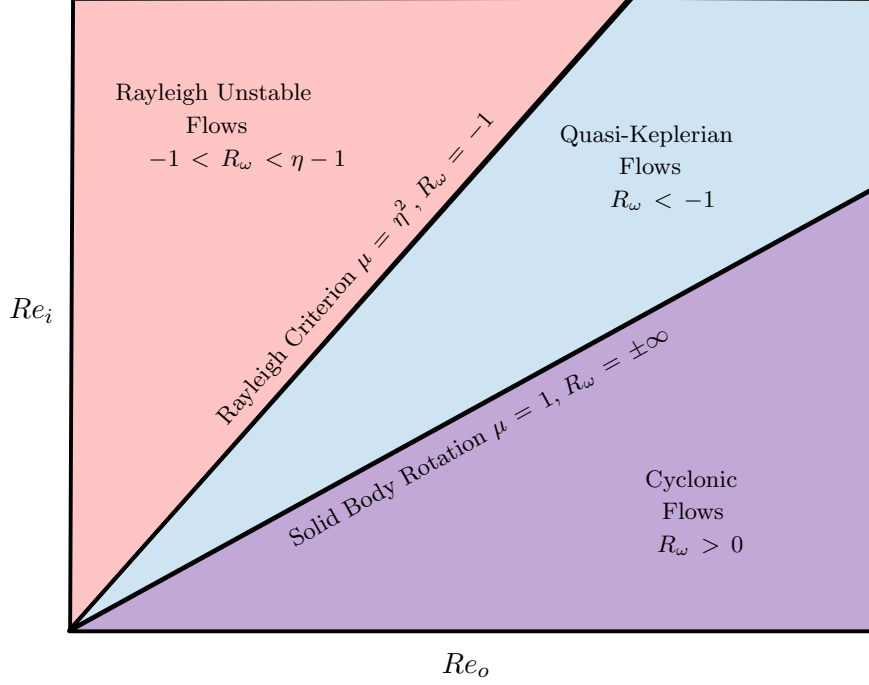
Figure 2.11: Flow regimes for co-rotating Taylor-Couette flow

2.8.4 Stability of quasi-Keplerian flows

One linearly stable flow regime that has received much attention in the recent literature is the so-called *quasi-Keplerian* regime (see Figure 2.11). In this co-rotating regime, the angular speed $|\omega|$ decreases radially outward ($\partial|\omega|/\partial r < 0$), while the magnitude of the specific angular momentum $|r^2\omega|$ increases radially inward ($\partial|r^2\omega|/\partial r > 0$). These co-rotating flows lie between the Rayleigh stability line (Eq. 5) and the solid body rotation line ($\omega_i = \omega_o$) and are widely used to model astrophysical objects like accretion disks. Classical stability theory predicts that such flows should be stable. However, the observed accretion rates of astrophysical disks cannot be accounted for by the transport of angular momentum resulting from molecular viscosity alone. This suggests that these flows are in fact turbulent. Several groups have recently made experimental attempts at establishing whether quasi-Keplerian Taylor-Couette flows are absolutely stable.

In 2006 Hantao Ji and his collaborators at the Princeton Plasma Physics Laboratory tested the stability of quasi-Keplerian flows in a series of experiments using a Taylor-Couette apparatus designed to minimize end effects. The end caps in the apparatus were split into

two rings that could be rotated independently of the cylinders themselves. By adjusting the rotation rates of these rings they were able to reduce the influence of end effects and achieve flows in the gap that more closely approximated the ideal Couette profile [48]. LDV measurements of the flow in the gap showed very low levels of velocity fluctuations throughout the quasi-Keplerian regime, suggesting that the flow remained laminar up to Reynolds numbers as high as 10^6 [49]. Ji et al. also noted that fluctuation levels increased significantly when the rotation rates of the end rings where not properly adjusted.

The results of Ji et al. were challenged in a 2011 paper by Paoletti and Lathrop of the University of Maryland. Paoletti and Lathrop measured the flux of angular momentum by measuring the torque on the inner cylinder for both co- and counter-rotating flows at Reynolds numbers of $\mathcal{O}\left(10^6\right)$ [50]. In order to minimize the influence of end effects they used a long test section and only measured the torque on the central region of the inner cylinder. They found that angular momentum transport was significantly enhanced at sufficiently high Re, even in the linearly stable regions of the (Re_i, Re_o) parameter space, including the quasi-Keplerian regime. Paoletti and Lathrop also established the existence of four different dynamical regimes that showed distinct torque scalings characterized by the Rossby number $Ro = (\omega_i - \omega_o)/\omega_o$. The Rossby number characterizes the relative importance of Coriolis forces and inertial forces in rotating flows.

Even though both groups attempted to avoid the influence of end effects, numerical simulations by Marc Avila have since suggested that these effects might nonetheless be important in both experiments and that they could lead to instability [53]. Avila's simulations showed that both experimental end wall configurations affect the flow globally. They also showed that the finite size of the Princeton and Maryland systems makes them unstable to traveling waves at Reynolds numbers as low as a few hundred for the Maryland experiment and ~ 1500 for the Princeton experiment. These instabilities can lead to a transition to turbulence at Reynolds numbers of a few thousand.

The stability of quasi-Keplerian flows is still the matter of much debate. In 2012 the Princeton group published the results of more detailed experiments that corroborated their 2006 results [51]. They concluded that the secondary flows induced by the end walls can be

centrifugally unstable and lead to instability in experiments where they are not carefully controlled. This was followed soon thereafter by a paper by the Maryland group, who, in collaboration with Detlef Lohse's group at the University of Twente, synthesized data from two different experimental facilities [125]. Once again, they concluded that quasi-Keplerian flows become turbulent at finite Re. They also argued that end effects could not account for the enhanced transport that they measured. More recently, Eric Edlund and Ji reported experiments where they purposely perturbed quasi-Keplerian flows with large finite-amplitude perturbations in the form of radial jets [55]. They found that the flow quickly laminarized, even for very large perturbations [55].

2.8.5 Exact Coherent Structures in Taylor-Couette flow

As discussed in Chapter 1, recent theoretical developments suggest that the dynamics of turbulence in shear flows are guided by unstable, finite-amplitude solutions to the Navier-Stokes equations called *exact coherent structures* (ECS) or invariant solutions [24, 25]. Such solutions have been identified in a variety of flows, including pipe flow [30], plane Couette flow and plane Poiseuille flow [126]. While the first exact coherent structures for Taylor-Couette flow were not calculated till 2009 [127, 128], Taylor-Couette flow played an important role in the discovery of the first invariant solutions by Nagata in 1990. Nagata started with a numerical simulation of Taylor vortex flow and looked for solutions that bifurcated from it as he performed a homotopy continuation to the plane Couette limit. In doing so, he discovered a pair of equilibria, the so-called "lower-branch" and "upper-branch" solutions for plane Couette flow [27].[18]

In 2009, Meseguer's group at the Universitat Politècnica de Catalunya reported the discovery of the first subcritical invariant solutions of Taylor-Couette flow [127, 128]. These solutions come in the form of two families of rotating spiral waves, a short wavelength one that bifurcates from circular Couette flow (Eq. 2) and a long wavelength one that does not. Even though they exist just below the linear stability boundary for counter-rotating flows, it is not clear if these solutions play a role in the dynamics of subcritical turbulence.

---

[18]These same equilibria were independently discovered by other means by Waleffe [29] and by Clever and Busse [28].

More recently, Deguchi et al. have reported the existence of localized invariant solutions for linearly stable counter-rotating flow that can be followed by numerical continuation into the Rayleigh-stable co-rotating regime [129]. Because these solutions exist well into the subcritical regime and consist of localized vortical structures, there is hope that they might form part of the backbone for sustained turbulence in the subcritical regime.

2.8.6 Spontaneous Transition with Outer Cylinder Rotation Only

One of the more detailed modern experimental investigations of the subcritical transition to turbulence in Taylor-Couette flows was performed by Burin and Czarnocki in 2012 [52]. They studied the transition to turbulence for flows where only the outer cylinder rotated for a variety of radius ratios and end cap configurations using flow visualization and laser Doppler velocimetry. For large radius ratios ($\eta = 0.97$), they observed that as Re_o was increased, turbulence spontaneously appeared at a roughly consistent critical Reynolds number Re_c. Turbulence typically started at the end caps and formed patches inclined relative to the azimuthal flow, which coalesced into spiral turbulence after about one minute (see Figure 2.12). Burin and Czarnocki also measured the angular frequency and pitch angles of the turbulent spirals as a function of Re_o, finding that both increased slightly with increasing Re_o. As Re_o was increased, the width of the turbulent band increased until eventually the entire domain was filled with turbulence. Throughout the transition region LDV measurements showed that the turbulence filled most of the gap radially and had turbulent fluctuations of about 10% of the mean flow velocity. As observed earlier by Coles and Van Atta [14, 92] and Andereck et al. [13], these states showed considerable hysteresis. When Re_o was reduced below Re_c, the turbulent bands were observed to lose coherence and break up into disconnected but long-lived patches.

For smaller radius ratios ($\eta = 0.55$ and 0.73), the transition sequence was markedly different with turbulence usually starting in the midplane of the test section. The initial turbulent patch was then observed to grow until it filled the entire annulus vertically. LDV measurements showed that it did not fill the entire gap radially but rather that turbulence was concentrated near the inner cylinder with mostly quiescent flow near the outer cylinder.
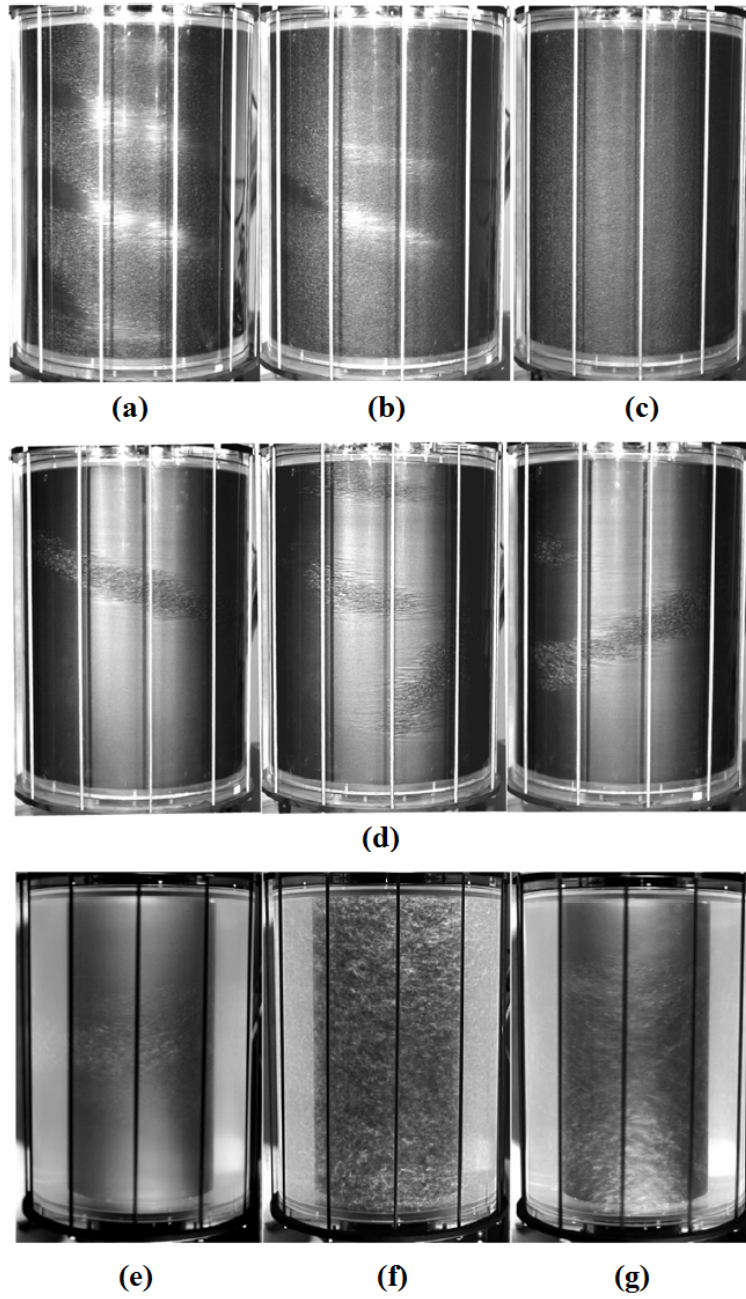
Figure 2.12: Burin and Czarnocki studied the subcritical transition to turbulence for different radius ratios. (a) For small gaps ($\eta = 0.97$), the transition begins with the sudden onset of spiral turbulence ($Re_o = 4500$). (b) As Re_o increases ($Re_o = 6500$), the width of the spiral grows until (c) it fills the entire domain ($Re_o = 7500$). (d) This transition exhibits hysteresis but the turbulent spirals are observed to break up into intermittent patches below $Re_c(Re_o = 2500)$. (e) For large gaps ($\eta = 0.55$), the transition typically starts near the midplane and (f) quickly fills the entire gap ($Re_o = 100000$). (g) As in the small gap case, the transition shows hysteresis with turbulence breaking up into localized patches ($Re_o = 50000$).

Further analysis showed that turbulence was mostly confined to regions of high shear, the location of which could be strongly influenced by the end cap conditions. This caused the transition for their large gap configurations, which have lower shear, to be shifted to much larger Reynolds numbers ($Re_c \sim 4500$ for $\eta = 0.97$ vs. $Re_c \sim 70000$ for $= 0.55$). As in the small gap case, significant hysteresis was observed as the Reynolds number was decreased below Re_c with the turbulence breaking up into large patches before relaminarization.

CHAPTER III

TRANSIENT TURBULENCE IN TAYLOR-COUETTE FLOW

One of the outstanding problems in using dynamical systems theory to describe the subcritical transition to turbulence is determining the kinds of dynamical objects that govern turbulent dynamics. One hypothesis that has been put forth is that turbulent dynamics are governed by a chaotic attractor [87]. In this picture, the laminar state is the only attracting state at low Reynolds numbers Re. As Re is increased a chaotic attractor appears. This attractor is not connected to the laminar solution, which remains linearly stable. However, finite-amplitude perturbations about the laminar state can put the system in the chaotic attractor's basin of attraction. Once on the attractor the flow's dynamics become turbulent. As Re increases the basin of attraction of the chaotic attractor grows, making it easier for random ambient fluctuations to take the system into the chaotic regime. At some critical Reynolds number Re_c, the basin of attraction for turbulence comes to encompass the entire state space and the dynamics become generically turbulent. Recent experiments and numerical simulations have shown that, in the transitional regime, the picture is more subtle and the dynamics appear to be governed by a chaotic saddle rather than a strange attractor [10].

This chapter discusses a series of experiments that were carried out to test these ideas in the context of linearly stable Taylor-Couette flows. Section 3.1 provides a review of the phenomenology associated with the subcritical transition in linearly stable shear flows with an emphasis on metastable turbulent transients. Section 3.2 gives a detailed description of the Taylor-Couette apparatus used and provides an overview of the flow visualization methods employed. The experimental procedure and data analysis methods are discussed in Sections 3.3 and 3.4. Experimental results are reported in Section 3.5. The bulk of these results were originally reported in D. Borrero-Echeverry, M.F. Schatz, and R. Tagg, "Transient turbulence in Taylor-Couette flow," *Physical Review E* **81**, 025301(R), 2010, which

included the first systematic study of the decay of turbulent states in Taylor-Couette flow. Additional unpublished results regarding the effects of system size, boundary conditions, and inner cylinder rotation on transient lifetimes are also presented. Section 3.6 discusses the experimental findings in the context of recent developments in the literature. Finally, Section 3.7 suggests directions for future research.

3.1 Background

Experiments in shear flows have shown that at sufficiently high Reynolds number, persistent states with complex spatiotemporal dynamics can be reached by finite-amplitude perturbations to the laminar flow even in cases where this is predicted to be linearly stable. These so-called *subcritical* transition scenarios appear to be quite generic and have been observed in flows ranging from pipe flow [130,131] and plane Couette flow [67,132] to plane Poiseuille flow [133–135] and boundary layer flow [136,137]. As noted in Chapter 2, several researchers have reported subcritical transition scenarios in Taylor-Couette flows dominated by outer cylinder rotation. However, this regime has not received nearly as much attention as supercritical Taylor-Couette flows and has not been characterized as well as other shear flows that undergo subcritical transitions to turbulence.

Subcritical shear flows share several common characteristics. In the transitional regime shear flows are often characterized by the coexistence of well-defined turbulent and laminar domains. These domains exhibit complex spatiotemporal dynamics and can be highly heterogeneous, which makes it hard to implement the statistical techniques traditionally used in turbulence research. Recent successes in interpreting the phenomenology of subcritical transitions in shear flows within the framework of dynamical systems theory are described in the reviews by Eckhardt [9][1] and by Eckhardt et al. [10].

Another common feature of transitional shear flows is that at sufficiently low Re intermittent states that appear to be asymptotically turbulent can relaminarize without prior indication. This behavior was first observed in numerical simulations of pipe flow by Brosa, who found that such turbulent episodes can be incredibly long-lived [138]. Furthermore, the

---

[1]Eckhardt's review focuses on transitional pipe flow, but other linearly stable shear flows exhibit qualitatively similar phenomenology and pose similar research questions.
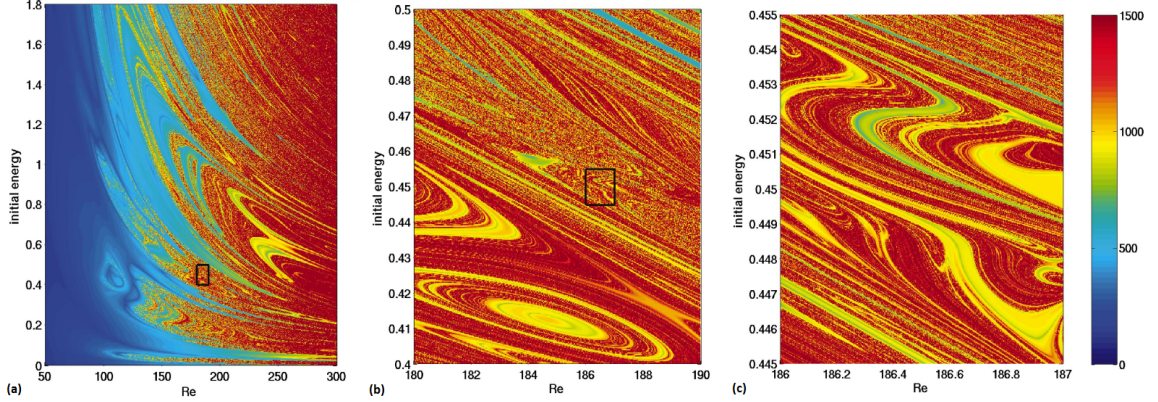
Figure 3.1: (a) The time to relaminarization of finite-amplitude perturbations shows strong dependence on the nature of the initial perturbation itself. The relaminarization times in numerical simulations of a low-dimensional model of shear flow exhibit fractal structure as the Reynolds number and the energy of the initial perturbation are varied. The maximum integration time before relaminarization is indicated by color with long-lived events shown in red and short-lived events shown in blue. (b)-(c) are progressive magnifications of (a) and show the delicate structure of the stable manifold of the turbulent state. Adapted from J. Moehlis, B. Eckhardt, and H. Faisst, "Fractal lifetimes in the transition to turbulence," *Chaos* **14**, p. S11, 2004. Copyright 2004 by the American Institute of Physics.

lifetimes of individual events show strong dependence on the details of the initial perturbation with qualitatively similar perturbations leading to wildly different lifetimes [139, 140]. As shown in Figure 3.1, the relationship between the details of a perturbation and the lifetime of the turbulent event that it triggers is highly non-trivial.

This behavior makes it difficult to come to any conclusions about the transition to turbulence from the results of individual experiments. However, insight can be gained by analyzing ensembles of experiments using qualitatively similar perturbations. Experimental and numerical studies in a variety of shear flows have shown that at fixed Re the lifetimes of turbulent transients initiated by qualitatively similar perturbations are exponentially distributed [115, 131, 139, 141–148].[2] More precisely, the probability P that a flow will still be turbulent after some time t is given by

$$P \sim \exp(-t/\tau) \tag{6}$$

---

[2]The lifetimes of turbulent episodes in superfluid ^4He have also been shown to follow an exponential distribution [149]. As discussed in Section 2.5, however, the behavior of superfluids and normal fluids can be wildly different, so it unclear whether a connection exists between the experiments in superfluid ^4He and those in viscous fluids.
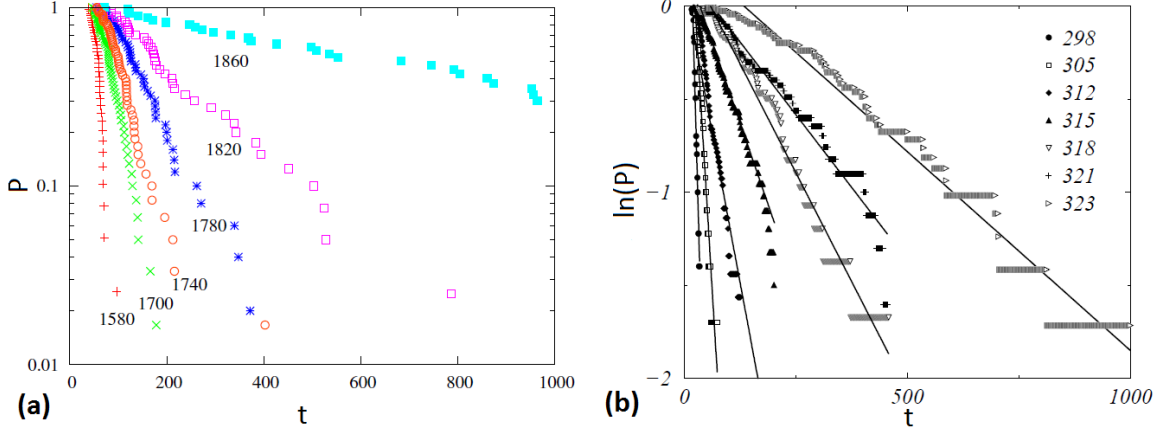
Figure 3.2: Decay probabilities are exponentially distributed in a variety of shear flows. (a) The characteristic lifetimes τ (given by the slope of P vs. t curves on a semi-log plot) in pipe flow simulations by Willis and Kerswell increase as Re increases from 1580 to 1860. (b) Qualitatively similar results were found experimentally in plane Couette flow by Bottin and Chaté as Re was increased from 298 to 323. (a) was adapted from A.P. Willis and R.R. Kerswell, "Critical Behavior in the Relaminarization of Localized Turbulence in Pipe Flow," *Phys. Rev. Lett.* **98**, 014501, 2007. Copyright 2007 American Physical Society. (b) was adapted from S. Bottin and H. Chaté, "Statistical analysis of the transition to turbulence in plane Couette flow," *Eur. Phys. J. B* **6**, 143-155, 1998. Copyright 2008 Springer-Verlag.

for large t, where the characteristic lifetime τ is a function of Reynolds number (see Figure 3.2). This distribution suggests that (at least at moderate Re) the turbulent state can be characterized by a chaotic repeller model [150–152]. Also known as chaotic saddles, chaotic repellers are hyperbolic dynamical objects that repel trajectories along some directions, but are attracting along others and exhibit chaotic dynamics within their stable manifolds. An exponential distribution of lifetimes also implies that the decay of turbulent transients is *memoryless* [153]. Formally, this means that the probability of decay during a certain time interval only depends on the duration of the interval and is independent of how long the turbulent episode has existed before the beginning of the interval.

The dependence of τ on Re has been the subject of much debate (see Figure 3.3 for an example from pipe flow). Some numerical simulations and experiments have concluded that at moderate Re the characteristic lifetimes of turbulent episodes increase with increasing Re until at some critical Reynolds number Re_c, they diverge and turbulence becomes sustained [67, 115, 142, 144]. At this point the system is thought to undergo a boundary crisis [154] after which the dynamics become associated with those of a chaotic attractor [9].
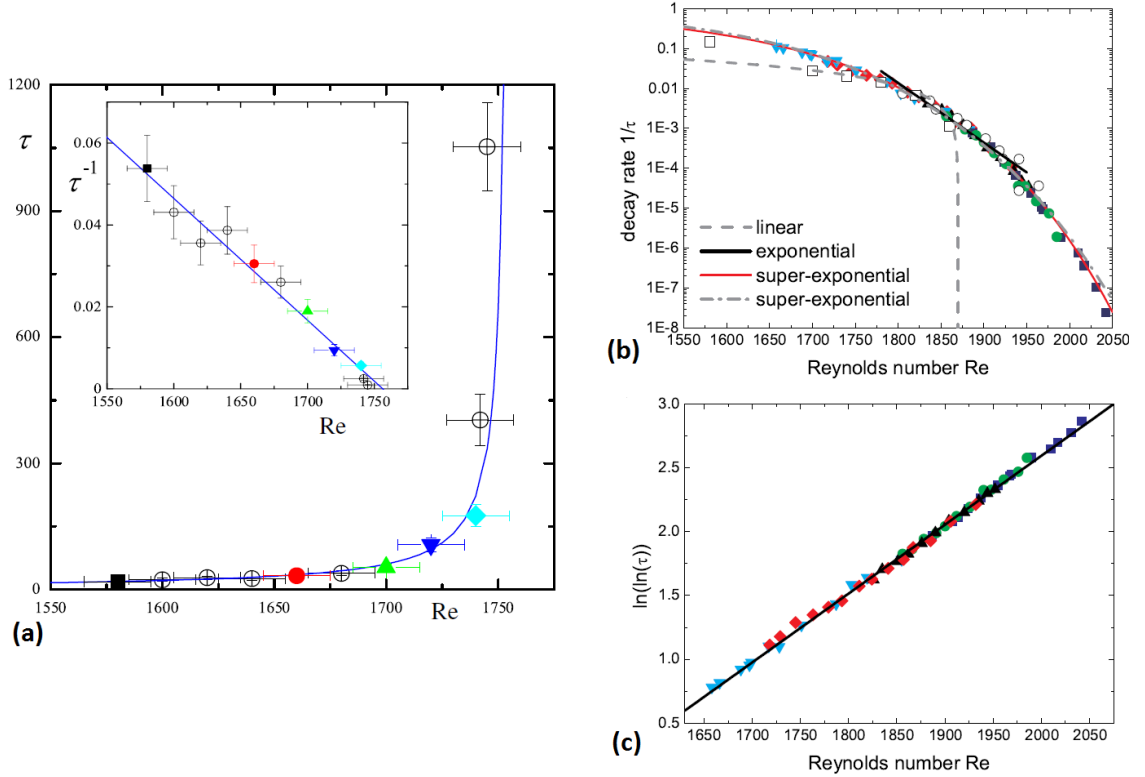
Figure 3.3: Lifetimes of turbulent puffs in pipe flow. (a) The experiments of Peixinho and Mullin suggested that there exists a critical Reynolds number above which the lifetimes of turbulent puffs diverges and turbulence becomes sustained. (b)-(c) Experiments by Hof et al. suggested that lifetimes increase super-exponentially but remain bounded for all Re. (a) adapted from J. Peixinho and T. Mullin, "Decay of Turbulence in Pipe Flow", *Phys. Rev. Lett.* **96**, 094501, 2006. (b) and (c) adapted from B. Hof et al., "Repeller or Attractor? Selecting the Dynamical Model for the Onset of Turbulence in Pipe Flow", *Phys. Rev. Lett.* **101**, 214501, 2008. Copyright American Physical Society 2006 and 2008.

Other experiments and simulations suggest that characteristic lifetimes do not diverge, so that even if they increase very rapidly with Re, they remain bounded for finite Re [143, 145, 146, 148, 155]. Such a scenario implies that turbulence in these systems is not a permanent state of the flow for *any Re* but is instead transient, if very long-lived. One interesting consequence of these results is that the turbulent state and the laminar state remain dynamically connected, which may allow for the possibility of controlling the transition using only small, local perturbations to the flow [156].

One of the reasons that the existence of a critical Reynolds number in linearly stable shear flows remains a subject of debate is that earlier studies have addressed the question using open flows such as pipe flow and plane Couette flow. This limits the maximum time

during which a turbulent episode may be observed and introduces complications associated with inlet conditions. Numerical exploration of this question has also proven to be problematic since many highly resolved simulations over long times are required to obtain significant statistics [147], straining today's fastest supercomputers.

This chapter presents the first measurements of the lifetimes of transitional states in Taylor-Couette flow. Several researchers have studied regimes of counter-rotating Taylor-Couette flow that exhibit coexisting turbulent and laminar domains. As discussed in Chapter 2, these have mostly been limited to studies of spiral turbulence and its dynamics [13,14,66,92,107,116,122,124] and to bursting regimes where there is an interplay between linear instability mechanisms and turbulent bursting phenomena [13, 109–113]. Only a few experiments have been carried out in configurations where only the outer cylinder rotates and the inner cylinder is fixed. These include the classic experiments of Taylor [65, 68], Wendt [70], Schult-Grunow [157], and Coles [14], and recent experiments by Alidai [158] and by Burin and Czarnocki [52].

In the subcritical regime Taylor-Couette flow shares much of the phenomenology observed in other shear flows. The transition to turbulence is abrupt and is characterized by spatially and temporally intermittent "patches" of turbulence[3] that coexist with a laminar background (see Fig. 3.4). Transition occurs despite theoretical predictions that circular Couette flow should to be linearly stable for all outer cylinder rotation rates as long as the inner cylinder is stationary [159]. Due to its periodicity, Taylor-Couette flow allows for arbitrarily long observation times and avoids the problems of contamination from inlets that plague plane Couette and pipe experiments. Furthermore, because Taylor-Couette flow has not previously been tested in this context, the experiments described here provide a test for the generality of trends observed in other shear flows.

---

[3]While subcritical Taylor-Couette flow share many of the qualitative features of other transitional shear flows, the term *patches* is used here so as to not make any unwarranted analogies with the much more well-characterized turbulent *puffs* in pipe flow or turbulent *spots* in boundary layer flows.
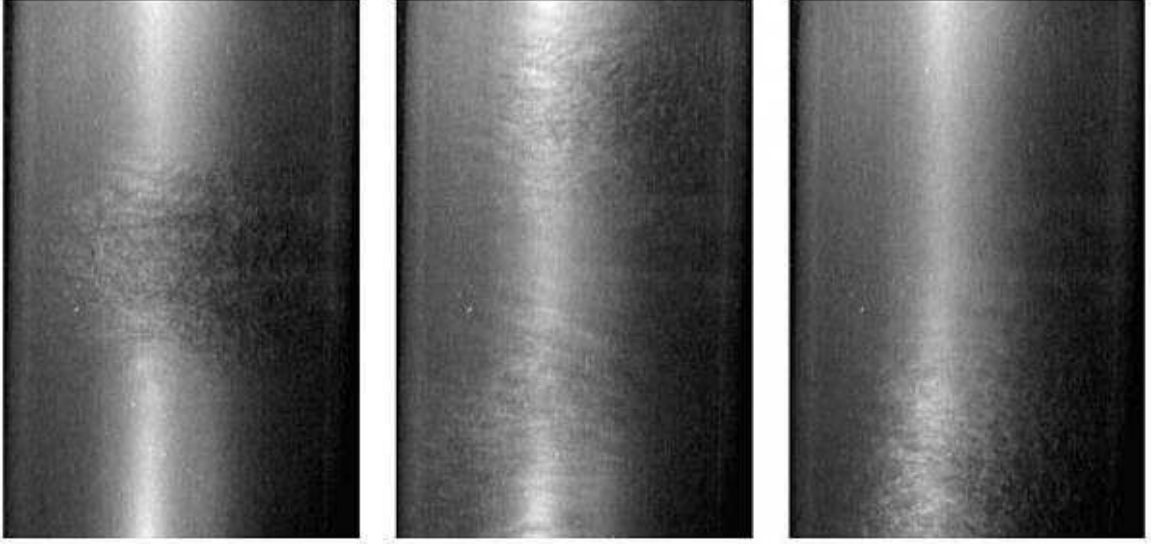
Figure 3.4: Photographs of turbulent patches in Taylor-Couette flow at $Re_o = 7500$ with only the outer cylinder rotating. In this regime, turbulent patches coexist with the laminar flow and exhibit complex spatiotemporal dynamics. The flow is visualized using Kalliroscope.

3.2 Experimental Apparatus

The experimental apparatus used in these experiments is a vertical Taylor-Couette system (shown in Figure 3.5) originally designed by Donald A. Hirst and constructed by the Machine Shop in the Department of Physics at the University of Texas at Austin [160]. Hirst used it to study how the dimension of the attractor in weakly chaotic Taylor-Couette flow depends on system size. The system features the ability to independently rotate the inner and outer cylinders and to adjust the height of the working volume, as well as a heat bath that enables the temperature to be carefully controlled.

3.2.1 Taylor-Couette Apparatus

The apparatus consisted of two independently rotating cylinders. The outer cylinder was made of a glass.[4] Its inside diameter was measured at 8 locations around the circumference at both ends and halfway along its length. The measurements were averaged resulting in a mean outer cylinder of radius r_o of 7.620 ± 0.008 cm. The inner cylinder was made of brass

---

[4]Hirst writes in his thesis that he used an outer cylinder made of Plexiglas. When it arrived at Georgia Tech, the apparatus had a glass outer cylinder with slightly smaller dimensions than those reported by Hirst. Attempts were made at establishing the origin of this cylinder, but were unsuccessful.

and was powder coated flat black at Miller's Powder Coating (Lilburn, Georgia). After powder coating, the inner cylinder diameter was measured at 8 radial positions at each of 3 locations along its length, resulting in a mean inner radius r_i of 6.638 ± 0.001 cm. Together with the outer radius measurement this gave a gap d of 0.982 cm and a radius ratio η of 0.871.

The bottom end cap was made of Teflon and fit onto a stainless steel table, which also made up the lower axle for the outer cylinder. The top end cap was also made of Teflon and had three holes through which push rods were inserted. These were attached to a stainless steel ring covered by a Teflon jacket that could be pushed along the length of the cylinder and defined the top boundary of the test section. By adjusting the position of the ring, the aspect ratio Γ of the system could be varied. The push rods were secured to a brass assembly that held the top bearing for the inner cylinder so that both ends of the test section rotated with the outer cylinder.[5] The experiments reported here were conducted at $\Gamma = 33.6$ unless otherwise noted.

Each cylinder was driven by a Compumotor M Drive M106-178 stepper motor with 25,000 steps per revolution and controlled using a Compumotor model 2100-1 indexer (Parker Hannifin, Rohnert Park, California). The indexers were controlled from a PC using Matlab's Instrument Control Toolbox (MathWorks Incorporated, Natick, Massachusetts). Sample code is provided in Section B.2.[6] The motors were mounted directly on the aluminum frame that supports the apparatus. The outer cylinder was connected to its respective motor using a W.M. Berg No. RC25-50 Row-L-ER® steel link chain (W.M. Berg Inc., East Rockway, New York). This was chosen for its durability while driving the outer cylinder at a constant rate for extended periods of time. The inner cylinder was connected to its motor using a W.M. Berg No. 3DCF-150-E Min-E-Pitch® dual ladder chain. This type of chain was determined to be more durable under the quick, impulsive driving required for the inner cylinder (see Section 3.3 for details). Mechanical drawings of the shaft adapters

---

[5]Hirst's original design allows the aspect ratio of the system to be actively adjusted by a stepper motor while the cylinders are rotating. This feature was not used here.

[6]While it is possible to control the indexers from the front panel, internal switches must be adjusted to set the velocity and acceleration ranges for the front panel switches. By using computer control the entire range of velocities and accelerations is available. The reader is referred to Ref. [161] for more details.
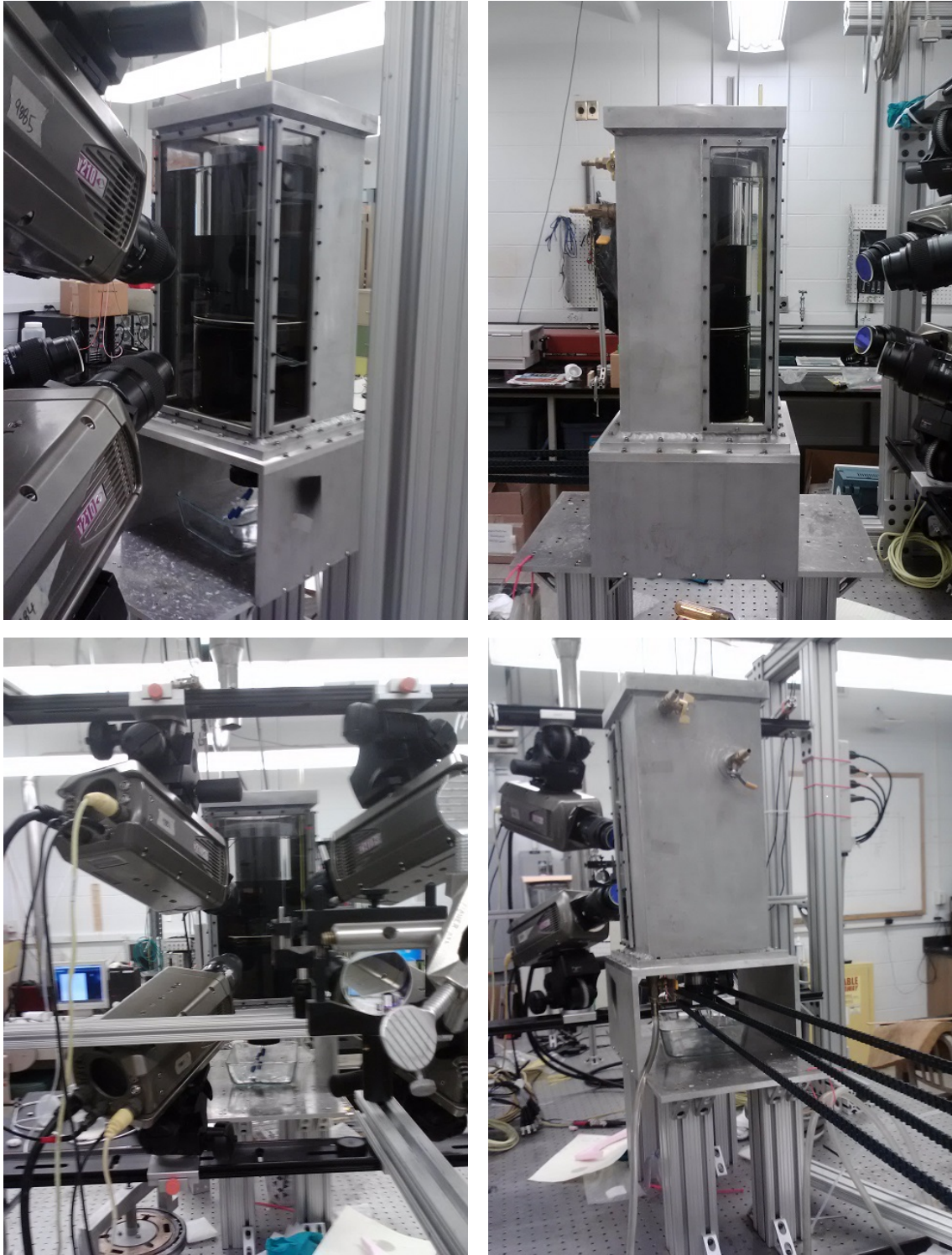
Figure 3.5: Hirst system. The Taylor-Couette apparatus used in these experiments was originally designed by D.A. Hirst at the University of Texas [160]. It features independently rotating cylinders, continuously adjustable aspect ratio, and the possibility of carefully regulating the operating temperature.

used to attach the sprockets to the motors and to the apparatus are given in Appendix C.

The native resolution of the indexers was improved by stepping down the motors using a 3:1 gear ratio. The accuracy of the indexer settings was tested by measuring the rotation rate of the cylinders using a Honeywell HMC1501 rotary displacement sensor (Honeywell Sensor Products, Plymouth, Minnesota). The HMC1501 provides an output voltage proportional to $\sin 2\phi$, where ϕ is the angle between an externally applied magnetic field and chip package. Permanent magnets were mounted diametrically across the inner cylinder sprocket and the top bearing assembly to generate constant magnetic fields that rotated with each cylinder. The HMC1501 was placed in this field on an externally mounted bracket and its output voltage was recorded using a Measurement Computing USB-1208FS data acquisition module (Measurement Computing, Norton, Massachusetts). The resulting signal was then analyzed by Fourier analysis to determine the rotation rates of the cylinders $\omega_{o,i}$.[7] For the range of rotation rates used in the experiments described here the angular velocities were determined to be within 0.5% of the indexer set point.

The working fluid was distilled water. The flow was visualized by mixing 2.2% Kalliroscope AQ 1000 (Kalliroscope Corporation, Groton, Massachusetts) by volume into the water. The viscosity of the resulting suspension was measured using a No. 50 Cannon-Fenske routine viscometer (Cannon Instrument Co., State College, Pennsylvania). It was found to have a kinematic viscosity ν of $1.0298 \pm 0.0025\,\mathrm{mm}^2/\mathrm{s}$ at $20.0°\mathrm{C}$, a 2% increase in the effective viscosity relative to pure water in agreement with that reported by Andereck et al. [13]. The rheology of the suspension was also studied using a stress-controlled rheometer and no deviations from the expected Newtonian behavior were found (see Figure 3.6 for details). Special care was taken while filling the apparatus to ensure that no air bubbles were trapped in the test section as these were found to be very efficient at tripping the transition to turbulence.[8]

In order to control variations in viscosity due to temperature fluctuations, the entire

---

[7]Note that since the output of the HMC1501 is proportional to $\sin 2\phi$, the peak frequency of the sensor output is twice the rotation frequency of the cylinders.

[8]Completely removing bubbles from the test section can be tricky. Rotating the inner cylinder can help detach bubbles from the cylinder walls. Rotating the outer cylinder accumulates small bubbles into larger ones that can be removed by plunging the top end ring until it hits the bottom of the test section.
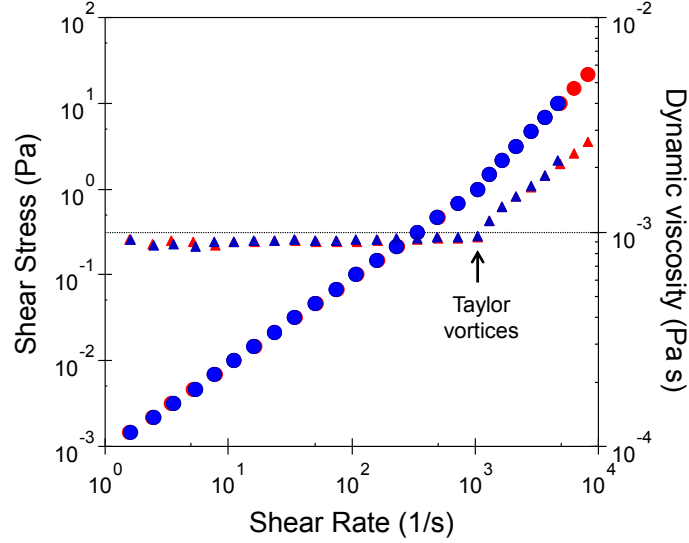
Figure 3.6: The rheological properties of the Kalliroscope suspension were measured using an MCR-501 stress-controlled rheometer with a double Couette geometry (Anton Paar, Graz, Austria). The shear rate (circles) was measured as a function of shear stress for distilled water (red) and a suspension of 2.2% Kalliroscope (blue). The effective viscosity (triangles) was calculated by taking the ratio of the shear stress to the shear rate. The break in the curves that appears at a shear rate of about 10^3 s^{-1} coincides with the theoretically predicted onset of Taylor vortices (black arrow) for the rheometer geometry. Measurements courtesy of B. Sierra-Martín and A. Fernández-Nieves of the Georgia Tech School of Physics.

apparatus was encased in a heat bath, which was supplied with chilled water using a Neslab RTE-210 refrigerated bath/chiller (Thermo Scientific, Newington, New Hampshire). The chiller was set to 20.00°C and the temperature in the bath was monitored using a Minco S1059PA5X6 platinum resistance thermometer (Minco Products, Inc., Fridley, Minnesota). 2-wire resistance measurements of the platinum resistance thermometer were carried out using a Hewlett-Packard HP 34401A multimeter (Hewlett-Packard Co., Palo Alto, California) and imported into Matlab using the Instrument Control Toolbox (see Appendix B.3). These were then converted to temperatures using the interpolant for temperature as a function of resistance provided by Minco [162]. The thermometer readings were observed to deviate by less than ±0.05°C over several days. The temperature in the working fluid itself was periodically measured using a Thermo Scientific ERTCO ASTM 63C compliant full immersion mercury thermometer with 0.1°C resolution and was found not to vary significantly from the temperature measured in the heat bath. These results, along with the geometric characteristics of the apparatus, allowed the outer cylinder Reynolds number $Re_o = r_o \omega_o d/\nu$

to be set to within 1%.

3.2.2 Flow Visualization

As mentioned earlier, the flow was visualized using the Kalliroscope technique. This technique works on the same principle as the aluminum powder technique first used in Taylor-Couette flows by Schultz-Grunow and Heim [82] (see Section 2.6). The first to use Kalliroscope visualization in Taylor-Couette flow were Swinney, Fenstermacher, and Gollub. Their original photographs are reproduced in Figure 3.7.[9]
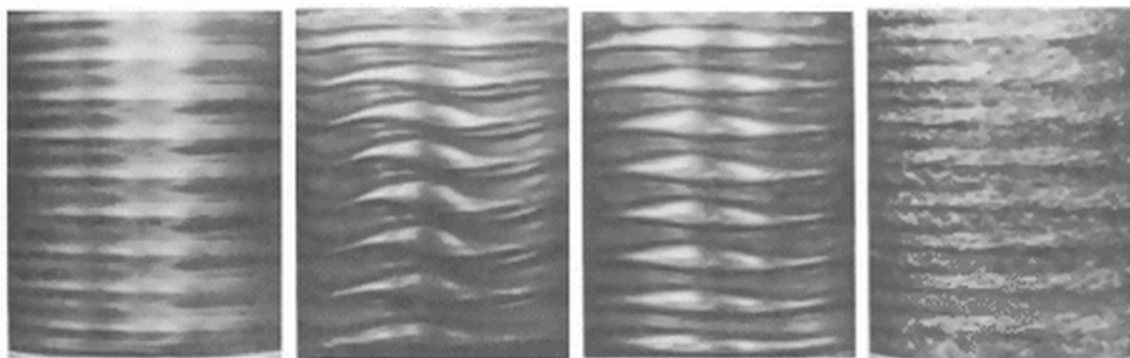
Figure 3.7: The first published images of Kalliroscope visualization of Taylor-Couette flow showing the supercritical transition to turbulence were published by H.L. Swinney, P.R. Fenstermacher, and J.P. Gollub in 1977. Some of these photos were reproduced in Swinney and Gollub's 1978 article "The Transition to Turbulence" in *Physics Today* [175]. Adapted from *Synergetics (Vol. II)*, H. Haken (ed.), 1977, Berlin, Germany: Springer-Verlag. Copyright 1977 Springer-Verlag.

Named after the Greek words *kalos*, *rheos*, and *skopien* meaning "beauty", "flow", and "seeing", the Kalliroscope technique is based on seeding the flow with minuscule guanine platelets that reflect light preferentially depending on their orientation [179]. Guanine is a commercial pigment extracted from fish scales and affords several advantages over other materials used for flow visualization with reflective flakes. For one, it has a significantly lower density (1.62 g/cc) than other commonly used flake materials (aluminum, mica, etc.).

---

[9]Kalliroscope was invented by artist Paul Matisse in the mid 1960s for use in "kinetic sculptures" [163]. Matisse was granted a patent for his invention [164] and began selling Kalliroscope commercially as early as 1968. However, its adoption by the fluid dynamics community appears to have been rather slow. A detailed search of the literature found only 14 references to Kalliroscope use during the 1970s [165–178]. The earliest reference to Kalliroscope visualization in the Taylor-Couette literature appears to be a monograph by Swinney, Fenstermacher, and Gollub in the second volume of Springer's Series on Synergetics [174]. By the mid 1980s Kalliroscope had largely replaced the aluminum powder technique as the flow visualization technique of choice for researchers studying Taylor-Couette flow.

Guanine flakes are also quite small with typical dimensions of approximately $30 \times 6 \times 0.07$ μm [169]. Because of their low density and small size guanine flakes can stay in suspended in water for long periods of time.[10] Guanine also has a high index of refraction ($n = 1.85$), which makes Kalliroscope particles easy to see in water even at very low concentrations [179]. This makes Kalliroscope visualization relatively unintrusive.[11]

While Kalliroscope is incredibly good at showing flow structure, it is interesting to note that even today, 35 years after its invention, it is not clear what it is that Kalliroscope visualization actually shows [181]. A few attempts have been made to understand this [181–184], but no consensus exists for general flows beyond the qualitative argument that platelets tend to align themselves with stream surfaces. Even taking this into account, the interpretation of Kalliroscope images depends on the details of the lighting arrangement. For example, in images of spiral turbulence by Andereck et al., where the flow is illuminated from outside the cylinders, turbulent bands appear dark [13]. In images of the same flow by Prigent and Dauchot, who illuminated their system with the light emitted by a fluorescent coating on the inner cylinder, turbulent bands appear bright [117]. More complicated lighting arrangements can elucidate additional flow features but complicate the interpretation of the flow structures even further [185].[12]

In the experiments described here, the flow was illuminated externally (see Section 3.2.3) and Kalliroscope images of coexisting laminar and turbulent domains were interpreted as follows: In the laminar domains, the stream surfaces are well-defined and smooth, so the alignment of the platelets is spatially correlated and they provide uniform reflection of the incident light, yielding bright areas. In the turbulent domains, the flow is erratic, so the platelets acquire random orientations, which lowers the effective reflectivity of the fluid.

---

[10]Some early experiments used perchloroethylene (C_2Cl_4), a solvent used in dry-cleaning, which has a density of 1.620 g/cc. This allowed Kalliroscope particles to remain suspended indefinitely. An art installation using Kalliroscope in perchloroethylene showed no "observable settling of the flakes" for over 15 years [179].

[11]As pointed out by Dominguez-Lerma et al. care must be taken when studying flows with poor mixing properties [180].

[12]While extracting quantitative flow data from Kalliroscope images has proven challenging, recent progress has been made in visualizing data from computer simulations using "virtual rheoscopic fluids" [184,186,187]. The idea here is to generate visualizations of numerically computed flow fields that emulate Kalliroscope, so that they can be compared directly with experimental flow visualization images.

This results in darker areas that show significant fluctuations in intensity. This effect is enhanced by the black powder coating on the inner cylinder.

3.2.3 Camera Setup, Lighting, and Image Acquisition

The flow was imaged using a Sony XC-77 monochrome CCD video camera (Sony Corporation of America, New York, New York) powered by an Aegis Electronics PS-12SU camera adapter/power supply (Aegis Electronic Group, Gilbert, Arizona). A 28 mm Nikon Nikkor f/2.8 AF-D lens (Nikon Incorporated, Melville, New York) was installed on the camera using a C-mount to F-mount adapter. The camera was mounted on a post approximately 1.2 m in front of the apparatus and was aimed at the middle of the test section and manually focused. The camera was turned on its side so that the longer dimension of the sensor extended vertically. This allowed the camera to capture a larger segment of the flow field. A Nikon PK-11 8 mm extension ring was used to help frame the images so that moving parts (e.g., the rods holding the adjustable upper end cap) were not in the frame. The resulting field of view covered a region of the flow that was approximately 25 cm tall and compromised $\sim 75\%$ of the total height of the test section.

Because the image analysis algorithm used to detect the presence of turbulence relies on detecting intensity fluctuations in the recorded images (see Section 3.4.1 for details), the camera's automatic gain correction was disabled to minimize unwanted intensity fluctuations. This was done by configuring the internal solder jumpers as shown in Figure 3.8. Additional fluctuations in image intensity were found to come from reflections of movement in the laboratory on the front window of the heat bath or from variations in ambient lighting. To eliminate these effects, the apparatus and camera setup were fully enclosed in a tent made of black plastic sheeting.

The flow was illuminated by two 15 W fluorescent lamps, which were placed horizontally in front of the apparatus; one above the test section and another below it as shown in Figure 3.9. The diffusers that came installed on the lamps were left on. Cardboard blinds were installed to ensure that only light reflected by the test section reached the camera. This improved the contrast in the captured images. The camera support was spray painted

(a)   (b)   (c)
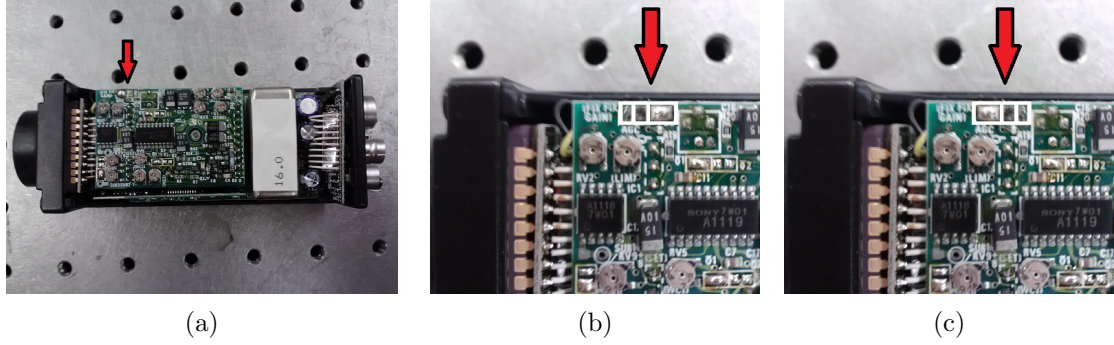
Figure 3.8: Disabling automatic gain correction on the Sony XC-77 camera requires the user to toggle internal solder jumpers. (a) The jumpers that set the XC-77's automatic gain correction mode are located on the upper left hand corner of the PR-89 board as shown by the red arrow. The PR-89 board is the topmost board when the camera housing is opened. (b) When jumper on the right is connected by soldering its two pads together and the jumper on the left is left disconnected, automatic gain correction is enabled. (c) Automatic gain correction can be disabled by disconnecting the jumper on the right and connecting the jumper on the left as shown.

flat black to prevent it from being reflected from the front window of the heat bath.

The camera output was recorded on a PC using a WinTV 44801 television tuner board (Hauppauge Computer Works, Hauppauge, New York), which was controlled using Matlab's Image Acquisition Toolbox (see Appendix B.1 for sample Matlab code). The camera output was connected to the composite video channel on the tuner board using RG59 coaxial cable. Images were acquired at a reduced resolution of 320×240 pixels to minimize storage requirements and facilitate real-time processing and analysis. Except for the three highest Reynolds numbers studied (see Section 3.3), the video was captured at 30 frames per second. At the highest Reynolds numbers, the frame rate was reduced to 5 frames per second due to data storage limitations since individual turbulent transients could last many hours. This reduced frame rate was determined to be sufficient to detect the presence of turbulent patches in the flow.

3.3 Experimental Procedure

Like plane Couette and pipe flows, linearly stable Taylor-Couette flow requires finite-amplitude perturbations to the base flow to initiate the transition to turbulence. In order to ensure that all experiments at a particular Reynolds number started from the same state,
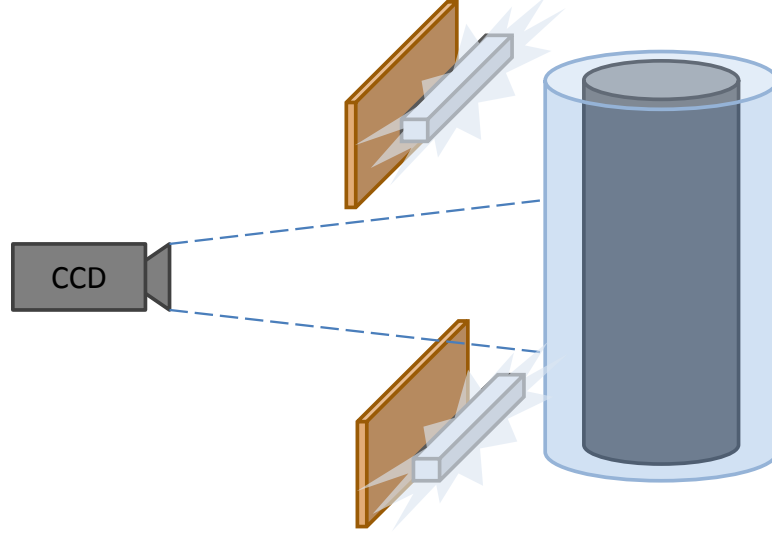
Figure 3.9: The flow was illuminated with two 15 W fluorescent lamps, which were placed above and below the test section. Cardboard blinds prevented light from the lamps from directly illuminating the camera.

the laminar state was first prepared by accelerating the outer cylinder to the desired Re_o. Care was taken not to accelerate the cylinder too quickly as rapid acceleration was found to trigger turbulence. The system was allowed to run in Couette flow for several minutes ($\sim$ 3 radial diffusion times $t_d = d^2/\nu$) in order to eliminate any transients. As will be shown in Chapter 4, the size of the perturbations needed to trip turbulence becomes smaller with increasing Reynolds number. It was determined that at $Re_o \sim 16{,}000$ turbulence was spontaneously triggered by ambient noise, so the experiments described here were conducted significantly below this threshold.[13]

Once laminar flow was established, the flow was perturbed by rapidly accelerating the inner cylinder in the direction opposite the rotation of the outer cylinder and immediately stopping it. The velocity profile of the inner cylinder is shown in Figure 3.10. This created a large global perturbation that disturbed the whole flow. As will be discussed in Section 3.5.4, the resulting distribution of lifetimes was not very sensitive to the details of the initial perturbation, so the perturbation profile shown in Figure 3.10 was used in

---

[13]The critical Reynolds number for spontaneous transition was determined by stepping up Re_o in steps of $\sim$ 150 every 3 minutes until transition was observed. This was measurement was repeated 5 times with similar results. For more details on the spontaneous transition to turbulence in Taylor-Couette flows with only the outer cylinder rotation, see the paper by Burin and Czarnocki [52].
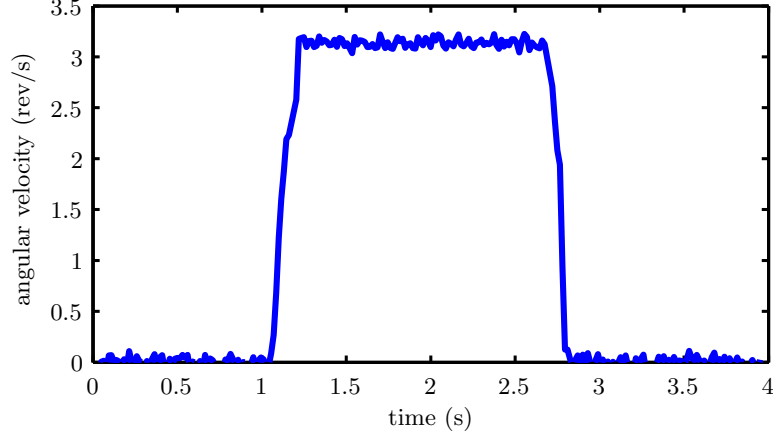
Figure 3.10: The angular velocity of the inner cylinder was measured as a function of time using a Honeywell HMC1501 rotary displacement sensor. The sensor signal was normalized, unwrapped and smoothed. The velocity was then calculated by numerical differentiation of the displacement data. The perturbation profile shown here was generated by setting the maximum *motor* velocity to 10 Hz, the maximum acceleration to 60 Hz/s, and the total motor displacement to 400,000 steps. The 3:1 gear ratio between the inner cylinder and the motor stepped this down to an inner cylinder rotation rate of 3.33 Hz.

all experiments unless noted otherwise. This perturbation will henceforth be referred to as the *standard perturbation*. The standard perturbation is qualitatively different from the localized perturbations used in earlier pipe flow experiments [142, 143, 146]. Instead, it is more similar to quenching experiments conducted in plane Couette flow [115]. The inner cylinder rotation rate was chosen so that it took the system well into the turbulent regime. After briefly exhibiting featureless turbulence, the flow relaxed to an intermittent state like the one shown in Fig. 3.4. This was monitored until the flow relaminarized and the lifetime of the event was recorded.

3.4 Data Analysis

3.4.1 Automated Detection of Turbulent Patches

Because of the large number of experiments required to characterize the statistical distributions of lifetimes, the monitoring of the flow was automated using realtime analysis of the video stream. As the video stream was imported into the computer, it was separated into ten frame segments. A frame from each segment was subtracted from a reference frame in the segment preceding it. The resulting image was thresholded to highlight only pixels that

were significantly different from the same pixel in the reference image to reduce noise. It was determined that a threshold value of 12 out of 255 for 8 bit images accurately distinguished between laminar and turbulent regions of the flow. The elements of this binary image were added together and the resulting number N was compared to an empirically determined threshold, $N_T = 300$. If N dropped below N_T for 30 seconds (turbulent patches were never observed to return after disappearing for more than a few seconds), the system stopped acquiring data and prepared for the next run. Figure 3.11 shows a typical time series of N.
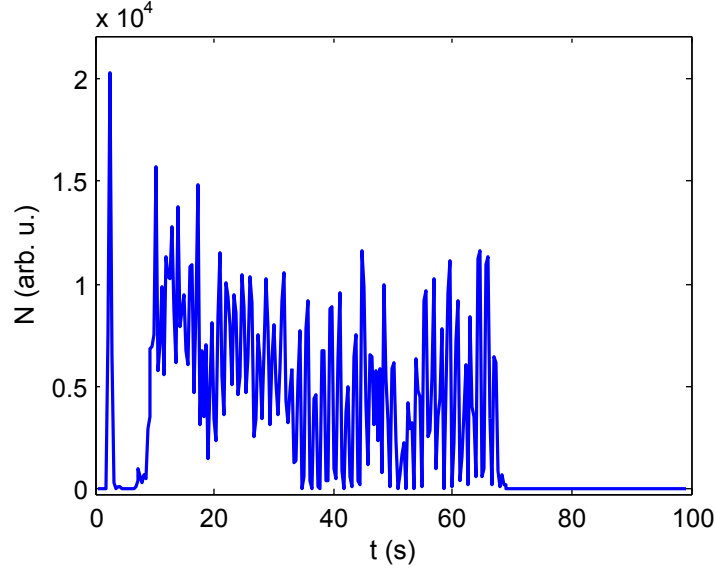
Figure 3.11: Typical turbulence signal N for the standard perturbation at $Re_o = 7305$ and $\Gamma = 23$. The initial perturbation is evident at $t = 2$ s. The large amplitude of the perturbation sets the majority of the flow rotating in the clockwise direction. As the flow relaxes to counter-clockwise rotation driven by the outer cylinder it goes through a short period of time where the flow is almost quiescent (4 s $< t < 8$ s). If the perturbation is successful the flow becomes turbulent resulting in a fluctuating signal. The apparent periodicity of the signal corresponds to turbulent patches coming into and out of the view of the camera as they circulate around the cylinder. At $t = 68$ s turbulence suddenly collapses, leaving behind purely laminar flow.

The image processing algorithm described above was found to be more robust during long experimental runs than subtracting a constant background image taken at the beginning of the experiment. This is because during long runs Kalliroscope is slowly deposited on the outer cylinder wall, which gradually changes the reflected light intensity even for completely laminar flow. The method employed here works around this by detecting only short-time variations in the captured images.

3.4.2 Calculating $\tau(Re_o)$

Repeating the experiment M times (between 200 and 1200 times depending on Re_o, see Table 1) gives significantly different results at fixed Re_o, as shown in Figure 3.12a. The statistics are better visualized by probability P that an event will survive up to time t. This was calculated as follows: For each time t, the fraction of events p that lasted at least as long as t was used as an estimator of $P(t)$. The sampling error in this estimate is given by [188]

$$\Delta P = \sqrt{\frac{p\,(1-p)}{M}}.\tag{7}$$

As shown in Figure 3.12b, $P(t)$ has two salient features. First, it has an exponentially decaying tail (i.e., $P(t) \sim exp(-(t-t_0)/\tau)$ for times greater than t_0, where t_0 is the time associated with the initial formation of the turbulent state. The typical lifetime τ can be estimated from the slope of a linear fit to the tail of the distribution on a semi-log plot. More precisely, it is given by the inverse of the slope parameter. The uncertainty in this measurement was calculated from the 95% confidence interval on the slope parameter of the fit. Second, a significant fraction ($\sim 30\%$) of the experiments relaminarized immediately after the perturbation. These short-lived events were not used in determining τ, but were used to provide an estimate for t_0. This was determined to be ~ 1200 advective time units[14] $t_a = d/r_o\omega_o$. For the range of Reynolds numbers studied here, $t_a \sim 0.012$ s. An alternative method to estimate t_0 and a discussion of how the choice of t_0 affects the measured values of τ is provided in the paper by Avila et al. [147].

3.5 Results

3.5.1 Scaling of τ with Re_o

The experiment outlined in Section 3.3 was repeated at various Reynolds numbers (see Appendix A for details). As shown in Figure 3.13, the survival probabilities show approximately exponential decay at all Reynolds numbers. Some deviations from exponential

---

[14]t_0 was incorrectly reported as 120 instead of 1200 in Borrero-Echeverry et al., *Phys. Rev. E* **81**, 025301(R), 2010.
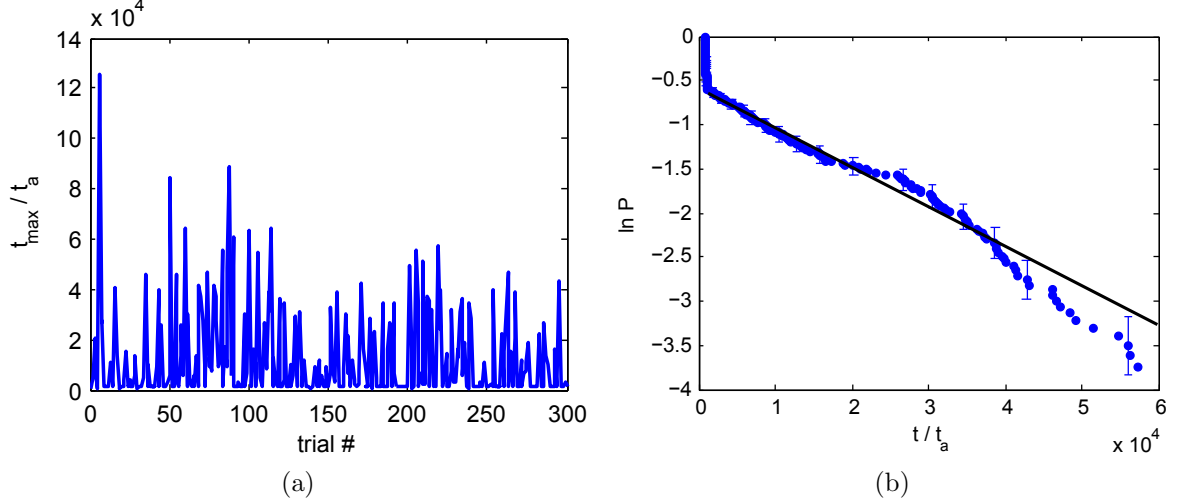
Figure 3.12: Experiments at constant Re_o yield turbulent events with lifetimes that vary significantly. (a) Lifetimes for 300 experiments at $Re_o = 8106$ with $\Gamma = 33.6$. Times are scaled by the advective time unit $t_a = d/r_o\,\omega_o$. (b) The probability P of a turbulent event persisting up to t approximately follows an exponential distribution for long times. The typical lifetime τ can be calculated from the slope of a weighted least-squares linear fit to the tail of the distribution (black line). For short times, the lifetimes of events depends on whether the initial perturbation puts the flow in the basin of attraction of the chaotic repeller. If the perturbation puts the flow in the basin of attraction of the laminar flow, the flow relaminarizes immediately, as evidenced by the sharp drop off in P at small t. Error bars indicate sampling error $(\Delta\,(ln\,P) = \Delta P\,/\,P)$ and are shown only at representative points.

behavior can be seen and are probably due to limited statistics (see Section 3.7.3 for a discussion of the abnormally large deviation observed for $Re_o = 6423$). In order to test this hypothesis, finite samples of exponentially distributed pseudo-random numbers were generated and their survival probabilities were calculated. Figure 3.14 compares the decay probability for experiments at $Re_o = 7111$ with two of the synthetic data sets. It is evident that the observed spread in the experimental data is comparable to the spread in the synthetic data, which also show some commonly observed trends like a slight downward curvature for large times due to the rarity of very long-lived transients. The exponential tails of the survival probabilities, a hallmark of chaotic repellers [150, 151], indicate that the decay of turbulence is memoryless. The same behavior has been reported in all previous studies of the decay of turbulence in plane Couette and pipe flows [115, 142–146, 155], as well as in studies of decaying magnetohydrodynamic turbulence [148] and transient turbulence
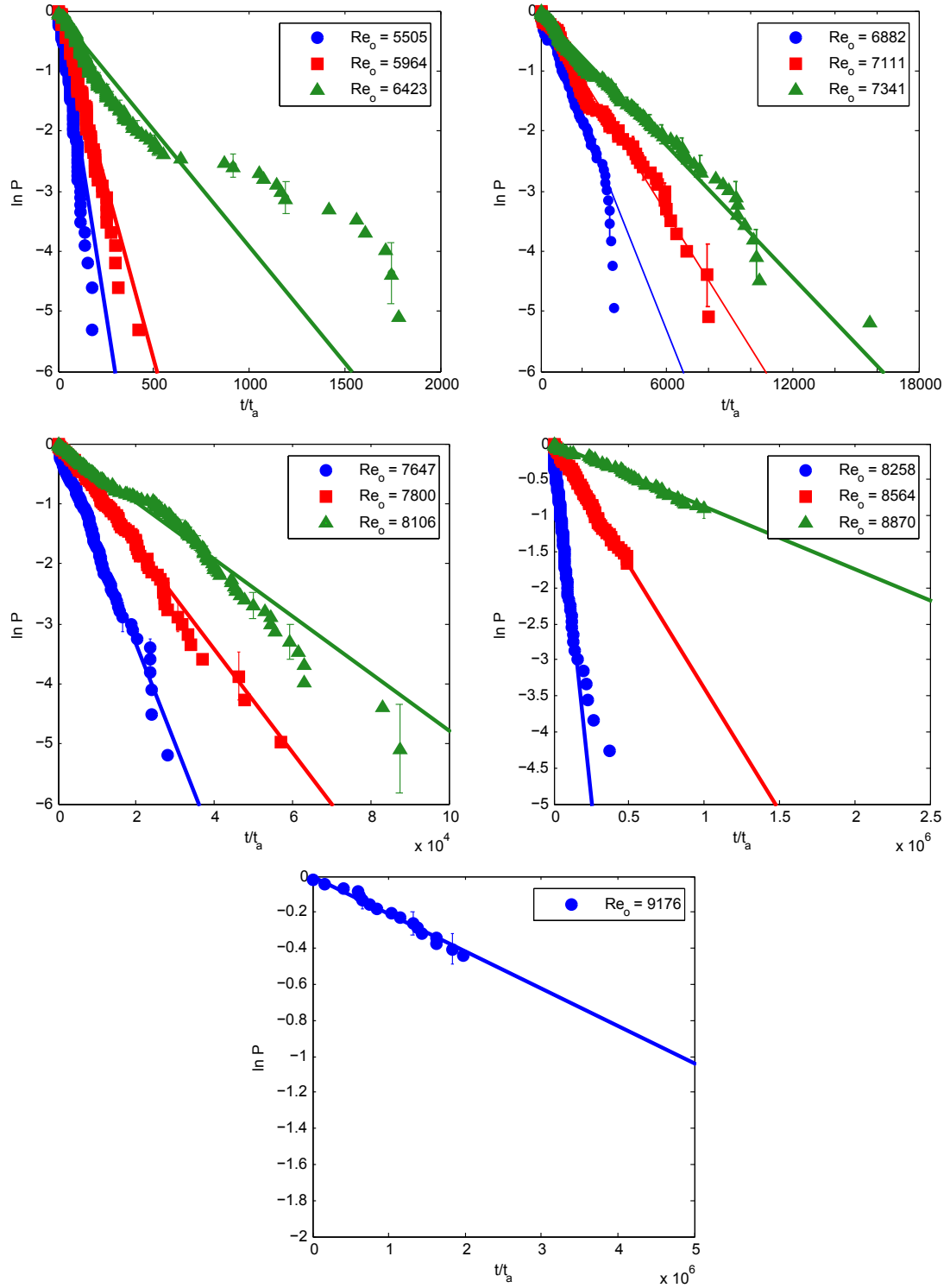
Figure 3.13: Probability of survival as a function of time for various Re_o at $\Gamma = 33.6$. The typical lifetime τ increases very quickly with increasing Re_o. The solid lines show the weighted least squares linear fits to the tails of the distributions. For $Re_o > 8500$ a maximum observation time was imposed as described in the text.

in superfluid helium II [149].
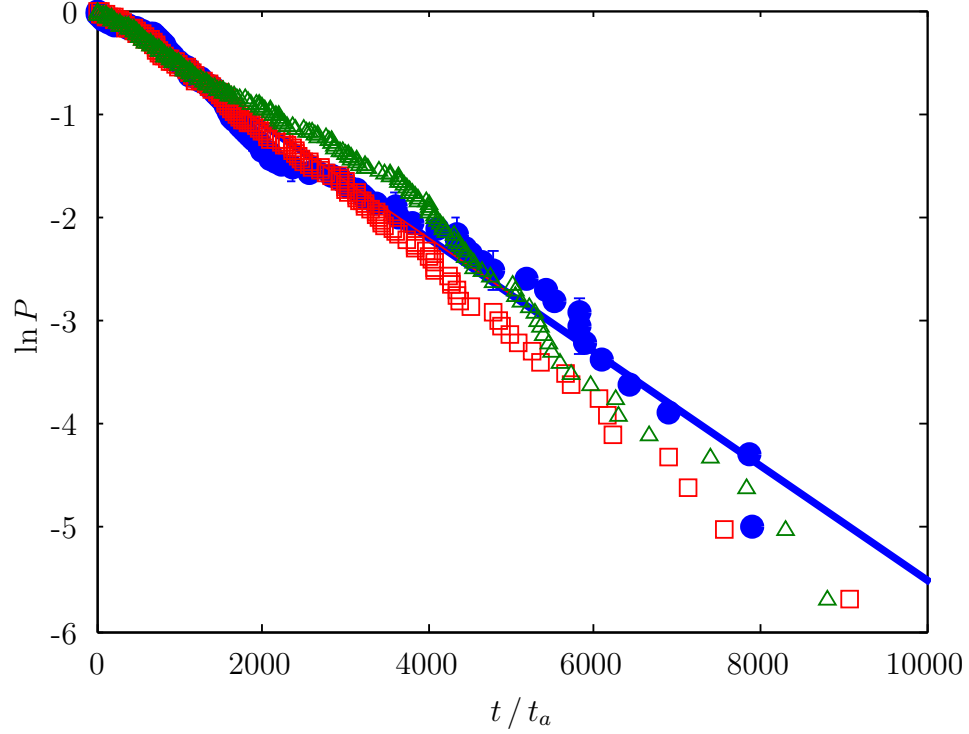
Figure 3.14: The decay probabilities of samples of 300 exponentially distributed pseudo-random numbers ($\triangle$,$\square$) with the same mean parameter as experiments at $Re_o = 7111$ show a similar statistical variation to experiments ($\bullet$).

As shown in Figure 3.15, the characteristic lifetimes, as measured from least squares fits of the exponential tails of $P(Re_o)$, increased very rapidly with Re_o. However, no Re_o was found for which decay was not eventually observed. At $Re_o = 9922$, an event was observed that lasted 29 hours before relaminarizing. Naturally, conducting the number of experiments required to obtain good lifetime statistics at higher Reynolds numbers was impractical, so maximum observation times were imposed for the highest Reynolds numbers studied ($Re_o = 8564, 8870, 9176$). Imposing a maximum observation time prevented the direct observation of the decays of the longest-lived events, but still left enough events of intermediate length to get good estimates of the characteristic lifetimes. This technique has been used successfully in studies of pipe flow, where turbulence is advected down the pipe and the maximum observation time is limited by the length of the pipe [33, 146]. To validate this procedure, it was used to measure the characteristic lifetime for $Re_o = 7111$.
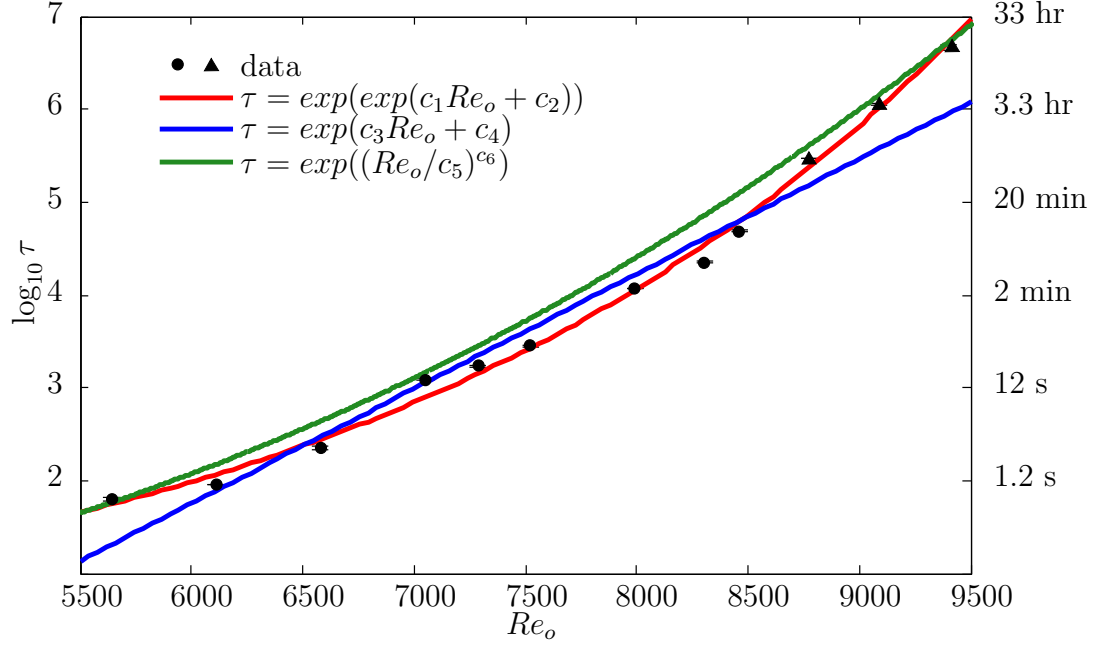
Figure 3.15: Characteristic lifetime τ grows faster than exponentially as a function of Re_o. Lifetimes are scaled in advective time units t_a. The points indicated with ● correspond to data sets for which all the decays were directly observed. The points indicated with ▲ correspond to data sets for which a maximum observation time was set. Errors in $\log_{10} \tau^{-1}$ are on the order of the symbol size and were estimated from the 95% confidence intervals for the slope parameter of the linear fits shown in Fig. 3.13.

The resulting lifetime differed from that measured by observing all events by less than 1%.

As is evident in Figure 3.15, a purely exponential growth model does not fit the data well and the lifetimes grow faster than exponentially with increasing Re_o. The lifetime data in Figure 3.15 was fit with the various functional forms proposed by Hof et al. [146] and it was found that

$$\tau^{-1}(Re_o) = exp(-exp(c_1 \, Re_o + c_2)), \tag{8}$$

with $c_1 = 3.61 \times 10^{-4}$ and $c_2 = -0.59$ best captured the observed trend (i.e., had the smallest residuals). While Eq. 8 visually fits the observed trend, goodness-of-fit statistics indicate that it is not statistically significant (i.e., $\chi_\nu^2 \gg 1$). As shown in Fig. 3.15, alternative fits to the data are possible (e.g., $\tau^{-1} = exp(-(Re_o/c_5)^{c_6})$ with $c_5 = 3305$ and $c_6 = 2.62$) and differentiating between them requires many more decades of data. Therefore, the claim cannot be made that Eq. 8 is the actual functional dependence of τ on Re_o. The important point is that the observed trend suggests that the lifetimes of turbulent transients remain
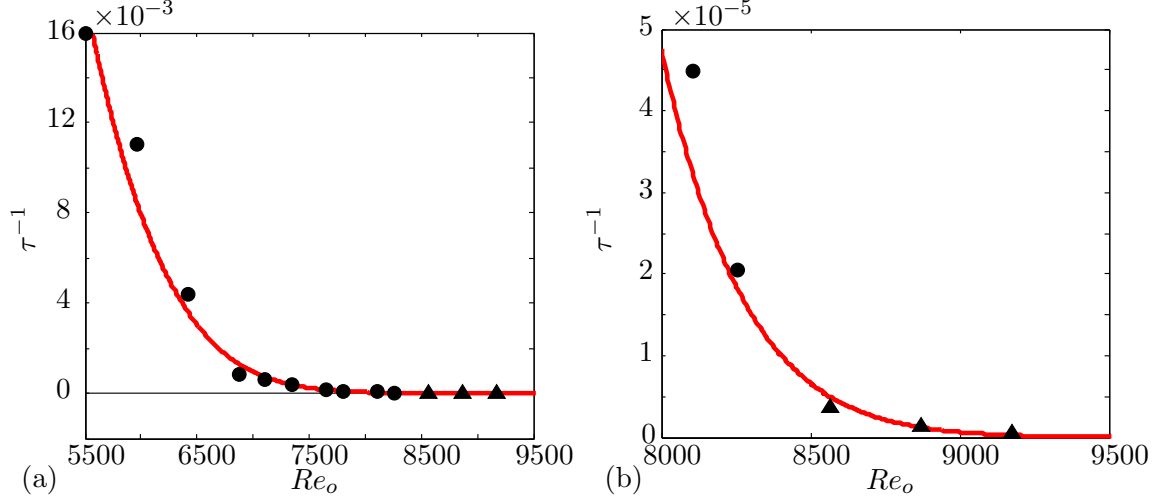
Figure 3.16: (a) The inverse of the measured lifetimes only approaches zero asymptotically with increasing Reynolds number. (b) Magnified view of (a) for large Re_o. ● correspond to experiments where all decays were observed directly. ▲ correspond to experiments where a maximum observation time was imposed.

bounded for increasing Re_o. If the lifetimes diverged, τ^{-1} would be expected to cross zero at some point. Instead they only approach zero asymptotically as shown in Figure 3.16. Attempts were also made to fit the data with functional forms that contain singularities (e.g., $\tau = A/(Re_c - Re_o)^\alpha$) but these fits result in unreasonably large overall scaling parameters, which suggests that if a critical Reynolds number exists it is far away from the regime studied here as shown in Figure 3.17.

3.5.2 Effects of System Size on τ

A natural extension of the work presented above is to measure the lifetimes of turbulent transients for different Taylor-Couette geometries. Experiments were conducted at a variety of aspect ratios and Reynolds numbers as summarized in Appendix A. It was observed that lifetimes increased at least exponentially with increasing Re_o, with the smaller aspect ratio configurations typically showing quicker decays at fixed Re_o than the larger aspect ratio ones. However, as can be seen in Figure 3.18a, the scaling of τ with Γ is non-trivial. For $Re_o < 8200$, the data for $\Gamma = 23$ closely follow the original data set at $\Gamma = 33.6$. However, above this value the two curves separate, with the measured lifetime at $\Gamma = 33.6$ at $Re_o = 8564$ almost a factor of 4 larger than that at $\Gamma = 23$. On the other hand, the decay constants
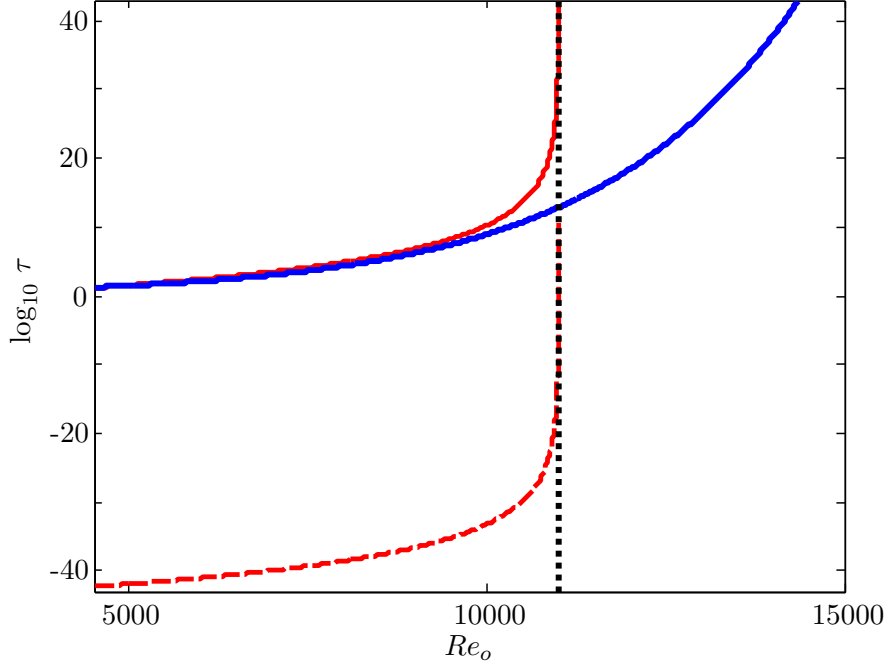
Figure 3.17: Multiplying a function that has a singularity by a very large number stretches the part of function that grows very slowly in such a way that it can be used to represent data that grows at a bounded rate by staying away from the singularity. This is the case for the lifetime data at $\Gamma = 33.6$, where fits of the type expected for critical phenomena ($\tau = A/(B - Re_o)^C$) have large overall scaling parameters of $\mathcal{O}\left(10^{43}\right)$. The best fit of this kind is shown with (solid red line) and without (dashed red line) the prefactor of $\mathcal{O}\left(10^{43}\right)$. It can be seen that the part of the function that is almost flat gets stretched out, so that for a range of Re_o it looks like super-exponential growth of the form $\tau(Re_o) = exp(exp(c_1 Re_o + c_2))$ (solid blue line). Similar results were obtained for fits to lifetime models of the form $\tau = exp(A/(Re_o - B)^C)$, which expected in systems undergoing transitions analogous to the ideal glass transition. Here A was found to be $\mathcal{O}\left(10^{82}\right)$.
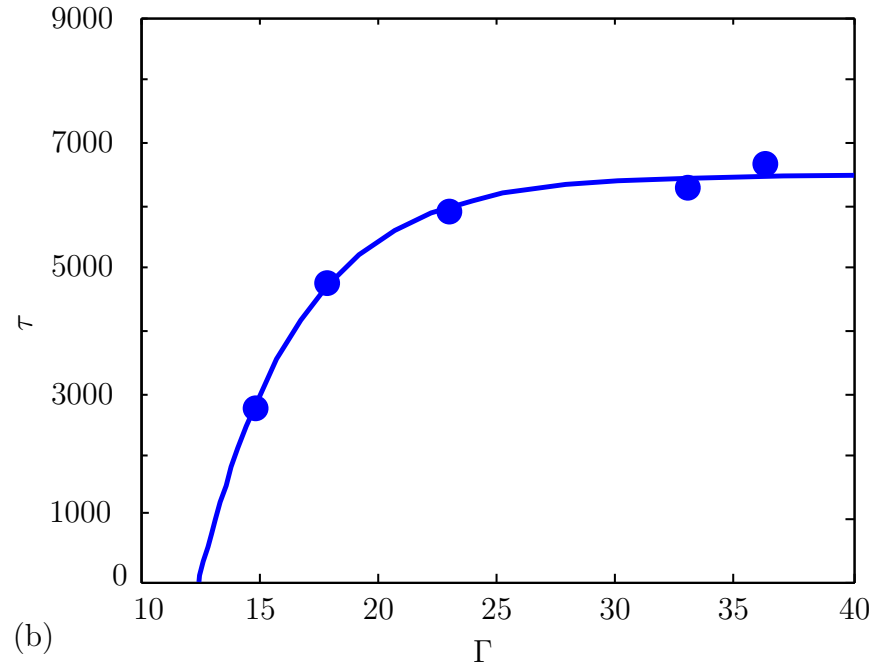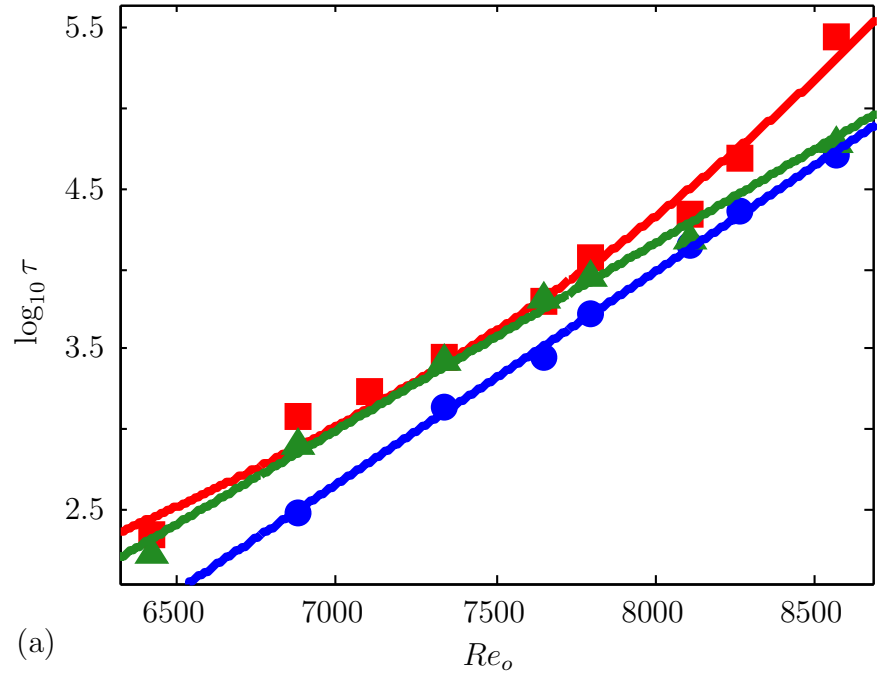
Figure 3.18: (a) The lifetimes of transient turbulence increase at least exponentially with Re_o for $\Gamma = 15$ (●), 23 (▲), and 33.6 (■). (b) At $Re_o = 7647$, the lifetimes appear to grow quickly as the system size increases before tapering off to a roughly constant value above $\Gamma \sim 25$. The solid line is a fit of of the form $\tau(\Gamma) = A(1 - exp(-B(\Gamma - \Gamma_c)))$ with $A = 6.62 \times 10^3$, $B = 0.235$, and $\Gamma_c = 12.6$.

for $\Gamma = 15$, start off much smaller for low Re_o, but grow more quickly than for the larger aspect ratios. Interestingly, neither of the reduced aspect ratio data sets show evidence of super-exponential scaling of τ with Re_o and are better represented by pure exponentials. It is possible that the range of Re_o studied at reduced Γ is too narrow to capture the super-exponential trend that might have been observed had studies been conducted for a wider range of Re_o. As an example, take the data presented in Figure 3.15. If only the central six data points are considered, the data is well fit by an exponential. It is only when *all* the data are taken into account that the super-exponential trend becomes apparent. A similar example can be found in the pipe flow literature where Hof et al. reported exponential scaling of transient lifetimes in their initial 2004 they found when they extended their study to a wider range of Reynolds numbers in 2008 [146].

Experiments over a greater number of aspect ratios were carried out at a fixed Re_o. It was found that the measured decay constants grew quickly with increasing Γ, but appeared to level off for $\Gamma \sim 25$. This suggested a least-squares fit of the data to

$$\tau(\Gamma) = A\left(1 - e^{-B(\Gamma - \Gamma_c)}\right), \tag{9}$$

which is shown in Figure 3.18b. By extrapolating this fit to small Γ, it was predicted that turbulent transients would not be observed for aspect ratios smaller than about 12.6. This hypothesis was tested by attempting to measure lifetimes at $\Gamma = 7.5$ and 10, where it was found that it was almost impossible to get persistent turbulence. This is evident in Figure 3.19, where the probability of events lasting longer than 100 or so non-dimensional time units (approx. 10 seconds) at $\Gamma = 7.5$ is very small.

3.5.3 Effects of End Conditions on τ

As noted by Schultz-Grunow [157] and more recently by Burin and Czarnocki [52], the end wall conditions in experimental Taylor-Couette apparatus play a significant role in the transition to turbulence. A preliminary test was conducted to check whether the end walls played a role in the decay of turbulent transients. A set of 150 long-lived events at several values of Re_o were analyzed to see if there was any region of the experimental domain where turbulent patches were more likely to decay. It was determined that when both end caps
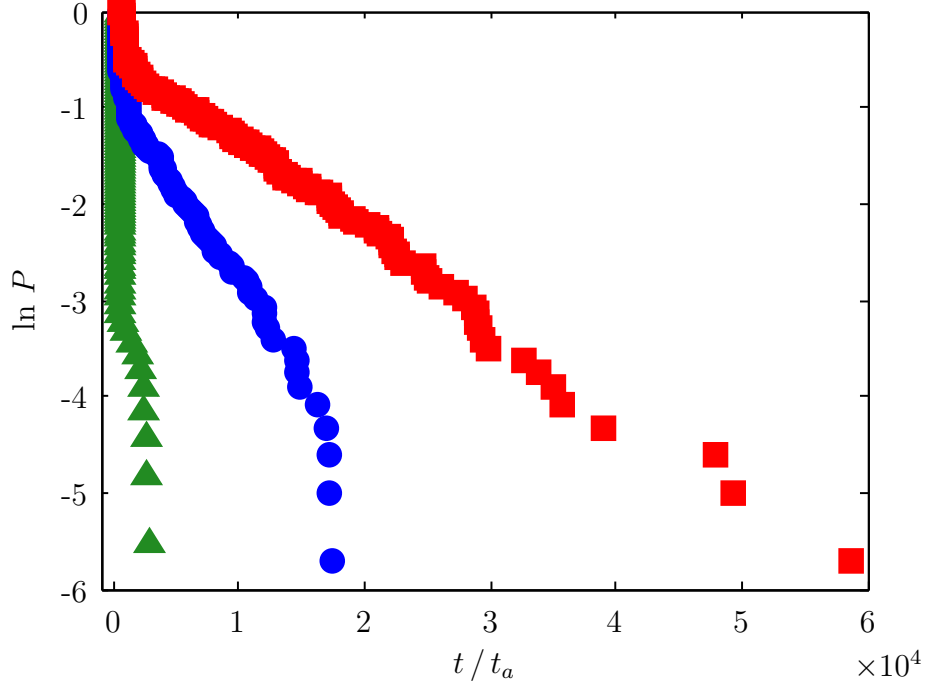
Figure 3.19: As the aspect ratio is reduced from 33.6 (■) to 15 (●) to 7.5 (▲), the fraction of events that lead to persistent turbulence drops dramatically.

rotated with the inner cylinder, all three regions were statistically equally likely with 37.3% of events disappearing in the top third of the domain, 29.6% of events disappearing in the middle of the domain, and 33.1% of events disappearing in the bottom third of the domain within a margin of error of about 7-8%. The slight difference in the probability of decay near the walls as opposed to the central region of the domain, though not statistically significant, could potentially be accounted for by the structure of secondary flows due to the finite size of the experimental apparatus. These are particularly strong in the boundary layers near the end caps (see Chapter 5) and may provide a source of energy for the turbulent patches.

A further test of the role of end walls conditions was conducted by leaving the top boundary free and performing a set of lifetime measurements at several different Reynolds numbers (runs 20-22 in Table 1). It was found that the fraction of events that relaminarized immediately almost doubled. The survival probabilities of long-lived events still had exponential tails, but the measured lifetimes were found to be significantly shorter than those measured with a solid end wall at the top, as shown in Figure 3.20. Furthermore, the dependence of τ on Re_o was not as strong as in the solid end wall case. As before, the final
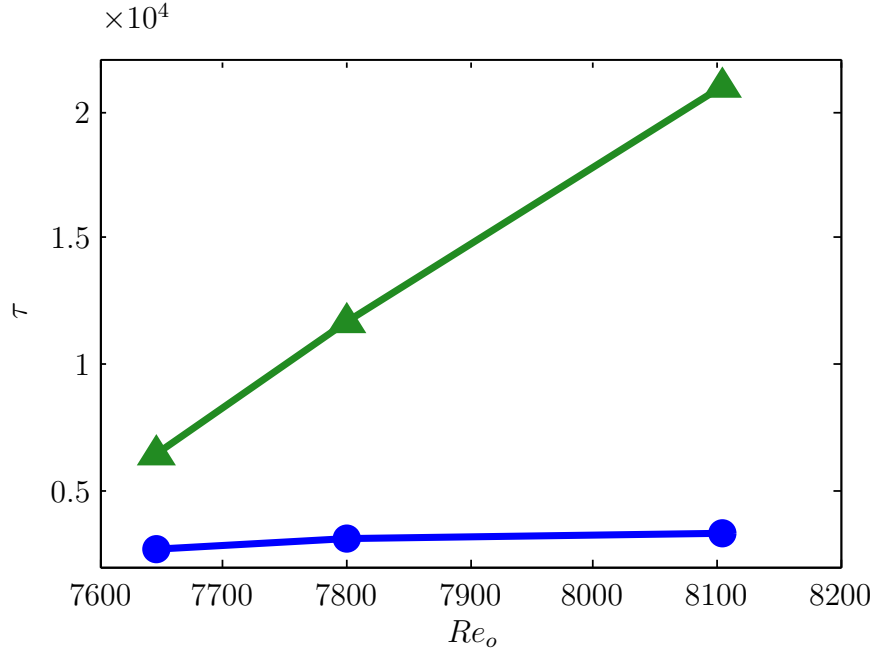
Figure 3.20: The lifetimes measured when the top surface was left free (●) are significantly shorter and do not depend as strongly on Re_o as the lifetimes measured when a top of the experimental domain was a solid wall rotating with the outer cylinder (▲).

location of the turbulent patch was recorded for a set of 260 experiments. The asymmetry of the experimental configuration was apparent in this data with 36.5% of cases disappearing near the top interface, 13.9% of cases disappearing in the middle third of the domain, and 49.6% of cases disappearing near the bottom boundary with a margin of error of about 6-7%. It is interesting to note the marked reduction in the fraction of events that disappear near the center of the domain. This might be explained by the fact that the secondary flow in this configuration takes the form of a single Ekman cell that fills the entire domain [158], so that there is an axial flow near the midplane that pushes the turbulent patches away from the middle section and toward the ends. Conversely, when both ends are solid walls, the secondary flow consists of a pair of Ekman cells, which meet at the midplane of the domain. This leads to zero axial velocity at the midplane (see Chapter 5), so that turbulent patches advected there are more likely to remain there.
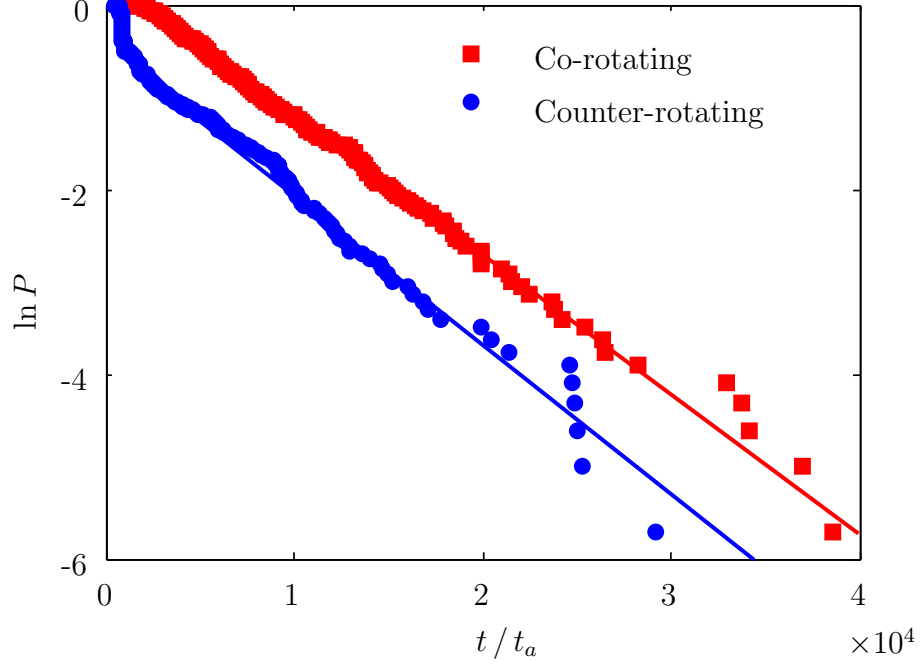
Figure 3.21: When the flow is perturbed by counter-rotating the inner cylinder ($\bullet$) a larger fraction of the events decay almost immediately than when the flow is perturbed by co-rotating it ($\blacksquare$) at $Re_o = 7647$. The amount of time that must pass before exponential decay is observed t_0 also changes. However, τ for both experiments is comparable with $\tau = 6190 \pm 107$ for the counter-rotating case and $\tau = 6520 \pm 33$ for the co-rotating one.

3.5.4 Effects of Different Perturbations on τ

As discussed in Section 3.4.2, a significant fraction ($\sim 30\%$) of experiments conducted using the standard perturbation relaminarized almost immediately after the perturbation. Because the standard perturbation disorganizes the fluid globally, one can think of it as moving the system away from the laminar attractor in a random direction in state space. If the perturbation puts the system in the basin of attraction of the turbulent state, the system will exhibit transient turbulent dynamics. If the perturbation leaves the system in the basin of attraction of the laminar state, turbulence decays immediately. This also means that different perturbations will show differing degrees of success exciting turbulent transients.

In order to test the dependence of the measured lifetimes to the details of the perturbation, five additional experimental runs were conducted at $Re_o = 7647$. The first of these consisted of co-rotating the inner cylinder instead of counter-rotating it. It was found that

this type of perturbation was more successful than the standard perturbation at inducing transition with almost all events leading to long-lived transients (see Figure 3.21). One possible explanation for the improved efficiency of co-rotating perturbations is that the wall speed of the inner cylinder for the standard perturbation profile is significantly greater than that of the outer cylinder. This means that during the perturbation, the flow mostly rotates in the same direction as the inner cylinder. After the perturbation, the flow must adjust to being driven by the outer cylinder only. In the case of the co-rotating perturbation, this transition consists of just slowing down to match the speed of the outer cylinder and the flow rotates in the same direction for the duration of the experiment. In the counter-rotating case, the flow must switch directions as it adjusts back to the outer cylinder rotation rate. In doing so, it passes through an intermediate state with very little net flow. This state is probably close to the laminar solution, which increases the likelihood of the flow relaminarizing. In addition to its improved efficiency, it was observed that the minimum time t_0 before exponential decay statistics were observed increased for co-rotating perturbations. The measured typical lifetime τ, however, was within 5% of the value for counter-rotating perturbations.

Another set of experiments were conducted to test how the different parameters of the standard perturbation affected the measured lifetimes. As shown in Figure 3.22, increases in the pulse duration of up to a factor of 10 did not significantly change the value of τ. This was also the case for a decrease in the inner cylinder acceleration by a factor of 60. The measured lifetimes were also insensitive to the maximum inner cylinder velocity as long as this was on the order of the speed of the outer cylinder. If the maximum speed was much lower, τ remained the same, but the fraction of events that relaminarized immediately increased dramatically.

A final set of experiments was conducted to test the sensitivity of the system to rapid quenching. This technique was used in lifetime measurements in pipe flow by Peixinho and Mullin [142] and in plane Couette flow by Bottin and Chaté [115]. The idea is that by initially perturbing the flow at a high Re, where the flow is fully turbulent, and then quickly quenching it down to a lower Re, the details of the initial perturbation can be ignored since
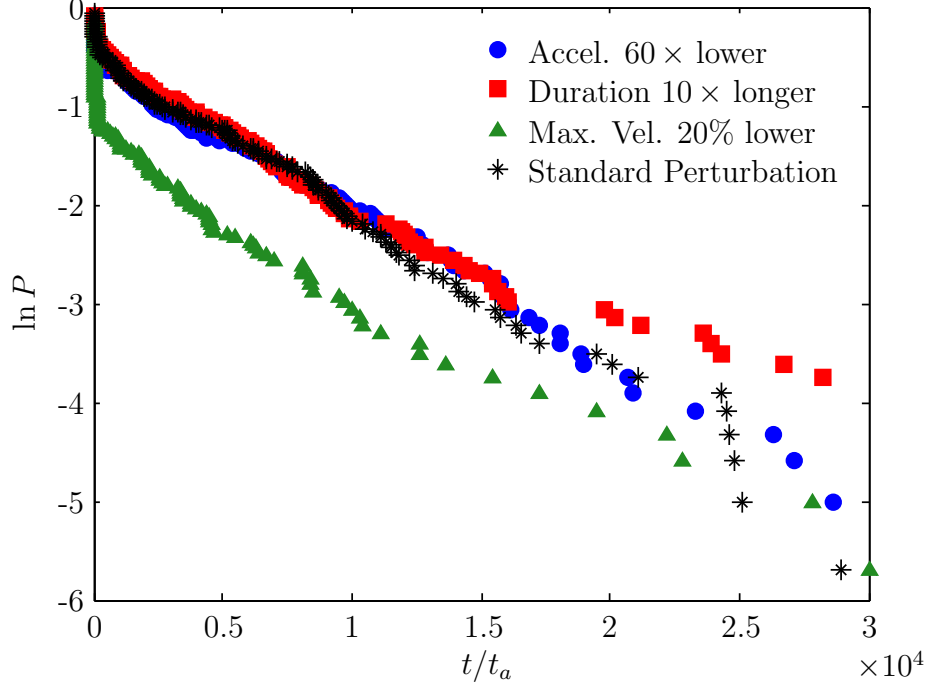
Figure 3.22: Varying the parameters of the standard perturbation profile does not significantly change τ, but can affect the efficiency of the perturbation.

the experiment effectively starts inside the turbulent attractor. A similar approach was taken here by perturbing the flow at $Re_o = 7647$, allowing it to run for a minute, and then quenching Re_o by 10%. It was observed that the system quickly adjusts to such changes in Re_o and the decay statistics "forget" that the system was originally at higher Re_o within a few seconds.

3.5.5 Effects of Co-/Counter-Rotation on τ

In all the cases discussed up to this point, the inner cylinder was allowed to come to rest at the end of the perturbation. As discussed in Chapter 2, inner cylinder rotation can significantly affect the dynamics of linear-stable Taylor-Couette flows. This brings up the obvious question: What effect does rotating the inner cylinder have on the lifetimes of turbulent transients? In order to address this question a series of experiments were conducted in which the inner cylinder continued to rotate slowly after the perturbation instead of coming to rest. As shown in Figure 3.24, it was found that τ increases if the cylinders counter-rotate and decreases if they co-rotate. This qualitative behavior could
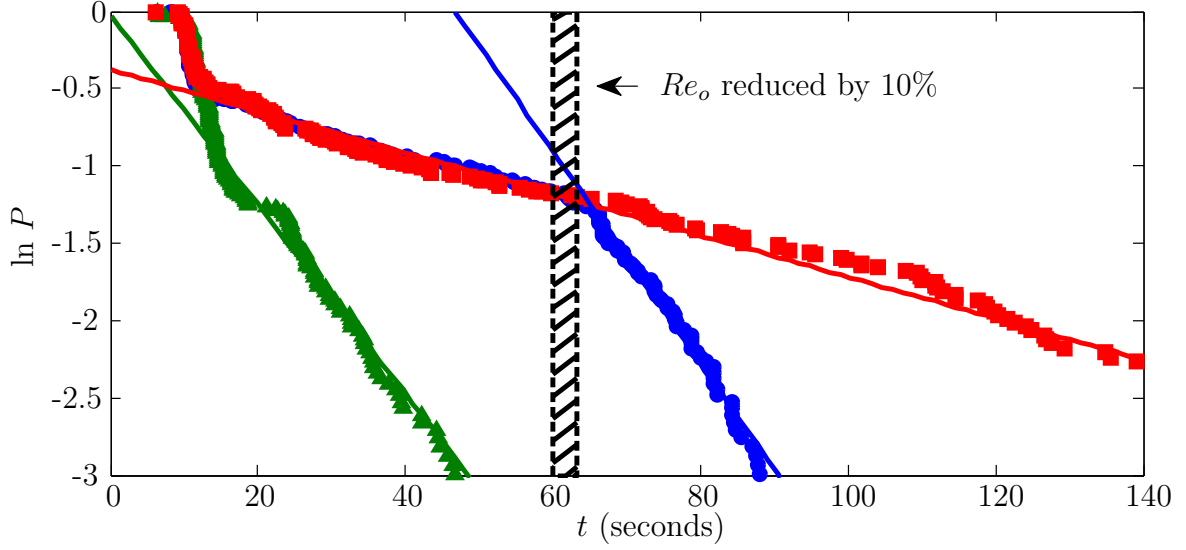
Figure 3.23: The system quickly adjusts to changes in Re_o. After a standard perturbation at $Re_o = 7647$, the system was allowed to run for 60 seconds, after which Re_o was reduced to 6882 (●) over 2 seconds. The decay statistics closely follow those of $Re_o = 7647$ (■) until the reduction in Re_o and then quickly changes to follow the statistics for $Re_o = 6882$ (▲).

have been guessed *a priori* since counter-rotation typically plays a destabilizing role, while co-rotation usually stabilizes the flow. An increase in τ for counter-rotating regimes could also be predicted by noting that the relative speed between the two cylinders is greater (for fixed Re_o), which increases the effective Reynolds number. A similar argument can be made for the observed decrease in τ for co-rotating cylinders. In order to compare the results of these experiments to the ones discussed earlier where the inner cylinder was fixed, it is convenient to define a shear Reynolds number as follows [12]:

$$Re_s = \frac{2}{1 + \eta} |\eta Re_o - Re_i|. \tag{10}$$

Figure 3.24 shows τ as a function of Re_s. It can be seen that inner cylinder rotation has a significant effect on the observed lifetimes with a 3% increase in Re_s leading to a sixteen-fold increase in τ. This effect is stronger than simply increasing the Reynolds number by rotating the outer cylinder more quickly. For the limited range of inner cylinder rotation rates studied here, the increase in τ seems to scale at least exponentially with inner cylinder rotation rate. The best fit exponential curve is given by $\tau(Re_s) = exp\,(aRe_s + b)$
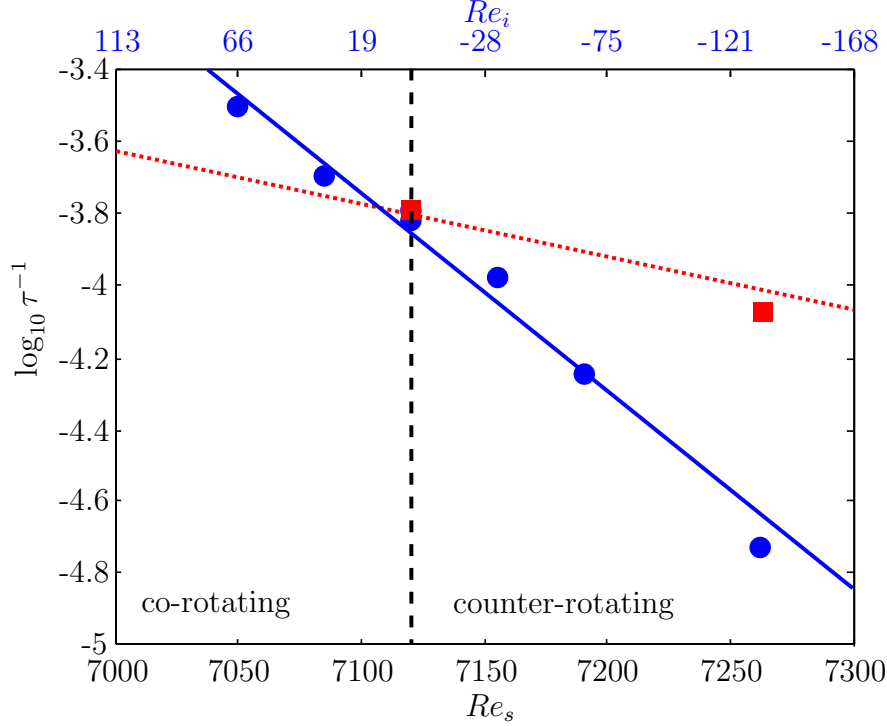
Figure 3.24: Inner cylinder rotation has a significant effect on the observed lifetimes. For a fixed Re_s, if the inner cylinder rotates after the perturbation ($\bullet$), the observed lifetimes defer significantly from those measured with the inner cylinder fixed ($\blacksquare$). Increasing/decreasing Re_s by rotating the inner cylinder has a stronger effect on lifetimes than increasing/decreasing it by changing the outer cylinder rotation rate. The increase is at least exponential (solid line) and potentially even super-exponential. The dotted line corresponds to the super-exponential trend calculated for $\tau(Re_s)$ using all the data for outer cylinder rotation only at $\Gamma = 33.6$.

with $a = 0.01319$ and $b = -85.06$.

3.6   Summary and Discussion

The experiments discussed here have shown that when only the outer cylinder rotates, transitional states in Taylor-Couette flow share many of the decay characteristics observed in other canonical shear flows. The exponential tails observed in the survival probability distributions suggest that the correct model for turbulence in the regime studied is a chaotic repeller [150–152]. It was also shown that characteristic decay times increase faster than exponentially with increasing Re_o but remain bounded for finite Re_o, in agreement with the most extensive data for pipe flow [146, 189]. The reader might wonder why this distinction matters. After all, extrapolating the observed trends out to Reynolds numbers of interest in

engineering applications would suggest that for all practical purposes turbulent transients would last unobservably for long times. The answer to this question lies in the fact that the existence of turbulent transients, even if these are very long-lived, implies a dynamical connection exists between the turbulent dynamics and laminar state. This opens up avenues for control using small perturbations that exploit this connection, as explained schematically in Figure 3.25, and developed in detail for low-dimensional dynamical systems by Shinbrot et al. [156]. The feasibility of relaminarizing transitional shear flows with small controls has been demonstrated in pipe flow by Hof et al. [190].

Having established the super-exponential but bounded growth of the lifetime of turbulent transients, the question arises as to what the scaling actually is. As discussed earlier the data collected here is insufficient to distinguish between different super-exponential scaling functions $\tau(Re_o)$. This, in fact, is the case for all experimental studies of turbulent transients conducted so far [146]. Addressing this question with simulations over a large range of Reynolds numbers is not feasible due to the large number of experimental runs and long simulation times needed to obtain good statistics. There is, however, a lone theoretical prediction by Goldenfeld et al. [191]. Goldenfeld and his collaborators showed that if it is assumed that a turbulent patch decays when the velocity fluctuations throughout the patch drop below a certain level (a reasonable assumption given the numerical evidence by various authors [140, 192, 193]), then the scaling for the typical lifetime patches as a function of Reynolds number can be derived from the theory of extreme statistics. The basic idea is that each region of the patch can be thought of as drawing a number from a random distribution once every temporal correlation time τ_0. This number can be thought of as corresponding to the size of the velocity fluctuations in that region. One region will draw the largest number x meaning that, by definition, all the other regions drew smaller numbers (i.e., had smaller velocity fluctuations). It turns out that the probability $F(x)$ that maximum x of M randomly selected numbers is less than some value X is governed by

$$F(X) = exp(-exp(-(X - \alpha)/\beta)), \qquad (11)$$

where α and β are parameters that depend on M. Goldenfeld et al. argue that since

"Large" control

Laminar flow

Basin boundary

Finite amplitude
perturbation

(a)

"Small" control

Dynamical connection
back to laminar flow

Finite amplitude
perturbation

Basin boundary

Laminar flow

(b)
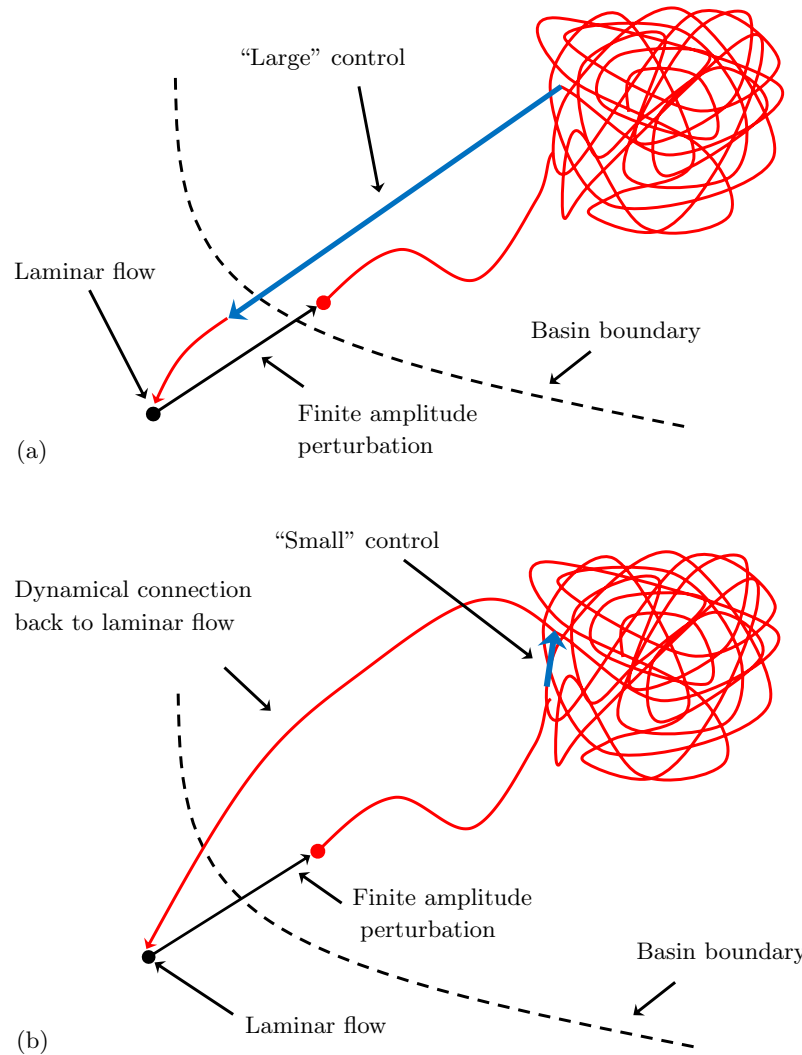
Figure 3.25: (a) If the turbulent state and the laminar solution are not dynamically connected, it is impossible to relaminarize the flow, except with a large, global control that puts the system in the neighborhood of the laminar flow. (b) However, if the dynamical connection exists, it is possible to apply a small, local perturbation to the flow that nudges the turbulent flow in the direction of the connecting branch and allowing the natural dynamics to relaminarize the flow.

the spatial correlations in a patch decrease as Re increases, this is equivalent to having effectively more regions, or larger M, so that it becomes harder and harder for x to be below the prescribed threshold for sustained turbulence X_c. This means that the system must draw more times before $x > X_c$ and the patch persists longer. The average number of draws until $x > X_c$ can then be shown to scale like $exp(exp(c_1 Re + c_2))$ for large M and so the average time till the patch decays follows a similar scaling law.

Another question that was addressed here was the dependence of the decay constants on the aspect ratio of the Taylor-Couette system. It was shown that there is a general trend for the decay constant in smaller aspect ratio systems to be smaller than those of larger aspect ratio systems. However, a general scaling was not obvious. At some Reynolds numbers, it was observed that τ grew quickly for increasing Γ at small aspect ratios but eventually approached an asymptotic value for $\Gamma > \sim 25$. Looking at the available data, it appears that the decay constants grow faster as a function of Re_o for larger systems. The aspect ratio dependence of turbulence lifetimes has also been studied by Alidai, who measured decay constants in a partially filled system with a free interface at the top surface [158]. His data, shown in Figure 3.26, show similar qualitative trends with increased lifetimes at larger Γ and the apparently faster increase in τ with Re_o for larger Γ.

The physical mechanism behind τ's dependence on aspect ratio is unclear. As pointed out by other researchers [13] and discussed in more detail in Chapter 5, the laminar state of finite-sized Taylor-Couette system is non-trivial [13]. The role played by end-effects (e.g., Ekman pumping) in relaminarization is still not well understood, although the experiments reported in Section 3.5.3 suggest that they might play an important role. Another possibility that was recently proposed by Manneville [192], who studied a simplified model of plane Couette flow, is that it might be possible for turbulence to become sustained globally even if it is transient locally. Manneville's argument extends earlier ideas by Pomeau [194], which suggest that the spatiotemporally complex state observed in subcritical transitions to turbulence can be thought of as a type of directed percolation problem [192]. The idea here is that the flow can be thought of as two phases, an "active" turbulent phase and an "absorbing" laminar phase. Over a certain time span, turbulent regions can contaminate
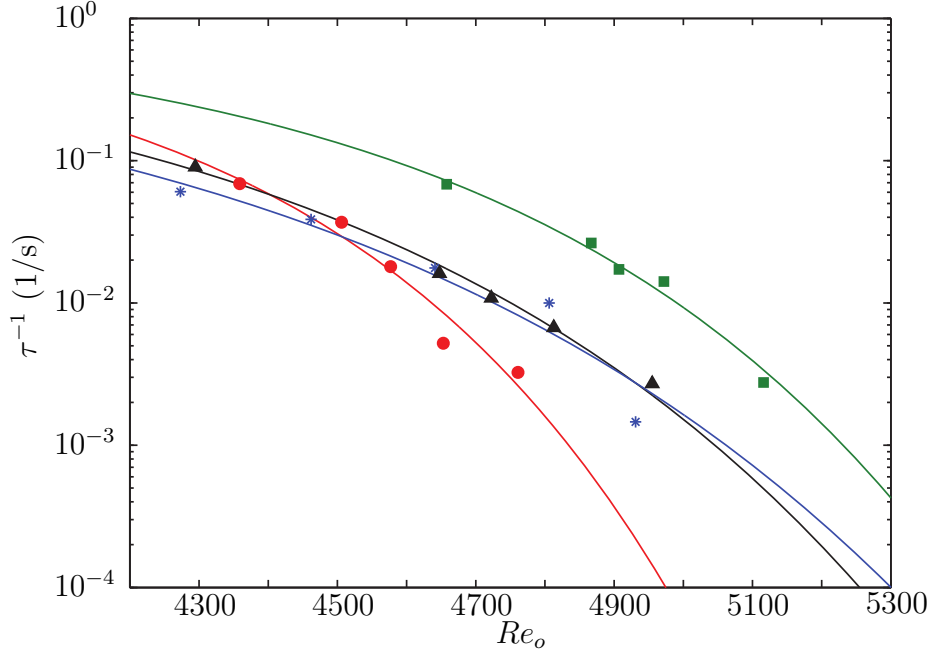
Figure 3.26: The lifetimes measured by Alidai for systems with a free surface at the top of the experimental domain at $\Gamma = 14$ (■), 18 (▲), and 20 (●) show qualitative agreement with his experiments with a solid end wall at $\Gamma = 22$ (∗). The solid lines are least-squares fits of the form $\tau(Re_o) = exp(-exp(c_1 Re_o + c_2))$. Adapted from A. Alidai, "Transient turbulence in Taylor-Couette flow," Masters thesis, Department of Mechanical Engineering, Delft University of Technology, Delft, The Netherlands, 2011.

nearby laminar regions or they can decay. In small systems, where there is a small number of regions, the probability that all turbulent regions relaminarize can be relatively large, so the observed lifetimes are small. In large systems, the probability that all turbulent regions decay at the same time is small, so turbulence persists longer (or indefinitely for large enough systems). The observed increases in lifetimes with increases in Γ are probably due to contributions from both finite-size effects, which depend on boundary conditions and affect the base flow, and from system size effects, which determine the dimensionality of the available state space independently of the specific boundary conditions.

The role of boundary conditions was studied by conducting experiments where the top surface of the experimental domain was left free. It was found that the exponential tails of the decay probabilities were maintained. However, the observed decay constants at fixed Re_o were found to be smaller and the scaling of τ with Re_o was found to be much weaker than in the case where the top boundary was a solid wall. It is interesting to compare these

findings with the results of Alidai, who conducted experiments with a free surface at several aspect ratios and Reynolds numbers (see Figure 3.26). Alidai's experiments confirm the finding that the exponential distribution of lifetimes is maintained when the top surface is free, which is consistent with numerical studies of turbulent transients in plane Couette flow in a doubly periodic computational domain without end walls [195]. Alidai also reported that triggering turbulent transients became more difficult, which led him to extend the duration of his perturbations. Unexpectedly, Alidai's data show significant increases in lifetimes with increasing Re_o. In some cases the dependence of τ on Re_o is stronger than in his experiments with a solid top wall. The source of the discrepancy between Alidai's experiments and those reported here is unknown.

Additional experiments were carried out to test the dependence of the measured decay constants on the type of perturbation used to initially trigger turbulence. It was found that while initial perturbations can affect decays that occur at short times and be more or less efficient at triggering turbulence, long-lived events that contribute to the exponential tails of the survival probabilities decay with the same exponential distribution regardless of the details of the initial perturbation. This observed independence of τ on the nature of the perturbation is consistent with experiments in pipe flow by de Lozar and Hof [196], who tested the effect of different perturbations on τ. They used a variety of perturbations including fluid injection, injection/suction of fluid, quenching fully turbulent flow, and the presence of a solid obstacle in the flow. They found that as long as the perturbation is large enough to cause the transition to turbulence in the first place, the decay statistics do not depend on the details of the perturbation. de Lozar and Hof also noted that t_0 depends on the nature of the initial perturbation, as observed here. Alidai, who used both fluid injections and counter-rotation of the inner cylinder in his experiments on turbulent transients in Taylor-Couette flow, found no significant dependence of τ on the type of perturbation used [158].

Finally, experiments were conducted to test the effect of weak inner cylinder notation on the decay constants for fixed Re_o. It was found that co-rotation stabilized the flow leading to the faster decay of turbulent transients. Conversely, counter-rotation destabilized the flow

and made the transient lifetimes longer. Analyzing the results in terms of a shear Reynolds number Re_s [12], showed that the transient lifetimes are more sensitive to inner cylinder rotation than to changes in Re_s due to changes in the outer cylinder rotation rate. While any extrapolation of these results to strongly co-/counter-rotating flows should be done with a healthy dose of skepticism, the strong stabilizing effect of co-rotation is consistent with the recent findings of Edlund and Ji [55], who showed that a class of linearly stable, co-rotating Taylor-Couette flows called Keplerian flows (see Section 2.8.4) are stable to a variety of large amplitude perturbations even at $Re \sim \mathcal{O}\left(10^6\right)$ and failed to detect persistent turbulence, even transiently.

3.7 Recommendations for Future Work

3.7.1 Effect of Boundary Conditions on the Lifetimes of Turbulent Transients

As discussed in Sections 3.5.2 and 3.5.3, the boundary conditions of the experimental domain can significantly affect the lifetimes of turbulent transients. So far, most of the experiments reported have been conducted in a rather limited range of geometries ($\eta \in [0.871, 0.917]$ and $\Gamma \in [15, 33.6]$). Even though the phenomenology in this domain is rich, Burin and Czarnocki [52] have shown that it can change drastically for Taylor-Couette flows of different geometries (see Section 2.8.6). Their experiments showed that for $0.55 < \eta < 0.73$ turbulence remains confined to a region near the inner cylinder. It is possible that turbulent transients in this regime might show some interesting behavior. It may also be interesting to study turbulent transients for aspect ratio greater than 40. In these geometries, spiral turbulence is observed for a range of Reynolds numbers, and it is possible that the interplay between the long-wavelength modulation of turbulent spots observed by Prigent et al. [66] and the decay processes for turbulent transients may lead to interesting dynamics. Both of these experiments could be carried out with cylinders currently available in the Pattern Formation and Control Lab.

Another natural extension of this work would be to try using different end conditions in the experimental domain. At this point the discrepancy, even at a qualitative level, between the behavior observed in the experiments where the top of the domain was a free

surface and similar experiments by Alidai [158] remains a mystery. This configuration might warrant further investigation. Alternatively, the end caps attached to the inner cylinder or split end rings could be used. As noted by Burin and Czarnocki, this significantly affects the Reynolds number for spontaneous transition, meaning that it is also likely to have a significant effect on transient lifetimes.

3.7.2 Effect of Rotation on the Lifetimes of Turbulent Transients

As discussed in Section 3.5.5, inner cylinder rotation greatly affects the lifetimes of turbulent transients. The experiments conducted here were originally conceived in terms of the traditional control parameters Re_i and Re_o. These are convenient experimental control parameters because they nondimensionalize the wall velocities. However, conducting experiments with varying Re_i at constant Re_o can make it difficult to isolate the physical processes that might lead to the observed variation in lifetimes. Dubrulle et al. [12] have proposed replacing the traditional control parameters with a dynamically motivated set of control parameters composed of the shear Reynolds number Re_s (Eq. 10) and a rotation number R_ω given by

$$R_\omega = (1 - \eta) \frac{Re_i + Re_o}{\eta Re_o - Re_i}. \tag{12}$$

These parameters are convenient from a theoretical perspective because they separate the influence of different physical effects, with Re_s capturing the influence of shear and R_ω measuring the influence of rotation. The work described here spans a wide range of Re_s but only a small range of R_ω between 0.141 and 0.153. It also only covers the cyclonic regime, where R_ω is positive. Recent experiments by Edlund and Ji [55] suggest that the stability of anti-cyclonic flows in the quasi-Keplerian regime (linearly stable flows with $R_\omega < -1$) may be very different than those of cyclonic flows. It is possible that experiments for a wider range of R_ω may lead to the discovery of new flow regimes with different lifetime scaling laws.

3.7.3 Boundary Crises and the Growth of the Turbulent Repeller

As shown in Figure 3.28b, the probability distribution calculated for $Re_o = 6423$ at $\Gamma = 33.6$ showed a large deviation from the exponential trend for long times. It is quite possible

that this is due to insufficient statistics (after throwing out transients that lasted less than t_0, only 149 events were used to calculate τ). However, recent numerical studies of chaotic repellers in plane Couette flow by Kreilos et al. [1] suggest an exciting alternative. Kreilos et al. showed that the size of the chaotic saddle governing turbulent transients grows via a series of very rapid bifurcations. First, a saddle-node bifurcation creates a pair of periodic orbits within the saddle. As Re is increased, this undergoes a cascade of bifurcations creating a chaotic attractor embedded within the chaotic saddle. As Re is increased even further, the attractor collides with its boundary and becomes "leaky" via a boundary crisis bifurcation, effectively combining with the original saddle in the process. The resulting saddle has a larger escape constant τ. This sequence of events is explained in more detail in Figure 3.27.

This whole bifurcation sequence occurs over a very narrow range of Reynolds numbers (~ 2) and is therefore unlikely to be observed directly in experiments. The upshot of Kreilos et al.'s work, however, is that the lifetimes of turbulent transient may vary non-smoothly for narrow ranges of Reynolds numbers. It may be possible that if an experimenter carried out lifetime measurements in the neighborhood of such a crisis event, slight variations in experimental conditions would lead her to sample some events from each side of the bifurcation. In order to test what measured probability distributions might look like, synthetic probability curves were generated by sampling 175 pseudo-random numbers at random from two exponential distributions. Figure 3.28a shows the results of one such numerical experiment. While it is naturally premature to suggest that the probability curve for $Re_o = 6423$ provides convincing evidence for the boundary crisis scenario proposed by Kreilos et al., the similarity between the two probability distributions is apparent. Repeating the experiments described in Section 3.3 to improve the available statistics would allow the determination of whether the transient lifetimes observed at $Re_o = 6423$ deviate from exponential (see, e.g., Figure 3.28c).

3.7.4 Spatiotemporal Intermittency and Sustained Turbulence

The observed scaling of transient lifetimes is in qualitative agreement with the most detailed studies of turbulent transients in pipe flow [146]. In that flow, a critical Reynolds number
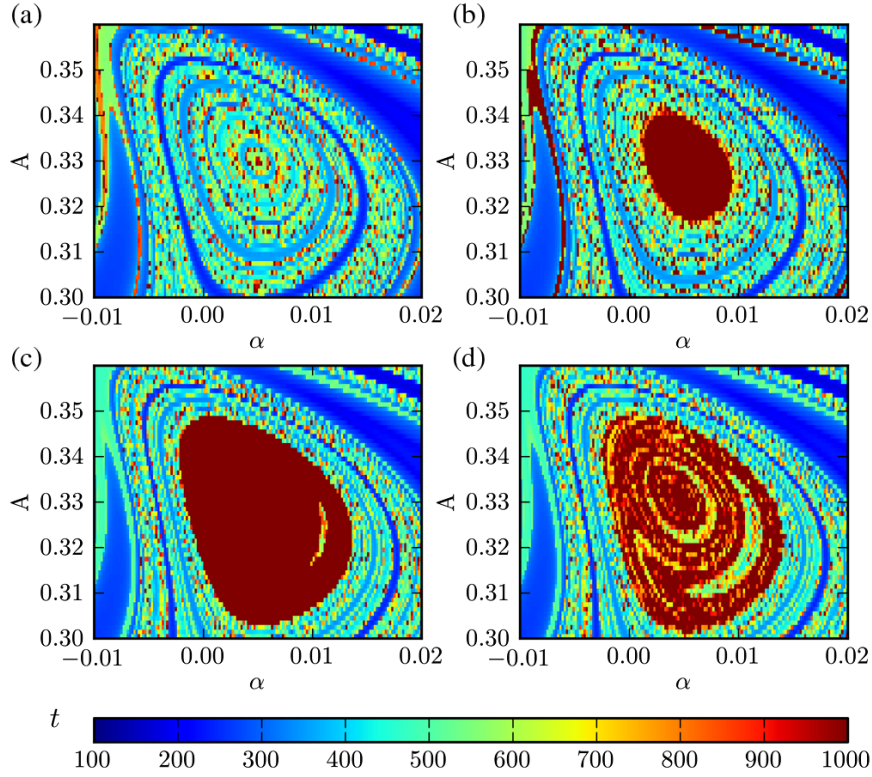
Figure 3.27: Two dimensional visualizations of the state space (see Ref. [1] for details), show that the chaotic saddle grows via the emergence and subsequent annihilation of a chaotic attractor in a boundary crisis. (a) At $Re = 248.5$, a pair of periodic orbits is formed in a saddle-node bifurcation inside the chaotic saddle. (b) As Re is increased, the stable orbit undergoes a bifurcation cascade, leading to a chaotic attractor at $Re = 249.1$, seen here as the red region of very long-lived events. (c) The attractor grows until, at $Re = 250.13$, it collides with its boundary basin and becomes "leaky" in a crisis bifurcation. (d) As the attractor breaks down, it comes to form a sort of saddle-within-a-saddle, shown here at $Re = 250.25$. In order to relaminarize, trajectories that start inside the inner region must first escape the inner saddle and then escape the outer saddle. Each of these processes has exponential decay statistics with different decay constants. The time constant for the inner region starts off much larger than the one for the outer region, but becomes progressively smaller with increasing Re, asymptotically approaching a value slightly larger than the decay constant of the outer region. As Re is increased further the dynamical connectivity between the two saddles increases via a series of heteroclinic bifurcations, merging the two regions into a single saddle with a longer time constant. Adapted from T. Kreilos et al. "Increasing Lifetimes and the Growing Saddles of Shear Flow Turbulence," *Phys. Rev. Lett.* **112**, 044503, 2014. Copyright 2014 by the American Physical Society.
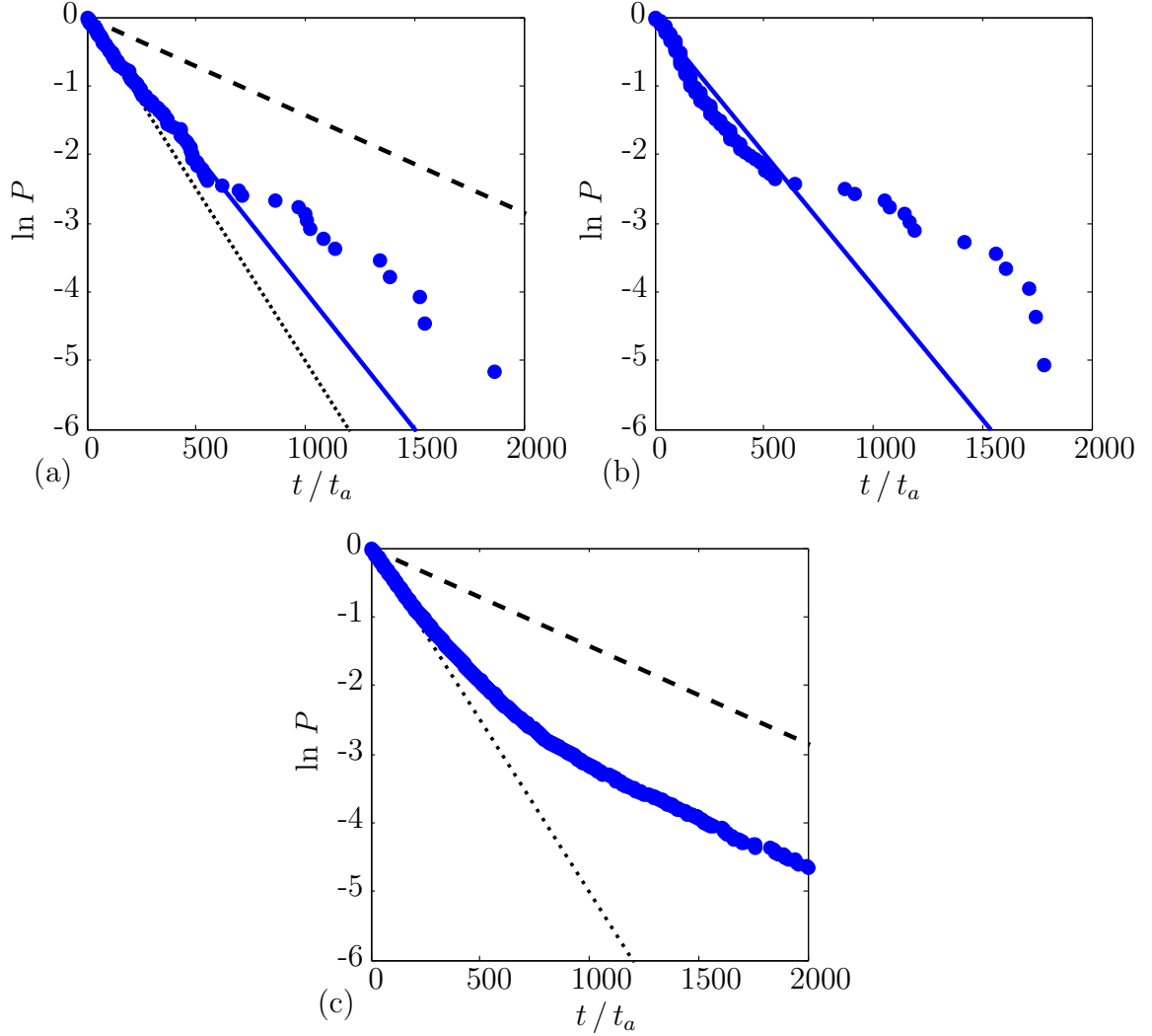
Figure 3.28: The deviation of the distribution of lifetimes at $Re_o = 6423$ for $\Gamma = 33.6$ is suggestive of the boundary crisis scenario proposed by Kreilos et al. (a) Distribution of 175 pseudo-random numbers taken at random from two exponential distributions with $\tau = 200$ (dotted line) and $\tau = 700$ (dashed line). The solid blue line is a weighted least squares linear fit. (b) Experimentally measured distribution of lifetimes for $Re_o = 6423$. (c) The distribution of 1500 pseudo-random numbers taken from the two exponential distributions shows significant deviations from a pure exponential that should be observable in sufficiently resolved experiments.
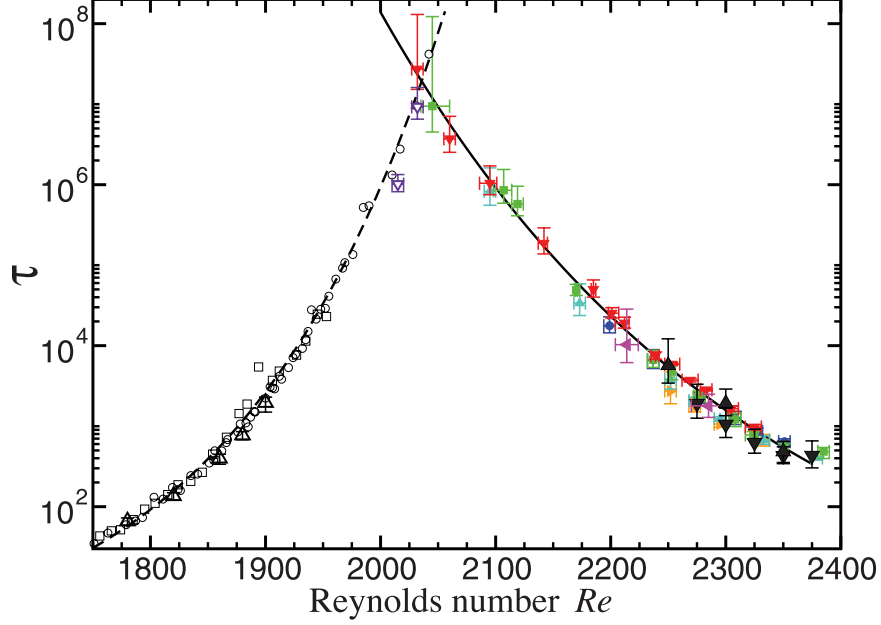
Figure 3.29: While the typical timescale before decay (open symbols) increases with Re, the typical time before a puff is likely to split (closed symbols) decreases. Turbulence becomes sustained when the typical time to decay exceeds the typical time to split.

has been reported above which turbulence is always observed unless the experiment is prepared with great care. Recent work by Avila et al. [189] has determined the mechanism by which turbulent transients lead to sustained turbulence. Avila and her collaborators discovered that localized turbulent regions called puffs can split before they decay. After a short maturation process, the resulting puffs follow the same statistics as the original puff (i.e., they have exponentially decaying survival probability and can split into more puffs themselves). They key to establishing the origin of the critical Reynolds number was found to be puff splitting. As Re is increased, the typical time before a puff splits decreases. Avila et al. concluded that when the typical time scale for a puff to split becomes shorter than the time scale for it to decay, turbulence can invade the entire domain even if individual puffs decay. Therefore, the transition to sustained turbulence in shear flows is not governed by an increase in temporal complexity as proposed by Ruelle and Takens [87], but rather falls within the framework of spatiotemporal intermittency envisioned by Pomeau [194]. During the experiments described here, the spatiotemporal evolution of turbulent patches in Taylor-Couette flow was observed to feature splitting events. This suggests that ultimately

the transition to persistent turbulence may be mediated by similar mechanisms as transition in pipe flow. However, in Taylor-Couette flow patches have the freedom to spread and split in both the streamwise and spanwise directions, which suggests that the transition will be more complicated [54]. Because of its periodicity, Taylor-Couette flow should allow for careful measurements of the increasing spatiotemporal complexity of turbulent patches with increasing Reynolds number.

CHAPTER IV

FINITE-AMPLITUDE THRESHOLDS FOR TRANSITION IN TAYLOR-COUETTE FLOW

One common feature of linearly stable flows is that, in order to trigger turbulence, the base flow must be perturbed by a finite-sized disturbance. The natural question arises of just how large the perturbation must be in order to initiate turbulence [9]. Experiments have shown that as the Reynolds number is increased, flows become more sensitive to perturbations, so that smaller perturbations are required to trigger turbulence [131, 197–205]. From the dynamical systems perspective, this reflects the fact that the basin of attraction of the laminar state becomes smaller with increasing Re. However, the rate at which the basin of attraction of the laminar state contracts with increasing Re is still a subject of debate [9].

The previous chapter discussed how large global perturbations to linearly stable Taylor-Couette flow can lead to transient turbulent episodes whose lifetimes increase rapidly with increasing Reynolds number. This chapter presents the results of the first experiments designed to investigate finite-amplitude thresholds for transition in linearly stable Taylor-Couette flow via small localized perturbations. Section 4.1 reviews the recent literature on finite-amplitude thresholds for transition in linearly stable shear flows. Section 4.2 discusses modifications that were made to the Hirst apparatus as a part of these experiments and gives details about the design and operation of the injection system that was used to generate disturbances to the flow. Section 4.3 outlines the experimental procedure. The results of the experiments are presented in Section 4.4 and discussed in Section 4.5. Section 4.6 provides suggestions for future extensions to this work.

4.1 Background

It is well-established that certain laminar shear flows are linearly stable for all Reynolds numbers. This class of flows includes pipe flow and plane Couette flow [4], as wells as certain regimes of Taylor-Couette flow [16]. Despite their stability to infinitesimal perturbations,

these flows are observed to become turbulent at sufficiently large Reynolds numbers. The critical Reynolds number for which turbulence occurs typically depends on the care with which the experiments are conducted [52, 204]. An illustrative example is the variety of critical Reynolds numbers reported for pipe flow. For example, in his pioneering studies of the transition to turbulence in pipe flow, Reynolds reported a critical Reynolds number of 2 260 when he used industrial pipe, but a higher value of 13 000 when he took additional care preparing the experiment and used precision bore tubing. Pfenniger showed that critical Reynolds numbers as high as 100 000 can be achieved with sufficient care [206]. A less famous, but analogous example can be found in the literature concerning linearly stable Taylor-Couette flows, as discussed in Section 2.6. By carefully controlling experimental conditions Schultz-Grunow was able to maintain laminar flows for outer cylinder Reynolds numbers that were over an order of magnitude than reported by other researchers [157]. Conversely, an analysis of the experiments of R.A. Bagnold [80] by Hunt et al. [81] suggests that Bagnold's apparatus underwent transition at much lower numbers than expected. This might be expected since the inner cylinder in Bagnold's apparatus had walls made of flexible rubber sheeting.

The fact that the transition Reynolds number of these linearly stable systems depends on the precision of the experimental setup suggests that finite-amplitude perturbations are required to trigger turbulence. It also suggests that as the Reynolds number increases, the size of the required perturbation becomes smaller. This observation presents the obvious question of how the size of the smallest perturbation that can trigger turbulence scales with Reynolds number. This question has received much attention over the last 20 years in a variety of shear flow configurations [131, 197–200, 202–205, 207–210]. The general consensus appears to be that in shear flows the critical perturbation amplitude scales asymptotically like Re^γ, where the critical exponent γ is negative. The exact value of γ has been the subject of recent debate and varies from flow to flow [199, 211]. Estimates from experiments and numerical data typically put γ in the interval between -1 and -2 [212], although theoretical considerations permit critical exponents as small as -4 [211]. The discussion is complicated by inherent difficulties in relating the types of perturbations accessible experimentally and

those that are easy to implement numerically and to study theoretically [213].

The value of γ can provide insight into the processes underlying the transition to turbulence [207, 214]. For example, if transition is only possible when the amplitude of the perturbation $\mathcal{A}$ is large enough so that nonlinear advection ($\mathcal{O}\left(\mathcal{A}^2\right)$) overcomes viscous dissipation ($\mathcal{O}\left(\mathcal{A}/Re\right)$), then a critical exponent of $\gamma = -1$ is expected [215]. Critical exponents smaller than -1 are predicted when non-normal amplification plays a role in the transition. Non-normal amplification, which is explained schematically in Figure 4.1, provides a mechanism by which finite-amplitude perturbations can be temporarily amplified via *linear* mechanisms until they become large enough to engage *nonlinear* mechanisms and cause transition [207]. Different critical exponents between -1 and -4 are predicted depending on the way the linear non-normal amplification mechanisms and the nonlinear terms exchange energy [207, 214]. The concept of non-normal amplification has become a central idea in the study of the subcritical transition to turbulence. For further discussion of the role played by non-normal amplification at the onset of turbulence in shear flows, the reader is referred to the review by Grossmann [212].

The non-normality of the Taylor-Couette operator was first demonstrated in 1993 by Gebhardt and Grossman [216]. However, the role of non-normal amplification for *general* Taylor-Couette flows would not be studied until 2002, when Alvaro Meseguer discovered that subcritical counter-rotating flows could exhibit significant transient growth.[1] Nonaxisymmetric modes showed the largest amplification, but axisymmetric streaks could also be amplified. Meseguer discovered a strong correlation between flow regimes where transient growth was significant and the flow regimes where Coles [14] observed spontaneous transitions to turbulence. Meseguer's work has recently been extended by Maretzke et al., who found significant transient growth in all linearly stable regimes of Taylor-Couette flow [219] with only slightly weaker amplification in the Rayleigh-stable regime than in Rayleigh-unstable ones. They also showed that the effectiveness of transient amplification (optimal transient growth) scales like $Re^{2/3}$, suggesting that these effects might be significant at

---

[1]Meseguer's paper cites a conference proceedings paper by Hristova et al. where they considered transient growth of axisymmetric perturbations in flow regimes approximating plane Couette flow [217]. This work was later published in Physics of Fluids [218].
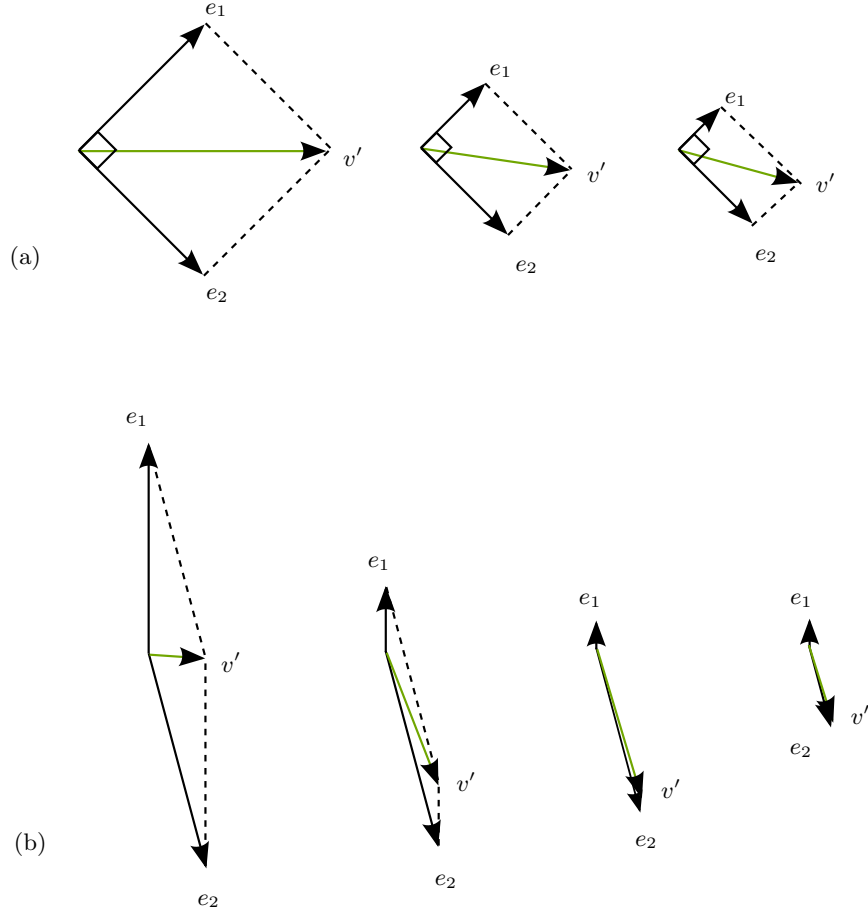
Figure 4.1: The non-normality of the linearized Taylor-Couette operator can lead to transient amplification of small perturbations. Suppose that a perturbation can be represented as a linear superposition of two eigenmodes e_1 and e_2, which are linearly stable with eigenvalues λ_1 and λ_2 such that $\lambda_1 > \lambda_2$. (a) If e_1 and e_2 are orthogonal, then a small perturbation v' will in general have small components in e_1 and e_2. As the modes decay in time, the magnitude of v' will also decay. (b) If e_1 and e_2 are not orthogonal, then the components of v' along e_1 and e_2 are not necessarily small, even though v' is small. If one modes decays faster than the other, the magnitude of v' can temporarily increase.

large Reynolds numbers. Unfortunately, none of the studies of non-normal amplification in Taylor-Couette flow up to now has yielded a prediction of the critical exponent for Taylor-Couette flow.

This chapter presents the first experimental attempt to measure finite-amplitude thresholds for the transition to turbulence in linearly stable Taylor-Couette flow and includes some preliminary estimates of the critical exponent. In the experiments reported here, the inner cylinder was held fixed while the outer cylinder rotated. Perturbations were generated by sucking and injecting fluid from ports on the inner cylinder wall. These types of perturbations have been used in similar investigations of transition thresholds in pipe flow [131, 200, 204], plane Couette flow [67, 115], and plane Poiseuille flow [205].

Fluid injections from the inner cylinder wall were first used by Malkiel et al. [99], who showed that, in certain co-rotating regimes, continuous suction/injection of fluid led to the periodic shedding of hairpin vortices, which grew in time and separated from the inner cylinder wall, before decaying further down stream. Malkiel and his collaborators analyzed their experimental findings in the context of the theoretical framework laid out earlier by Levinski and Cohen [98] and found good agreement. The theory of Levinski and Cohen provides a sufficient criterion for stability[2], i.e., it can predict when perturbations will not grow. However, it only provides a necessary condition for instability, meaning that it can only predict where perturbations might grow.

Fluid injections at the wall were also used by Alidai as part of his investigation of turbulent transients in Taylor-Couette flow [158]. Alidai showed that fluid injections were capable of triggering turbulent transients and that the lifetimes of these transients were similar to those initiated by global perturbations. Unfortunately, Alidai does not discuss the details nor amplitudes of the perturbations used. More recently, Edlund and Ji [55] have

---

[2]Formally, Levinski and Cohen's theory defines stability in terms of the growth of fluid impulse instead of the usual energy criterion. The fluid impulse is given by

$$p = \frac{1}{2} \int r \times \omega\left(r\right)\, dV,$$

where r is the position vector, ω is the disturbance vorticity, dV is the differential volume element, and the integral extends over the entire flow. It captures the geometrical growth of localized vortices. The growth of the fluid impulse does not necessarily imply growth in energy or vice versa.

used fluid injections to test the stability of quasi-Keplerian flows. This family of linearly stable co-rotating flows lie between the solid body rotation line and the Rayleigh line in the Re_o-Re_i plane and have received much attention recently as part of the debate on the stability of astrophysical disks [12]. Edlund and Ji found that quasi-Keplerian flows appear to be stable to large perturbations for Reynolds numbers as large as $10^5 - 10^6$, which is contrary to the earlier findings of Paoletti et al. [125].

4.2 Experimental Apparatus

In order to study finite-amplitude thresholds for transition, several modifications were made to the original Taylor-Couette apparatus described in Chapter 3. In the fall of 2011, the original outer cylinder ($r_o = 7.62$ cm) of the Hirst apparatus cracked. Several attempts were made to find a suitable replacement, but it was impossible to find a cylinder with the same dimensions and optical quality. A new precision bore glass cylinder of larger diameter was purchased from the Duran Group (Wertheim, Germany). This was measured at three locations along its length yielding a mean radius of 8.003 ± 0.002 cm. Matching end caps and end rings were fabricated from glass-filled Delrin. Mechanical drawings for these parts are provided in Appendix C.

In order to allow direct comparison with fully-resolved simulations currently underway in the group of Roman Grigoriev, the experiments discussed in this chapter were conducted at a small aspect ratio of 5.26. A spacer made of anodized aluminum was inserted into the gap to raise the test section for better optical access. The spacer was held in place against the outer cylinder with o-rings and rotated with it. Originally, the spacer filled the entire gap radially, but it was observed that any misalignment between the spacer and the inner cylinder caused pumping of fluid from the gap between them into the test section. This effect was minimized by modifying the spacer so that it had an L-shaped cross-section to allow the fluid between the spacer and the inner cylinder to flow more freely. This is shown schematically in Figure 4.2.

In order to minimize vibrations from the stepper motors, they were mounted on a separate optical table. The cylinders were driven by W.M. Berg Flex-E-Grip timing belts
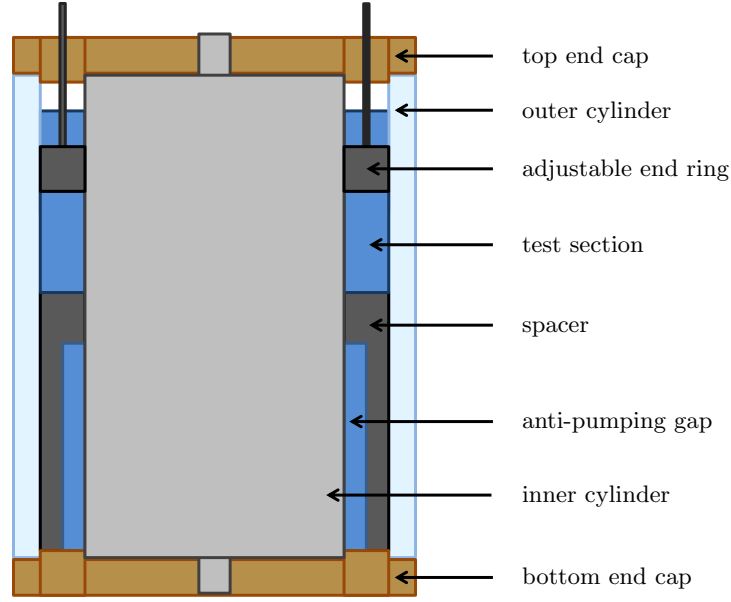
Figure 4.2: The spacer had an L-shaped cross-section to minimize pumping effects due to any misalignment between it and the inner cylinder.

(part no. 37TB-320). The outer cylinder was driven at a 1:1 gear ratio, so that the motor did not have to spin too fast to achieve the desired Reynolds number. The inner cylinder was driven at 12:26 gear ratio to improve on the resolution of the indexer. This allowed steps in Re_i of 1.7.

4.2.1 New Inner Cylinder with Jets

In order to have a source of controllable finite-amplitude disturbances a new inner cylinder was constructed. This cylinder was made of naval bronze and had an outer radius of 7.239 ± 0.001 cm. Like the inner cylinder used in the experiments of Chapter 3, it was powder-coated flat black at Miller's Powder Coating (Lilburn, Georgia). The cylinder was hollow and a line of 84 holes was drilled into the cylinder wall, which served as ports through which fluid could be injected or withdrawn to perturb the flow. The holes were spaced evenly by 4.19 mm and had diameters of 2.5 mm. They were tapped with #3-56 threads, which allowed them to be fitted with miniature barbed fittings for $1/16''$ inner diameter tubing (McMaster-Carr part no. 5454K74) or plugged from the inside with 316 stainless steel cap screws. The ends of the cylinder were removable to allow access to the interior of the cylinder so that tubing could be connected to the ports. The tubing was fed
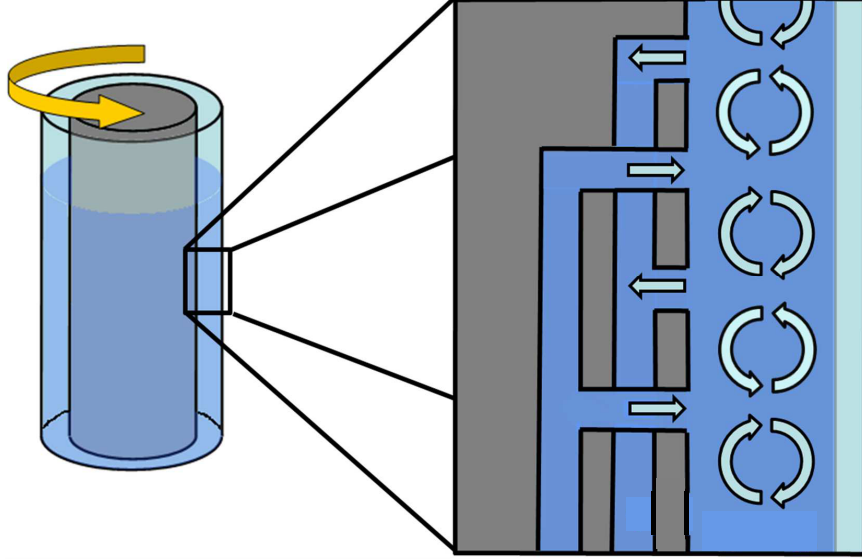
Figure 4.3: Ports were built into the wall of the inner cylinder, so that fluid could be injected/withdrawn in order to induce streamwise vorticity.

through the bottom shaft, which was hollowed out. It was connected to an injection system (described below) with 2-way micro tubing valves (Cole-Parmer part no. EW-06473-10), which allowed the ports to be closed off when the injection system was not in use. The ports that were used for the injection/withdrawal of fluid (hereafter called jets) were fitted with precision ruby orifices with a radius r_{jet} of 0.381 mm (part no. RB-82453, Bird Precision, Waltham, Massachusetts). These ensured that the flow from the jets was as uniform as possible. Unused ports were smoothed over with bees' wax. Mechanical drawings for the new inner cylinder are provided in Appendix D. When used with the glass cylinder from the Duran Group, the new cylinder gives a gap of 7.61 mm and a radius ratio of 0.905.

4.2.2 Injection System

The injection system was based on the design used by Peixinho and Mullin [204] in their investigations of finite-amplitude thresholds for transition in pipe flow. It consisted of a Harvard Apparatus No. 55-2222 syringe pump (Harvard Apparatus, Holliston, Massachusetts), which was modified as shown in Figure 4.4 to allow it to inject and withdraw fluid simultaneously. Because the syringe pump takes a relatively long time before coming up to speed, the flow was first diverted into a reservoir. Once the syringe pump had accelerated

to full speed, a high speed solenoid valve switched the flow into the lines feeding the jets as shown in Figure 4.5. A 3-way particle tolerant solenoid valve (Cole-Parmer, Vernon Hills, Illinois, part no. EW-98305-42) was chosen for its excellent chemical resistance (for use with the NH_4SCN-based refractive index matching solutions used during tomographic PIV measurements) and short response time (15 ms). The valves were controlled with a computer using TTL signals from Measurement Computing's USB-1208FS data acquisition module to switch a driver circuit (see Appendix B.4 for details).

4.2.3 Flow Visualization and Working Fluid

The working fluid was distilled water with 2% Kalliroscope AQ 1000 added for flow visualization. For more details on Kalliroscope visualization, the reader is referred to Section 3.2.2. The flow was illuminated with fluorescent lamps as shown in Figure 3.9. While the temperature of the fluid was not actively regulated, it was monitored by using a Thermo Scientific ERTCO ASTM 63C compliant full immersion mercury thermometer with $0.1°C$ resolution and found not to vary by more than $0.25°C$ with a mean temperature of $24.2°C$. The fluid was periodically stirred by spinning the inner cylinder at high speed to ensure a uniform distribution of Kalliroscope. The syringes in the injection system were cycled through the jets several times to ensure that any air in the supply lines was removed. Special care was taken to remove any air bubbles from the test section because these were observed to be quite efficient at triggering turbulence.

4.3 Experimental Procedure

The outer cylinder was first accelerated at a moderate rate to $Re_o = 5168$ with the inner cylinder held fixed. Preliminary experiments showed that the flow would never become turbulent below this Reynolds number (see Figure 4.6). The rotation rate of the outer cylinder was then slowly increased at a rate of 0.02 Hz/s^2. This slow acceleration was necessary to ensure that the flow did not become turbulent spontaneously. Once the desired Re_o was reached, the flow was allowed to equilibrate for 60 seconds (~ 1 viscous diffusion time across the gap). The flow was then perturbed by injecting and/or withdrawing a small amount of fluid through the jets on the inner cylinder wall. The volume of the
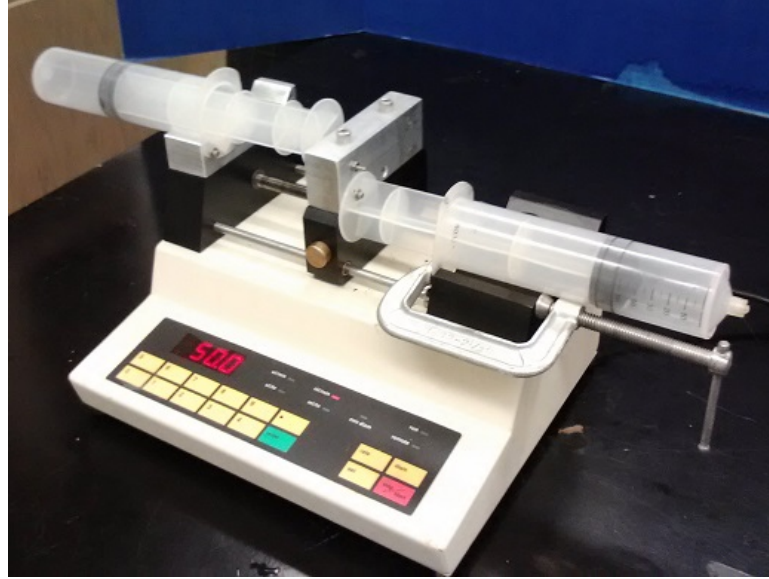
Figure 4.4: The Harvard Apparatus No. 55-2222 syringe pump was modified so that it could be used for simultaneous injection and suction. An aluminum syringe holder was added on the left end of the pump, allowing a second set of syringes to operate in the direction opposite to the manufacturer's design. An aluminum block was bolted to the pusher block allowing the plungers on the syringes, which normally just rest against the pusher block, to be bolted to it. The barrels of syringes on the right side of the pump were bolted to the aluminum blocks. The barrels of syringes on the left side of the pump were clamped to the syringe pump body. Together, these modifications allowed the syringe pump to draw fluid in addition to injecting it and operate in both directions.
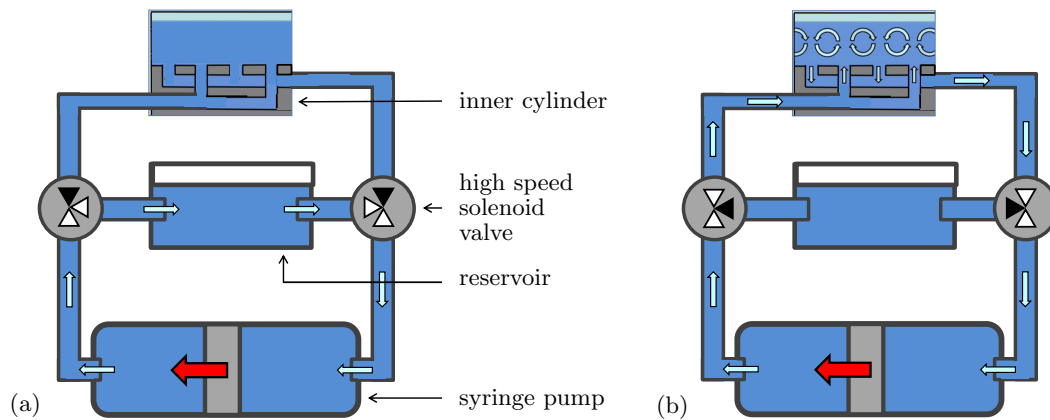
Figure 4.5: Schematic of the injection system. (a) When the syringe pump first starts, the solenoid valves divert the flow so that fluid is injected/withdrawn from a reservoir. (b) Once the pump is up to speed the valves are switched allowing fluid to flow to/from the inner cylinder. After the perturbation has been active for the desired amount of time, the valves are switched back, and the syringe pump is ramped down. The fast action of the solenoid valves allows for boxcar shaped perturbations, similar to those used by Peixinho and Mullin [204].
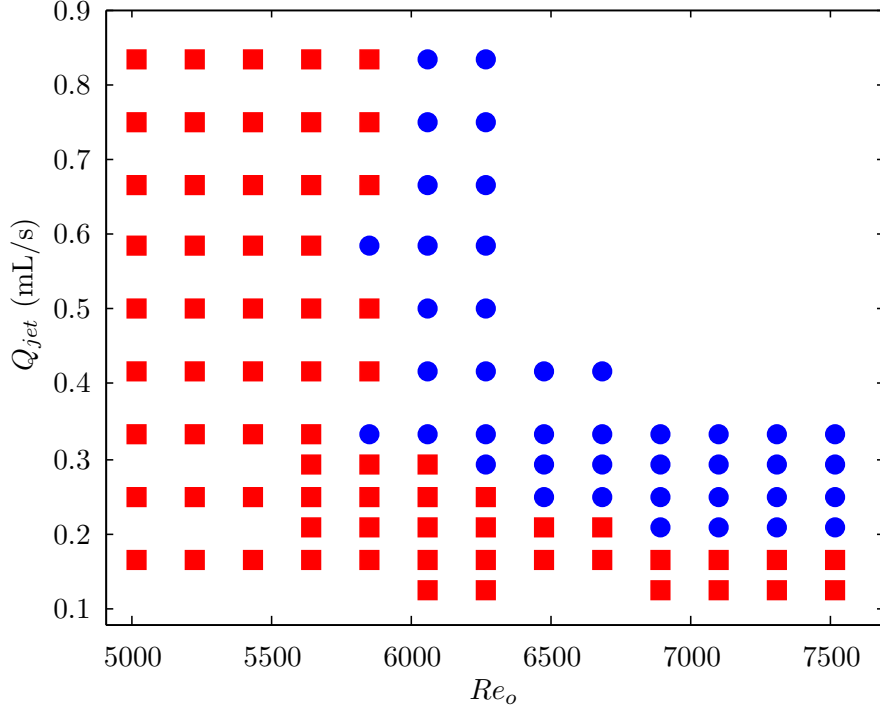
Figure 4.6: Preliminary experiments were conducted where the jets were run continuously for 30 seconds at a prescribed volumetric flow rate Q_{jet}. Conditions that led to turbulence are marked with blue circles($\bullet$). Conditions that remained laminar are marked with red squares ($\blacksquare$). Turbulence was never observed for $Re_o < 5168$.

fluid injected/withdrawn from the test section varied from experiment to experiment but never exceeded 0.2% of the test section volume. The volumetric flow rate through the jets never exceed 0.7% of the flow rate through a meridional cross-section (θ = constant) of the test section. Similar perturbations have been used in studies of transition thresholds in pipe flow [131, 200, 204], in studies of the subcritical transition to turbulence in plane Couette flow [115, 198], and in the study of turbulent transients in Taylor-Couette flow by Alidai [158].

The injection created a small localized perturbation, which was monitored by eye. Trials were categorized according to the evolution of the perturbation. Perturbations were typically observed either to decay completely within a couple of revolutions of the outer cylinder ($1 - 2$ seconds) or to grow and lead to turbulence that filled most of the gap. If turbulence was still present after 15 seconds ($\sim$ 30 revolutions of the outer cylinder), the perturbation was considered successful. A fraction of the successful trials were observed for 3 additional minutes. A few long-lived transient events similar to those discussed in Chapter 3 were

observed. These trials were categorized as successful since they put the system in the basin of attraction of the turbulent state, regardless of whether this is actually asymptotically stable.

4.4 Results

The experiment described above was repeated 20 times each for different combinations of Re_o and volume flow rate Q_{jet} through the jets. The injections lasted 250 ms. The jets were configured as shown schematically in Figure 4.3 so that the four jets alternated between injecting and suctioning fluid. This type of perturbation will henceforth be referred to as a push/pull perturbation to distinguish it from pure injection or pure suction. The results of these experiments are summarized in Figure 4.7. As expected, larger perturbations were found to be more successful at triggering turbulence. Furthermore, the size of the perturbation required to trigger turbulence was found to decrease with increasing Re_o. A clear threshold was observed with the probability of a perturbation being successful increasing rapidly for increasing perturbation flow rate at fixed Re_o.

In order to study the dependence of the critical perturbation amplitude quantitatively, a nondimensional perturbation amplitude in the spirit of the one used by Peixinho and Mullin [204] was adopted. The flux through the jets was made nondimensional by scaling it by the flux through a meridional plane of the Taylor-Couette apparatus Φ_{TC}, which was calculated under the assumption that the mean flow in the gap is purely azimuthal and flows with a mean velocity of one half of the outer cylinder speed U_o. The nondimensional perturbation amplitude $\mathcal{A}$ is then given by:

$$\mathcal{A} = \frac{\Phi_{jet}}{\Phi_{TC}} = \frac{Q_{jet}/2\,\pi r_{jet}^2}{\frac{1}{2}\,U_o\,\Gamma d^2/\Gamma d^2} = \frac{Q_{jet}}{\pi r_{jet}^2\,U_o}. \tag{13}$$

As shown in Figure 4.8, the success rate for perturbations as a function of nondimensional perturbation amplitude varies significantly with Re_o. As Re_o is increased, the sharpness of the transition becomes more pronounced as is evidenced by comparing the data for $Re_o = 6687$ and the data for $Re_o = 8369$. In the former case, the increase in the success rate is gradual, but in the latter case the transition is quite sharp and occurs at smaller

103

Q_{jet} (mL/s)	6687	7105	7523	7941	8359
0.75	1.00	0.95	1.00	0.95	1.00
0.71	0.95	1.00	1.00	0.95	1.00
0.67	0.90	0.95	1.00	1.00	1.00
0.63	0.75	0.85	0.90	0.95	1.00
0.58	0.60	0.75	0.90	0.90	1.00
0.54	0.45	0.45	0.60	0.75	0.95
0.50	0.20	0.30	0.30	0.55	0.80
0.46	0.10	0.15	0.20	0.35	0.45
0.42	0.00	0.10	0.10	0.15	0.10
0.38	0.00	0.05	0.05	0.05	0.10
0.33	0.00	0.00	0.00	0.05	0.05
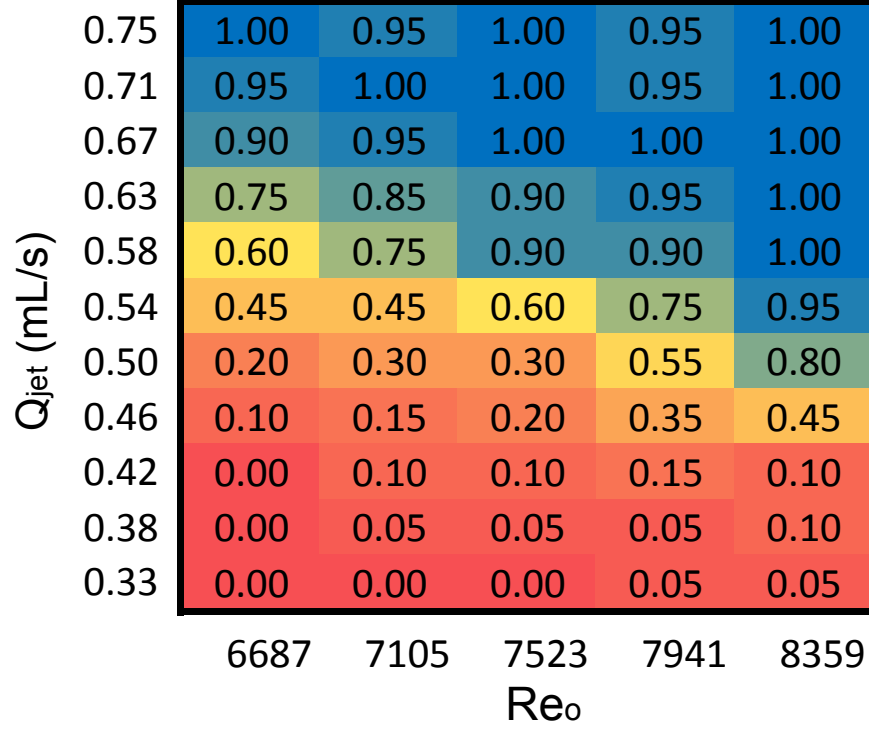
Figure 4.7: The probability that a 250 ms push/pull perturbation with flow rate Q_{jet} will trigger the transition to turbulence as a function of Re_o. Each cell summarizes the results of 20 experiments and is color coded by the fraction of events that led to persistent turbulence.

perturbation amplitudes. Despite their quantitative differences, all the curves share a characteristic S-shape, which suggested that they might be made to collapse onto a single curve by proper rescaling.

Experiments and theoretical predictions for other shear flows suggest that the critical amplitude should scale like Re^γ, where $\gamma \in [-21/4, -1]$ [131, 197–200, 202–205, 207–210]. The data was rescaled by Re_o^γ for the different values reported in the literature and it was determined that scaling the perturbation amplitude by Re_o^2 resulted in the best collapse of the data. In order to keep the scaling parameter of $\mathcal{O}(1)$, the Reynolds number itself was scaled by $Re_{min} = 5168$, which was the highest Reynolds number for which no long-lived turbulence was observed in preliminary experiments independent of perturbation strength. The rescaled data are shown in Figure 4.9.[3] The collapse of the data onto a single master curve by rescaling suggests that the critical perturbation amplitude scales like Re_o^{-2}. A more

---

[3]Since the scaling by Re_{min} multiplies all the data equally, the choice of Re_{min} does not affect any of the results presented here.
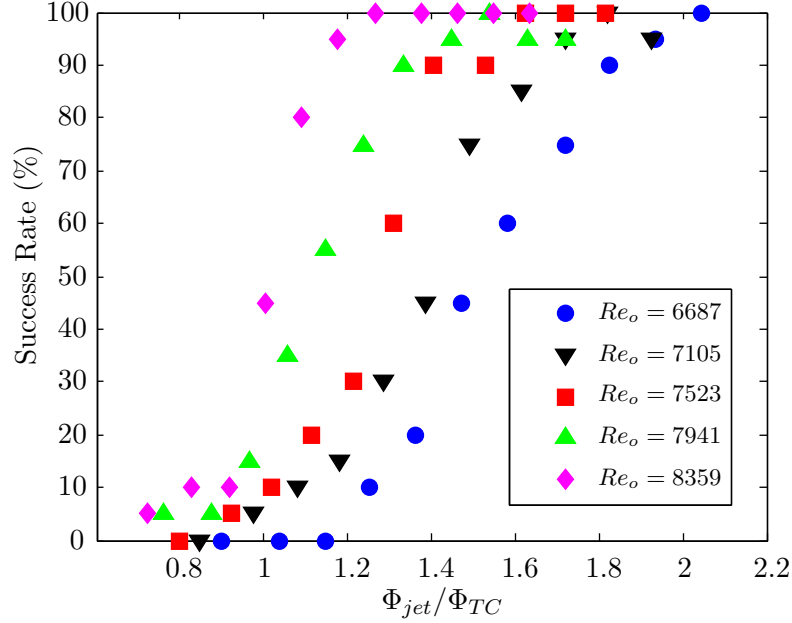
Figure 4.8: The success rate of push/pull perturbations depends strongly on Re_o.

quantitative estimate of the critical exponent was calculated as follows: First, the critical perturbation amplitude $\mathcal{A}_c$ was defined as the point when 85% of trials led to persistent turbulence. Next, the data was interpolated for each value of Re_o to estimate $\mathcal{A}_c$. Finally, these data were plotted on a log-log plot of $\mathcal{A}_c$ vs. Re_o and a linear fit was performed using least-squares regression. This analysis yielded a critical exponent of -2.0 ± 0.4, as given by the slope of the linear fit. The uncertainty in γ was estimated from the 95% confidence interval for the slope parameter of the linear fit.

Experiments in pipe flow have shown that the scaling of the critical perturbation amplitude can vary based on the kind of perturbation used [204]. In order to test if this is also the case in Taylor-Couette flow, a series of experiments were carried out using 250 ms perturbations that consisted only of fluid injections from two jets without suction from the remaining two. The results of these experiments were almost exactly the same as those using push/pull disturbances and yielded a critical exponent of -1.9 ± 0.6. An attempt was made to repeat the experiments using only suction as a perturbation. However, it was found that using suction exclusively never triggered turbulence, at least for the flow rates possible with the available syringe pump. Flow visualization confirmed that the suction from the jets did actually disturb the flow, but no transition was observed. Possible explanations for
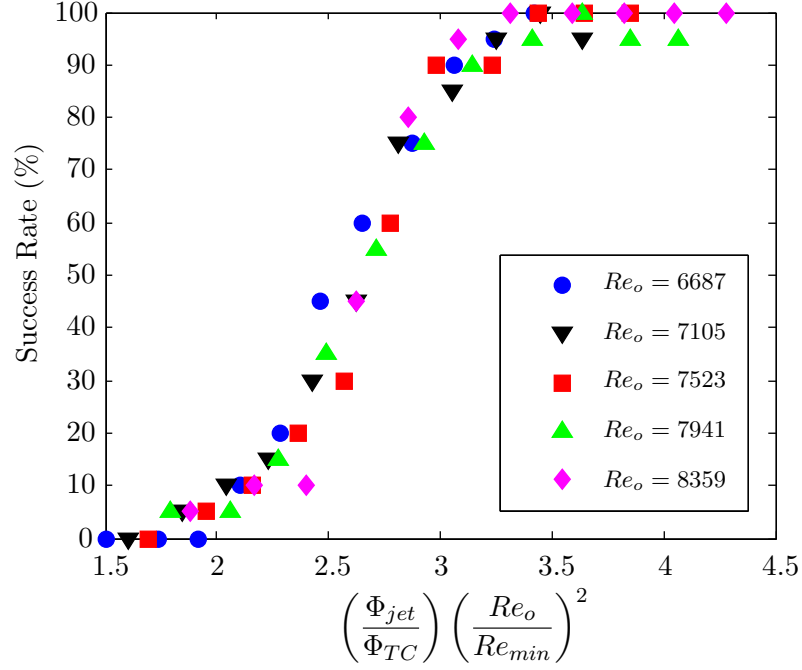
Figure 4.9: Scaling $\mathcal{A}$ by Re_o^2 collapses the data onto a single master curve. This suggests that the critical perturbation amplitude scales like Re_o^{-2}.
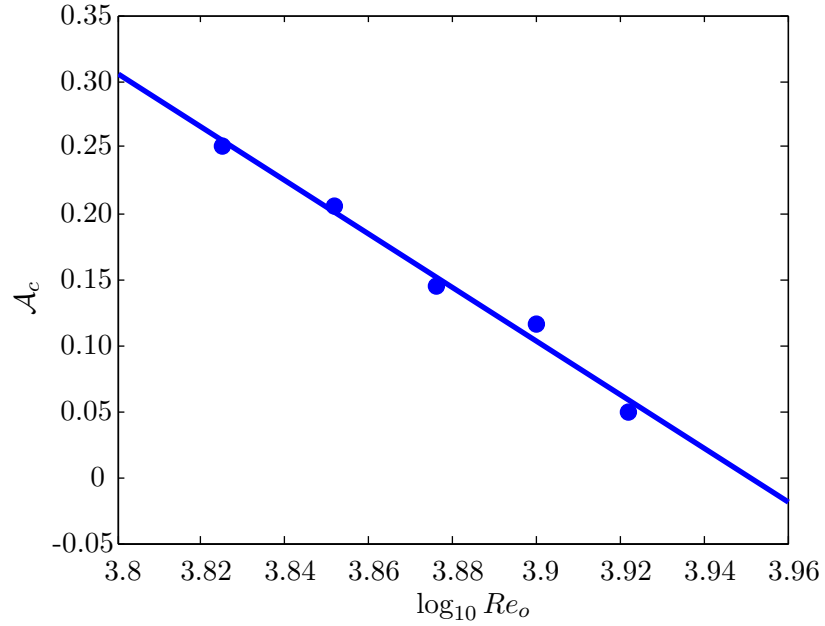
Figure 4.10: A linear fit on a log-log plot of $\mathcal{A}_c$ vs Re_o yields a critical exponent of -2.0 with a 95% confidence interval of ± 0.4.

this phenomenon are discussed in Section 4.5.

The experiments described here were carried out, in part, as preliminary flow visualization experiments for the tomographic PIV measurements that will be discussed in Chapter 6. One of the goals of those experiments was to study the growth of a turbulent spot from a localized perturbation. For this reason, it was convenient to use a perturbation that fit (at least initially) within the measurement volume of the tomographic PIV system, which spans an arc of about 36°. The spatial extent of the perturbation can be estimated by assuming that the perturbation is advected by the rotating outer wall. Under this assumption the spatial extent of a perturbation that last for a time δt is given by

$$L = U_o \, \delta t. \tag{14}$$

For the typical Reynolds numbers studied here, this means that a 250 ms perturbation will have an initial spatial extent of 200–250 mm. This is about 42%-53% of the circumference of the test section and significantly larger than the tomographic PIV measurement volume. For this reason, another set of experiments was conducted using perturbations that lasted only 50 ms. The shortened duration led to perturbations that had an initial spatial extent of about 40-50 mm and spanned an arc of $30° - 37°$.

The results of these experiments are summarized in Figure 4.11. Qualitatively, the data follow a similar trend to the data for 250 ms perturbations; only perturbations larger than a critical amplitude trigger turbulence, which becomes smaller with increasing Re_o. However, there are also some obvious differences. For one, the critical amplitude is shifted toward larger perturbations than those observed for 250 ms perturbations. As shown in Figure 4.13, the transition also appears to be less sharp except in the case of $Re_o = 8359$, where a particularly sharp transition is observed.

As might be expected from the discontinuity and lack of smoothness of the data seen in Figure 4.13, the data are not as easily collapsed onto a master curve by rescaling. The best results were obtained by rescaling the data by $Re_o^{5/2}$ and are shown in Figure 4.12. Obvious deviations from the master curve can be seen for the less continuous data sets ($Re_o = 6687$ and $Re_o = 8359$). A critical exponent of -3.1 was calculated using the same procedure as
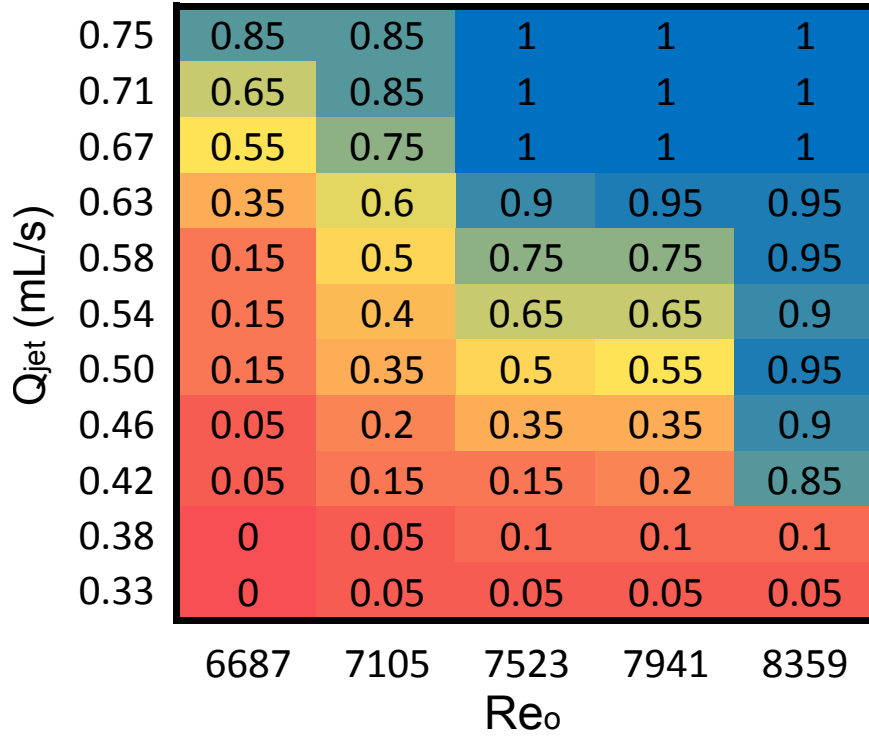
Figure 4.11: The probability that a 50 ms push/pull perturbation with flow rate Q_{jet} will trigger the transition to turbulence as a function of Re_o. Each cell summarizes the results of 20 experiments and is color coded by the fraction of events that led to persistent turbulence.
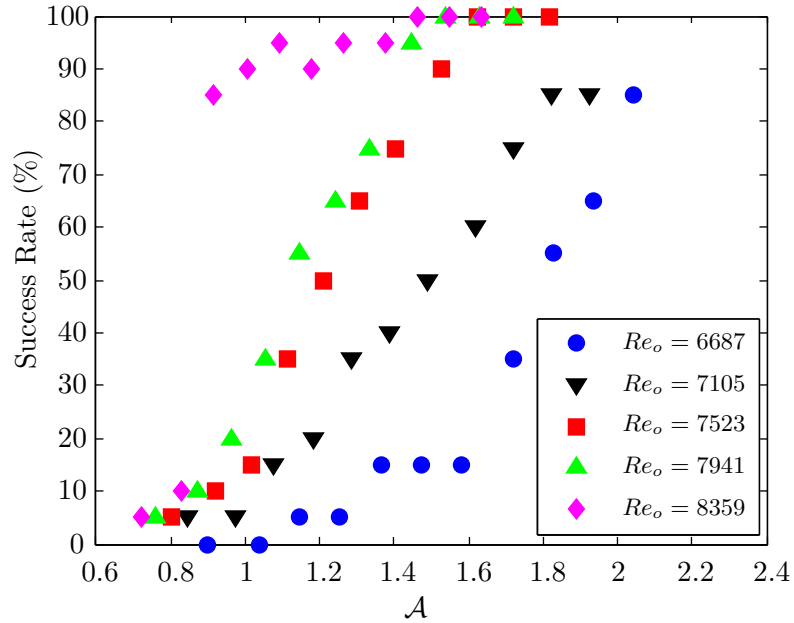
Figure 4.12: The transition between perturbations that successfully initiate turbulence and those that do not is not as sharp for 50 ms perturbations as for 250 ms perturbations. The critical amplitude is also observed to increase.
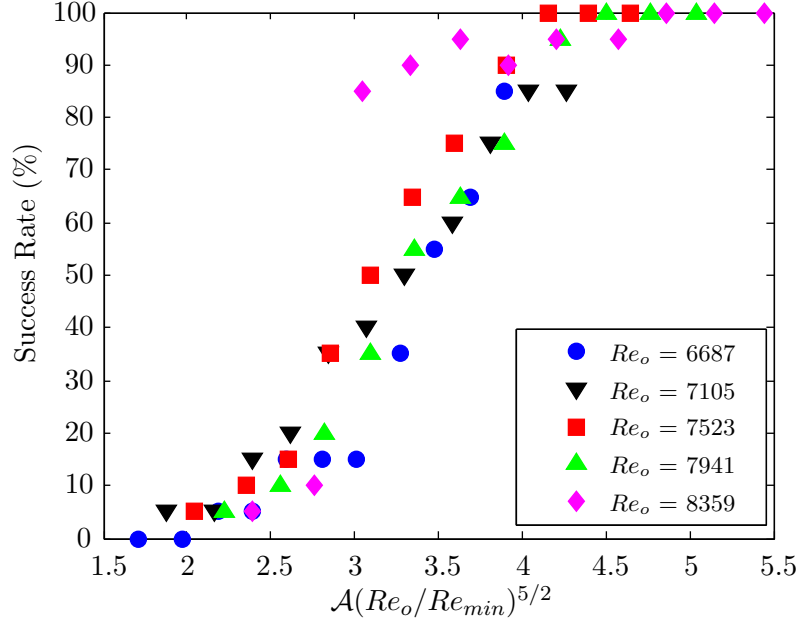
Figure 4.13: The data for perturbations with a 50 ms duration do not collapse as neatly upon rescaling as the data for perturbations lasting 250 ms.

was used for the 250 ms data set. This had a large margin of error of ± 1.5. If only the smoother data sets (Re_o= 7105, 7523, and 7941) were included, the critical exponent was estimated to be -2.6 ± 1.4.

4.5 Summary and Discussion

The experiments reported in the previous section demonstrated that like other linearly stable shear flows, Taylor-Couette flow with the inner cylinder held fixed can be destabilized by finite-amplitude perturbations. In order for transition to occur, the outer Reynolds number must be sufficiently high and the perturbation must exceed a critical amplitude, which becomes smaller with increasing Re_o. For a range of perturbation amplitudes, the process is probabilistic with some perturbations leading to turbulence while other qualitatively similar ones relaminarize immediately. This reflects the complicated structure of the boundary separating the turbulent and laminar regions in state space [9,220]. As in the case of spontaneous transition, if the perturbation is successful, the transition is catastrophic and the flow evolves immediately into a state with complex spatiotemporal dynamics at many different spatial and temporal scales. As in the experiments of Chapter 3, these states are characterized by the coexistence of turbulent and laminar domains.

Some preliminary experiments reported here showed that for the Taylor-Couette geometry used here there is a minimum Reynolds number of ~ 5168 below which sustained turbulence could not be observed. Similar observations have been made by various authors in other shear flows like plane Couette [67, 115, 198] and pipe flow [131, 141, 204, 208]. Over the last decade researchers have confirmed the existence of exact finite-amplitude solutions to the Navier-Stokes equations in these flows [24, 27–30, 221]. These unstable solutions are thought to guide the evolution of turbulent dynamics. However, experimental and numerical studies have shown that there exists a range of Reynolds numbers between where these solutions first emerge and where sustained turbulence is first observed. This observation brings the obvious question: "What happens in state space between the appearance of the first coherent structures and the experimental observation of turbulence?" [9]. The 2014 discovery of finite-amplitude solutions in subcritical regimes of Taylor-Couette flow by Deguchi et al. [129], adds another player to this discussion and the measurements provided here could provide guidance for numerical studies of this intermediate regime.

The next set of experiments showed that the critical perturbation amplitude scales algebraically with Re_o, i.e., $\mathcal{A}_c \sim Re_o{}^\gamma$. For push/pull perturbations lasting 250 ms, a critical exponent of -2 was found. A similar value of -1.9 was found for perturbations where only injection was used. It is interesting to contrast this finding with the pipe flow results of Peixinho and Mullin [204], who found that push/pull perturbations had threshold amplitudes about an order of magnitude smaller than simple injection and that the two kinds of perturbations led to different critical exponents. They hypothesized that it is suction that gives push/pull disturbances their additional effectiveness. The reason for this is that suction draws fast moving fluid from the center of the flow toward the wall and generates an inflection point in the velocity profile, which leads to instability according to Rayleigh's inflection point theorem [222]. Peixinho and Mullin did not directly test this hypothesis with suction only experiments. In this context, it is interesting to note that in the experiments described here, perturbations consisting only of suction were never observed to trigger turbulence, even at the highest flow rates possible with the current system. An obvious solution to this puzzling observation would be to assume a malfunction

of the suction system. However, flow visualization experiments showed clear evidence that the base flow was perturbed.

In order to understand the asymmetry between injection and suction, it is informative to calculate the typical velocity of the fluid as it exits/enters the jets. This is given by

$$\Phi_{jet} = \frac{1}{2} \frac{Q_{jet}}{\pi r_{jet}^2},\tag{15}$$

where the factor of two comes from the fact that the jets were connected in pairs. For the range of volumetric flow rates used here, Eq. 15 gives typical flow velocities between 37 and 82 cm/s. At these velocities, the jet would cross the gap in between 8 and 20 ms. Taken together with the fact that the gap between the cylinders is only about 10 times the jet diameter, it is obvious that the jet does not have the time nor room to become smoothly entrained into the mean flow, so it collides with the outer cylinder wall. When it does so, the jet itself becomes turbulent. On the other hand, when fluid is withdrawn from the test section through the jet nozzles, it goes into the small diameter tubing that leads back to the syringe pump and no additional turbulence is induced. Therefore, it becomes apparent that for the experimental configuration used here, the instability mechanism is mediated by the complex interaction of the jets with the outer cylinder wall and not by the type of smooth injections of streamwise vorticity that were conceived when the perturbation system was designed. The similar scaling laws observed for push/pull perturbations and pure injections can then be understood as emerging from the fact that only the injection part of the push/pull disturbance is significantly perturbing the flow. Naturally, it would be ideal to have a perturbation with simple structure like the one shown in Figure 4.3, but it was found that if the injection rate was low enough so that the jet was able to turn before colliding with the outer wall, the perturbation was too weak to cause transition for the entire range of Reynolds numbers studied. While it is possible to drive the system to higher Re_o, where the system may be more sensitive to these small perturbations, the flow becomes highly unstable beyond $Re_o \sim 9000$ and it becomes difficult to prepare the system so that it does not become turbulent spontaneously.

When the perturbation duration was reduced to 50 ms, it was observed that the system
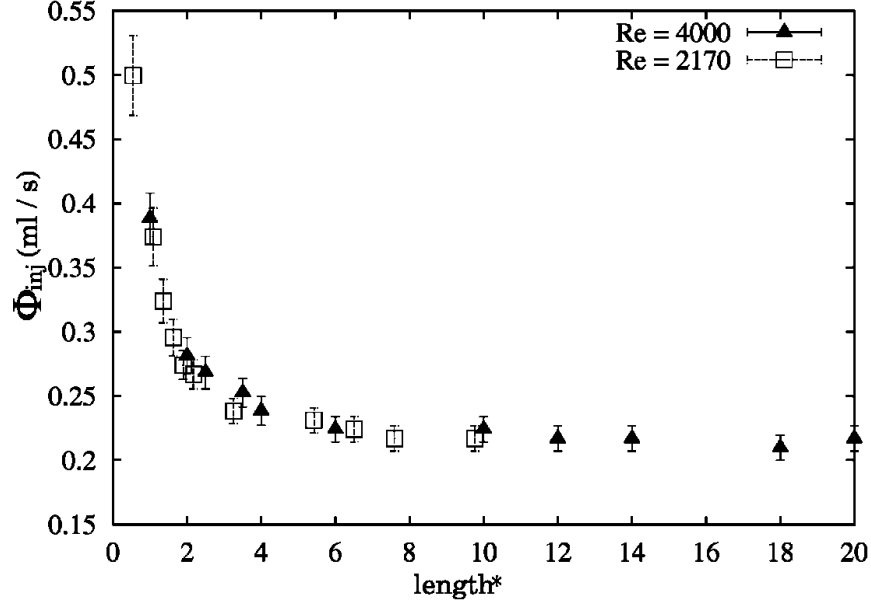
Figure 4.14: In pipe flow, the critical perturbation amplitude increases nonlinearly as the "length" of the perturbation drops below ~ 6 pipe diameters. The length of the perturbation is given by the mean flow speed times the duration of the perturbation. Adapted from B.Hof, A. Juel, and T. Mullin, "Scaling of the Turbulence Transition Threshold in a Pipe", *Phys. Rev. Lett.* **91**, 244502, 2003. Copyright 2003 by the American Physical Society.

generally required larger perturbations to undergo transition for a given Re_o. This observation is in qualitative agreement with the pipe flow experiments of Hof et al. [200, 204, 208], who showed that when the length of the perturbation (defined as the mean flow speed times the duration of the perturbation) is less than about 6 pipe diameters, the critical perturbation amplitude increased nonlinearly with decreasing perturbation length (see Figure 4.14). Using a similar definition of perturbation length using one half the outer cylinder wall speed as proxy for the mean flow speed, the perturbations used here ranged between 2.6 and 3.3 gap widths for the 50 ms perturbations and 13.2 and 16.5 gap widths for the 250 ms perturbations. Assuming that the results of Hof et al. map over to Taylor-Couette flow, the difference in the critical amplitudes observed for the two data sets should be expected. As shown by Peixinho and Mullin, however, the dependence of the critical amplitude on perturbation duration, jet diameter and orientation, and Reynolds number is not a simple one [204]. The relatively small data set gathered here is not large enough to draw a definitive quantitative relationship between pulse duration and critical amplitude. While it is

possible that the observed differences in critical transition amplitudes are indicative of the underlying physics, it is also possible that some of the observed scatter in the data is due to the fact that the response time of the solenoid valves is about 15 ms, which comparable to the duration of the 50 ms perturbations. This could be tested by using faster valves like the injectors from an automobile engine, which have switching times of ~ 1 ms.[4]

Critical exponents were calculated for the two data sets. It was found that for 250 ms perturbations, the critical exponent was approximately -2. For the experiments with 50 ms perturbations, the critical exponent was between -2.6 and -3.5, although this data set was significantly more noisy than in the 250 ms case. The observed power law dependence of critical amplitude on Reynolds number ($\mathcal{A} \sim Re^\gamma$) has been predicted for shear flows [207], although the exact value can depend on the flow configuration [199]. While numerous estimates exist for different flows [131, 197–200, 202–205, 207–210], the work presented here constitutes the first time that the critical exponent has been estimated for linearly stable Taylor-Couette flow. It is interesting to note, that the majority of the critical exponents reported for other shear flows lie in the interval $\gamma \in [-1.5, -1]$, which makes the critical exponents calculated here somewhat unique. That being said, the critical exponents reported here are within the bounds predicted by the theory of Kreiss et al., who established a lower bound of $\gamma > -21/4$ for plane Couette flow based on energy considerations. This bound has recently been improved upon by Henningson and Kreiss, who showed that γ must be greater than -4 [211]. Although most of the experimental and numerical evidence suggests that the critical exponents for shear flows lie between -1 and -1.5, critical exponents of exactly $\gamma = -2$ and $\gamma = -3$ have been predicted by some early low-dimensional models of parallel shear flows (see Ref. [214] for a detailed discussion), so the values reported here are not outside the realm of possibility.

The values of the critical exponents reported here should be taken with a grain of salt, given the limited data. One major source of uncertainty in these measurements is the limited number of trials performed. The statistical uncertainty in determining the proportion of

---

[4]The perturbation system used by Tom Mullin's group at Manchester uses the injectors for a late model Ford Escort (unknown model year). The key is that the injectors do not have the spray nozzles used in modern cars [223].
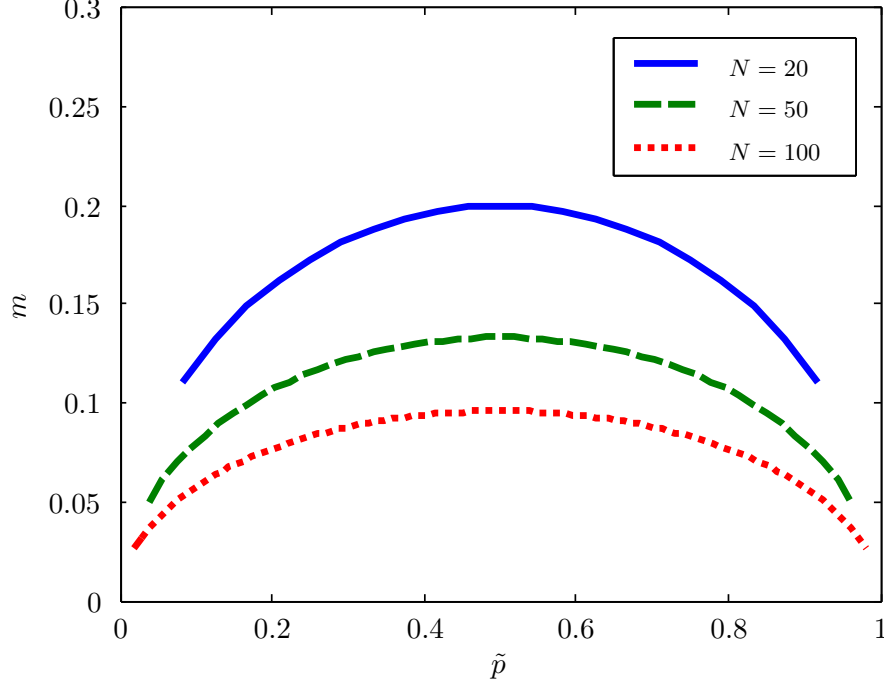
Figure 4.15: Margin of error m as a function of proportion estimate $\tilde{p}$ for different sample sizes. The Wilson estimate of binomial proportion $\tilde{p}$ is given by $\tilde{p} = (X + 2)/(N + 4)$ where X is the number of successes and N is the number of trials [188]. The margin of error at a 95% confidence level is given by $m = 1.96\sqrt{\tilde{p}(1 - \tilde{p})/(N + 4)}$. Wilson intervals provide better coverage probability than normal approximation confidence interval for small numbers of trials and for proportion estimates near 0 or 1.

disturbances that lead to turbulence with only 20 trials per combination of perturbation amplitude and Re_o can be quite large. Figure 4.15 shows the margin of error as a function of the estimated proportion as predicted using Wilson intervals [188] for different sample sizes. It is evident that even if 100 trials were performed for each combination of parameters, the uncertainty in the proportion estimates would still be of order 3-8%. For $N = 20$, the margin of error in the measured proportions is between 10% and 20%. The statistical uncertainty inherent in deriving threshold amplitudes from numerical and experimental data has been largely under appreciated in the literature and even the most detailed studies have only used sample sizes of ~ 40, which give uncertainties of $\mathcal{O}(10\%)$.

Regardless of whether the actual values of the critical exponents reported here are quantitatively accurate, the more important result is that $\gamma < -1$. A critical exponent of exactly $\gamma = -1$, as has been reported by some authors [199, 200, 205, 220], would be expected if transition occurred when the effects of the nonlinear advection term in the

evolution equations for the perturbation ($\mathcal{O}\left(\mathcal{A}^2\right)$) exceeded viscous dissipation ($\mathcal{O}\left(\mathcal{A}/Re\right)$) [215]. The balance of these two terms sets an upper bound on the value of γ. However, a critical exponent less than -1 is expected when the effects of non-normal amplification are important [207]. In this case, linear mechanisms allow small perturbations to temporarily grow before decaying away. This transient amplification allows perturbations to grow large enough to engage the nonlinearity and lead to turbulence. The critical exponents measured here, suggest that transient growth may play a part in the transition to turbulence in linearly stable Taylor-Couette flows, although how exactly this comes into play may be tricky to discern from the complex spatial structure of the perturbations used.

4.6 Recommendations for Future Work

The pipe flow literature suggests some natural extensions to the work presented here. One question that was not addressed here is how the specific details of the perturbation affect the observed scaling of the critical perturbation amplitude. Experiments in pipe flow have shown that the effectiveness of push/pull disturbances depends strongly on their orientation [204]. Jet pairs oriented at an angle to the mean flow trigger turbulence more effectively than jet pairs oriented parallel or perpendicular to it, a fact that is reflected in different critical exponents for the two types of perturbations. In order to unravel the complex dependence of transition threshold on perturbation geometry, experiments could be carried out using different jet diameters and different jet spacings. Both of these experiments could be carried out with the existing Taylor-Couette apparatus.

The additional complexity of the Taylor-Couette geometry also suggests some extensions to this work that have no analog in pipe flows. For example, the effectiveness of perturbations in triggering turbulence could be studied as a function of aspect ratio. During the experiments reported in Chapter 3, it was observed that it was harder to make smaller aspect ratio configurations transition to turbulence using large global perturbations. This suggests that finite-amplitude thresholds should show some dependence on aspect ratio. Alternatively, localized finite-amplitude perturbations could be applied at different locations in the flow to help understand the role of secondary flows and finite-size effects on

transition. For example, jets could be used to reinforce or suppress Ekman pumping near the end caps in order to accentuate or curb its effect on transition.

Testing the effect of controlled finite-amplitude disturbances on the transition scenarios observed in systems with different radius ratios may also lead to interesting results. For example, Burin and Czarnocki [52] have noted that in small gap systems with only the outer cylinder rotating turbulence fills the whole gap radially. On the other hand, turbulence is concentrated near the inner cylinder for systems with a large gap. It might be of interest to study the sensitivity of such flows to perturbations as a function of radial position. One possible way to do this would be to use poloxamer solutions as a working fluid. These solutions undergo a sharp gel transition as a function of temperature, which might be employed as a local perturbation that could be triggered optically by focusing a laser at a particular radial position.[5]

To date, no theoretical prediction for the critical exponent for the transition threshold in linearly stable Taylor-Couette flow has been made. Meseguer has shown that non-normal amplification should play a role in this regime [224], which suggests that the critical exponent should be less than -1. As mentioned earlier, Kreiss et al. have calculated a lower bound for the critical exponent in plane Couette flow of $-21/4$. In their paper they assert that their theory "may be extended to other geometries such as Hagen-Poiseuille and Taylor-Couette flow," with only minor modifications. While this is outside of the scope of this dissertation, such an extension might prove significant. Improvements to the theory of Kreiss et al. by Henningson and Kreiss [211] should be taken into account in any such theory. Numerical simulations on the growth of perturbations in Taylor-Couette flow are also missing from the literature and could provide useful scaling information with which to compare experiments. Such a numerical study should be designed keeping in mind the type of perturbations that are experimentally accessible. A discussion of this issue in the context of pipe flow is provided by Trefethen et al. [213] and by Mellibovsky and Meseguer [202].

As discussed earlier, Maretzke et al. [219] have recently expanded the earlier work of

---

[5]These solutions have significantly higher viscosity than water, so much higher rotation rates might be necessary to observe turbulence. They are also non-Newtonian, which presents further complications.

Meseguer [224] and performed analytical and numerical calculations of the optimal transient growth rate in different flow regimes. They found that the maximal transient growth rate is correlated with the experimentally observed subcritical transition boundaries. This led them to propose that the maximal non-normal amplification rate in a particular flow regime may be a useful measure of subcritical instability in Taylor-Couette flow. Maretzke et al. also proposed a semi-empirical model, which estimates that a threshold shear Reynolds number[6] Re_T below which turbulence cannot be sustained is approximated by

$$Re_T = a(\eta)^{-3/2} \left(880 \pm 370\right), \tag{16}$$

where

$$a\left(\eta\right) = a_o + a_1\eta \left(1 - \frac{1}{3}\eta^2\right) + a_2\eta^2 \left(1 - \frac{2}{3}\right) \tag{17}$$

with $a_0 = 9.218 \times 10^{-3}$, $a_1 = 0.1198$, and $a_2 - 9.072 \times 10^{-2}$. This predicts a threshold shear Reynolds number between 35985 and 88198 for the geometry used here, which is significantly higher than the observed value of 4910. However, the geometry used here has a small aspect ratio ($\Gamma = 5.26$), so it is possible that their theory, which assumes infinite cylinders, does not apply. Extending the preliminary work presented to a larger variety of geometries could be used to test the validity of their model.

One final point that was not discussed earlier is the relatively large scale of the perturbations needed to successfully trigger turbulence in linearly stable Taylor-Couette flow. These perturbations have fluxes of the same order as the streamwise flux in the base flow, i.e., $\mathcal{A} \sim \mathcal{O}\left(1\right)$, even though the fluid volumes involved are actually quite small. While it is difficult to compare the critical amplitudes even for different experimental implementations of the same flow [213], it is interesting to note that the critical perturbation amplitudes in pipe flow experiments are of $\mathcal{O}\left(10^{-2}\right) - \mathcal{O}\left(10^{-3}\right)$ [204]. It is currently unknown whether this large discrepancy is actually physical, but given that the perturbations were nondimensionalized in a similar fashion to Ref. [204], the difference is curious. A speculative argument may be made that this difference has something to do with the added stability that is afforded to Taylor-Couette flows by rotation. This is supported by the observation

---

[6]See Ref. [12] for a discussion of shear Reynolds numbers.

that, even at large amplitudes, pure suction perturbations failed to trigger turbulence. Only the strongly nonlinear interaction between the injected jets and the outer cylinder wall was observed to initiate the transition to turbulence. It is possible that experiments for different counter-rotating, but linearly stable, Taylor-Couette flows might provide a resolution to this question. In such an analysis, the effects of shear and rotation could be separated by considering the control parameters proposed by Dubrulle et al. [12], as discussed in Sections 3.5.5 and 3.7.2.

NUMERICAL SIMULATIONS OF THE LAMINAR VELOCITY FIELD FOR FINITE-SIZE TAYLOR-COUETTE FLOW

Researchers going back to Couette and Mallock have noted that the flow in experimental Taylor-Couette systems deviates from the ideal Couette profile (Eq. 2) due the influence of the end walls. Here, the no slip boundary condition drives the flow in such a way that pressure forces are not balanced by centrifugal effects [48], leading to the formation of a pair of large axisymmetric vortices known as Ekman cells [13]. These can result in significant distortion of the azimuthal velocity profile and the emergence of weak axial and radial flows [46]. As part of the effort to understand the phenomenology of the subcritical transition, the laminar flow was numerically computed in finite domains with the same geometry as the experimental apparatus to check how closely the experimental flow approximated the ideal laminar solution. The simulations also provided a reference against which tomographic PIV measurements could be calibrated and proved useful in locating of the measurement volume, as will be discussed in Section 6.4.1. The simulations were carried out using the commercial computational fluid dynamics package Fluent 14.5, which is available as part of the ANSYS Workbench engineering simulations platform (ANSYS Inc., Canonsburg, Pennsylvania).

The rest of this chapter is organized as follows: Section 5.1 formulates the problem as an axisymmetric swirling flow. Section 5.2 discusses the details of the computational domain and Section 5.3 outlines the numerical methods used. The results of the simulations are presented in Section 5.4 and their implications for experiments are discussed in Section 5.5.

5.1 *Problem Formulation*

The problem was formulated as an incompressible, steady, axisymmetric swirling flow in which the azimuthal or "swirl" velocity component is governed by the following momentum

equation:

$$\frac{\partial}{\partial t}\left(v_\theta\right) + \frac{1}{r}\frac{\partial}{\partial z}\left(rv_z v_\theta\right) + \frac{1}{r}\frac{\partial}{\partial r}\left(rv_r v_\theta\right) = \nu\frac{1}{r}\frac{\partial}{\partial z}\left[r\frac{\partial v_\theta}{\partial z}\right] + \nu\frac{1}{r^2}\frac{\partial}{\partial r}\left[r^3\frac{\partial}{\partial r}\left(\frac{v_\theta}{r}\right)\right] - \frac{v_r v_\theta}{r}. \quad (18)$$

This is solved concurrently with a two dimensional Navier-Stokes equation for the radial and axial velocities. The fluid properties were adjusted according to the parameters of the working fluid in the experiment that was to be simulated. No slip boundary conditions were used for the end caps and the cylinder walls.

5.2   Domain Geometry and Meshing

The computational domain was generated using ANSYS's DesignModeler. It consisted of a simple rectangle spanning the radial and axial dimensions of the experimental test section. The end walls rotated with the outer cylinder. Meshing was performed using ANSYS's Meshing software. Because of the simplicity of the geometry, a rectilinear grid was used. The grid spacing was biased in both the axial and radial directions to improve resolution near the walls where more complex flow features were expected. The grid resolution was increased until further increases in resolution did not improve the solutions. The solutions were also validated against three-dimensional calculations by Michael Krygier of Roman Grigoriev's group and good agreement was found.

5.3   Numerical Methods

The simulations were carried out using Fluent's "pressure-based" solver, which is a finite volumes implementation of the projection method. In order to accelerate convergence the momentum and pressure correction equations were solved as a coupled system. Gradients were evaluated using a least squares cell-based method. The pressure correction was solved on a staggered grid using PRESTO! discretization. The in-plane momentum and out-of plane "swirl" velocity equations were formulated using a second order upwind scheme. Pseudo-transient relaxation was used to speed up convergence. The simulation was initialized using Fluent's "hybrid" initialization, which uses a potential flow approximation to provide an initial guess for the solver. Convergence of the solution was monitored by checking the absolute residuals of the continuity equation and the axial, radial, and swirl
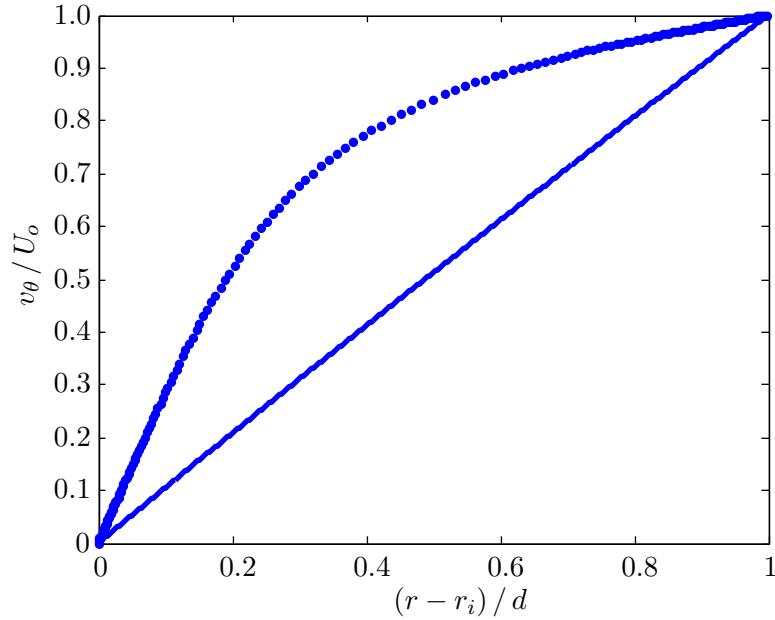
Figure 5.1: The azimuthal velocity profile (●) in the midplane (z=0) deviates significantly from ideal Couette profile (solid line). The velocities shown here are normalized by the outer cylinder wall speed U_o.

velocities until they all fell below 10^{-6}.[1] For more details on Fluent's implementation of the various numerical schemes used here, the reader is referred to the ANSYS Fluent Theory Guide [225].

5.4   Results

The axisymmetric laminar solution was simulated for an aspect ratio of 5.26 at an outer Reynolds number of 7750 with the inner cylinder held fixed. As might be expected from the work of Coles and Van Atta [46], the velocity profile significantly deviates from the ideal Couette profile (see Figure 5.1). The flow is faster than predicted throughout the gap and has a strong gradient near the inner cylinder wall. As shown in Figures 5.2 and 5.3a, the azimuthal velocity profile is fairly uniform except in a thin boundary layer near the end caps.

The distortion of the azimuthal velocity profile is driven by secondary axial and radial flows that are driven by the no-slip boundary condition at the end caps. This prevents

---

[1]The velocity equations converged much faster than the continuity equation. The absolute residuals of the velocities in the converged solutions were $\mathcal{O}\left(10^{-8}\right)$ for most simulations.
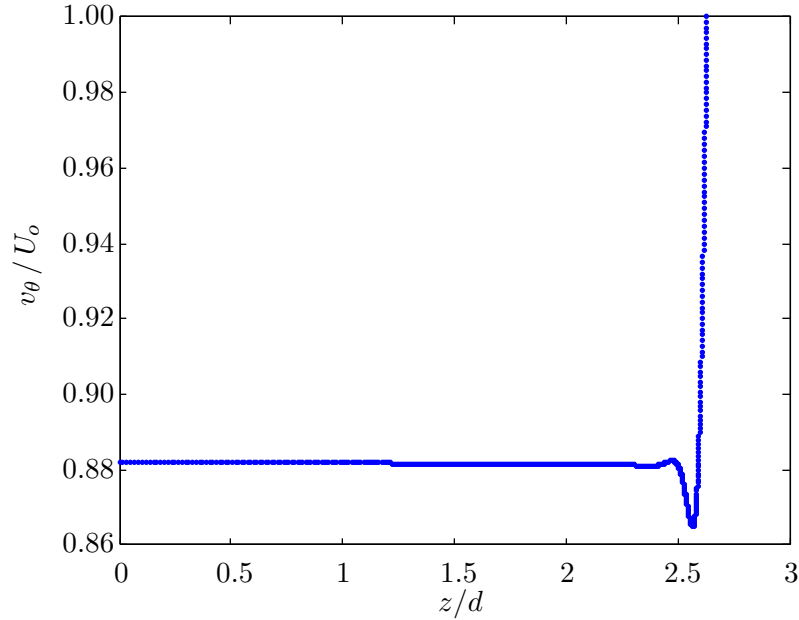
Figure 5.2: The azimuthal velocity profile at mid-gap $(r = \frac{1}{2}(r_i + r_o))$ does not vary significantly as a function of the axial coordinate z, except for thin boundary layers near the end caps, which have a thickness of approximately 2 mm. Only the top half of the test section is shown for clarity, but the flow is symmetric about $z = 0$.

the build up of a pressure gradient to balance the centrifugal force on fluid near the ends and causes it to flow radially outward, as shown in Figure 5.3b. The strongest radial flow, which can reach about 4% of the outer cylinder wall speed, is concentrated near the end caps. The much weaker return flow is distributed almost uniformly throughout the rest of the test section and drives fast moving fluid from near the outer cylinder inward leading to the observed distortion of the azimuthal velocity profile. The radial flow is accompanied by a slightly weaker axial flow, which is concentrated near the inner cylinder wall (see Figure 5.3c). Together they form a pair of counter-rotating vortices called Ekman cells, which are visible in Figure 5.3d.

5.5   Discussion

The results discussed above have important implications for experiments testing the stability of linearly stable Taylor-Couette flow. For one, they show that this experimental configuration does not generate a faithful approximation of the ideal flow between infinitely long cylinders. This is to be expected given the small aspect ratio of the system, which was chosen so that fully three-dimensional direct numerical simulations with the same geometry
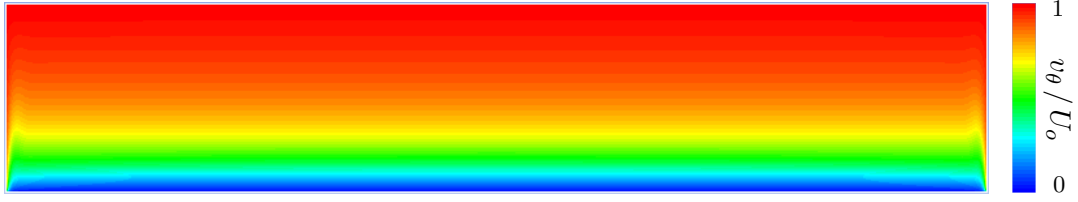
(a)

(b)
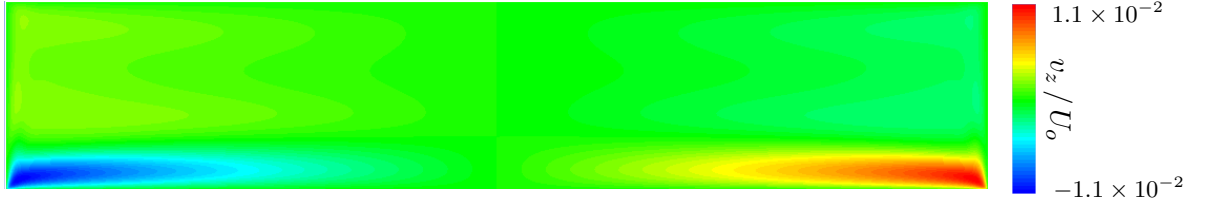
(c)
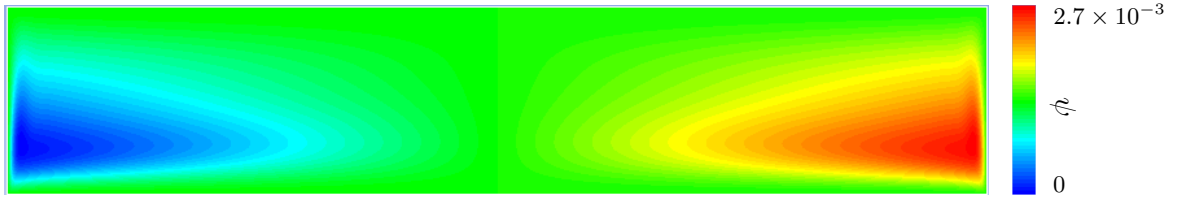
(d)

Figure 5.3: Iso-contours of (a) azimuthal velocity v_θ, (b) radial velocity v_r, (c) axial velocity v_z, and (d) stream function ψ in the r-z plane. The computational domain has been rotated by 90°, so that the inner cylinder is at the bottom of the figures. (a) The azimuthal velocity profile is mostly uniform throughout the gap with the exception of a small region near the end caps. (b) The end caps force an outward flow, which is concentrated in a thin boundary layer. The return flow is spread throughout the rest of the gap and is much weaker. (c) The induced axial flow is concentrated near the inner cylinder and is weaker than the radial flow . (d) Together, the axial and radial flows form a pair of weak, counter-rotating cells that fill most of the gap.
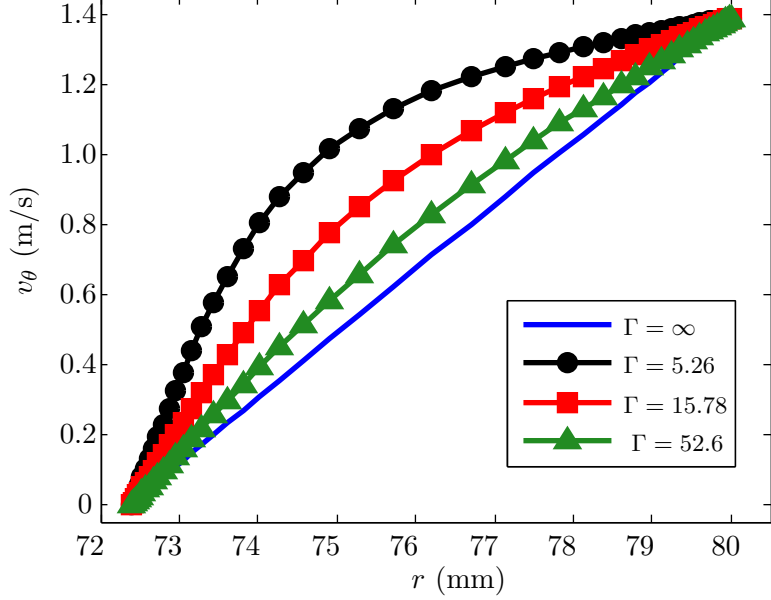
Figure 5.4: Azimuthal velocity profiles across the gap for various aspect ratios at $Re_o = 7750$.

as the experiments could be conducted. However, it is interesting to check other experimental configurations and see if yield better results. One approach taken by researchers going all the way back to Wendt [70] and Taylor [2, 65, 68] has been to use systems with a large aspect ratio. Figure 5.4 shows the results of simulations carried out at a variety of aspect ratios accessible with the current apparatus. It can be seen that even at aspect ratios that some authors [5, 13] have considered to be "large" ($\Gamma >\sim 30$), high Reynolds number flows with only the outer cylinder rotating deviate significantly from the ideal flow profile.

The observed distortions also present challenges for particle image velocimetry (PIV) measurements of the flow. As discussed above, the flow profile in the small aspect ratio configuration has a significant velocity gradient near the inner cylinder wall. Resolving velocity gradients using PIV is difficult in general [226], but can be especially tricky if the gradient is near a wall. Any interrogation window that encompasses the wall will necessarily contain subregions that do not contain particles. That means that these subregions do not contribute to the correlation and thus the velocity calculated for that interrogation window is biased toward the velocity of the subregion that *does* contain particles. If the velocity gradient near the wall is large, this means that velocity measurements near the wall will significantly overestimate the local fluid velocity.
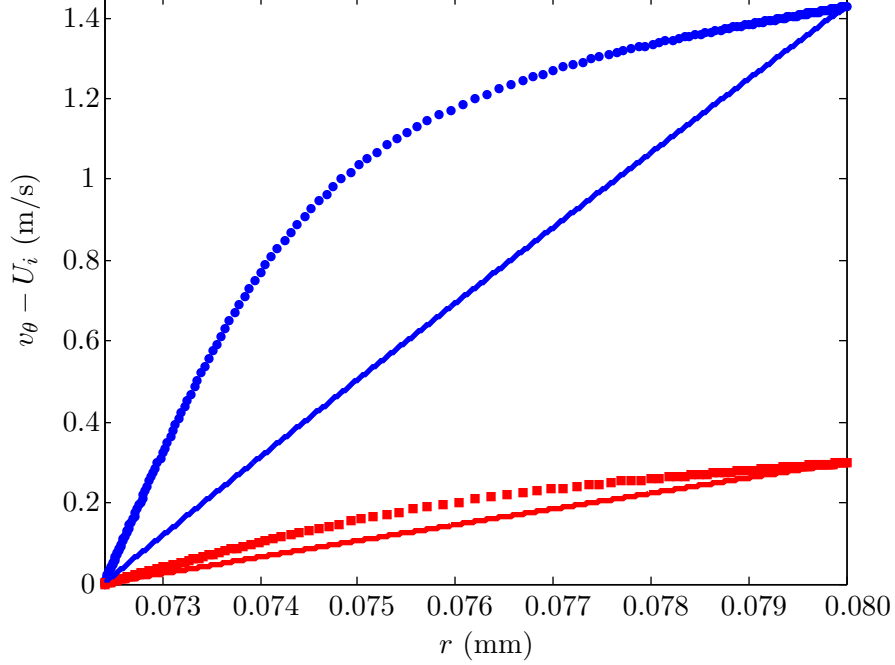
Figure 5.5: The azimuthal velocity profile relative as seen from the frame of reference of the inner cylinder wall for $(Re_i, Re_o) = (0, 7750)$ (●) and for $(Re_i, Re_o) = (-625, 1000)$ (■). By counter-rotating the cylinders a subcritical flow with small velocity gradients and low mean flow can be established. The solid lines correspond to the ideal ($\Gamma \to \infty$) circular Couette profile.

The types of simulations described here can help inform future experiments. Recently, additional calculations were carried out as part of ongoing studies of subcritical transitions to turbulence in counter-rotating flows. The same Fluent code and computational domain were used but the boundary conditions were adjusted so that $Re_o = 1000$ and $Re_i = -625$. This flow was observed to become spontaneously turbulent in flow visualization experiments when the inner cylinder Reynolds number was increased to about 628. Once it becomes turbulent, the transition exhibits hysteresis, suggesting that the transition is subcritical. Figure 5.5 compares the results of these simulations to the velocity profile computed when only the outer cylinder was allowed to rotate. It can be seen that even though this flow is close to unstable, it does not have particularly strong velocity gradients. Furthermore, the velocities are much smaller so that the cross-correlation step in tomographic PIV should be significantly faster since the search radius for correlation peaks could be smaller. The flow could also be imaged a lower frame rate meaning that the flow could be observed for longer periods of time. Because the mean flow rate is close to zero, turbulent structures should

advect by the measurement volume much more slowly so that their dynamics might be studied more effectively. At this time, the injection system is not configured for injections while the inner cylinder is rotating but this could be achieved with a rotary joint (e.g., McMaster-Carr part no. 9177K512).

CHAPTER VI

IMPLEMENTATION OF TOMOGRAPHIC PIV FOR TAYLOR-COUETTE FLOWS

Recent advances in computational power have spurred on the development of a new understanding of turbulent dynamics based on dynamical systems theory [9, 10, 24, 25, 227]. In this framework, a particular fluid flow can be thought of as a trajectory in an infinite-dimensional state space comprised of all possible flows. Each instantaneous velocity field then corresponds to a point in this space. The dynamics of trajectories are guided by unstable invariant solutions called *exact coherent structures*, which guide the flow in the same manner that fixed points, limit cycles, and periodic orbits guide dynamics in low-dimensional dynamical systems. The numerical evidence for existence of exact coherent structures is extensive [25, 27–31, 54, 126, 127, 129, 221, 228–232] and a unified picture of their role in turbulent dynamics has begun to emerge [8, 9, 24, 26, 227, 233–239].

On the experimental front, however, progress has been slower. Because of their inherent three-dimensionality, finding evidence for the existence of exact coherent structures puts even today's most advanced experimental techniques to the test. This chapter presents some of the first attempts at spatially and temporally-resolved measurements of three-dimensional flow structures in turbulent Taylor-Couette flow using tomographic particle image velocimetry (PIV). This recently developed velocimetry technique shows promise in providing experimental support to ongoing numerical and theoretical studies. Section 6.1 reviews earlier studies of Taylor-Couette flow using different variants of PIV. Section 6.2 provides an in-depth description of the tomographic PIV system, including details pertaining to the design of a custom-built three-dimensional calibration target that was fabricated as part of this work. The experimental procedure and data processing methods are discussed in Section 6.3. A discussion of data post-processing techniques is presented in Section 6.4. These include visualization techniques for volumetric data, as well as methods to locate the

measurement volume relative to the natural cylindrical coordinate system to allow the comparison of experimental data with numerical simulations. Some preliminary experimental results are presented in Section 6.5. These include tomographic PIV measurements of the laminar profile, Taylor vortices, and the growth of localized perturbations generated using the injection system described in Chapter 4. A summary is provided in Section 6.6.

6.1 Background

6.1.1 Previous Investigations of Taylor-Couette flow Using PIV

While PIV has become a workhorse in experimental fluid mechanics over the last two decades [226, 240], its use in the study of Taylor-Couette flows has been comparatively limited. In 1997, Baumert et al. were the first to use planar PIV in Taylor-Couette flow. The used it to study the viscoelastic instability of a Boger fluid [241]. This was followed shortly thereafter by a 1998 paper by Wereley and Lueptow, who used planar PIV to measure the radial and axial velocities of non-wavy and wavy Taylor vortex flow in a meridional plane ($\theta = $ constant) [242]. They found that while the velocity field for Taylor vortex flow agreed with what one would predict from flow visualization experiments, the spatiotemporal dynamics of the vortex cores in wavy Taylor vortex flow are quite complicated with significant interactions and fluid transport between adjacent vortices. Wereley and Lueptow extended this work to Taylor-Couette flows with imposed axial flow in 1999 [243].

About the same time Malkiel et al. used planar PIV to study the evolution of finite-amplitude perturbations to linearly stable Taylor-Couette flows [99]. By measuring the velocity field in the midplane of the system, they were able to show that, in certain co-rotating regimes, sufficiently large perturbations near the inner cylinder wall could grow to form hairpin vortices that separated from the wall and were stretched by the mean flow. Their results agreed well with earlier theoretical predictions by Levinski and Cohen [98].

Planar PIV has since been used by a variety of researchers. Wereley et al. [244] studied transport in particle-laden Taylor-Couette flows with a porous inner cylinder. Judat et al. used PIV to study the effects of macro- and micro-scale mixing on precipitation dynamics in a Taylor-Couette reactor with axial flow [245]. Smieszek and Egbers used planar PIV

to study flow bifurcations in Taylor-Couette flows of non-Newtonian fluids [246]. Wang et al. performed planar PIV measurements of turbulent Taylor vortex flow [247]. Coufort et al. studied the relationship between hydrodynamics and flocculation in a Taylor-Couette reactor [248]. Racina and Kind used PIV to study local dissipation rates of turbulent kinetic energy in turbulent Taylor-Couette flow [249]. Abcha et al. used PIV to establish a qualitative relationship between the reflected light intensity in Kalliroscope visualizations and the local radial velocity [183]. Deng et al. used PIV to study of the formation of Taylor vortices in a large gap, small aspect ratio system [250]. Lee et al. used planar PIV to study the effects of axial wall slits in the outer cylinder on the supercritical transition sequence [251]. Sathe et al. used PIV in their study of the transition sequence in a two fluid Taylor-Couette configuration [252]. van Hout and Katz studied the mean flow and turbulent statistics in high Re counter-rotating Taylor-Couette flow [253]. Huisman et al. [254] performed planar PIV measurements to study angular momentum transport in strongly turbulent (Re_i up to 2×10^6) Taylor-Couette flow, finding good agreement with the scaling predicted for the so-called ultimate turbulence regime [255].

The first and, until quite recently, only measurements of a three-dimensional velocity field in Taylor-Couette flow were performed by Akonur and Lueptow in 2003 [256]. By exploiting the temporal periodicity of wavy Taylor vortex flow, Akonur and Lueptow were able to reconstruct the full three-dimensional field by phase-averaging a series of planar PIV measurements in different latitudinal ($z = $ constant) and meridional planes. In an accompanying paper [257], Akonur and Lueptow used these three dimensional velocity measurements to study the role of chaotic advection in the mixing properties of these flows. More recently, Ravelet et al. performed stereoscopic PIV measurements of turbulent Taylor-Couette flow. This technique allowed them to measure all three velocity components in a meridional plane [258]. These data were used to study the origin of changes observed in torque scaling as the rotation number R_ω (see Section 3.7.2) was varied at high Reynolds number.

6.1.2 Volumetric PIV

The recent advent of volumetric velocimetry techniques [259] has made it possible to study the types of complex three-dimensional structures that arise in transitional Taylor-Couette flows. These techniques include holographic PIV [260–264], scanning light sheet PIV [265–268], defocusing PIV, and tomographic PIV. Each of these techniques has its own advantages and drawbacks. Brief reviews of the operating principles of each of these techniques are provided in the book by Adrian and Westerweel [226]. The advantages and disadvantages of several of these techniques are reviewed in the article by Arroyo and Hinsch [259].

In holographic PIV, the particle positions are recorded on holographic film. The hologram is then projected and the particle positions are reconstructed by scanning a camera through the three-dimensional projection. This process is slow and requires developing of holographic film in dark room conditions, making it unsuitable for time-resolved measurements of the evolution of turbulent structures [269]. Furthermore, while holographic PIV provides very high spatial resolution [261], the required optics are quite complex and technical limitations constrain its applicability to small measurement volumes of a few cubic millimeters [270]. This makes it unsuitable for the study of the spatially extended turbulent structures observed in the turbulent Taylor-Couette flows in the subcritical regime. Recent attempts have been made to address some of the shortfalls of holographic PIV by replacing holographic film by digital recordings [263, 271], but the technique is not yet robust enough to perform the kind of spatially- and temporally-resolved measurements that are required to study the *dynamics* of turbulent flows.

Scanning light sheet PIV (SLS-PIV) is a variation of basic planar PIV where the light sheet is scanned through a volume and a series of images are taken with the light sheet illuminating different planes [265–268]. The idea is that if these are taken at sufficiently short time intervals, the particle field is essentially frozen in time and the three-dimensional particle field can be reconstructed. While this approach allows the use of high seeding densities and hence provides high spatial resolution, the assumption that the flow does not evolve as the laser sheet scans through the volume sets an obvious limit on the temporal resolution of the measurement. This technique shows great promise in moderate speed flows

but is not easily extended to flows with velocities higher than about 1 m/s [270]. The curved interfaces present in Taylor-Couette setups make scanning the light sheet uniformly through the measurement volume tricky and make SLS-PIV difficult to implement in this geometry. It may be possible to overcome these difficulties by using careful ray-tracing in design of the optics train. This approach has been used recently to perform high-precision laser Doppler velocimetry measurements of Taylor-Couette flow at high Reynolds numbers [272], although it is unclear if this method would be easy to implement for volumetric illumination by a scanning light sheet.

Another approach that has been employed to achieve volumetric measurements of flow fields is defocusing PIV [273–276]. In this technique, the whole measurement volume is illuminated simultaneously and imaged using three offset apertures using one [273] or more sensors [275]. Because the apertures are offset from the optical axis, a single particle is projected onto the sensor not as a single point, but as a triangular arrangement of defocused spots. The size of the triangle is related to the the distance between the imaged particle and the focal surface of the lens [277],[1] so that given knowledge of the aperture geometry and the recorded images, the three dimensional locations of the particles can be extracted for PIV interrogation. The simplicity of defocusing PIV makes it an attractive candidate for the study of turbulent dynamics, but the spatial resolution and maximum measurement volume of commercially available defocusing PIV systems is still limited.

Originally introduced by Elsinga et al. in 2006 [279], tomographic PIV has recently emerged as flexible option for three-dimensional velocity measurements [270]. Like defocusing PIV, tomographic PIV uses volumetric illumination. The three-dimensional positions of particles are reconstructed numerically from images of the measurement volume captured from different direction using multiple cameras (typically four). Unlike in 3D particle tracking methods, where the positions of individual particles are directly estimated by triangulation [280], the particle field in tomographic PIV is reconstructed using optical tomography

---

[1]In a sense, the multiple apertures used in defocusing PIV play the inverse role to that played by the Hartmann mask in focusing optics in astrophotography [278].

techniques. These are usually based on the multiplicative algebraic reconstruction technique (MART) [281], which iteratively attempts to generate the particle distribution that resulted in the captured images. The mapping between the measurement volume and the image sensors is generated using calibration techniques similar to those employed in stereoscopic PIV, although the tolerances on the calibration are more stringent in tomographic PIV than in stereo PIV. Once the particle distribution in the measurement volume has been reconstructed, the velocity field can be calculated using three-dimensional extensions of standard cross-correlation algorithms typically used in planar PIV [279]. Tomographic PIV remains an active area of research. Recent developments in the field are reviewed in the 2013 article by Scarano [270].

Tokgoz et al. [282] have recently used Taylor-Couette flow to assess the spatial resolution and accuracy of tomographic PIV. They performed velocimetry measurements in the circular Couette, Taylor vortex, and featureless turbulence regimes and found that tomographic PIV was able to accurately resolve the laminar and Taylor vortex regimes. In order to test the accuracy of tomographic PIV in the turbulent regime, Tokgoz et al. used their three-dimensional data to calculate the energy dissipation rate. They compared this result to estimates of energy dissipation rate from torque measurements and found that tomographic PIV adequately resolved all the scales at $Re = 3800$, but was unable to completely resolve the flow at $Re = 14000$ and 47000. As part of their study, Tokgoz et al. conducted a systematic investigation of the effects of different parameters of PIV interrogation such as interrogation window size and overlap on the measured dissipation rates and determined that the resolution of tomographic PIV measurements is more sensitive to interrogation window size changes than to changes in overlap.

6.2   Experimental Setup

The experiments described in this chapter were conducted with the same experimental configuration described in Chapter 4. The outer cylinder was made of glass and had a radius of 80 mm. The inner cylinder was made of naval bronze, which was powder coated flat black and had a radius of 72.4 mm. The gap between the cylinders was, therefore, 7.6

mm and the radius ratio was 0.905. The aspect ratio of the test section was set to 5.26 gap widths (4.00 cm) by adjusting the position of the top end ring. In order to improve optical access, the test section was elevated by inserting an aluminum spacer into the bottom of the gap. Both ends of the test section (the end ring and the spacer) rotated with the outer cylinder. The stepper motors were mounted on a separate optical table and the cylinders were driven using timing belts to minimize mechanical noise.

6.2.1 Cameras

The flow was imaged using four high-speed Phantom v210 cameras (Vision Research, Wayne, NJ), which can achieve frame rates of up to 2190 frames per second. These high frame rates were needed to accurately resolve the turbulent dynamics of flows with only the outer cylinder rotating. In this configuration, the outer cylinder wall speeds required to maintain turbulence can be as high as 1-2 m/s. Each camera was equipped with a 105 mm f/2.8 AF Micro-Nikor lens (Nikon Incorporated, Melville, New York). The cameras were mounted on rigid optical rails using three-axis geared heads (model no. 400, Manfrotto, Cassola, Italy). They were arranged in the standard "cross" configuration [283–286] shown in Figure 6.1. The geared heads were arranged so that the fields of view of the cameras overlapped as much as possible. The typical field of view spanned about 50 mm × 38 mm in the center of the test section. In order to extend the depth of field across the gap, the aperture was set f/11.

6.2.1.1 Scheimpflug adapters

As discussed by Elsinga et al. [279] and by Scarano [270], the quality of tomographic reconstruction depends on the angle subtended by the cameras. Ideally, the larger the angle between the cameras, the better the reconstruction. In practice, the angle between the cameras is limited by the imaging optics. When the camera sensor is not parallel to the desired plane of focus, the image will not be uniformly in focus. This distortion can be corrected for by tilting the lens relative to the sensor plane until it satisfies the Scheimpflug condition [287]. For the tomographic PIV measurement reported here this was achieved by using LaVision's Scheimpflug Camera Lens Adapter v1 (part no. 1108196, LaVision,

Figure 6.1: Phantom v210 cameras in the standard "cross" configuration. The cameras are equipped with 105 mm Nikon Micro lenses, LaVision Scheimpflug mounts, and Edmund Optics 550 nm long-pass filters.

(a)   (b)   (c)
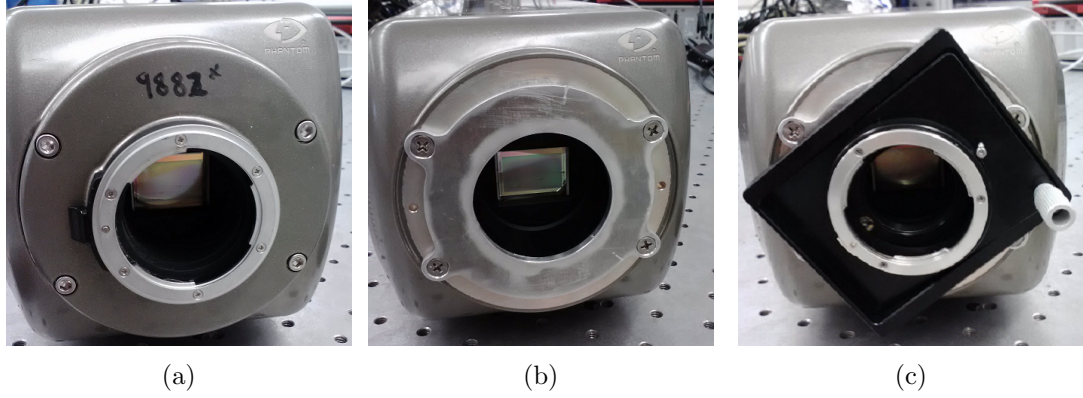
Figure 6.2: Installing the LaVision Scheimpflug Camera Lens Adapter on a Vision Research Phantom v210 Camera (a) The Phantom v210 comes with a standard Nikon F-mount and has a deeply recessed sensor. This prevents the use of tilt mounts directly on the camera since their use would place lenses too far from the sensor to focus correctly. (b) This can be remedied by replacing the F-mount with a custom face plate that puts lenses mounted on the LaVision tilt mount closer to the sensor. (c) The tilt mount can be rotated to satisfy the Scheimpflug condition for compound angles before locking it down with set screws.

Ypsilanti, Michigan). The v1 allows the lens to be tilted in one-dimension. By rotating the v1 relative to the camera body, compound angles can be accommodated.

6.2.1.2   Mounting the Scheimpflug adapters

The Phantom v210 features a deeply recessed sensor housing. Therefore, attaching the tilt mount directly to the front of the camera (e.g., via the standard Nikon F-mount or the optional C-mount adapter) will result in the lens being too far from the sensor and limit the working distance over which the lens can be properly focused. This can be *partially* corrected by removing the F-mount and replacing it with a narrower, custom face plate designed by Deepak Adhikari at the University of Minnesota.[2] In this way, the tilt mount (and therefore the lens) are much closer to the sensor and the range of usable working distances improves. The tilt mount can also be rotated to satisfy the Scheimpflug condition for compound viewing angles without having to rotate the camera body, which makes it easier to achieve overlapping fields of view. For more details, see Figure 6.2. Mechanical drawings for Dr. Adhikari's original face plate design are included in Appendix C.

---

[2]Currently a postdoctoral associate in the group of Prof. Donald Webster in Georgia Tech's School of Civil and Environmental Engineering.

(a)

(b)
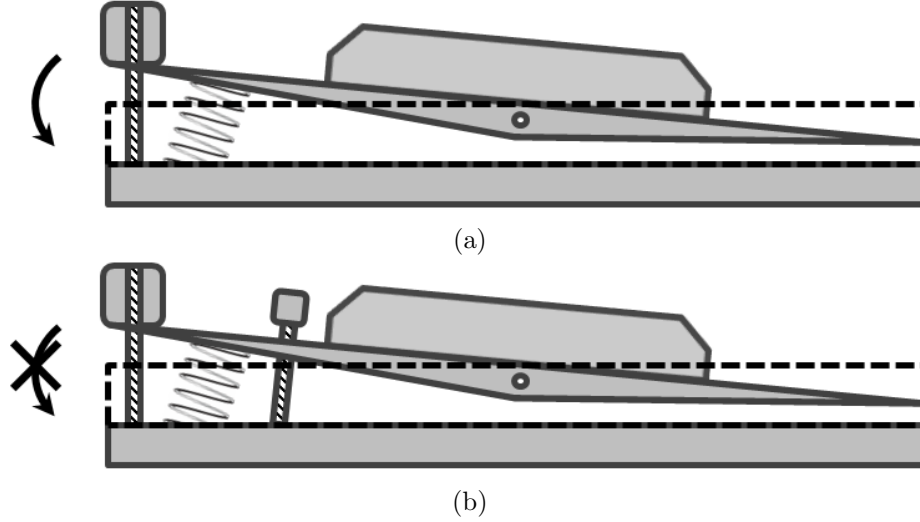
Figure 6.3: Cutout schematic of the LaVision Scheimpflug Camera Lens Adapter with locking screw (a) LaVision's tilt mount works by using a spring to push on the mount head. The head pivots on the mount body until it stops against an adjustable knob. (b) A locking screw (UNC #4-40) was installed on the head to prevent it from oscillating. Once the tilt mount is adjusted to the desired angle, the screw is tightened and pushes against the mount body, locking the head in place.

6.2.1.3 Preventing vibration in the tilt mount

LaVision's tilt mount uses a spring to push on the head, which pivots on the mount body until it stops against an adjustment knob as shown in Figure 6.3a. This knob prevents the head from rotating away from the body. However, it does not prevent the head from rotating back towards the body if sufficient external forcing is applied to overcome the spring. When the camera is subjected to mechanical vibration, the mount head can oscillate, leading to difficulties in tomographic reconstruction. In order to prevent this, a threaded hole (UNC #4-40) was made on mount head to allow the installation of a locking screw. When tightened against the tilt mount body, this screw locks the head in place as shown in Figure 6.3b.

6.2.1.4 Turning camera fans on/off

The CMOS sensors on the Phantom v210 cameras can generate a lot of heat. In order to keep the sensors cool, the cameras are equipped with several fans that provide air cooling. The fans also introduce undesirable vibrations to the system, which can degrade the quality of the tomographic PIV measurement, especially when long focal length objectives or high

magnification are used. In order to reduce these vibrations, it is advantageous to turn the camera fans off while taking data. Unfortunately, neither LaVision's DaVis nor Vision Research's Phantom Camera Control (PCC) software provides a straightforward way to do this.

However, it is possible to turn off the fans by temporarily adjusting the setpoint for the camera's temperature control system to a temperature much higher than the default setting ($40°C$), so that the camera senses that it is so far from overheating that cooling is not necessary. This can be done by connecting to the camera via Telnet and issuing the appropriate commands. Care must be taken to reset the cameras to the default setpoint after acquiring data to prevent overheating and possible damage to the cameras.

Because each camera requires a separate Telnet session, turning the camera fans on/off by hand can be cumbersome. However, the procedure can be automated by using TST10.exe, a Telnet scripting tool by Albert Yale.[3] TST10.exe allows the user to automatically initiate a Telnet session and send the Telnet server (i.e., the camera) a series of commands stored in an input file. By scripting TST10.exe calls within a batch file all the camera fans can be turned off at a click of the mouse and automatically restarted after some predetermined time to guard against accidental overheating.

As an example, consider the input file `fan1off.txt`, shown below:

```
100.100.103.254 7115
SEND "set hw.tsetcam 99\m"
WAIT "Ok!"
```

When executed from the Windows command line using TST10.exe, `fan1off.txt` will initiate a Telnet session with the camera at IP address "`100.100.103.254`" over port "`7115`" (Notice that Phantom cameras use port 7115 for Telnet instead of the usual 23.). It will then change the setpoint for the temperature control system to "`99`", so that the fans will not come on until the sensor temperature reaches $99°C$. Finally, it will confirm that the command has been executed by waiting for the camera to return the string "`Ok!`". Once it reaches the end of the input file, TST10.exe will terminate the Telnet session.

---

[3]This software is no longer supported by Mr. Yale but is readily available for download on the Internet.

Separate input files must be written for each camera and include that camera's IP address. Individual camera IP addresses can be found by clicking on their icons in the Setup window of DaVis or by going to the Camera Info menu within the Live tab in PCC. Additionally, input files must be created to turn the camera fans back on (i.e., return the temperature control system setpoint to the default `40`). Then, a batch file can be created to run all the Telnet sessions automatically. Such a file would look something like `fansoff.bat`, which assumes that both TST10.exe and the various input files are stored in `C:\Users\LaVision\` and is shown below:

```
C:\Users\LaVision\TST10.exe /r:C:\Users\LaVision\fan1off.txt
C:\Users\LaVision\TST10.exe /r:C:\Users\LaVision\fan2off.txt
C:\Users\LaVision\TST10.exe /r:C:\Users\LaVision\fan3off.txt
C:\Users\LaVision\TST10.exe /r:C:\Users\LaVision\fan4off.txt
timeout /t 100
C:\Users\LaVision\TST10.exe /r:C:\Users\LaVision\fan1on.txt
C:\Users\LaVision\TST10.exe /r:C:\Users\LaVision\fan2on.txt
C:\Users\LaVision\TST10.exe /r:C:\Users\LaVision\fan3on.txt
C:\Users\LaVision\TST10.exe /r:C:\Users\LaVision\fan4on.txt
```

This batch file sends the commands to each of the four cameras in the tomographic PIV system to turn off its cooling fans, waits for "`100`" seconds or for the user to hit ENTER, and then, sends the commands to turn the cooling fans back on.

6.2.1.5 Image acquisition and timing

The four cameras were controlled using the DaVis software package, which interfaced with the cameras via a dedicated timing unit (LaVision High Speed Controller, model no. 1108075). This unit provides the timing signals necessary to synchronize the cameras and trigger acquisition. The wiring diagram for a single camera is shown Figure 6.4. In order to record images each camera requires two signals. The first of these is the frame synchronization signal (F-SYNC), which originates from the output labeled "Cam 1"-"Cam 4" on the CAMERA port of the high speed controller. Each camera must have its own individual F-SYNC signal, which is connected directly to the F-SYNC connector on the camera body. DaVis mounts the cameras in order of ascending serial number[4] and it is

---

[4]The Phantom v210s used here have serial numbers 9882, 9883, 9884, and 9885. Davis mounts camera 9882 as camera 1, 9883 as camera 2, etc.
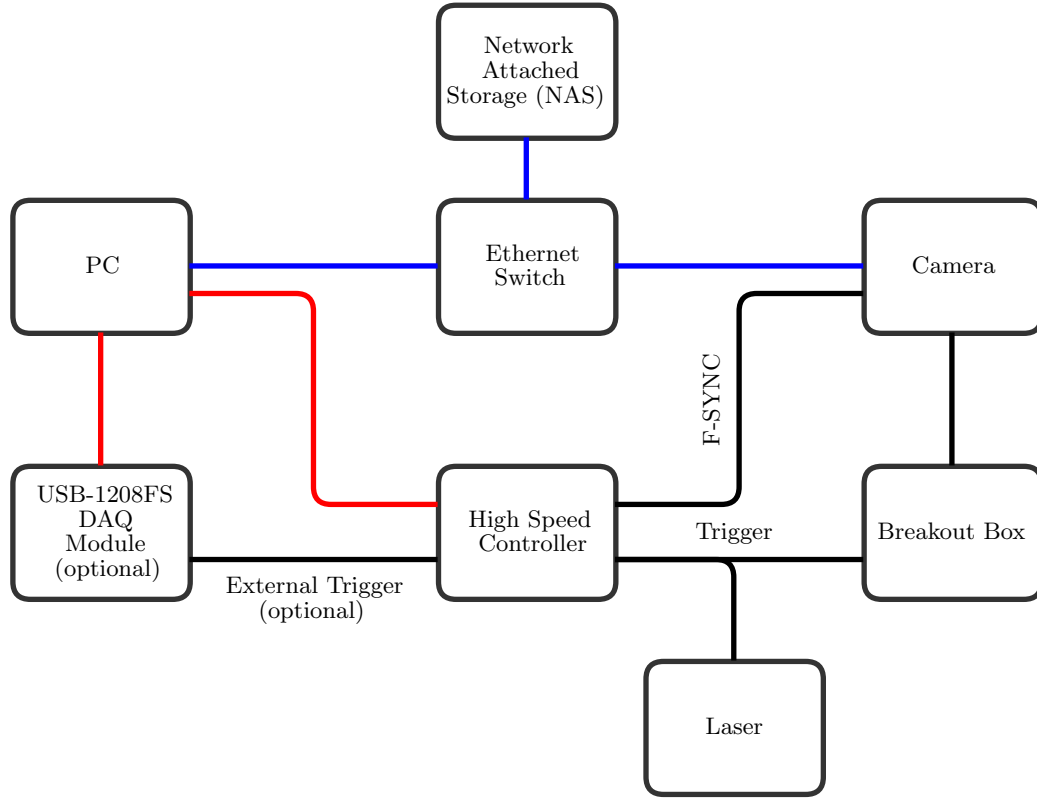
Figure 6.4: Wiring diagram for Phantom v210 camera. Blue lines denote Ethernet connections using CAT-6 cables. Black lines denote connections using BNC cables. Red lines denotes connections using USB cables.

important to connect the correct F-SYNC signal to each camera (e.g., the Cam 1 signal, should go to camera 1). The second required signal is the trigger signal, which initiates recording. This signal originates from the "UserTrigger" output of the CAMERA port on the high-speed controller. Typically, all four cameras share the same trigger signal, which is connected to the cameras through the "TRIGGER" channel on special breakout boxes (Vision Research, model no. VRI-BOB-2T) that connect to the CAPTURE connector on the camera bodies.

In addition to the timing signals, DaVis communicates with the cameras via Ethernet. This connection is used to configure the various settings (exposure time, e.g.) in the camera software. In order for DaVis to recognize the cameras, the two must be on the same TCP/IP subnet. While it is possible to change the IP addresses of the camera via Telnet, it much easier to configure the data acquisition computer (and any network attached storage units

or file servers) to the correct subnet. By default the camera IP addresses reside on the 100.100.x.x subnet (subnet mask 255.255.0.0).

When the cameras are first turned on, any captured images will typically have patterned noise in the form of vertical stripes. This can be corrected by performing an "Intensity Correction", which is available from the Camera dialog in the Davis Recording Window. The intensity correction must be performed with a lens cap attached to the camera and depends on the frame rate and exposure time settings for a particular camera. If either of these settings is changed, the intensity correction must be repeated. Another useful feature that can be found in the Camera dialog is the "Add an offset (+/-)" button. In order for tomographic reconstruction to work correctly regions that do not have particles should be as close to black as possible (i.e., have zero counts). It was found that adding an offset of -20 counts, canceled out much of the thermal noise from the sensor, making the background almost perfectly black.

Another aspect that was important to the work presented here was to synchronize the start of the image acquisition sequence with the injection of fluid that was used to trigger turbulence. This was achieved by configuring the system to accept an external trigger from the DaVis Recording window. This setting can be found under the Device Settings tab in the Timing menu, where it is labeled as "Source". If this field is set to "external", the system will wait after the "Start Recording" button is pressed until it receives a TTL high signal on the "Trigger" input of the TRIGGER INPUT port on the high speed controller. An example of how such a trigger might be implemented in Matlab using a Measurement Computing USB-1208FS is provided in Appendix B.4. The Timing menu in DaVis also allows the capture of a fixed number of images into a rolling buffer before the trigger signal, which is controlled in the "Trigger Image" dialog, so that events preceding the trigger by a fixed amount of time can be recorded.

6.2.2   Nd:YLF Laser

The measurement volume was illuminated from the front of the apparatus using a Q-switched frequency-doubled neodymium-doped yttrium lithium fluoride (Nd:YLF) laser
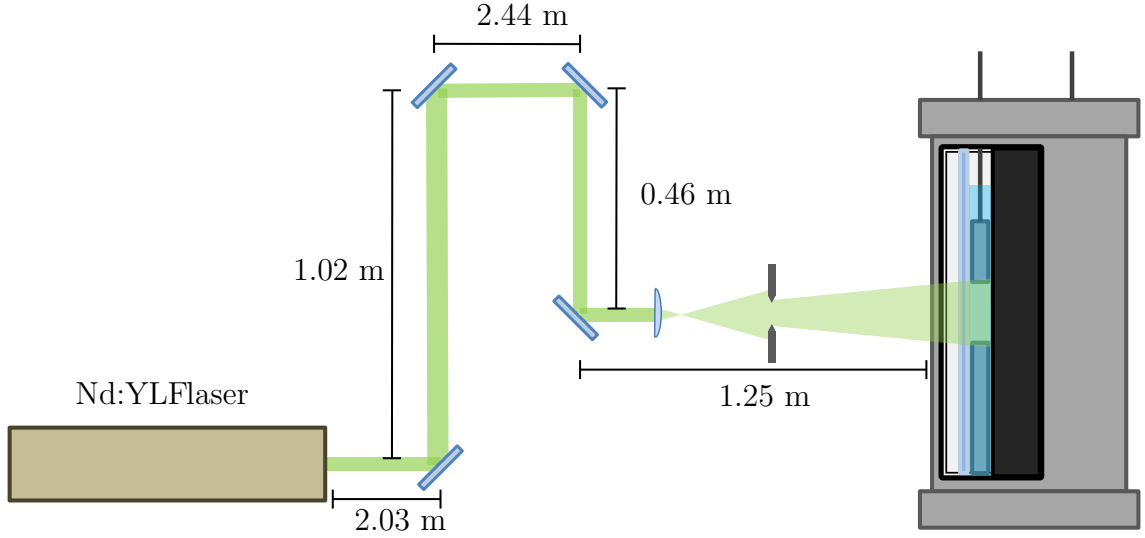
Figure 6.5: Laser guiding optics (drawing not to scale).

(Quantronix 527/DP-H) with a wavelength of 527 nm. The Q-switch was externally trig-gered using the same trigger signal used for the cameras, which was connected to the control module via the J105 connector on the back of the unit. The 527/DP-H had a pulse dura-tion of 150 ns, which was much shorter than any of the timescales in the flow, obviating the need for shuttering. The short duration of the laser pulse effectively sets the exposure during data acquisition, but it is useful to configure the cameras to the maximum allowable exposure for the desired frame rate. This helps with the acquisition of calibration images, which are taken using halogen illumination that is much less intense than the laser.

The location of the 220 VAC line in the laboratory made it necessary to steer the laser beam to the apparatus as shown in Figure 6.5. This was done using Edmund Optics 45° Nd:YAG laser line mirrors (Edmund Optics part no. 45-991), which have greater than 98% reflectance at 527 nm. The use of high reflectivity mirrors was necessary to minimize the losses in beam intensity since the Nd:YLF laser only had a maximum output of $\sim$4-5 mJ/pulse at 2kHz, which is at the lower limit of what is typically needed for tomographic PIV measurements [270]. Earlier attempts using mirrors with 90% reflectance resulted in images with poor contrast since almost 35% of the already scarce laser light was lost in the optics train.

Because the ratio of the width to the height of the measurement volume was almost unity

(4:3), a single 150 mm plano-convex with anti-reflective coating for 532 nm light (Edmund Optics part no. 69-409) was used to expand the beam. Four razor blades mounted on bar-type lens holder were used to create a rectangular aperture. This assured that the edges of the illuminated volume were sharp and that only the more uniform central part of the Gaussian beam was used. The relatively shallow depth of the measurement volume (~ 1 cm) and the small divergence angle of the lens made it so that the cross-section of the illuminated volume varied by less 0.3 mm throughout its depth.

6.2.3 Particles

A critical part of any PIV measurement is the choice of particles [288]. A primary consideration when selecting particles is that they must scatter (or in the case of fluorescent particles emit) sufficient light to be distinguishable from the background when imaged. However, the particles must also accurately follow the flow without changing it and be available in sufficient quantities to be able to properly seed the flow densely enough that measurement has the desired spatial resolution. Performing volumetric PIV in a Taylor-Couette system with a large radius ratio like the one used here will almost always require the experimenter to capture images of particles near a wall. This can be tricky since the light reflecting from the walls can wash out the particle images. This can be avoided by using fluorescent particles, which absorb the illuminating laser light and re-emit at a different wavelength. The laser light can then be filtered out with appropriate optical filters, resulting in higher contrast images. Another advantage of using fluorescent particles is that unlike simple scattering, which is strongly anisotropic for small particles, fluorescence can be considered to be isotropic. This means that images from different cameras will have similar brightness and contrast, which is beneficial for the tomographic reconstruction of the measurement volume.

In this work, the cameras were outfitted with long-pass filters from Edmund Optics with a cutoff wavelength of 550 nm (Edmund Optics part no. 64-700), which had an optical density of 2 in the rejection band. The filters had a diameter of 50 mm and were mounted on 52 mm rings from old UV camera filters using hot glue, so that they could be mounted

directly on the front of the camera lenses as shown in Figure 6.1.

6.2.3.1 Fluorescent particles for use in water

Commercial fluorescent particles can be prohibitively expensive. For this reason, custom-made fluorescent particles were made by dyeing Sepabeads SP20SS (synthetic adsorbant resin particles manufactured by the Mitsubishi Chemical Corporation of Tokyo, Japan) with rhodamine following the advice of Prof. Satoshi Someya of the National Institute of Advanced Industrial Science and Technology in Japan. Sepabeads are highly porous particles made of cross-linked styrene-divinylbenzene and are used as a sorbent in high performance liquid chromatography (HPLC). Prof. Someya and his collaborators have previously used Sepabeads dyed with rhodamine to study two-dimensional, flow-induced vibrations of cylindrical bodies in cross-flow [289].

Before beginning the dyeing process, the Sepabeads were separated by size using a set of U.S. standard sieves with mesh openings ranging in size from 45 to 75 microns (Dual Manufacturing Company, Franklin Park, Illinois). The majority of the particles were found to be in the 63-75 micron range, although a significant fraction fell outside this range[5]. For the work presented here, the particles in 45-53 micron range were selected and dyed by stirring them overnight in a concentrated solution of rhodamine 6G dissolved in ethanol. Rhodamine 6G was chosen because of its high quantum yield ($\sim$0.95) and because its absorption peak (531 nm) is well-suited to excitation with an Nd:YLF laser (see Figure 6.6 for more details). The particles were then washed by placing them in a No. 450 standard sieve (32 micron mesh openings) and running tap water over them for 30 minutes. Finally, the particles were dried for several hours in an oven at 60°C. Drying the particles made them easier to store and prevented the slow leaching of rhodamine into the liquid phase that occurs if they are stored in suspension.

To use the dyed particles, they were pre-wetted by stirring them in distilled water

---

[5]Sepabeads SP20SS vary in size between 45 and 150 microns with very few particles outside of this range. Mitsubishi Chemical manufactures a variety of synthetic adsorbent resin particles in a wide range of sizes. Their Diaion HP20 series provides larger particles, while their MCI Gel CHP20 line offers smaller ones. Of particular interest for use in tomographic PIV are MCI Gels CHP20/P20 and CHP20/P30, which have mean sizes of 20 and 30 microns, respectively. These, however, are significantly more costly than Sepabeads.

overnight. Because Sepabeads are naturally hydrophobic, a small amount of Micro-90 concentrated cleaning solution (International Products Corporation, Burlington, New Jersey) was added as a surfactant to prevent clumping. Pre-wetting the particles also allowed water to fill their pores making them closer to neutrally buoyant.

6.2.3.2 *Fluorescent particles for use in ammonium thiocyanate solutions*

In order to minimize the distortion caused by imaging through the curved surfaces of the outer cylinder, a concentrated ammonium thiocyanate (NH_4SCN) solution with a refractive index matching that of the cylinder was used as a working fluid in some of this work (see Section 6.2.4 below). While the dyed Sepabeads described above work well in water, they tend to float in the denser NH_4SCN solution making it difficult to maintain a sufficiently high concentration in the working volume in cases where the flow does not mix well and must be observed for extended periods of time. For this reason, more dense fluorescent particles were made following a slightly modified version of the procedure described by Pedocchi et al. for making particles from polyester casting resin stained with rhodamine [291].

Given the relatively low energy per pulse of the Nd:YLF laser used in this work ($\sim 4-5$ mJ/pulse) and the small lens apertures required to maintain particles in focus throughout the measurement volume, the rhodamine concentration prescribed by Pedocchi et al. (0.1% by volume) was found to be too low to provide a detectable fluorescence signal. Therefore, particles with higher rhodamine concentration were fabricated as follows: About 100 milliliters of Aristocrat Deep Clear polyester casting resin (BDC Epoxy Systems, Santa Fe Springs, California) was stirred together with 3 grams of rhodamine 6G powder until the rhodamine was dissolved. This high concentration of rhodamine makes the resin opaque and gives it an olive green color. Because rhodamine dissolves readily in the uncured polyester resin, dissolving the rhodamine in water before mixing it (as described by Pedocchi et. al.) was found to be unnecessary. The resin was then mixed with the catalyst as directed by the manufacturer's instructions and allowed to harden in a polyethylene mold that had been prepared with Castin' Craft mold release (Environmental Technology Inc., Fields Landing, California). The resulting block of resin was then ground with a Ryobi 1/4 sheet sander

144

(a)

(b)
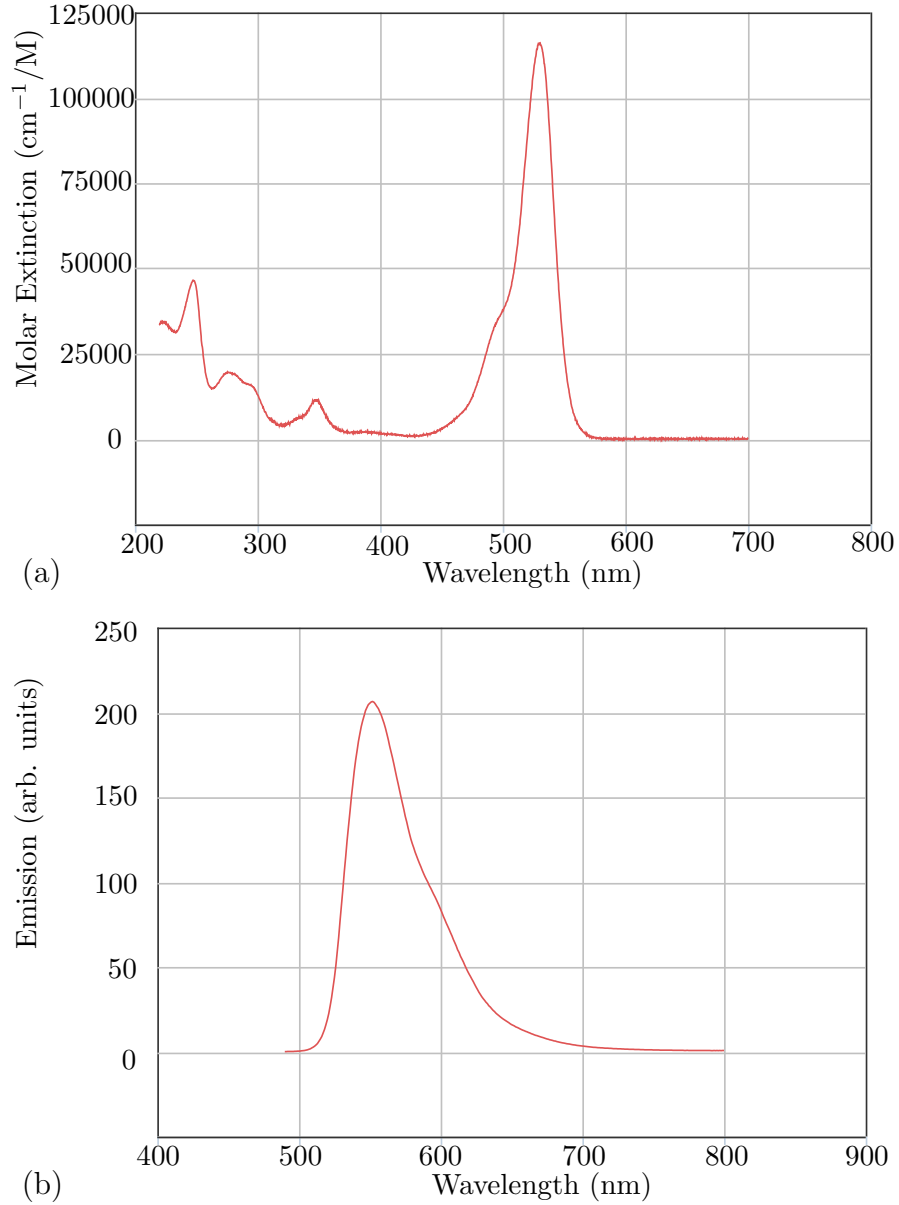
Figure 6.6: Absorption and Emission Spectra of Rhodamine 6G. (a) Rhodamine 6G has an absorption peak at 531 nm and a high quantum efficiency of 0.95 (compared to 0.7 for rhodamine B, for example). This makes it well-suited to excitation with the 527 nm line of a frequency-doubled Nd:YLF laser. (b) Its emission peak is at 552 nm, which is just above the 550 nm cutoff wavelength for the long-pass optical filters used in this work. The peak is skewed toward higher wavelengths such that 91% of the emitted light is emitted at wavelengths higher than 550 nm. Figures adapted from spectra made publicly available by the Oregon Medical Laser Center. [290]

using 120 grit silicon carbide sandpaper.[6] The resulting powder had a bright pink color

In order to make the particles more closely mono-disperse, the powder was wet sieved using U.S. standard sieves. The majority of the resulting particles were found to be smaller than finest sieve available (25 microns). Particles that were caught between the two finest sieves (25 and 32 microns) were selected as PIV tracers for their relatively uniform size. As can be seen in Figure 6.7, however, their shapes can vary quite substantially and are are not particularly smooth. Estimates of the bulk density of the resin give a bulk density of ~1.24 g/cc in agreement with the literature [291, 292].
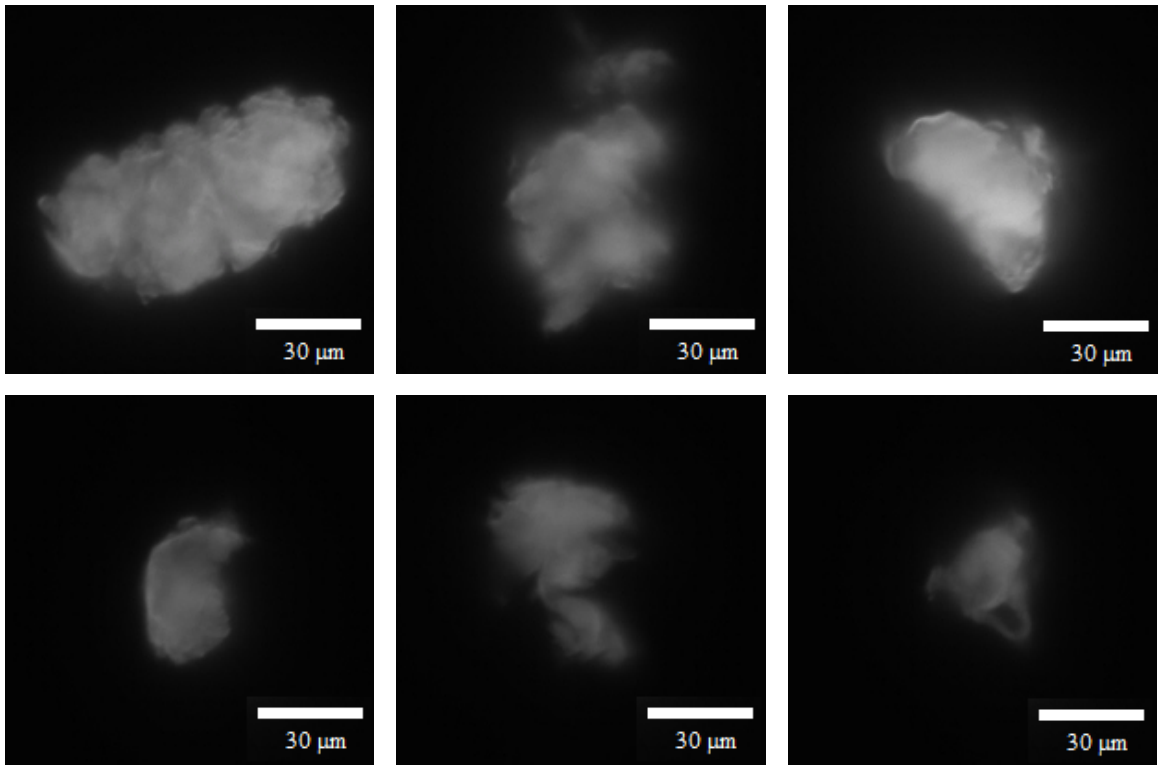
Figure 6.7: Micrographs of polyester resin particles stained with rhodamine 6G. The particles where illuminated with 488 nm light and were imaged using a Nikon Eclipse TE-2000 inverted microscope equipped with an optical long-pass filter with a cutoff wavelength of 510 nm. Images courtesy of Prof. Jennifer Curtis and Louis McLane of the Georgia Tech School of Physics.

---

[6]The resin block can be ground much more efficiently using an electric coffee grinder but the coffee grinder is destroyed in the process.

<center>(a)   (b)</center>
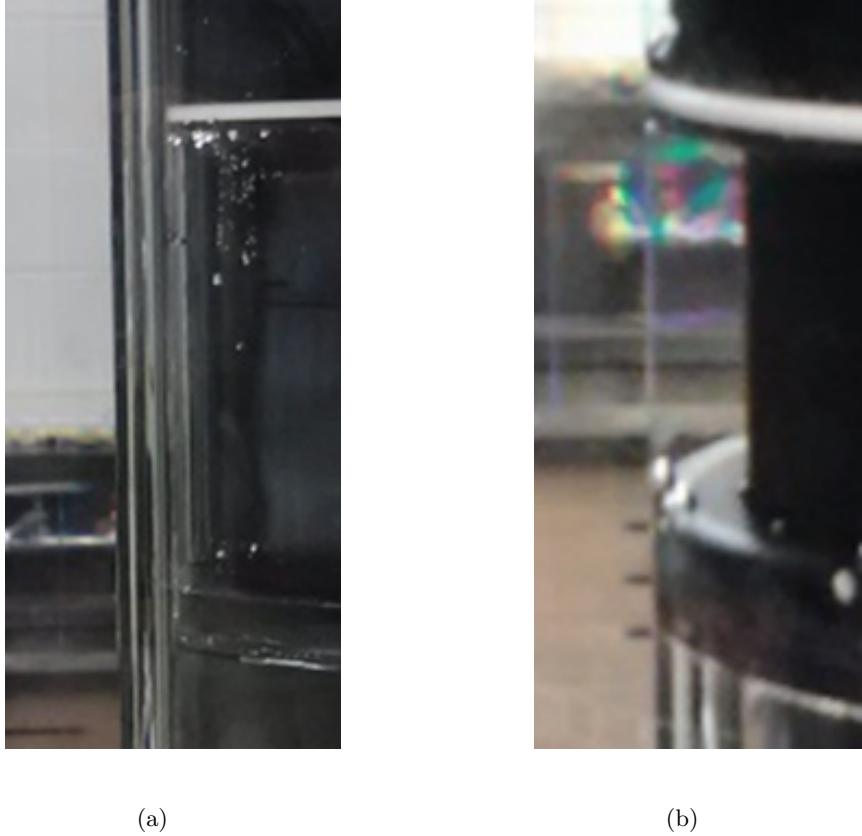
Figure 6.8: The heat bath was filled with a mineral oil mixture with the same index of refraction as the glass cylinder. (a) When the test section was filled with water there was significant distortion due to the refractive index mismatch between the glass cylinder and the water. (b) By filling the test section with ammonium thiocyanate solution, the distortion is reduced and the gap between the cylinders becomes apparent.

6.2.4 Refractive Index Matching

In performing tomographic PIV measurements of Taylor-Couette flow the experimenter must perforce image through the two (inner and outer) curved surfaces of the outer cylinder. As discussed by Ravelet et al. [258] and by Huisman et al. [272], this can introduce errors when taking velocity measurements near the outer cylinder wall. In order to minimize distortion from the outer cylinder, the heat bath and the test section were filled with a refractive index-matched fluid (see Figure 6.8). A similar approach was taken by Wereley and Lueptow [242] in their pioneering PIV measurements of Taylor-Couette flow.

<center>147</center>

In order to minimize distortion from the outside surface of the outer cylinder, the heat bath was filled with a mixture of commercially available mineral oils. McMaster-Carr sells two grades of mineral oil. The index of refraction of the two oils as a function of temperature was measured using an Atago 3850 PAL-RI hand-held refractometer (Atago Company, Tokyo, Japan), as shown in Figure 6.9. The 3850 PAL-RI measures the refractive index of liquids at 588 nm with an accuracy of ±0.0003 and was calibrated using HPLC grade water. It was found that the light viscosity oil (McMaster-Carr part no. 3190K629) has an index of refraction of 1.467 at 20°C. The heavy viscosity oil (McMaster-Carr part no. 3190K632) has an index of refraction of 1.477 at 20°C. By mixing the two, it was possible to match the index of refraction of the glass cylinder (n=1.473).

The manufacturer specifies the refractive index of the glass cylinder as 1.473 at 587.6 nm [293]. However, the fluorescent particles used here have an emission peak at 552 nm, which raises the question of whether the refractive index is correctly matched at this wavelength. While specific data for the outer cylinder material were not available, the effects of chromatic aberration were estimated by using publicly available data for commercial borosilicate glass (SCHOTT BK7). The index of refraction of BK7 is about 0.0017 higher at 552 nm than 588 nm [294]. Luckily, this coincides with the increase in the refractive index of mineral oil over this range of wavelengths, which is about 0.0018 [295], so the effects of chromatic aberration should be small.

The index of refraction of mixtures of the two grades of oil with volume fractions of high viscosity oil ranging from 57% to 75% were measured at room temperature ($\sim$23°C). Using these data, which are shown in Figure 6.10, it was determined that a mixture with 68.8% high viscosity oil by volume would result in a mixture with an index of refraction of 1.473. This mixture had a kinematic viscosity of 72 cSt, which made it too viscous to pump directly with the Neslab RTE-210 refrigerated bath used in the experiments of Chapter 3. Attempts were made at using a stronger secondary pump to pump the oil through a heat exchanger submerged in the refrigerated bath, but it was determined that the pump heated the oil mixture significantly, leading to visible refractive index gradients
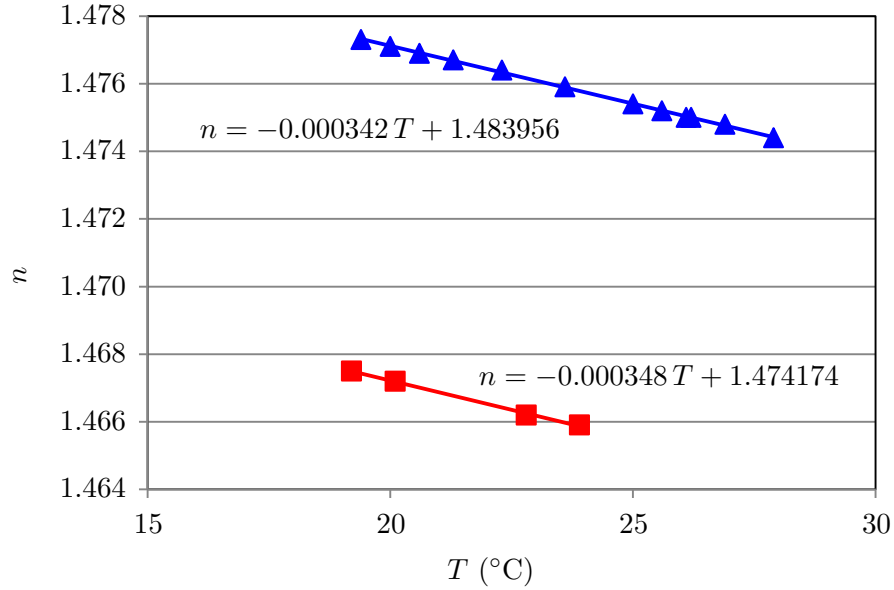
Figure 6.9: Index of refraction of McMaster-Carr mineral oils as a function of temperature. ▲ are data for heavy viscosity oil. ■ are data for light viscosity oil.

in the bath. Therefore, experiments were conducted at room temperature and the outer cylinder was allowed to rotate for several minutes to mix the oil before taking data. The temperature of the oil in the bath was monitored with an immersion thermometer and the outer cylinder rotation rate was adjusted to obtain the desired Reynolds number in the test section. All experiments were conducted between $23°C$ and $25°C$, which meant that the index of refraction of the mineral oil mixture varied by less than 0.001.

6.2.4.2 Refractive index matching using NH₄SCN solution

Because of the high viscosity of the mineral oil, it was not possible to rotate the outer cylinder fast enough to generate turbulence in the test section without generating significant mechanical noise. For this reason, a refractive index matching solution based on ammonium thiocyanate (NH_4SCN) was formulated. Ammonium thiocyanate solutions have previously been used as a refractive index-matching medium by several researchers [296–300]. NH_4SCN was chosen because its aqueous solutions have physical properties that are closer to those of water compared to other common refractive index matching solutions like aqueous sodium iodide solutions [301–303]. For example, whereas a sodium iodide solution with the index of refraction of borosilicate glass has a specific gravity of ∼1.7 and a kinematic viscosity of ∼2.5
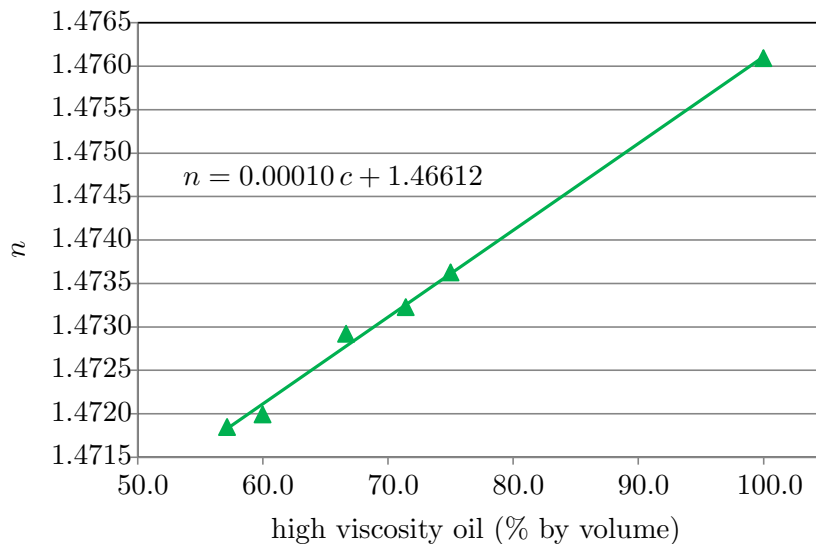
Figure 6.10: Index of refraction of mineral oil mixtures as a function of high viscosity oil volume fraction. The data have been compensated for variations in temperature of up to $1°C$ at the time of the data was taken by assuming a temperature coefficient of $3.45 \times 10^{-4}/°C$.

cSt [303], the equivalent NH_4SCN solution has a specific gravity of 1.13 and a kinematic viscosity of 1.41 cSt at $23°C$. Such a solution can be prepared by mixing 55.1% NH_4SCN by weight in water. Because the solvation process is endothermic, it is useful to gently heat the mixture as the the NH_4SCN dissolves. The kinematic viscosity for this solution was measured as a function of temperature using a No. 50 Cannon-Fenske routine viscometer. It was found this was well by a linear model given by $\nu(T) = 1.867 - 0.01967T$ cSt, where T is the fluid temperature in degrees Celsius. In this work ACS reagent grade ($\geq 97.5\%$ pure) NH_4SCN was used (product no. 221988, Sigma Aldrich, St. Louis, Missouri). This had some insoluble impurities that were filtered out using filter paper.

Care should be taken when using ammonium thiocyanate as a refractive index-matching fluid since it is mildly toxic. While NH_4SCN is compatible with most plastics and with glass, it can corrode exposed metals. Tests were run which showed that it is compatible with aluminum (both plain and anodized) and 316 stainless steel. Brass and bronze parts will blacken do not appear to be damaged beyond that. After long term exposure to brass, the solution becomes slightly blue/green. NH_4SCN solutions were found to quickly corrode plain steel and 304 multipurpose stainless steel. Contact with steel made the solutions turn a deep red.
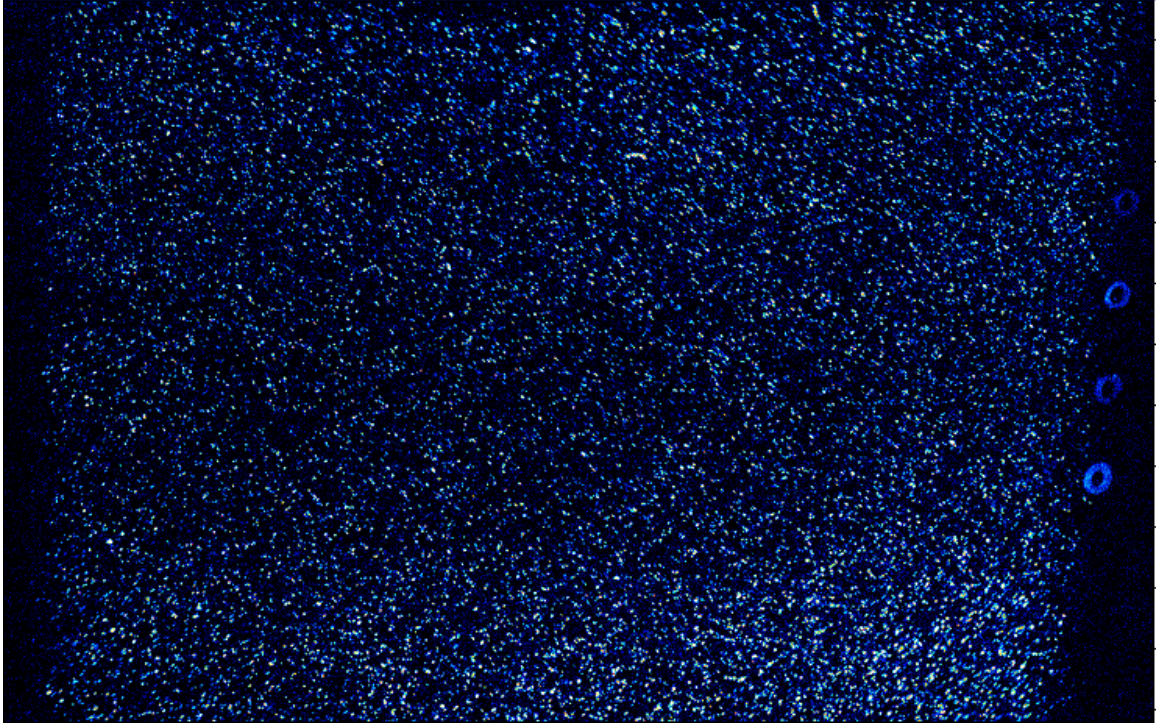
Figure 6.11: Typical raw image at 0.025 ppp displayed using the default color map in DaVis using a bit shift of 128. The ruby nozzles on the jets strongly fluoresce under the stray laser light, can be seen on the left edge of the image.

6.3   Experimental Procedure

6.3.1   Image Acquisition and Pre-Processing

The system was prepared by mixing particles into the working fluid until a particle density of about 0.025 particles per pixel (ppp) was achieved (see Figure 6.11). The number of particles in the images was estimated by detecting the number of intensity peaks in the images. This was done using the "Test 2D peak detection" button in the volume self-calibration menu in DaVis and setting the maximum number of possible particles to 10^6. While Elsinga et al. suggested a maximum particle density of 0.05 ppp in their original formulation of tomographic PIV [279], the seeding density of 0.025 ppp was chosen to account for the additional complexity of imaging through curved, moving walls introduced by Taylor-Couette flow, as proposed by Tokgoz et al. [282]. That being said, Michaelis et al. [304] have shown recently particle concentrations up to 0.10 ppp can be successfully reconstructed using the standard multiplicative algebraic reconstruction technique (MART),

so it may be possible to use increased particle densities to improve the spatial resolution of future measurements.

After the correct particle concentration was achieved, the temperature of the working fluid was measured using a mercury immersion thermometer. The syringes on the injection system were run back and forth so that they were primed with fluid at the same particle concentration and temperature as the test section. The outer cylinder was accelerated at 0.02 Hz/s^2 until $Re_o = 7750$. The wall speed was adjusted to compensate for the temperature dependence of the kinematic viscosity of the working fluid. Once the desired Reynolds number was achieved, the system was allowed to run for 2 minutes. Ideally, the system would be allowed to equilibrate for a longer time, but it was found that the Ekman circulation depleted the particles from the midplane of the flow, so 2 minutes ($\sim$ 2 viscous diffusion times across the gap) was used as a compromise.

At this point, a 50 ms push/pull perturbation with a volumetric flow rate of 50 mL/min was injected into the test section using the injection system described in Chapter 4. Image acquisition was externally triggered using the digital signal that switched the valves in the injection system. The cameras were configured so that they acquired 250 frames before the perturbation was triggered, which provided a sample of the laminar flow before the perturbation. Once the images were captured the were downloaded to a network attached storage unit (ReadyNAS 516, NETGEAR, San Jose, California) where they were stored for processing using the distributed computing cluster described in Appendix F.[7]

Because of the relatively low energy per pulse of the available Nd:YLF laser, the images were rather faint and most of the signal was captured in the least significant bits of the camera sensors. These bits are inherently noisier than more significant bits. In order improve the quality of the images before reconstruction, the images were pre-processed using DaVis's built-in image processing capabilities. Examples of the images before and after pre-processing are shown in Figure 6.12. A sliding minimum subtraction filter with a 5×5 pixel kernel was applied to accentuate the particles relative to the background. This

---

[7]Because image pre-processing is a relatively fast process that generates a lot of network traffic. This can lead to errors if more than 7-8 nodes are used for image pre-processing. This is not the case for more computationally intensive procedures like volume reconstruction and the calculation of velocity vectors.

<div align="center">(a)   (b)</div>
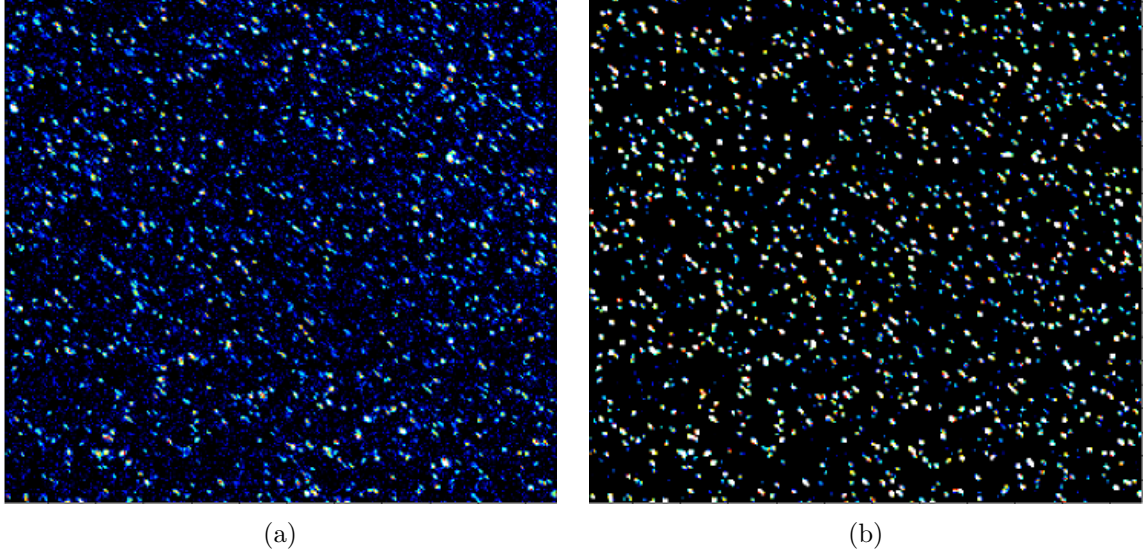
Figure 6.12: (a) A sub-region of a raw image displayed at 128 bit shift using DaVis's default color map. (b) The same sub-region after pre-processing displayed at 4k bit shift.

filter makes it so that dark (but non-zero intensity) regions within 5 pixels of a particle get zeroed out. In order to compensate for the lack of uniformity of the illumination and variations in intensity between different pulses, the images were normalized to local average over 20×20 pixel windows. Because the images were somewhat noisy due to the low light levels, the images were first smoothed with a 3×3 Gaussian filter and then resharpened. This effectively makes the individual particles peaks more uniform and blob like without significantly changing their size and improves their overlap during cross-correlation. In order to remove any remaining noise in the dark spaces between particles, 10 counts were subtracted from every pixel. In order to improve the dynamic range, the images were multiplied by a constant factor of 100. Finally, areas of the images that were outside of the illuminated volumes were masked out. Because there are no bright particles in these regions, the various filters result in significant noise in these regions, so it is important to exclude these from the reconstruction process.

6.3.2 Calibration

In order for tomographic reconstruction to work, a relationship M_i must be established between points $\boldsymbol{P} = (X, Y, Z)$ in physical space and their images $\boldsymbol{p}_i = (x_i, y_i)$ on the i

cameras (here $i \in [1, 2, 3, 4]$), such that

$$\boldsymbol{p}_i = M_i(\boldsymbol{P}). \tag{19}$$

The error in the mapping must be less than 0.4 pixels and preferably less than 0.1 pixels [279]. As in stereoscopic PIV [305], the mapping function can be estimated using images taken as a known template pattern is traversed through the measurement volume. These data are then fit to either a pinhole model (typically used for measurements in air) or a third order polynomial model (typically used in measurements in water) [306].

Attempts were made to use this technique by traversing a LaVision Micro Calibration Plate (part no. 1108939) across the measurement volume. This target consists of a glass slide with three dot patterns of different geometries printed on it. The medium sized target, which has a square grid of 0.12 mm dots spaced 0.5 mm apart, was cut out by the Glass Shop in the School of Chemistry and attached to a flat aluminum rod with epoxy. The target was then inserted into the test section through a slot that was cut into the top outer cylinder bearing support and traversed using a computer controlled micro-positioner (model no. ESP300, Newport Corporation, Irvine, CA). It was found that the constrained geometry of the test section made it difficult to accurately orient and move the calibration plate. The small size of the calibration plate also made it so that only the central 20 mm of the measurement volume could be calibrated.

In order make the calibration procedure more robust a three-dimensional calibration target was developed. This target, which is shown in Figure 6.13, was machined into the side of an aluminum end ring. The target consisted of two planes that that were offset by 0.794 mm. Each plane had a regular grid of dots spaced 3.175 mm apart. In order to ensure that there was sufficient contrast between the dots and the rest of the target, the aluminum was anodized flat black by Metal Finishers of Atlanta (Lilburn, Georgia) and the dots were made by breaking the anodizing with a 3/0 center drill exposing the bare aluminum below. The resulting holes had a diameter of 0.508 mm and were potted with bees' wax, so that they reflected light more uniformly. The three-dimensional target provided two calibration planes that virtually filled the field of view and provided over 100
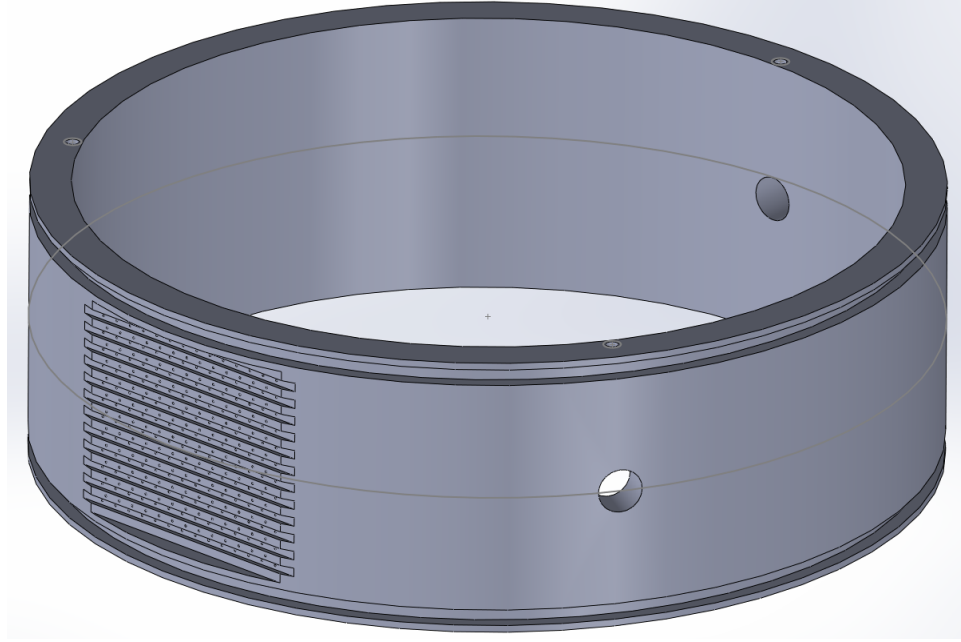
Figure 6.13: A three-dimensional calibration target was machined into the side of the top end ring. This consisted of two planes of dots separated by 0.794 mm, which were staggered relative to each other. The dots on each plane were on a square grid with 3.175 mm between dots. The center of the front plane was 4.039 mm from the inner cylinder.

reference points per plane. Detailed mechanical drawings and technical details about the design of the calibration target are provided in Appendix E.

The calibration target was illuminated with a halogen floodlight (McMaster-Carr part no. 1549K13) and set of calibration images was taken before each experimental run. It is useful to set the exposure to the maximum possible duration before taking the calibration. These were processed using LaVision's DaVis software. During the calibration process both the heat bath and the test section were filled with fluid. The calibration data was used to provide an initial guess for the mapping function, which was assumed to be a third order polynomial. The estimated calibration error (average deviation to mark) was typically less than 0.8 pixels. As mentioned earlier, calibration error greater than 0.4 pixels can lead to loss of accuracy during tomographic reconstruction. Furthermore, the mapping function needs to be correctly extrapolated away from the calibration planes in order to compensate for any distortion in the imaging optics.

In order to improve the calibration, the volume self-calibration procedure developed by

Wieneke [307] was employed. This technique attempts to locate individual particles by triangulation as in three-dimensional particle tracking. The residual triangulation error or *disparity* can then be used to correct the mapping function. In order to make this technique more robust, statistics of the disparity vectors for a large number of particles are gathered over different areas of the flow from different images. These are used iteratively to estimate the optimal correction for the mapping function. In the case of Taylor-Couette flow, special care needs to be taken during self-calibration because the sampled volume is not rectangular as in typical tomographic PIV experiments. Regions of the illuminated volume that do not have particles can be dominated by noise, which can lead to spurious disparity vectors. In order to minimize this effect, it is convenient to start with a small volume near the center of the test section and use only a relatively small number of particles to calculate disparity vectors for a small number of sub-volumes. The resulting disparity vector field should be judiciously filtered using the universal outlier detection and smoothed, so that the correction to the mapping function is smooth. It is much better to perform a few more iterations of self-calibration, than to mess up the calibration function with a discontinuous correction. Once the disparity level drops, the calibration volume can be expanded and more sub-volumes added. This procedure is repeated until satisfactory disparity levels are achieved throughout the measurement volume. For more information about the implementation of Wienecke's volume self-calibration method, the reader is referred to LaVision's FlowMaster Tomographic PIV User's Manual [308].

6.3.3 Volume Reconstruction

Since the introduction of tomographic PIV [279], significant efforts have gone into developing new algorithms to increase its accuracy and reduce its computational cost. As discussed earlier, tomographic PIV measurements require two main steps. First, the volume is reconstructed from a set of recorded images. Then, velocity fields are obtained by using cross-correlation of the volumes using standard PIV algorithms extended to three dimensions. While particle cross-correlation algorithms are well understood (see the books by Raffel et al. [240] and Adrian and Westerweel [226] for extensive reviews), reconstruction techniques

are still in their infancy and have been the focus of much recent research [279, 309–314]. While the mainstay of tomographic reconstruction has traditionally been the multiplicative algebraic reconstruction technique (MART), simultaneous MART (SMART) [311] has recently emerged as a much more efficient solution. Both of these algorithm are iterative procedure and much of the computational effort goes into the first couple of iterations. In order to speed up their convergence, it is useful to initialize the algorithm using a multiplicative line-of-sight reconstruction (MLOS). LaVision's has implemented SMART reconstruction with MLOS initialization in a procedure that they call FastMART.[8] This algorithm is tens of times faster than MART and ideal for processing time-series of tomographic PIV data.

6.3.3.1 Convergence of FastMART algorithm

Even though FastMART is much faster than MART, tomographic reconstruction is still very time consuming, with additional FastMART iterations improving the accuracy of the reconstruction but adding to the processing time. For this reason, the convergence rate of the FastMART algorithm as a function of the number of FastMART iterations was tested.[9] Since the real particle distribution in an experimental volume is unknown, a reference volume was created by reconstructing it using 40 FastMART iterations using DaVis's default settings. This many iterations would never be used in practice and it was assumed that the result of such a reconstruction converged as closely as possible to the real particle distribution. The same volume was then reconstructed with only 3 FastMART iterations. The results were compared by subtracting the two volumes voxel by voxel and then summing over the whole volume and normalizing the difference by the total intensity in the reference volume, i.e., the reconstruction quality[10]

---

[8]Formally, FastMART actually implements a proprietary algorithm called CSMART, which differs from SMART in the way that data from different cameras is incorporated into the reconstruction [315].

[9]Note that in general this depends on experimental conditions such as seeding density, background noise, etc. and should be tested independently for experimental configurations much different than the one described here

[10]Note: The definition of reconstruction quality used here is different from the commonly used definition introduced by Elsinga et al. [279].
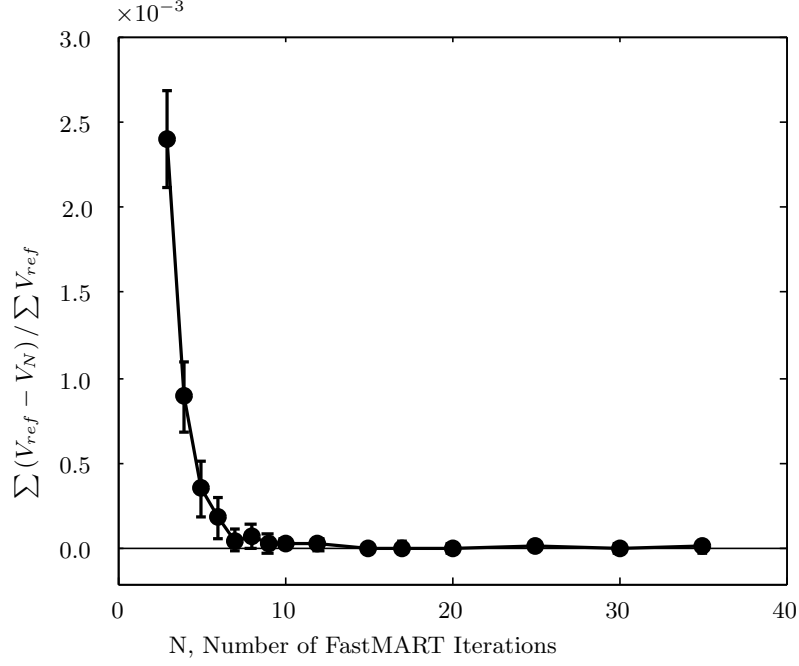
Figure 6.14: Reconstruction quality as a function of FastMART iterations averaged over 5 independent trials. Error bars show standard deviation of reconstruction quality between trials.

$$Q = \frac{\sum\limits_{X,Y,Z} V_{ref}\left(X,Y,Z\right) - V_N\left(X,Y,Z\right)}{\sum\limits_{X,Y,Z} V_{ref}\left(X,Y,Z\right).} \qquad (20)$$

The procedure was repeated for 5 different volumes for varying numbers of FastMART iterations. The results are summarized in Figure 6.14. It was found that for the seeding densities and imaging parameters used in this work, no significant gains in reconstruction quality are achieved by increasing the number of FastMART iterations beyond 15 iterations with only minor gains beyond 7. Considering that each additional FastMART iteration adds about an one hour of processing time on the distributed processing cluster for a full camera buffer (5478 sets of four images), 7 iterations was chosen as a good compromise between reconstruction quality and processing speed.

Once a set of images is converted into a volumetric intensity field, it is important to check the quality of the reconstruction. This can be done using the z-profile extraction tool in DaVis, although this can be deceiving because of the curved nature of the test section. A more convenient way to check the quality of the reconstruction is to generate a synthetic
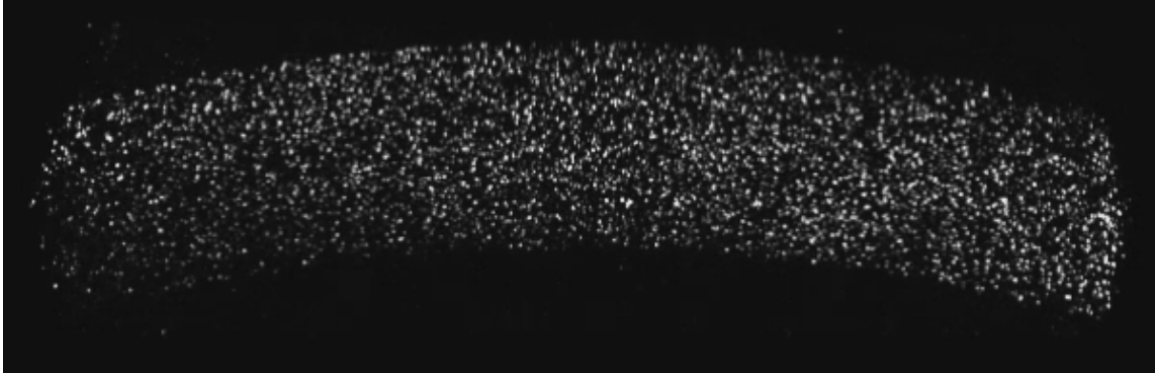
Figure 6.15: A synthetic view of the reconstructed volume looking down the axial direction. The inner and outer walls are clearly visible as interfaces where there is a sudden decrease in particle density.

view of the measurement volume that looks down along the axial direction through the volume. Figure 6.15 shows such a view. A poor reconstruction will have a significant number of particles outside of the curved test volume.

6.3.4 Particle Cross-Correlation

Once the time-series of images are reconstructed into a time-series of three-dimensional volumes, velocity vectors can be calculated by analyzing the changes in the particle distributions between successive volumes. Analogously to planar PIV, the volume is divided into a series of sub-volumes and the most likely displacement of the fluid in that volume is calculated by looking for the peak in the spatial cross-correlation function. In planar PIV, where the number of particles per pixel can be quite high, this is usually achieved most efficiently using spectral (Fast Fourier Transform-based) implementations of the cross-correlation function. However, in tomographic PIV, the number of particles per voxel is typically low and the resulting data structures can be quite sparse. In this case, a direct correlation of the volumetric data can be significantly more efficient.

This is typically done in an iterative multi-step fashion [226], where a smaller number of larger interrogation volumes is used to provide an initial estimate for the displacements and capture large scale motion, which is then refined using smaller interrogation volumes. Within a single step (fixed interrogation window size), a multi-pass approach can be used to improve the quality of the correlation by deforming the interrogation volumes to account for

Figure 6.16: Typical parameters for direct correlation.

the deformation of the fluid element being measured [316]. As with volume reconstruction, there is a trade off between the number of correlation steps and passes, which increase the accuracy of the measurement, and the computational time. Typical processing parameters used here are shown in Figure 6.16. For a detailed description of the various processing parameters, the reader is referred to LaVision's FlowMaster Tomographic PIV User's Guide [308] and to the book by Adrian and Westerweel [226].

6.4   Data Analysis

6.4.1   Locating the Measurement Volume

Typical implementations of tomographic PIV are designed to measure velocity components in a three-dimensional Cartesian coordinate system. This makes it challenging to interpret measurements in Taylor-Couette flow, which are more naturally expressed in cylindrical coordinates. Previous investigators have bypassed this complication by looking at data in the plane where the radial direction and the Cartesian axis through the measurement volume coincide [282] (see Figure 6.17). Alternatively, they have evaluated quantities like energy dissipation, which are invariant under coordinate transformations. However, in order to compare experimentally measured flow structures with numerical results, a coordinate transform must be established to convert between the Cartesian system of the flow measurements and the cylindrical coordinates used in simulations.
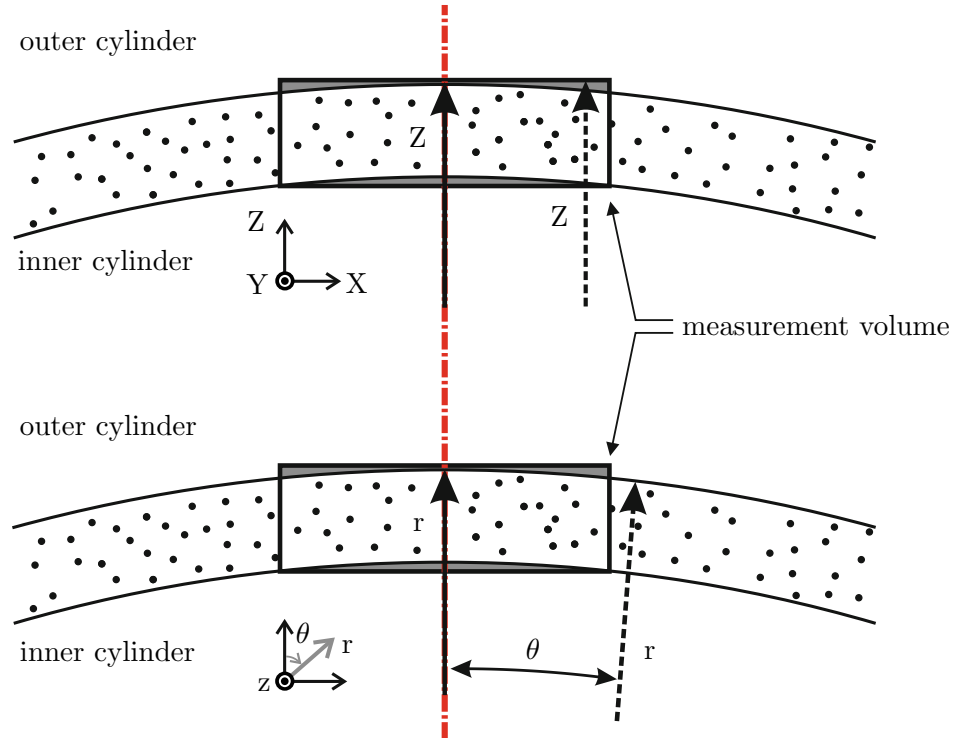
Figure 6.17: DaVis's tomographic PIV package is designed for rectangular measurement volumes and returns vector positions and components in a Cartesian coordinate system $(X.Y, Z)$. The Taylor-Couette problem is more naturally expressed in terms of cylindrical coordinates (r, θ, z). In order to transform data from one coordinate system to another, the location of the axis of symmetry must be determined. Adapted from S. Tokgoz et al. "Spatial resolution and dissipation rate estimation in Taylor-Couette flow for tomographic PIV," *Exp. Fluids* **53**, pp. 561-583, 2012. Copyright 2012 by Springer.
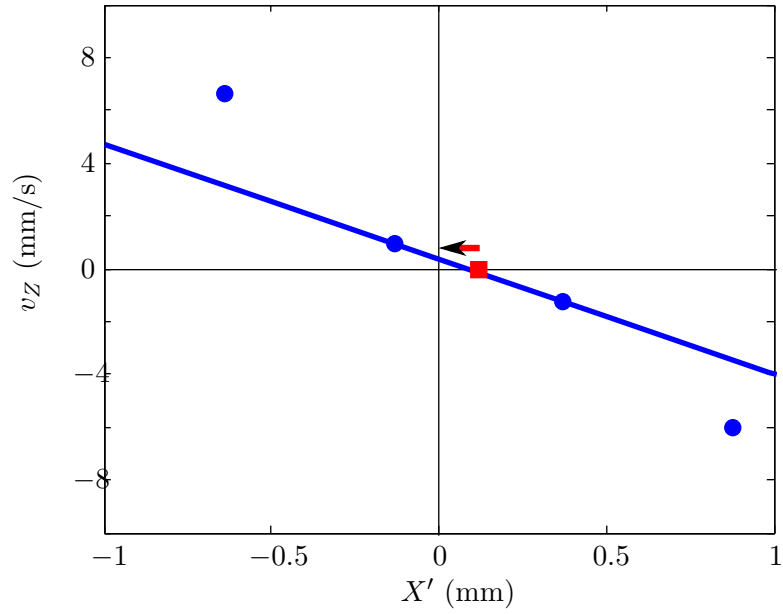
Figure 6.18: The PIV software originally return the velocity data in a Cartesian coordinate system (X', Y', Z') that is set by the initial calibration. The goal is to find a shift ΔX, which maps the data to a new coordinate system $X = X' + \Delta X, Y', Z'$, such that $v_Z(X = 0, Y, Z) = 0$. This can be done by plotting the data for v_Z (●) along a line of constant Y' and Z' as a function of X'. The data can be interpolated to find where the zero crossing (■). The distance between the zero crossing and $X' = 0$ (red arrow) gives an estimate for ΔX.

In principle this should be straightforward, but in practice it is complicated by the fact that the position of the symmetry axis relative to the measurement volume is only known approximately. A two-step method was devised to locate the measurement volume using the measurements of the axisymmetric laminar flow that were taken before the perturbation was injected. The first step established the shift along the X direction by which the experimental data must be shifted so that the $X = 0$ plane coincided with the $\theta = 0$ plane, as outlined in Figures 6.18 and 6.19. Once this shift was applied, the data for v_X as a function of Z in the $X = 0$ plane were compared to the data from the axisymmetric simulations discussed in Chapter 5. The numerical data were shifted in the Z direction by a small amount ΔZ and the norm of the difference between the two velocity fields was calculated. The minimum in the norm as a function of ΔZ provided and estimate of the optimal shift such that the $Z = 0$ plane was tangent to the inner cylinder. Theoretically, a similar approach could be taken with the Y coordinate. However, as discussed in Chapter 5, the base flow has very weak axial dependence except near the end caps, making it difficult to locate the measurement volume axially. Taking measurements of a flow with stronger axial dependence and/or larger axial or radial components such as Taylor vortex flow before or after taking other data would allow for such a calibration. Once the measurement volume is located, spurious vectors that fall outside of it but were not thrown out by the universal outlier detection filter can be masked out.

6.4.2 Post-processing Data for Analysis of Turbulent Structures

Even though the procedure outlined in the previous section provides a good way to locate the measurement volume and allows the flow to be broken down into components in cylindrical coordinates, visualizing turbulent structures can still be tricky. The turbulent intensity is only about 10%, meaning that turbulent structures are often obscured by the mean flow in raw vector fields. A natural solution to this problem would be to subtract the mean flow. However, because of the relatively short duration of the time series that can be taken given the memory limitations of the high-speed cameras and the spatiotemporally intermittent nature of the flows investigated here, averaging the data can sometimes
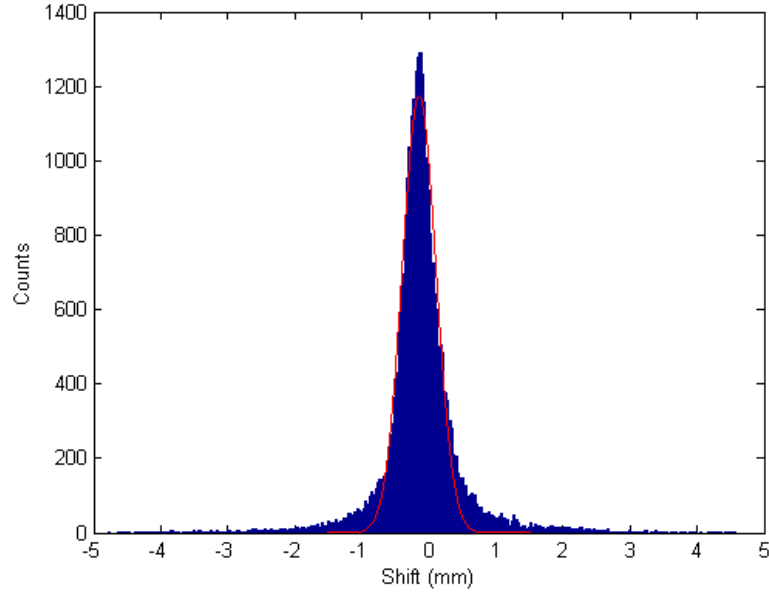
Figure 6.19: Because the PIV data is inherently noisy, an estimate of ΔX from a single line of data is not robust. In order to obtain a more robust estimate, the procedure outlined in Figure 6.18 was repeated for many lines at different values of Y' and Z' for data from 50 laminar velocity field. The resulting estimates for ΔX were histogrammed and the resulting distribution was fit with a Gaussian (red). The centroid of the Gaussian provides a more robust estimate for ΔX.

(a)

(b)
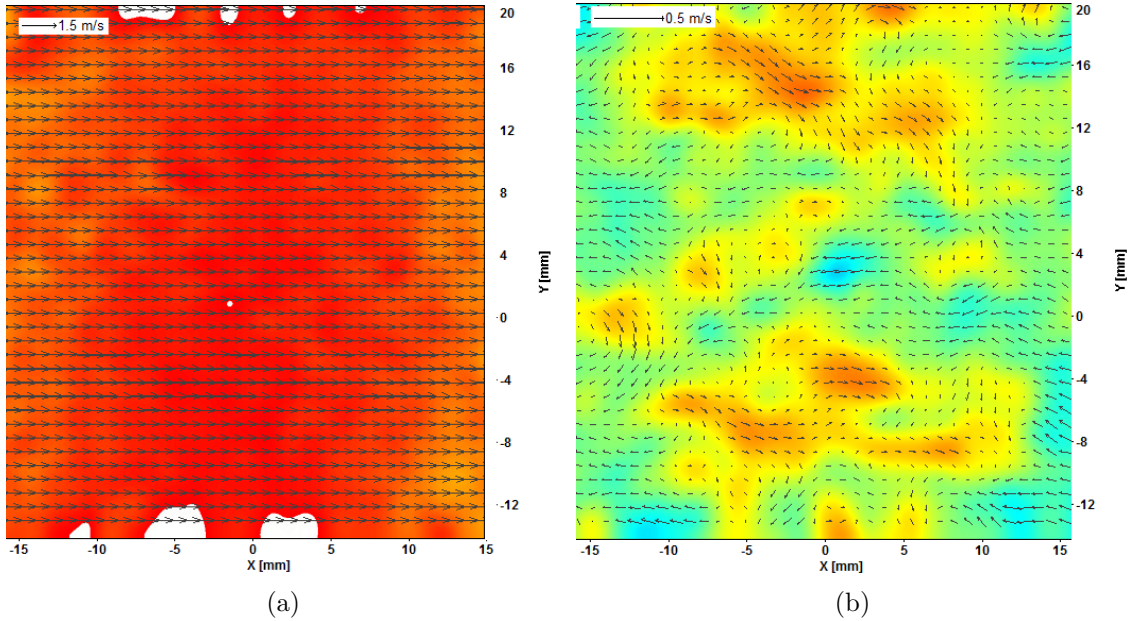
Figure 6.20: (a) Raw vector field at $Re_o = 7750$ in the $Z = 4.99$ mm plane. The color map represents the X component of velocity. No significant structure is evident. (b) After background subtraction and spatiotemporal filtering, the turbulent structures becomes apparent.

return somewhat non-uniform background fields. It was determined that a time-averaged measurement laminar flow, taken prior to the triggering of turbulence by a fluid injection, provided a more robust background.

It is also useful to exploit the coherence of the turbulent structures to eliminate noise in the measurements. Because the evolution of the turbulent structures is slow relative to the acquisition rate of the cameras, applying a running Gaussian filter of length 3 was used to smooth the data in time. Judicious use of a $3 \times 3 \times 3$ Gaussian spatial filter can also help provide a smoother data set while preserving local velocity gradients. The effect of this post-processing procedure is shown in Figure 6.20.

Another post-processing technique that is useful for extracting turbulent structures is to use point-wise vortex extraction criteria based on the eigenvalues of the velocity gradient tensor. These quantities become accessible because tomographic PIV allows all the components of the velocity gradient tensor to be measured directly. In this work it was found that Hunt et al.'s [317] Q-criterion provided the best visualization. For a discussion of other vortex identification schemes, the reader is referred to Section 9.5 of the book by Adrian and Westerweel [226]. The Galilean invariant Q is given by

$$Q = \frac{1}{2} \left(\frac{\partial u_i}{\partial x_i} \frac{\partial u_i}{\partial x_i} - \frac{\partial u_i}{\partial x_j} \frac{\partial u_j}{\partial x_i} \right) \tag{21}$$

where u_i is the velocity component along the x_i direction. The value of Q depends on the relative strength of rotational, antisymmetric part of the velocity gradient tensor to that of the symmetric, shearing part. Where Q is positive, rotation dominates over shear suggesting that a point is part of a vortex. Vortices can be visualized by looking at iso-surfaces of Q. Using the Q-criterion is useful because it can extract turbulent features even without background subtraction or transformation of the coordinate system. Figure 6.21 shows a visualization of Taylor rolls using the Q-criterion.

6.5   Preliminary Results

A series of tomographic PIV measurements of the growth of perturbations into persistent turbulent spots was begun in spring of 2014. Because the measurement volume cannot capture the entire flow, the following strategy was employed to capture the different phases
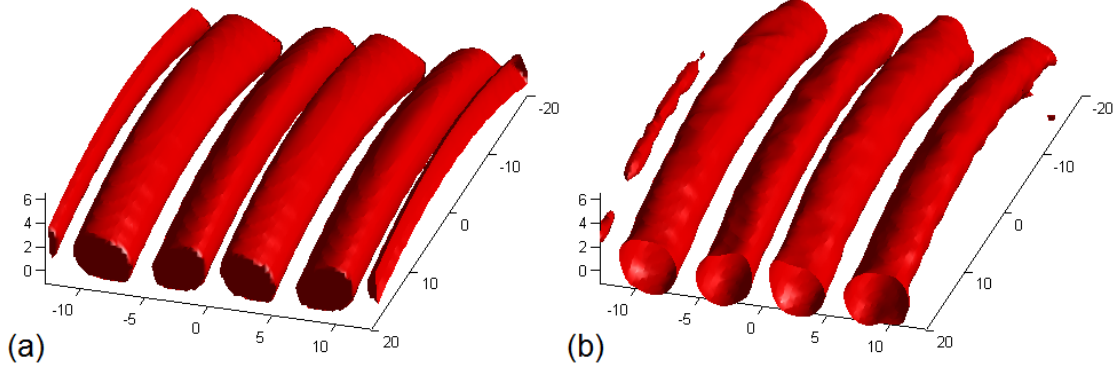
Figure 6.21: (a) $Q = 2 \times 10^{-5}$ iso-surface from numerical simulation of Taylor rolls at $(Re_i, Re_o) = (870, 0)$. (b) $Q = 2 \times 10^{-5}$ iso-surface from time average of 20 tomographic PIV measurements of Taylor rolls at $(Re_i, Re_o) = (870, 0)$. Numerical simulation courtesy of Michael Krygier.

of the spot's evolution: First, the jets were positioned just outside and upstream of the measurement volume. The system was prepared as outlined in Section 6.3.1. A set of calibration images using the three-dimensional calibration target were taken for reference. The outer cylinder was then slowly accelerated until $Re_o = 7750$. Once the desired Reynolds number was achieved a 50 mL/min push/pull perturbation with a duration of 50 ms was applied to the flow. Image acquisition was triggered with the same signal that switched the valves to provide a well-determined time stamp. The cameras were configured so that 250 frames consisting of laminar flow were captured pre-trigger so that the measurement volume could be located later. A small amount of Kalliroscope ($\sim 0.1\%$ by volume) was added to the working fluid (NH$_4$SCN-based refractive index matching solution) to verify that the flow became turbulent after the perturbation and not before. The Kalliroscope generated a slight shimmering as it scattered the incident laser light, but the density used was low enough so that it did not affect the fluorescence signal from the seeding particles. Once the whole camera buffer (5478 frames) had downloaded to the network attached storage unit, the inner cylinder was rotated so that the jets were moved upstream by 36° (about the same angular displacement covered the measurement volume) and the experiment was repeated. Overall, 9 angular positions were covered with three data sets taken at each location.

Although the perturbations were not repeatable in detail, the hope is that by varying the position of the jets the evolution of typical spots could be investigated. This work is

166

currently under way. Tomographic PIV generates huge amounts of data ($\sim 2 \times 10^5$ three-dimensional vectors per frame), so processing the acquired data set is a massive undertaking. To date this has generated over 14 terabytes of data, which are currently being evaluated. Figures 6.22 and 6.23 show examples of some of the types of analyses that can be conducted.

6.6 Summary

This chapter described the implementation of tomographic PIV measurements for the study of the turbulent structures that emerge during the subcritical transition to turbulence in Taylor-Couette flow. Taylor-Couette flow presents some special challenges that are not typically present in other tomographic PIV applications. The system has many moving parts and can be inherently noisy. For this reason, several steps where taken to mitigate mechanical vibration including modification the tilt mounts used to correct for distortion due to off-axis imaging and shutting down the cooling fans on the high-speed cameras. Performing tomographic PIV measurements in small gap Taylor-Couette apparatus also presents some challenges when it comes to calibration of the mapping function used for tomographic reconstruction. It was shown that this process can be simplified by using a three-dimensional target similar to those used in stereoscopic PIV and by extrapolating the mapping function using volume self-calibration. Distortions due to imaging through the curved glass surfaces can be corrected by using refractive index matching fluids. In particular, it was found that aqueous solutions of ammonium thiocyanate are particularly well-suited to tomographic PIV studies of mechanically-driven turbulence, since they allow for higher Reynolds numbers with lower mechanical forcing. Their density can also be well-matched by easy to make fluorescent particles, whose use provides significant advantages when imaging near walls or other interfaces. Work is currently underway to process a series of time-resolved tomographic PIV measurements. The scale of this project exceeds most published tomographic PIV studies by several orders of magnitude with several tens of thousands of frames of data already reconstructed.
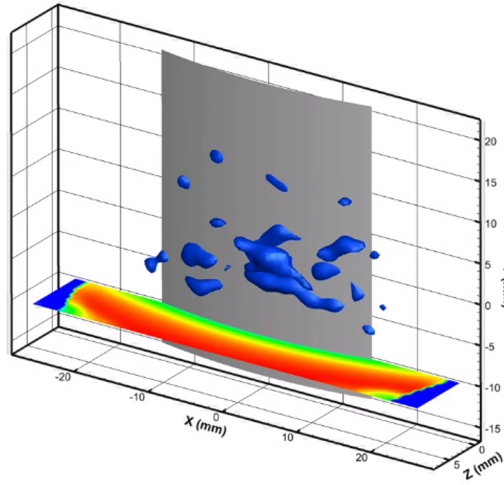
(a)
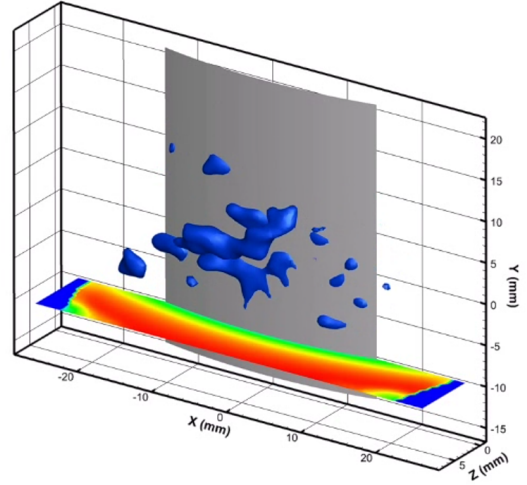
(b)
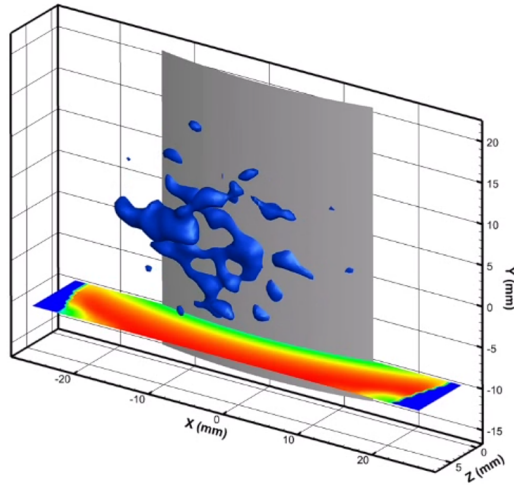
(c)
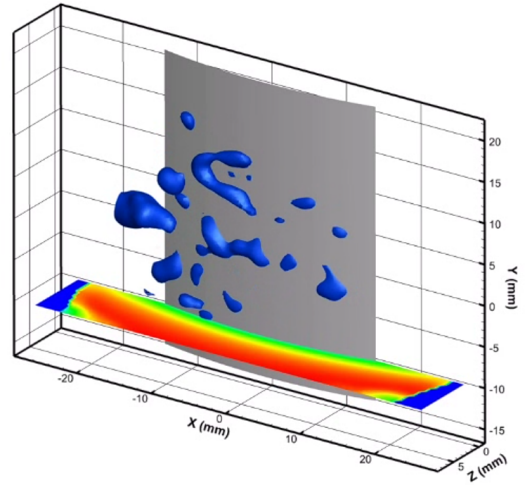
(d)

Figure 6.22: Vortical structures in a turbulent spot as they advect through the measurement volume (a)-(d). A horseshoe-like structure is visible in (d), which suggests that hairpin vortices may play a role in subcritical Taylor-Couette flow like they do in other near-wall turbulence.
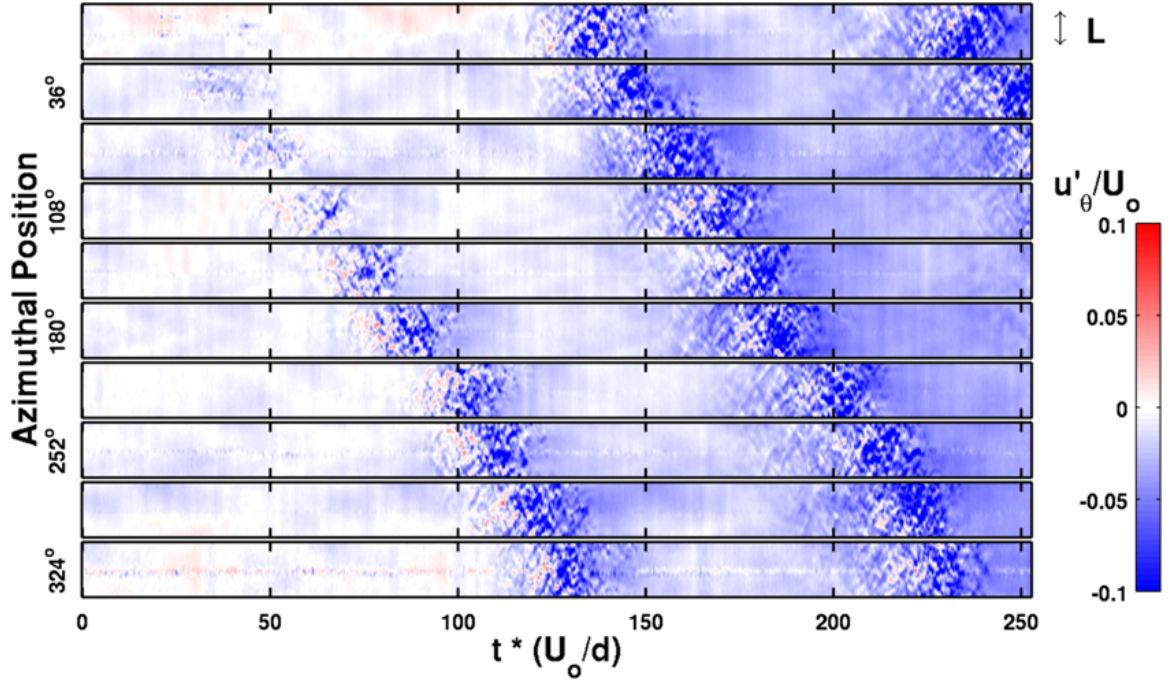
Figure 6.23: Because the turbulent structures evolve relatively slowly, they only change slightly as they are advected through the measurement volume. The spatial structure can be constructed by extracting a velocity measurement at a particular plane or line (in this case a line extending axial in the middle of the gap in the $X = 0$ plane) and creating a space-time diagram [318]. Here, turbulent intensity of the azimuthal component of velocity shows the growth of the spot as it circles around the test section and comes back around through the measurement volume.

CHAPTER VII

CLOSING REMARKS

7.1 Summary

The research presented in this dissertation is a first step toward understanding the transition to turbulence in linearly stable Taylor-Couette flows. The stability of this flow was probed using a variety of experimental techniques to elucidate different aspects of the transition mechanisms. It was shown that in this important, yet frequently ignored regime, Taylor-Couette flow shares many of the features of other linearly stable shear flows that have dominated recent discussions about subcritical transitions to turbulence. While some of these flows are perhaps more computationally and theoretically tractable than the Taylor-Couette problem (or at the very least do not include the additional complication of rotation), none of these is as robust an experimental platform as Taylor-Couette flow. It is hoped that the work presented here will convince future researchers that the Taylor-Couette system can be as useful a tool in the study of the subcritical transition to turbulence, as it was in the study of supercritical transitions to turbulence in previous decades.

After an extensive review of the scattered literature concerning linearly stable Taylor-Couette flows, it was shown that when only the outer cylinder rotates, metastable turbulent states can be reached by applying finite-amplitude perturbation to the flow in the form of sudden counter rotation of the inner cylinder. At fixed outer Reynolds number Re_o, the survival probability of these turbulent transients decays exponentially with a characteristic lifetime τ that depends on Re_o, independently of how the turbulent state is first generated. From the standpoint of dynamical systems, this suggests that the turbulent dynamics in this regime are guided by a strange saddle. It was determined that τ increases very quickly with Re_o, so that a change in Re_o of less than a factor of two leads to an increase of τ by about five orders of magnitude. However, the data suggest that even though the growth of τ with Re_o is faster than exponential, it appears to be bounded. This implies

that the turbulent dynamics remain dynamically connected to the laminar state, which opens up the possibility of controlling the transition to turbulence using small control signals. Additional experiments were conducted to probe the dependence of τ on boundary conditions. While qualitatively, these data suggest that τ becomes smaller as the system size becomes decreases, the relationship between boundary conditions and the lifetimes of turbulent transient is non-trivial.

The first set of experiments reported here showed that finite-amplitude perturbations to linearly stable Taylor-Couette flow can lead to long-lived turbulent episodes. However, they did not address the issue of how large a perturbation must be in order to trigger turbulence. This question was addressed in a second set of experiments that perturbed the flow using controlled injections of fluid into the test section through holes on the inner cylinder wall. It was determined that there exists a minimum Reynolds number below which turbulence could not be initiated independent of the strength $\mathcal{A}$ of the perturbation. Above this threshold, the strength of the perturbation required to trigger turbulence decreased with increasing Re_o. The critical amplitude $\mathcal{A}_c$ was observed to scale as a power law with increasing Reynolds number with a critical exponents of approximately -2. Because this value is smaller than -1, it suggests that non-normal amplification plays a role in the growth of perturbations into persistent turbulent spots. One interesting aspect of these experiments is that they showed that the minimum perturbation required to trigger turbulence in linearly stable Taylor-Couette flow is much larger than that observed in other shear flows, which may be a result of the stabilizing effects of rotation.

Simple axisymmetric simulations of laminar flows were carried out to obtain a baseline to calibrate tomographic PIV measurements of Taylor-Couette flow. These were carried out using the commercial computational fluid dynamics package Fluent and should be easy to repeat by future researchers studying other flow regimes. In particular, the simulations showed that certain linearly stable, counter-rotating regimes might be more suitable for tomographic PIV investigations than those with only outer cylinder rotation, which was used here. While not shown here, these simulations can also be used to quickly ($\mathcal{O}\,(5\text{minutes})$) obtain other axisymmetric flows such as Taylor vortices, which can be useful calibration

flows.

Finally, the implementation of tomographic PIV in the Taylor-Couette geometry was discussed in detail. Many technical aspects were discussed including issues that arise during data acquisition and imaging. Other useful data was provided regarding the fabrication of fluorescent particles and refractive index-matching solutions. Detailed explanations of the many steps required to obtain useful velocimetry data were provided and challenges specific to Taylor-Couette flow were discussed. Some of the analysis methods currently being used to study volumetric velocimetry data were discussed and examples were given of how they might be used to study the growth of turbulent spots from localized perturbations.

7.2   Original Contributions

Original contributions presented in this dissertation include:

- The first measurements of the statistics of the lifetimes of turbulent super-transients in Taylor-Couette flow. It was shown that for long times, the lifetimes are exponentially distributed as has been observed in other canonical shear flows like pipe flow and plane Couette flow. This work suggests that Taylor-Couette flow, with its well-known robustness as a platform for precision experimental work, may be ideally suited to study the subcritical transition to turbulence.

- The first measurement of the scaling of transient lifetimes with Reynolds number. These were observed to grow super-exponentially but remain bounded at finite Reynolds number, at least for the range of Reynolds number studied. The data scale approximately as $\exp(\exp(aRe_o + b))$, in agreement with theoretical predictions based on extremal statistics theory.

- The first systematic study of finite-amplitude thresholds for the subcritical transition to turbulence in Taylor-Couette flow. An estimate of the minimal Reynolds number where turbulence can persist was provided and the amplitude of the minimum perturbation size was shown to scale as a power law in Re_o with a critical exponent of approximately -2.

- A systematic study of the effects of system size on transient lifetimes. It was concluded that in smaller systems, turbulence is less persistent, consistent with ideas linking the transition to turbulence to directed percolation problems and the transition to chaos via spatiotemporal intermittency.

- The first study of the effects of rotation the lifetimes of turbulent transients. By using weak co-/counter-rotating flows, it was shown that rotation plays an important role in the subcritical transition to turbulence. Changes in the shear Reynolds number Re_s due to differential rotation of the two cylinders were shown to have a stronger effect on turbulent lifetimes than than changes in Re_s due to changes in the outer cylinder wall speed in experiments where the inner cylinder was held fixed.

- Performed tomographic PIV measurements of the growth of a localized perturbation into a turbulent spot.

- Perfomed volumetric velocity field measurements of various Taylor-Couette flows and validated them against numerical simulations showing generally good agreement.

- Compiled a comprehensive review of the literature concerning the subcritical transition to turbulence in Taylor-Couette flow spanning the entire history of the problem. This in-depth review should prove useful to researchers as they formulate new questions about this traditionally overlooked problem.

- Adapted the tomographic PIV technique in order to overcome the challenges presented for this type of measurement by the Taylor-Couette geometry. These include imaging through and near curved, moving walls and mechanical noise.

- The design and fabrication of a perturbation system, including a specially designed inner cylinder, high-speed valve system, and modified syringe pump, which allowed the perturbation of Taylor-Couette flow via injection/withdrawal of fluid from the test section.

- Developed a method for turning off the on-board fans in the Phantom v210 cameras for use in applications were vibration needs to be minimized.

- The development and fabrication of a custom three-dimensional calibration target for tomographic PIV measurements in the Taylor-Couette geometry. This target greatly improves the quality of the calibration and expands the size of the measurement volume that can be calibrated, as well as making the calibration operation significantly faster and easier.

- Development of refractive index matching fluids to alleviate optical distortion while imaging through the curved interfaces of the Taylor-Couette system. Ammonium thiocyanate solutions were shown to be ideally suited to perform time-resolved tomographic PIV measurements since their relatively low viscosity allowed for higher Reynolds numbers to be reached at lower flow speeds.

- A prediction from numerical simulations of circular Couette flow in finite-size Taylor-Couette geometries that counter-rotating flows may be better suited to tomographic PIV measurements due to the smaller velocity gradients present in those flows.

- Developed a method for locating measurement volume relative to the natural cylindrical coordinate system of the Taylor-Couette geometry using laminar flow measurements. The method is robust to measurement noise and makes possible the comparison of velocity fields from numerical simulations and experiments.

LIFETIME DATA FOR TRANSIENT TURBULENCE

Table 1: Experimental Runs at $\Gamma = 33.6$

Run	Re_o	Re_i	# of trials	τ	σ_τ	Notes
1	5505	0	1200	6.27×10^1	1.91×10^0	
2	5964	0	600	9.05×10^1	1.76×10^0	
3	6423	0	300	2.27×10^2	9.49×10^0	
4	6882	0	300	1.23×10^3	4.21×10^1	
5	7111	0	300	1.72×10^3	5.50×10^1	
6	7341	0	300	2.83×10^3	6.82×10^1	
7	7647	0	300	6.19×10^3	1.07×10^2	
8	7800	0	300	1.17×10^4	1.34×10^2	
9	8106	0	300	2.23×10^4	5.08×10^2	
10	8258	0	300	4.87×10^4	9.31×10^2	
11	8564	0	200	2.77×10^5	6.58×10^3	Max. observation time = 1.5 hr
12	8870	0	200	7.37×10^5	6.26×10^4	Max. observation time = 3 hrs
13	9176	0	200	1.99×10^6	3.86×10^5	Max. observation time = 6 hrs
14	7647	-132.6	208	5.30×10^4	7.54×10^2	
15	7647	-66.3	300	1.76×10^4	3.50×10^2	
16	7647	-33.1	300	9.39×10^3	1.98×10^2	
17	7647	0	300	6.52×10^3	3.34×10^1	Co-rotating perturbation
18	7647	33.1	200	4.94×10^3	4.11×10^1	Co-rotating perturbation
19	7647	66.3	200	3.17×10^3	5.01×10^1	Co-rotating perturbation
20	7647	0	300	2.76×10^3	9.98×10^1	Free surface at top boundary
21	7800	0	300	3.14×10^3	5.99×10^1	Free surface at top boundary
22	8106	0	300	3.29×10^3	4.59×10^1	Free surface at top boundary
23	7647	0	300			Re_o reduced to 6882 after 60 s

Table 2: Experimental Runs at $\Gamma = 23$

Run	Re_o	Re_i	# of trials	τ	σ_τ	Notes
1	6423	0	300	2.20×10^2	7.70×10^0	Co-rotating perturbation
2	6882	0	300	8.10×10^2	5.59×10^0	Co-rotating perturbation
3	7341	0	300	2.76×10^3	3.36×10^1	Co-rotating perturbation
4	7647	0	900	6.10×10^3	1.59×10^2	Co-rotating perturbation
5	7800	0	300	9.15×10^3	5.66×10^1	Co-rotating perturbation
6	8106	0	297	1.55×10^4	1.39×10^2	Co-rotating perturbation
7	8564	0	300	6.14×10^4	3.05×10^3	Co-rotating perturbation

Table 3: Experimental Runs at $\Gamma = 15$

Run	Re_o	Re_i	# of trials	τ	σ_τ	Notes
1	6882	0	300	3.03×10^2	5.87×10^0	Co-rotating perturbation
2	7341	0	900	1.41×10^3	1.22×10^1	Co-rotating perturbation
3	7647	0	300	2.84×10^3	2.25×10^1	Co-rotating perturbation
4	7800	0	300	5.20×10^3	8.59×10^1	
5	8106	0	300	1.39×10^4	1.25×10^2	Co-rotating perturbation
6	8258	0	122	2.24×10^4	9.88×10^2	
7	8564	0	300	5.09×10^4	2.37×10^2	Co-rotating perturbation

Table 4: Experimental Runs at $Re_o = 7647$ for Variable Aspect Ratio.

Run	Re_o	Γ	# of trials	τ	σ_τ	Notes
1	7647	15.0	300	2.84×10^3	1.14×10^1	Co-rotating perturbation
2	7647	18.1	900	4.88×10^3	2.16×10^1	Co-rotating perturbation
3	7647	23.3	300	6.01×10^3	3.84×10^1	Co-rotating perturbation
4	7647	33.6	300	6.42×10^3	5.56×10^1	
5	7647	36.9	300	6.79×10^3	6.69×10^1	Co-rotating perturbation

APPENDIX B

MATLAB CODES

B.1   wintvimaq.m: Image Acquisition Using WinTV Cards

This function is an example of several similar codes that were used to acquire images for the work described in Chapter 3. It uses Matlab's Image Acquisition Toolbox to interface with a WinTV television tuner card, which is used as a frame grabber. The code captures `N` frames from an NTSC video stream using a Matlab `videoinput` object. Frames are captured at `fps` frames per second.[1] Because the output of the Sony XC-77 camera (see Section 3.2.3) is monochrome, frames are flattened from the three color channels in the NTSC standard to a single 8-bit `grayscale` channel. This saves hard drive space and makes it faster to process frames in realtime.

Frames are continuously logged to memory. For every `fpf` frames that are acquired the subfunction `FrameSave` is called. FrameSave pulls `fpf` frames from the beginning of the buffer and writes them to disk as a single .mat file along with their time stamps, clearing room in the buffer for new frames. While this example only writes frames to disk, additional "realtime" processing could be done on the frames within FrameSave before saving them. In fact, this is how turbulent transients were monitored (see Section 3.3 for details). The result is a series of sequentially numbered .mat files that each contain `fpf` frames.

The video decoding on the WinTV 44801 is performed by Conexant's Fusion 878A PCI interface chipset. Because production of the Fusion 878A stopped in the early 2000's, drivers are only available for Microsoft operating systems up to Windows XP. Linux drivers exist but multiple hardware/software conflicts are reported online. At the time that these experiments were carried out, Matlab's Image Acquisition Toolbox was not supported on Linux systems, so no attempts were made to use WinTV cards in Linux. However, Linux may provide an avenue for continued use of legacy 878A-based WinTV cards.

---

[1]Only integer fractions of 30 are allowable frame rates (i.e. 15, 10, 7.5, 6, etc.).

```matlab
function wintvimaq(N)

    global fpf fps % Make variables that will pass to FrameSave global

    % Clean up any image acquisition that may have stayed open
    try, delete(imaqfind), catch, end

    % Set acquisition parameters
    fps = 30; % Frame rate in frames per second
    fpf = 5; % Frames to be saved per .mat file

    % Create and configure video input and set resolution
    vi1 = videoinput('winvideo',1,'RGB555_320x240');
    vi1.FrameGrabInterval = floor(30/fps); % Set frame rate
    vi1.ReturnedColorSpace = 'grayscale'; % Flatten signal to grayscale
    vi1.SelectedSourceName = 'composite'; % Set correct input mode
    set(vi1,'FramesPerTrigger',N,'LoggingMode','memory');

    % After fpf frames are acquired save them to a .mat file w/ FrameSave
    set(vi1,'FramesAcquiredFcn',@FrameSave,'FramesAcquiredFcnCount',fpf);

    % Initialize counter for filenames
    vi1.UserData = 1;

    % Take three pictures (prevents over-saturated images when the video
    % stream is first started)
    g = getsnapshot(vi1); g = getsnapshot(vi1); g = getsnapshot(vi1);

    start(vi1); % Start video stream
    wait(vi1,N/fps); % Wait until N frames have been captured
    stop(vi1) %Stop video stream
    clear global fpf fps, delete(vi1), end % Clear workspace
end

% Saves fpf frames to a file called "vi1.UserData".mat
function FrameSave(vi1,event)

    global fpf fps

    % Get data from video input object
    [data,time] = getdata(vi1,vi1.FramesAcquiredFcnCount);

    filename = ['file',num2str(vi1.UserData),'.mat']; % Set filename
    % -v6 option speeds up save process to help prevent buffer overflow
    save(filename,'data','time','-v6'); % Save fpf frames to .mat file
    vi1.UserData = vi1.UserData + 1; % Update counter for next filename
end
```

B.2 *indexercmd.m: Controlling Compumotor Indexers Using RS-232*

This function is an example of how to control a Compumotor model 2100 indexer using Matlab's Instrument Control Toolbox. It uses a Matlab `serial` object to send commands to the indexer using the RS-232 serial communications interface. The computer and the indexer must be connected via a *null modem* serial cable. While the indexer has a DB-25 connector, most modern computers use DE-9 connectors for serial communications. However, only a few pins are actually used to set up the RS-232 interface, so the use of standard 25-pin to 9-pin adapters is acceptable.

`indexercmd.m` is an example of the code that was used to perturb laminar flow with a sudden rotation of the inner cylinder in the experiments described in Chapter 3. It starts by creating a `serial` object called `s`. Most of the default settings for `serial` objects (baud rate of 9600 bps, 8 data bits, 1 stop bit, no parity bit, and no flow control) are compatible with the indexer. The only major exception is the `Terminator` character, which is used to signal the end of a command. The indexer uses the space character, which has an ASCII code of `32`. Once `s` is configured, serial communications are opened using `fopen`. A command sequence `pulse` is assembled using `sprintf`. In this case it would read:

```
E MN D400000 A60 V10 G
```

Here `E` enables remote operation of the indexer and disables front panel operation. `MN` sets the indexer to "preset" mode, which means that the motor will rotate by a preset number of steps. In this example, the motor will ramp up to a maximum rotation rate of 10 Hz (set by `V10`) at an angular acceleration of 60 Hz/s^2 (set by `A60`), continue at 10 Hz, and then decelerate at 60 Hz/s^2 until it stops. The total angular displacement will be 400,000 steps (set by `D400000`) and the resulting motion will have a trapezoidal velocity profile. The command `G` tells the indexer to execute the previous list of commands (i.e., the motor will not actually start until it receives a `G` command). The command sequence is sent to the indexer using the `fprintf` Matlab command. Once the command sequence is sent an additional command (`F`) is sent to return control to the front panel and serial communications are closed by closing `s` using `fclose`. Note that the indexer executes

commands serially, so the F command will not prevent any of the previous commands from executing.

While the example used here is very simple, the indexer features an extensive command language that allows the programming of significantly more complex motions. One useful variation of the code shown here is to replace the MN command with MC. This sets the indexer to "continuous" mode meaning that it will ramp up to the maximum velocity and continue rotating at that speed. In this case, the D400000 command is extraneous. Additional commands, including those used to trigger the execution of a command sequence based on external trigger signals, are discussed in detail in the *Compumotor Model 2100 Indexer User Guide* [161]. This also documents troubleshooting procedures for serial communications and describes the function of a series of internal switches that alter the operation of the indexer.

```
function indexercmd

    % Clean up any serial connections that stayed open
    try, fclose(instrfind), catch, end

    % Create and open serial connection with indexer
    s = serial('COM1');
    s.Terminator = 32; % set terminator character to "space" (ASCII 32)
    fopen(s)

    % Set perturbation parameters
    delay = 10; % Set delay (in seconds) before perturbation is initiated
    accel = 60; % Acceleration rate in rev/s/s
    vel = 10; % Maximum angular velocity in rev/s
    dis = 400000; % Number of steps to take 25000 steps = 1 rev

    % Create perturbation command string with perturbation parameters
    pulse = sprintf('E MN A%d V%d D%d G',accel,vel,dis);
    pause(delay), fprintf(s,pulse) % Send perturbation command to indexer.

    % Close serial connection to indexer
    fprintf(s,'F') % Return control to front panel
    fclose(s)
end
```

B.3 *measuretemp.m: Temperature Measurements Using HP 34401A Multimeter and Minco S1059PA5X6 Platinum Resistance Thermometer*

This function is an example of how to import resistance measurements from the Hewlett-Packard HP 33401A multimeter into Matlab using the RS-232 serial communications interface. This was used together with the Minco S1059PA5X6 platinum resistance thermometer (PTD) to monitor the temperature of the heat bath.

`measuretemp.m` creates a Matlab `serial` object called `m`, which has the appropriate settings to communicated with the HP 33401A. The configuration of the RS-232 interface on the HP 33401A can be modified from the system menu and its settings must agree with those used to initialize `m`. The HP 33401A is configured to take `10` measurements close to `150` Ω with a precision of `0.3` % (the HP 33401A will automatically set the range to achieve the desired accuracy up to 6 1/2 digits) with `1` second between measurements. These measurements are averaged and converted to temperature measurements using a polynomial interpolating function provided by Minco for the PTD's temperature vs. resistance curve, which is implemented in the subfunction `RtoT`.

The HP 34401 can be configured for a variety of automated measurements. Details are provided in the *Hewlett-Packard HP 34401A Multimeter User's Guide* [319]. The calibration data for the platinum resistance thermometer can be found in *Calibration Report No. 2789* from Minco Products [162].

181

```
function temp = measuretemp;

    % Close any serial objects accidentally left open
    try, fclose(instrfind), catch, end

    % Configure and open serial communication with HP 33401A
    m = serial('COM4','BaudRate', 1200, 'StopBits',2,'Parity','none',...
            'DataBits',8);
    m.InputBufferSize = 32768;
    fopen(m);

    % Configure HP 33401A for remote operation
    fprintf(m,'*RST'); pause(1)
    fprintf(m,'SYSTEM:REMOTE');

    % Configure resistance measurements of ~ 150 Ohms with
    % 0.3 % accuracy (range automatically selected by HP 33401A)
    fprintf(m,'CONFIGURE:RESISTANCE 150,0.3');
    fprintf(m,'TRIGGER:SOURCE IMMEDIATE'); % Set immediate triggering
    fprintf(m,'SAMPLE:COUNT 10'); % Set 10 measurements per trigger
    fprintf(m,'TRIGGER:DELAY 1'); % Measurements are taken 1 second apart

    % Trigger resistance measurements and import into Matlab
    fprintf(m,':READ?');
    pause(12)
    R = fscanf(m);
    % Parse comma delimited string into doubles
    resistance = str2double(strread(R,'%s','delimiter',','));
    data = mean(resistance); % Take mean resistance reading

    % Close serial communications with the multimeter
    fclose(m); delete(m); clear m;

    % Convert resistance measurement to temperature
    temp = RtoT(data)

end

% Converts resistance to temperature using Minco interpolating function
function T = RtoT(R)
    W = R/100.1224;
    Wref = W + 1.2221536e-4*(W-1) + 3.1997114e-4*(W-1)^2;
    D = [439.932854 472.418020 37.684494 7.472018 2.920828 0.005184...
        -0.963864 -0.188732 0.191203 0.049025];
    T = 0; % Temperature in Celsius, set to 273.15 if needed in Kelvin
    for i = 1:10, T = T + D(i)*((Wref - 2.64)/1.64)^(i-1); end
end
```

B.4 perturb.m: Control Program for Injection System

This function controls the injection system that runs the jets used for finite-amplitude perturbations used in the experiments of Chapters 4 and 6. It uses Matlab's Instrument Control Toolbox to implement the RS-232 serial communications interface to communicate with the Harvard Apparatus 55-2222 syringe pump. It also uses the Data Acquisition Toolbox to interface with a Measurement Computing USB-1208FS data acquisition module,[2] which provides digital I/O signals that control high speed solenoid valves. This can also be used to trigger the cameras used in tomographic PIV measurements.

`perturb.m` takes three inputs. `PulseDuration` is the duration of the perturbation in seconds.[3] `FlowRate` is the flow rate from a single syringe in mL/min. This example assumes that 140 mL Kendall Monoject syringes (Covidien AG, Mansfield, Massachusetts) with a `37.5` mm bore are being used (Fisher Scientific part no. 22-257-152). `PumpDirection` takes a value of `+/-1` and controls the direction of the pusher block on the syringe pump.

`perturb.m` first creates a digital I/O object called `DIO` with two channels called `trigger` and `valve`. It then creates a serial I/O object called `s1`, which is used to configure the syringe pump. A brief TTL pulse is then sent on `trigger`. When this is connected to the "Trigger" input on the Trigger port of LaVision's High-Speed Controller, it can be used to start the cameras' data acquisition. For this to work, external triggering must be enabled within DaVis. `perturb.m` then starts running the syringe pump, which initially injects/withdraws fluid from a reservoir. After waiting for `2` seconds to let the syringe pump come up to speed, it sends a TTL high to the circuit that drives the solenoid valves. This switches the valves so that the fluid being injected/withdrawn by the syringes now flows to/from the jets on the inner cylinder. The driver circuit and its operation are described in Figure B.1. After waiting for the desired `PulseDuration`, it switches the valves back, and stops the pump. Control is then returned to the front panel of the syringe pump and `DIO` and `s1` are closed to release the hardware so it can be used by other programs.

---

[2]Measurement Computing's data acquistion hardware is only supported in 32-bit installations of Matlab.
[3]In this implementation, timing is handled in software using Matlab's `pause` command. This is only accurate up to a couple of milliseconds. More accurate timing can be achieved using a microcontroller like an Arduino.
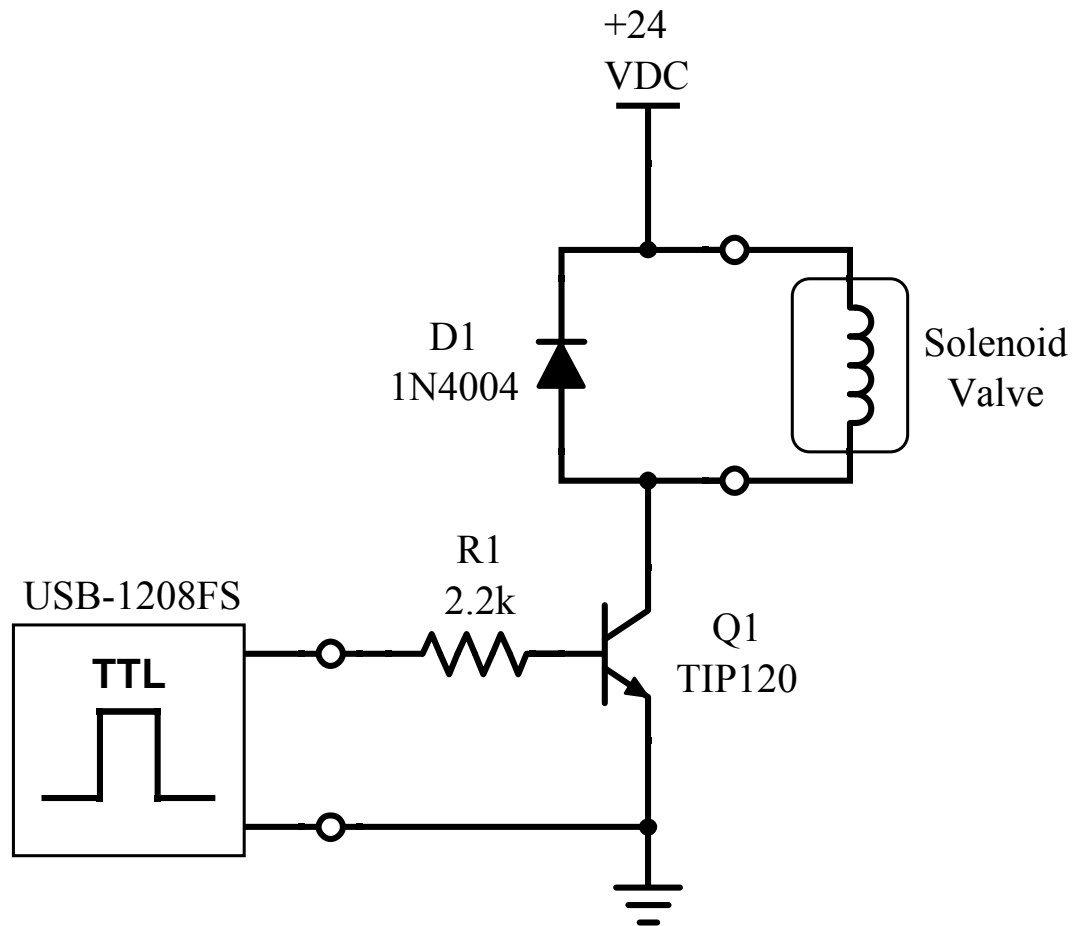
Figure B.1: Solenoid driver circuit for injector valves. When the TTL signal from the USB-1208FS is set to high, the TIP120 transistor switches open allowing current from the 24 VDC power supply to flow through the solenoid valve's coil and switches the valve. The power supply must be able to source at least 115 mA of current. A 1N4004 diode in parallel to the solenoid valve prevents the large back EMF that generated when the current is suddenly switched off from damaging the driver circuit.

```matlab
function perturb(PulseDuration,FlowRate,PumpDirection)

    % Open digital I/O channel on port A0 on USB-1208FS
    DIO = digitalio('mcc','0');
    trigger = addline(DIO,2,0,'out');
    valve = addline(DIO,1,0,'out');

    % Open serial communications and configure syringe pump
    s1 = serial('COM5','StopBits',2,'Terminator',13);
    fopen(s1);
    fprintf(s1,'MMD 37.5'); pause(0.3) % Set syringe bore diameter in mm
    output = sprintf('MLM %0.2f',FlowRate);
    fprintf(s1,output); pause(0.3) % Set flow rate in mL/min

    % Send trigger pulse to cameras
    putvalue(trigger,1), putvalue(trigger,0)

    % Run syringe pump
    if PumpDirection == 1
        fprintf(s1,'RUN');
    elseif PumpDirection == -1
        fprintf(s1,'REV'); % Run pump in the forward direction
    end
    pause(2)
    putvalue(valve,1) % Open valves
    pause(PulseDuration)
    putvalue(valve,0) % Close valves
    pause(1)
    fprintf(s1,'STP'); % Stop pump

    % Return control to syringe pump front panel
    % and clean up resources
    fprintf(s1,'KEY');
    fclose(s1);
    delete(s1), delete(DIO)
    clear s1 DIO

end
```

APPENDIX C

CAD DRAWINGS

This appendix contains CAD drawings for various parts that were fabricated for use with the Hirst system. While some of them were designed for use with the original cylinder that came with the Hirst system, which is now broken, they should provide a good starting point from which to design parts for use with the new, larger cylinders from the Duran Group.
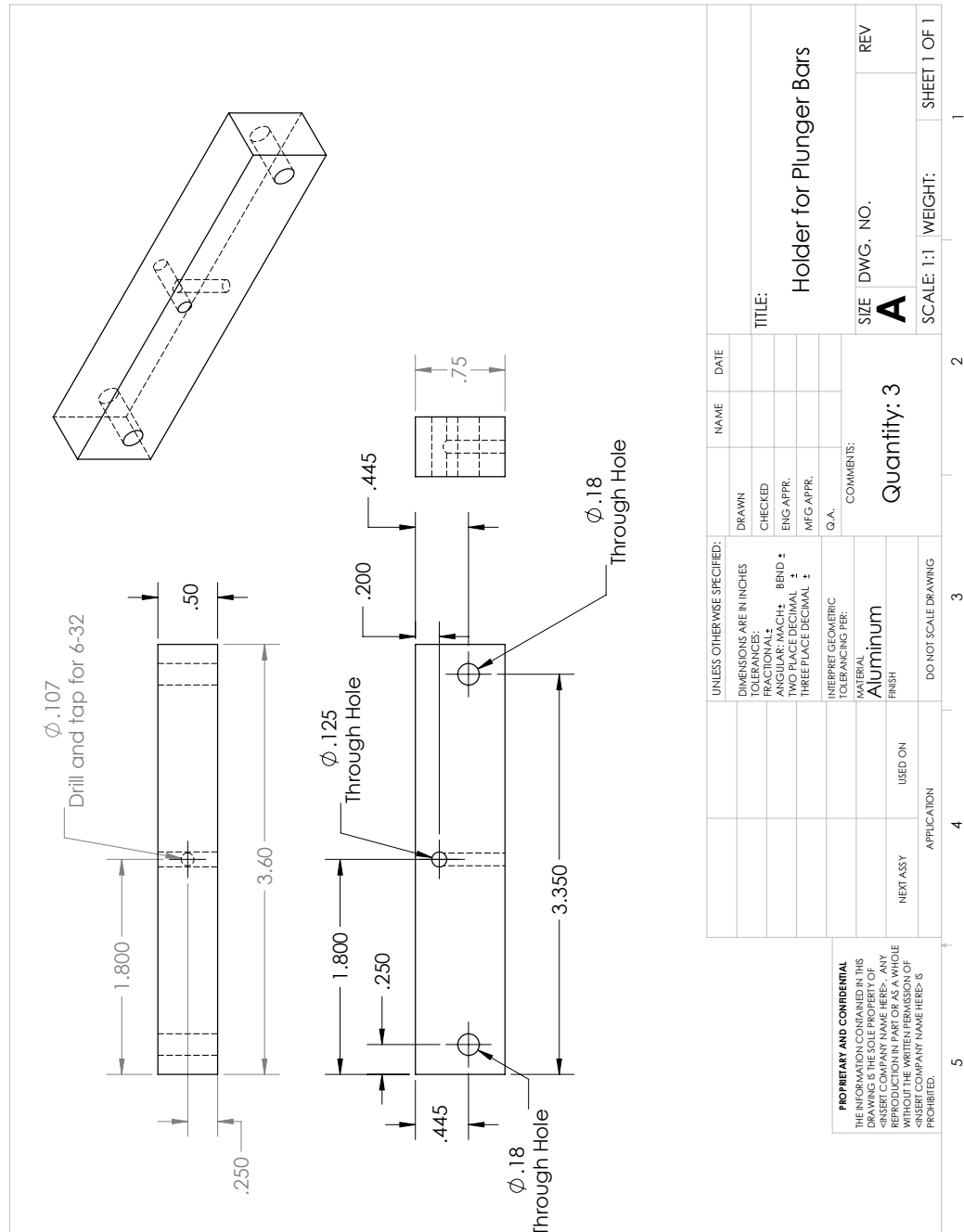
Figure C.1: Mechanical Drawing for the Adjustment Blocks for the End Ring. These pieces allowed the push rods that hold the top end ring to be locked down. They attach to the holes on the upper bearing support that were originally mount points for the Interior Outer Cylinder Bearing Retainer.
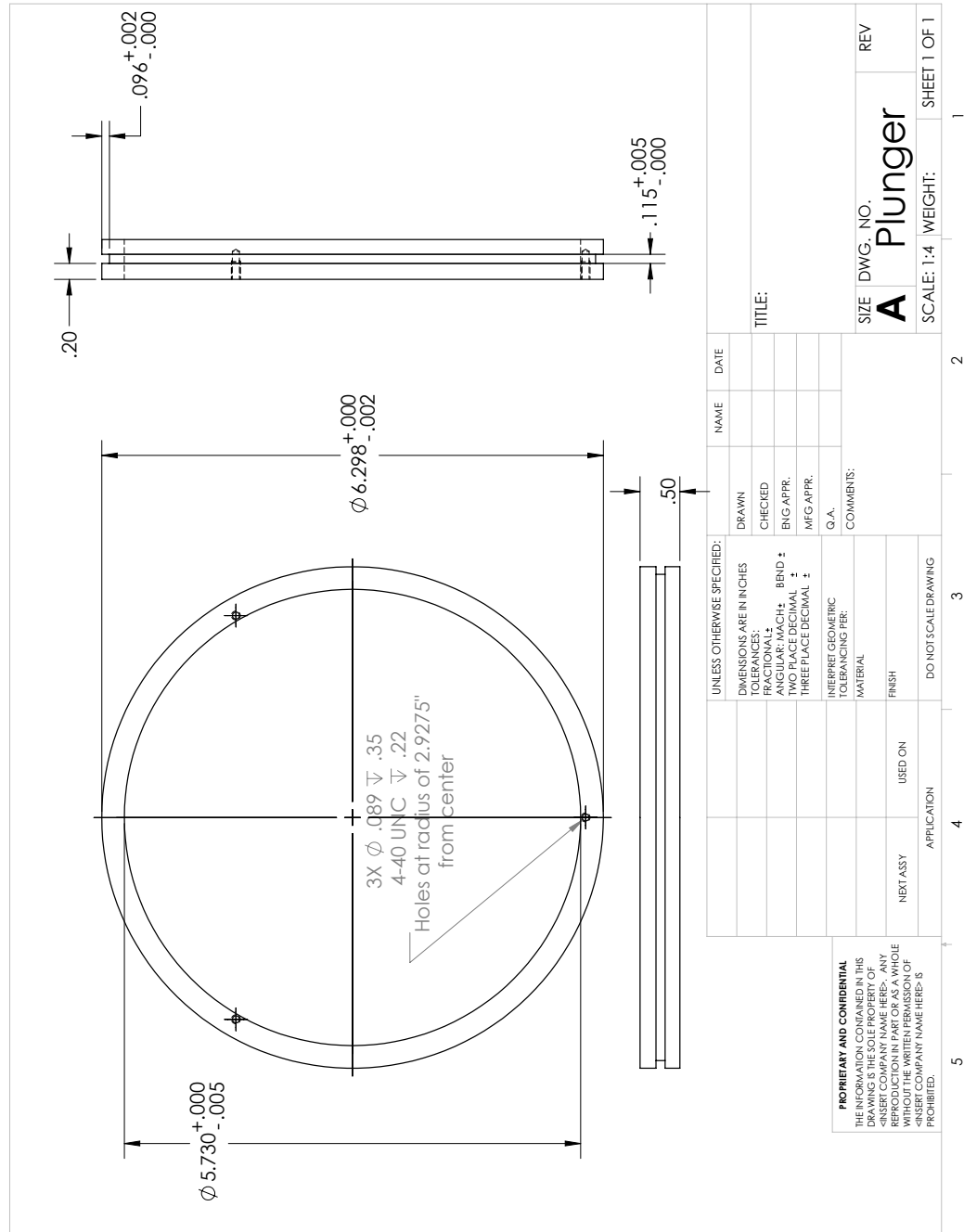
Figure C.2: Mechanical Drawing for the Top End Ring for $r_o = 80.00$ mm and $r_i = 72.4$ mm. This part sets the adjustable top boundary of the test section. The position of the attachment points for the push rods is fairly critical.
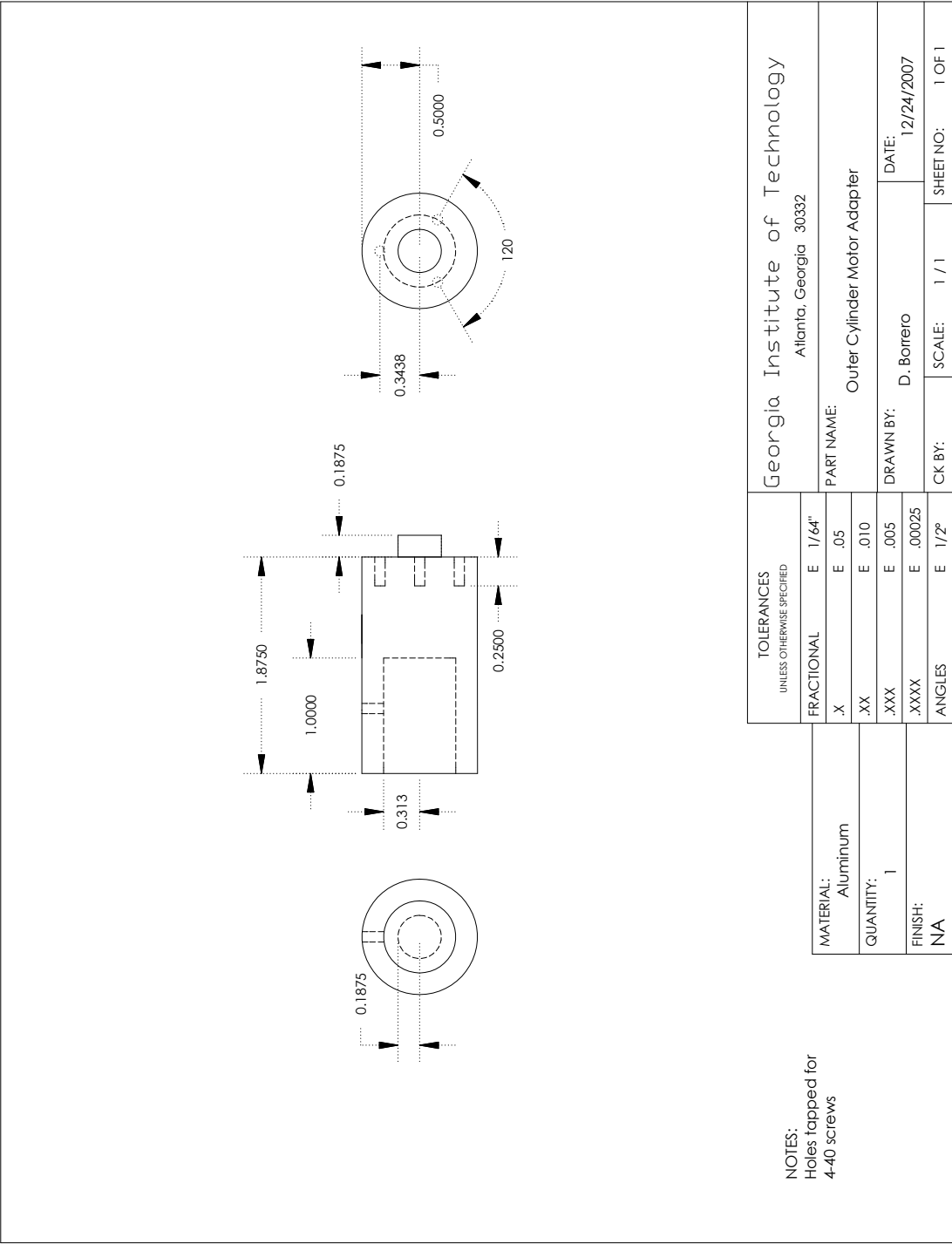
Figure C.3: Mechanical Drawing for the Outer Cylinder Motor Adapter for use with Row-L-ER chains. Used to mount sprocket on motor shaft for outer cylinder.
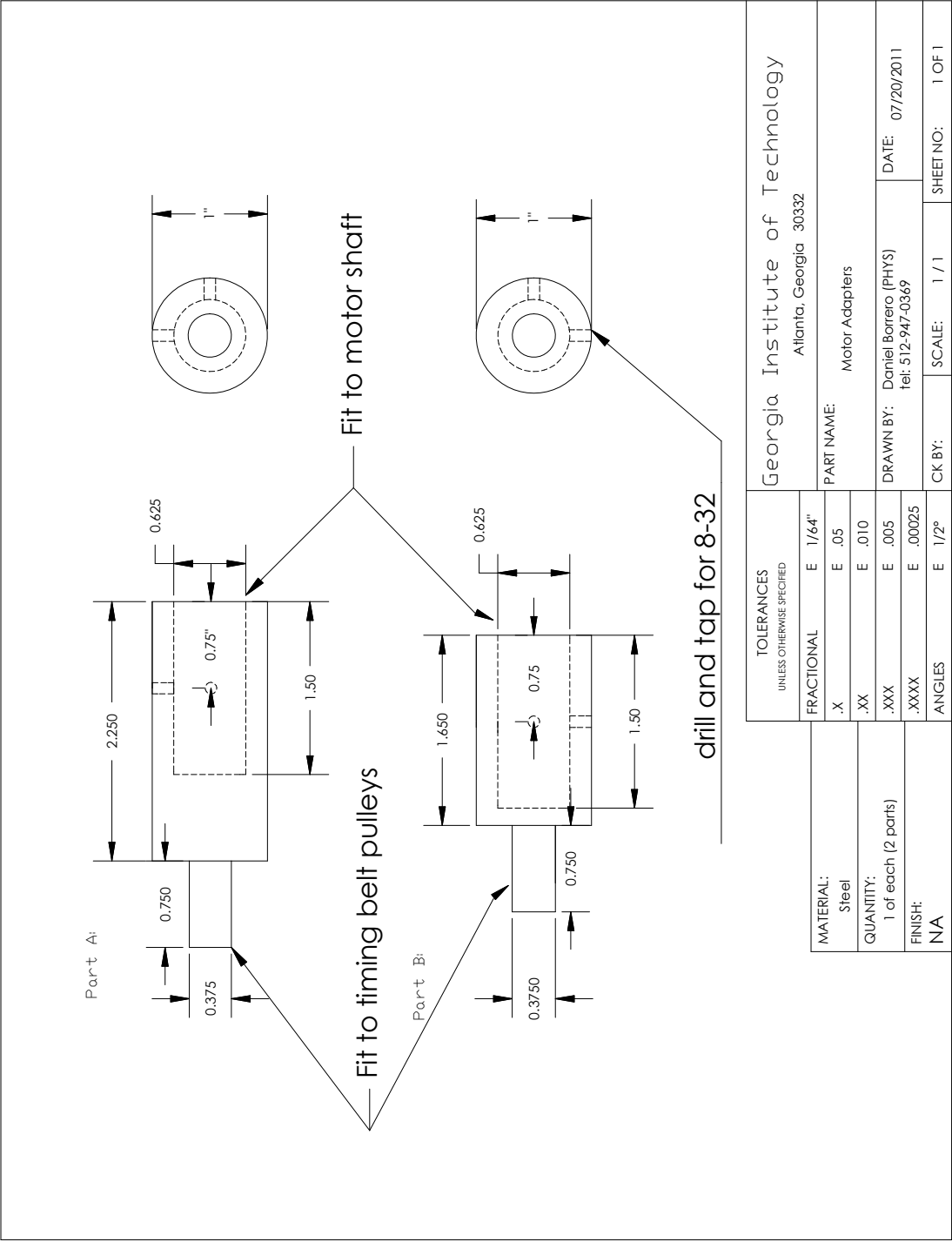
Figure C.4: Mechanical Drawing for the Motor Adapters for use with timing belts. Used in the experiments of Chapter 6.
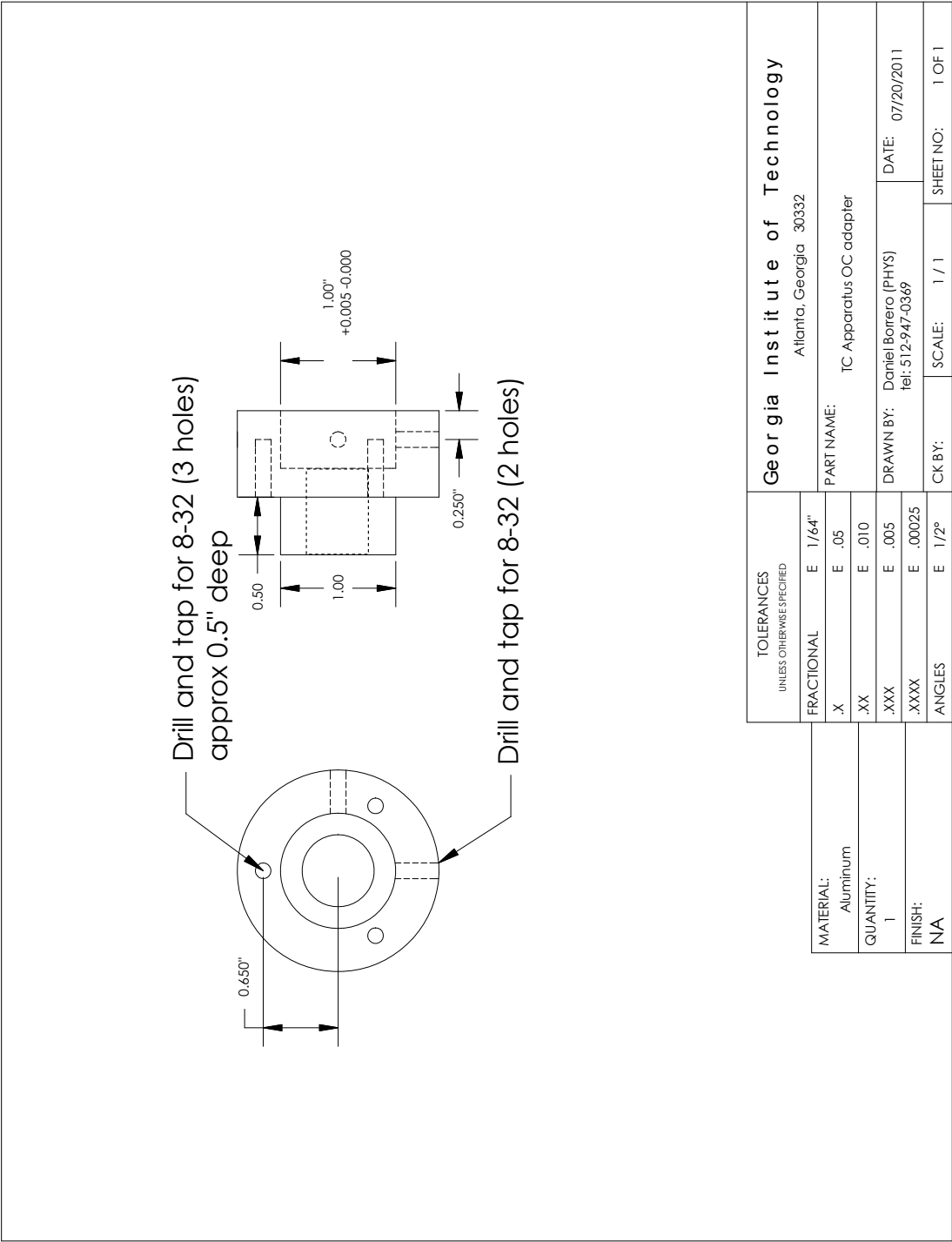
Figure C.5: Mechanical Drawing for Outer Cylinder Shaft Adapter for Timing Belts and Row-L-ER Chains.
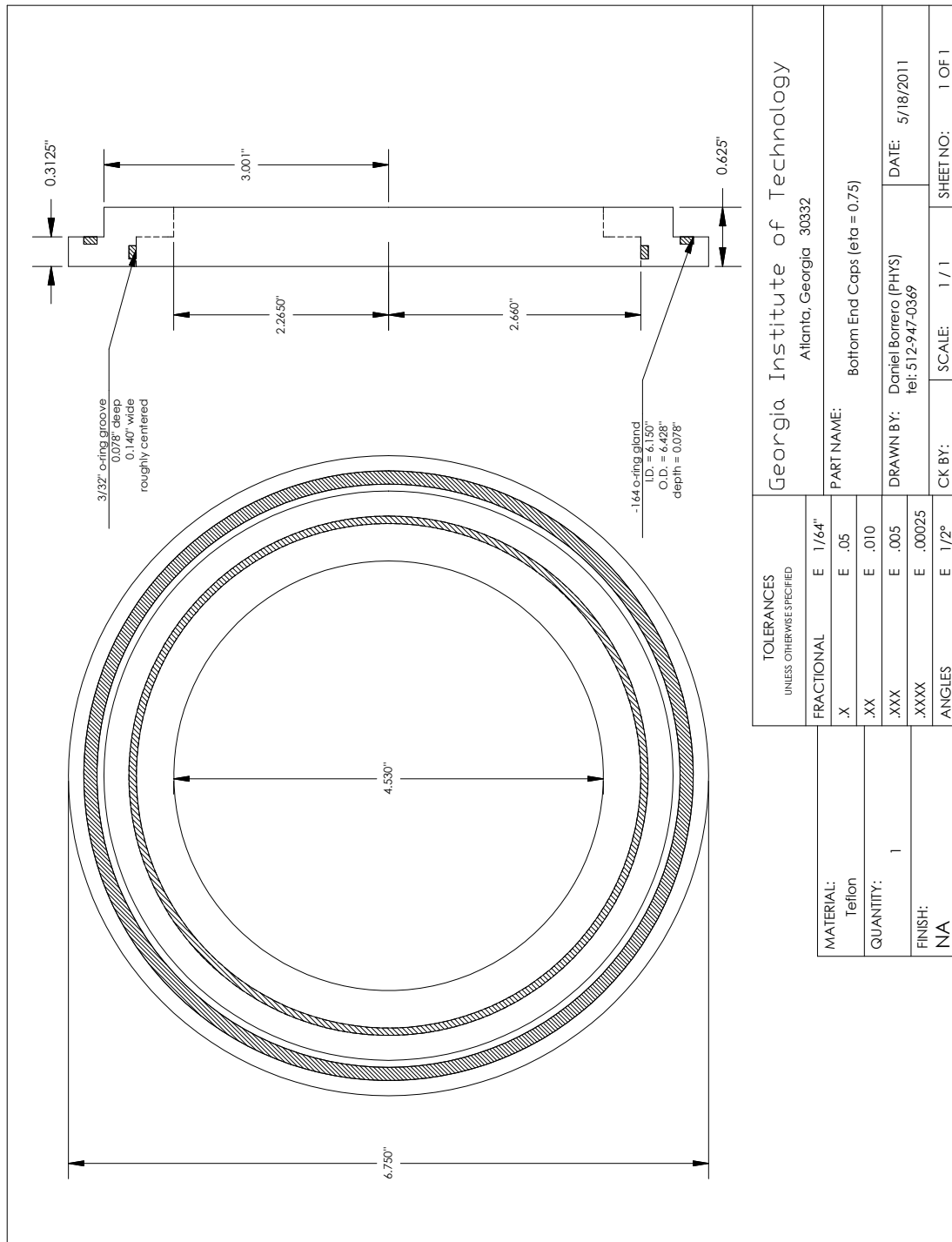
Figure C.6: Mechanical Drawing for the End Cap for $r_o = 7.620$ cm and $r_i = 5.679$ cm (η = 0.754).
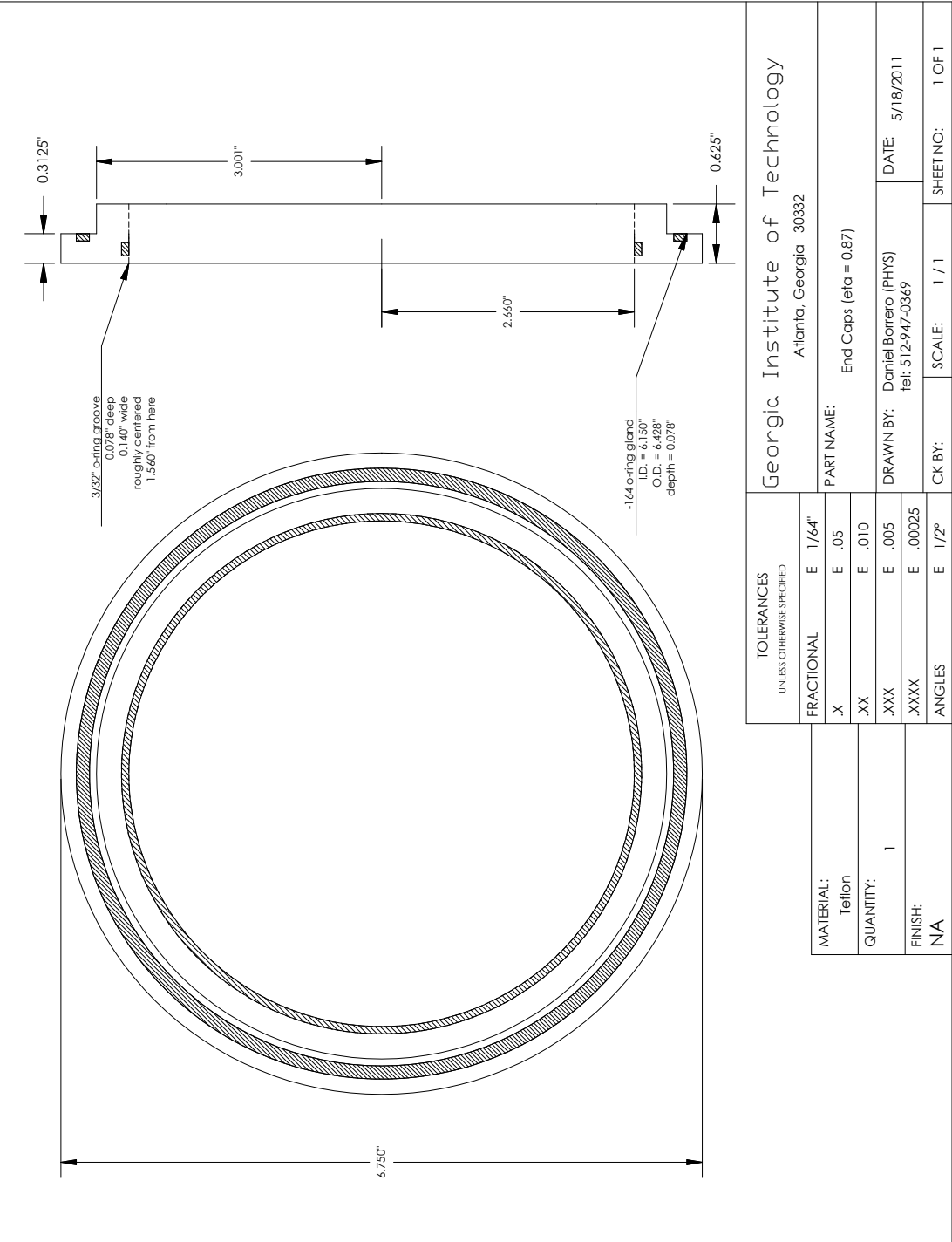
Figure C.7: Mechanical Drawing for the End Cap for $r_o = 7.620$ cm and $r_i = 6.638$ cm ($\eta = 0.871$).
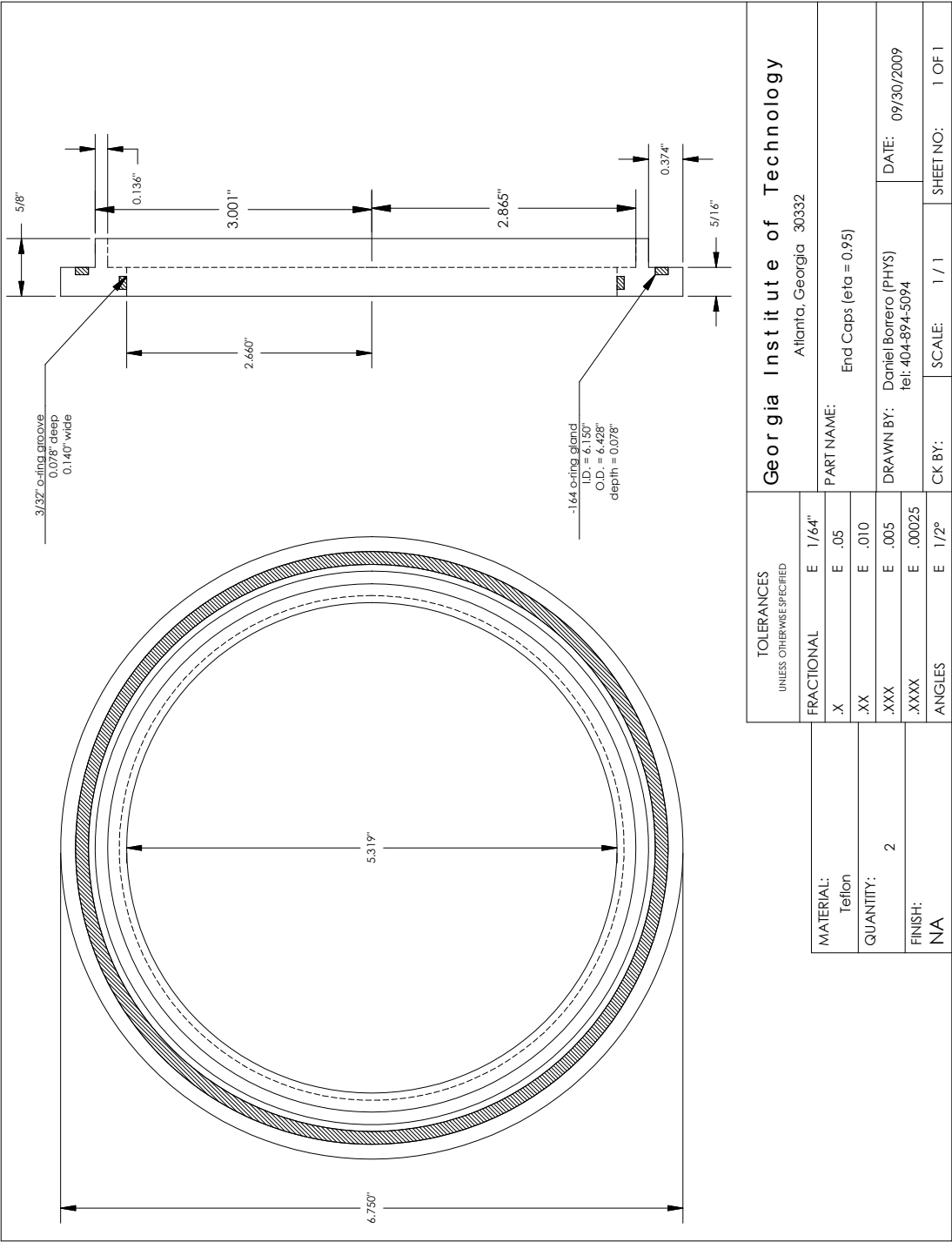
Figure C.8: Mechanical Drawing for the End Cap for $r_o = 7.620$ cm and $r_i = 7.239$ cm ($\eta = 0.950$).
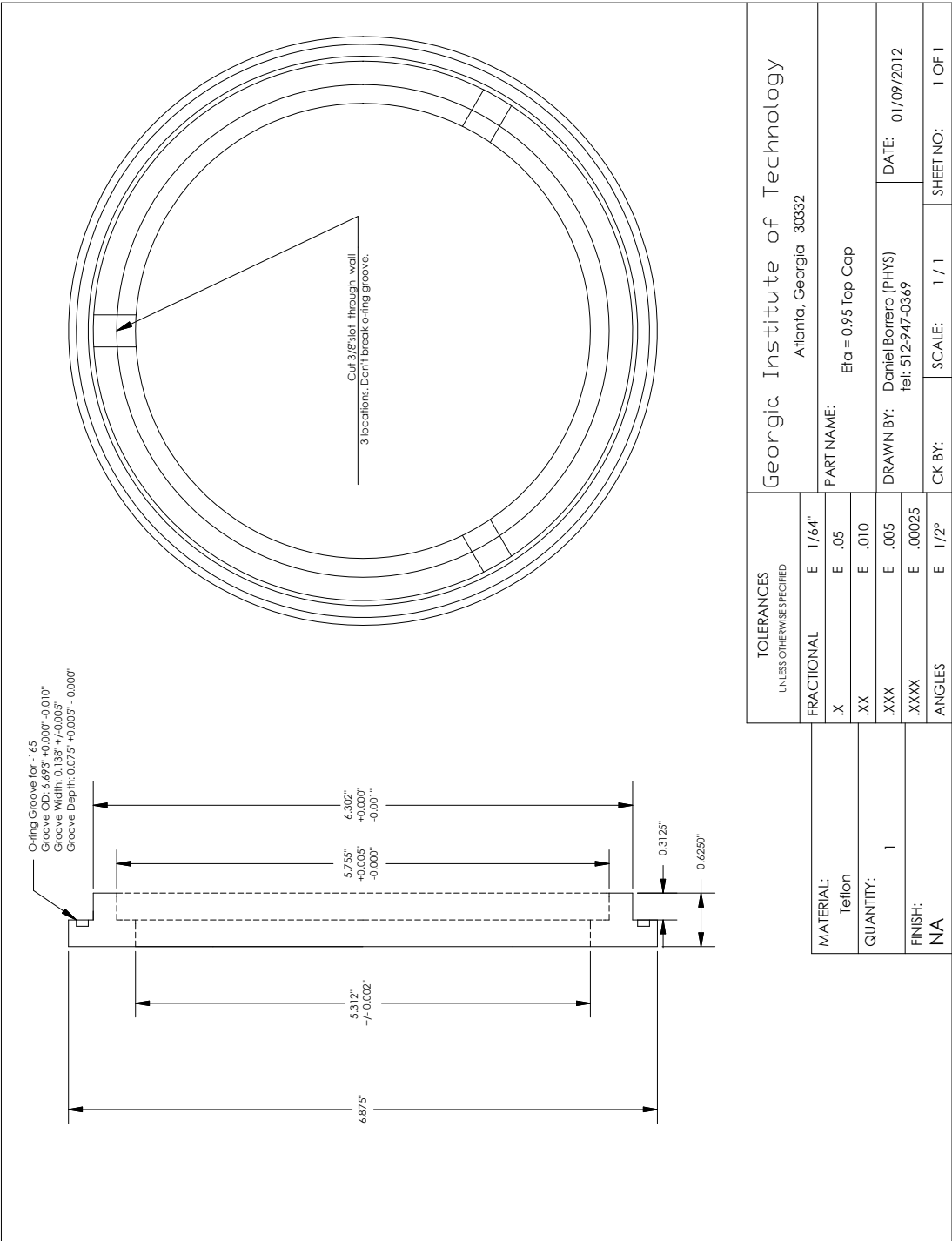
Figure C.9: Mechanical Drawing for the Top End Cap for $r_o = 8.000$ cm and $r_i = 7.239$ cm ($\eta = 0.905$) using the new lower outer cylinder end (Figure C.11).
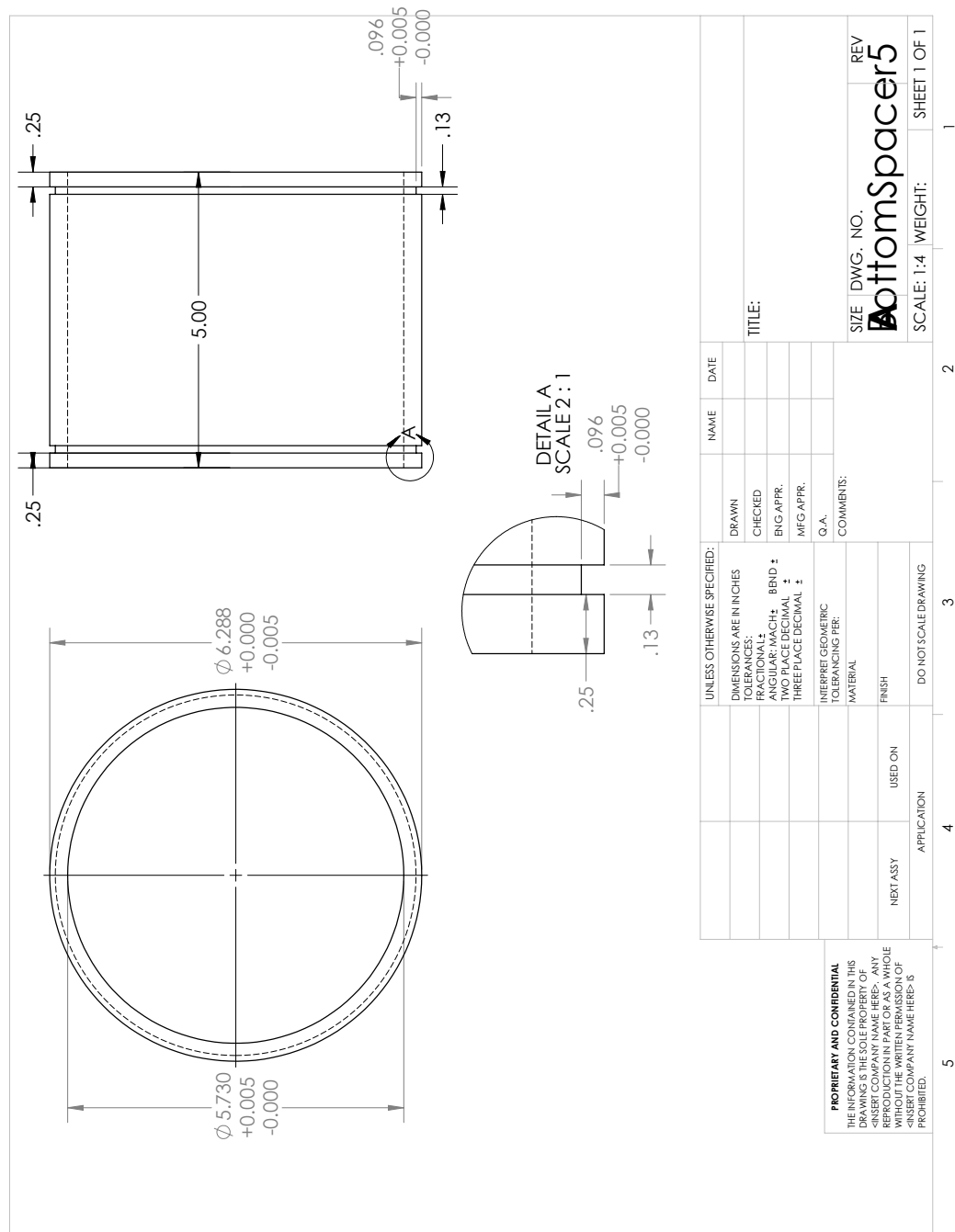
Figure C.10: Mechanical Drawing for 5 in. spacer for $r_o = 8.000$ cm and $r_i = 7.239$ cm ($\eta = 0.905$). This part can be inserted into the bottom of the test section to lift it for tomographic PIV measurements.
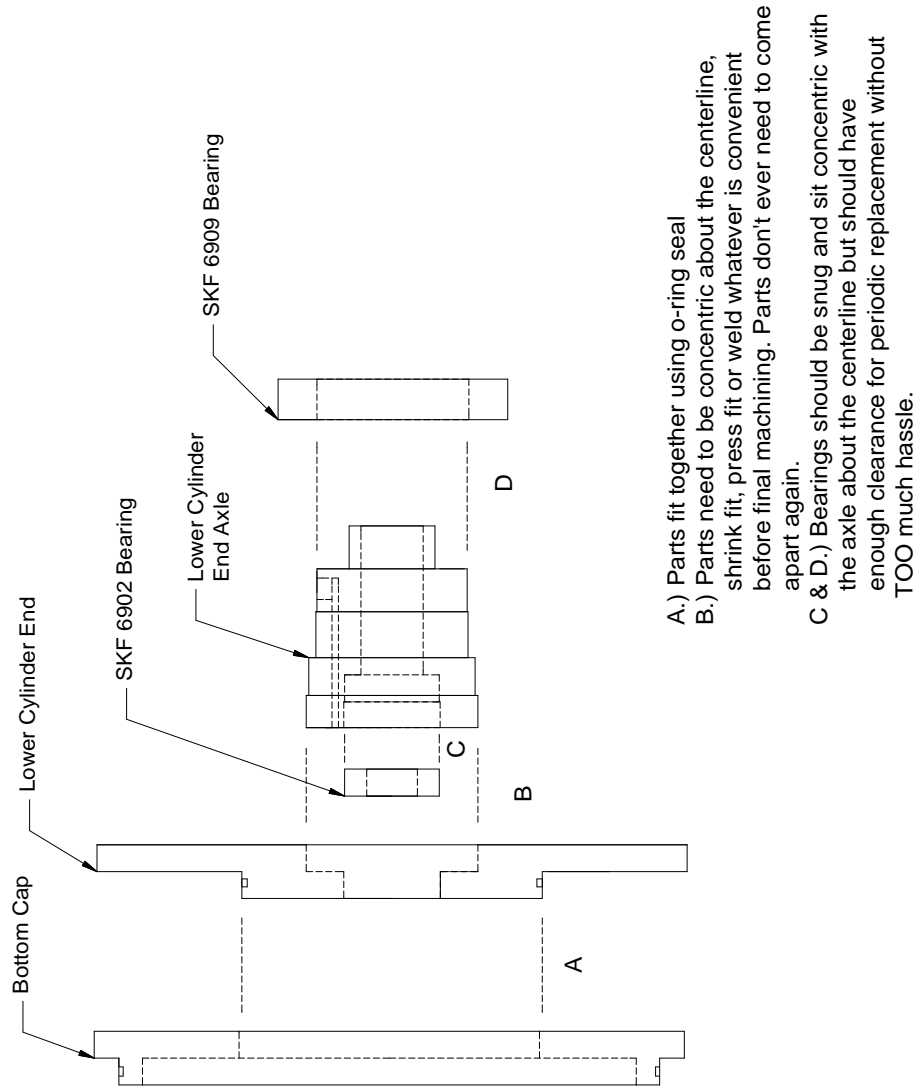
Figure C.11: Assembly Drawing for Bottom Assembly for use with $r_o = 8.000$ cm outer cylinder. This assembly was designed to be able to use smaller inner cylinders in the future. For individual part drawings see Figures C.12-C.14.
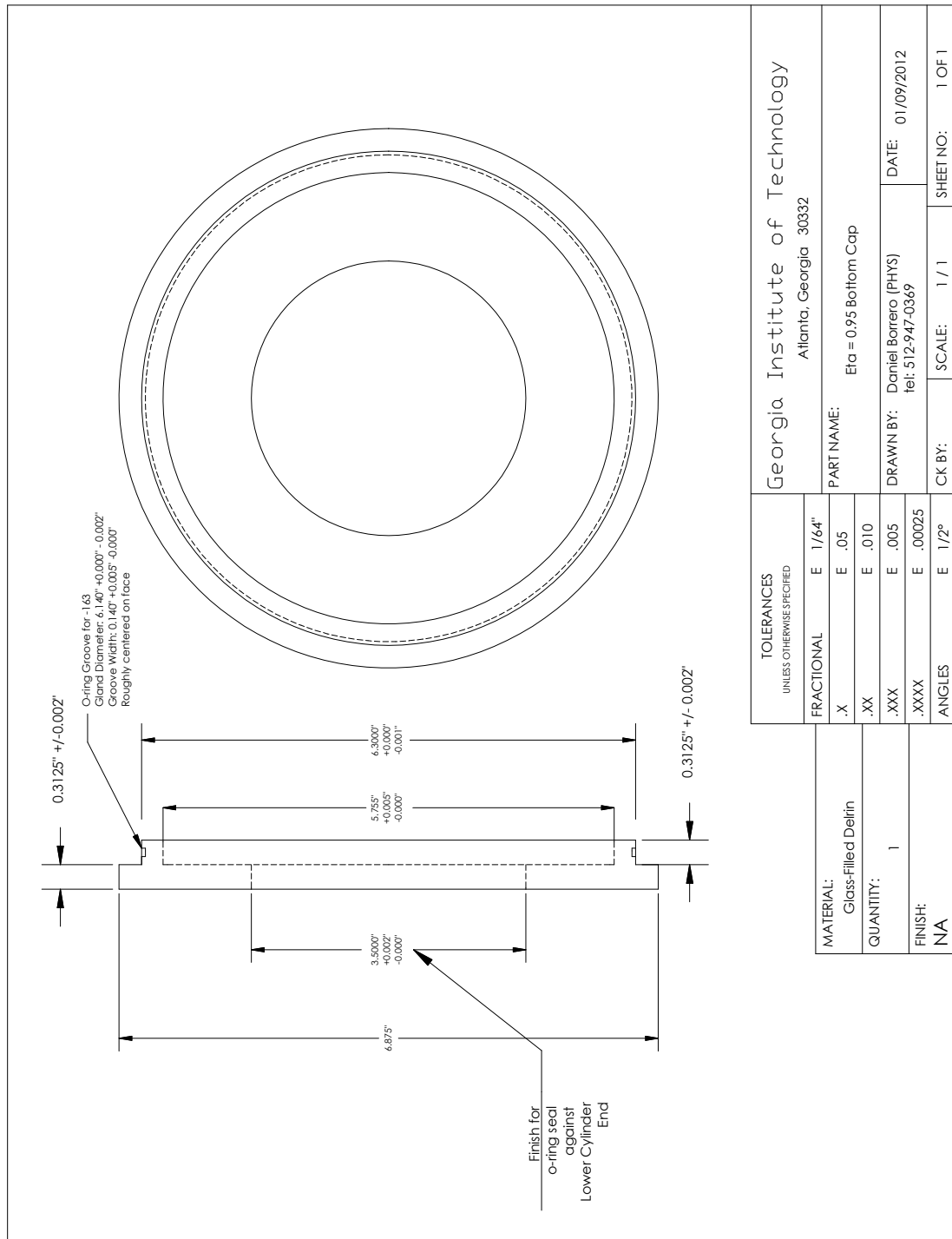
Figure C.12: Mechanical Drawing for the Bottom End Cap for $r_o = 8.000$ cm and $r_i = 7.239$ cm ($\eta = 0.905$) using new lower outer cylinder end (Figure C.11).
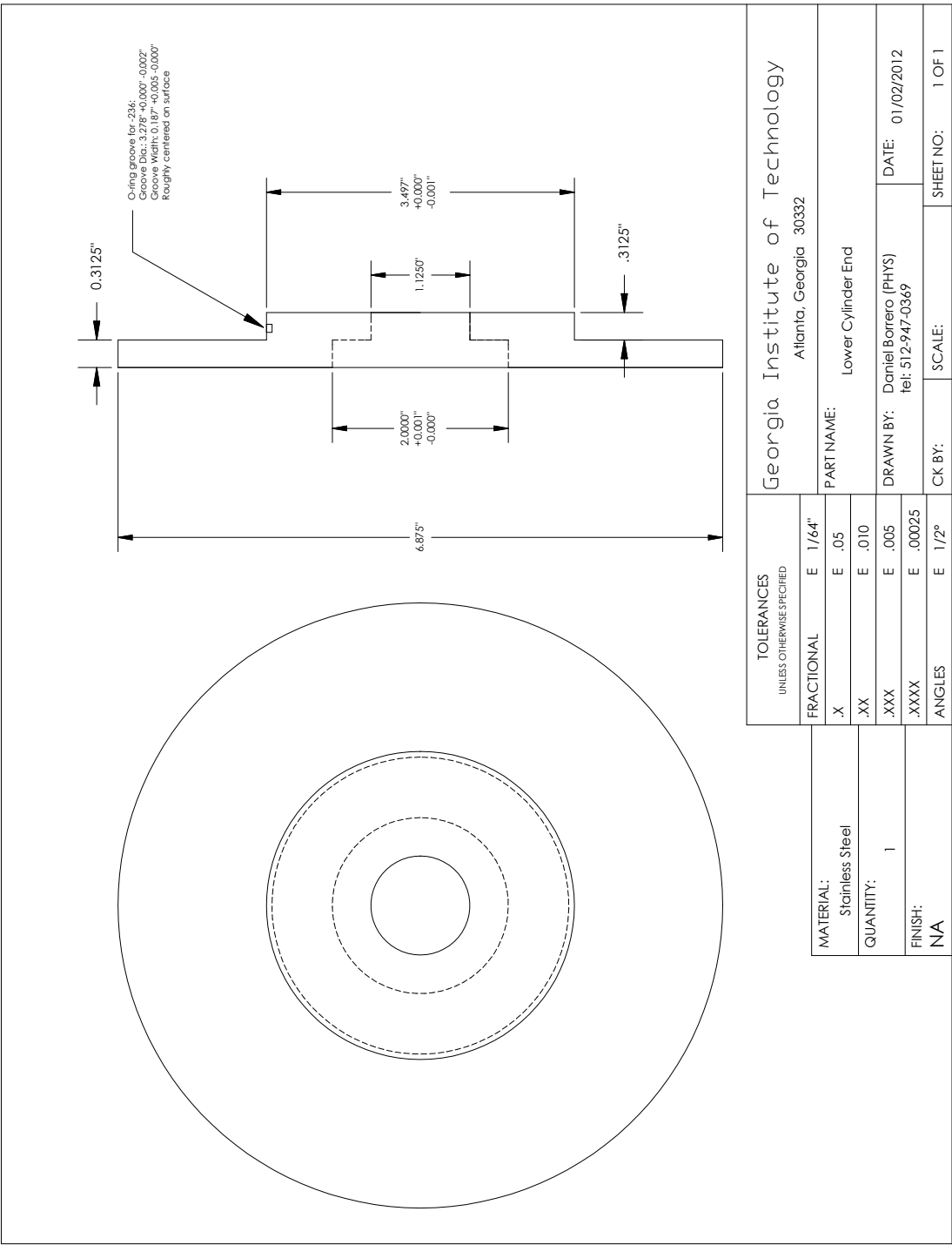
Figure C.13: Mechanical Drawing for New Outer Cylinder Lower End.
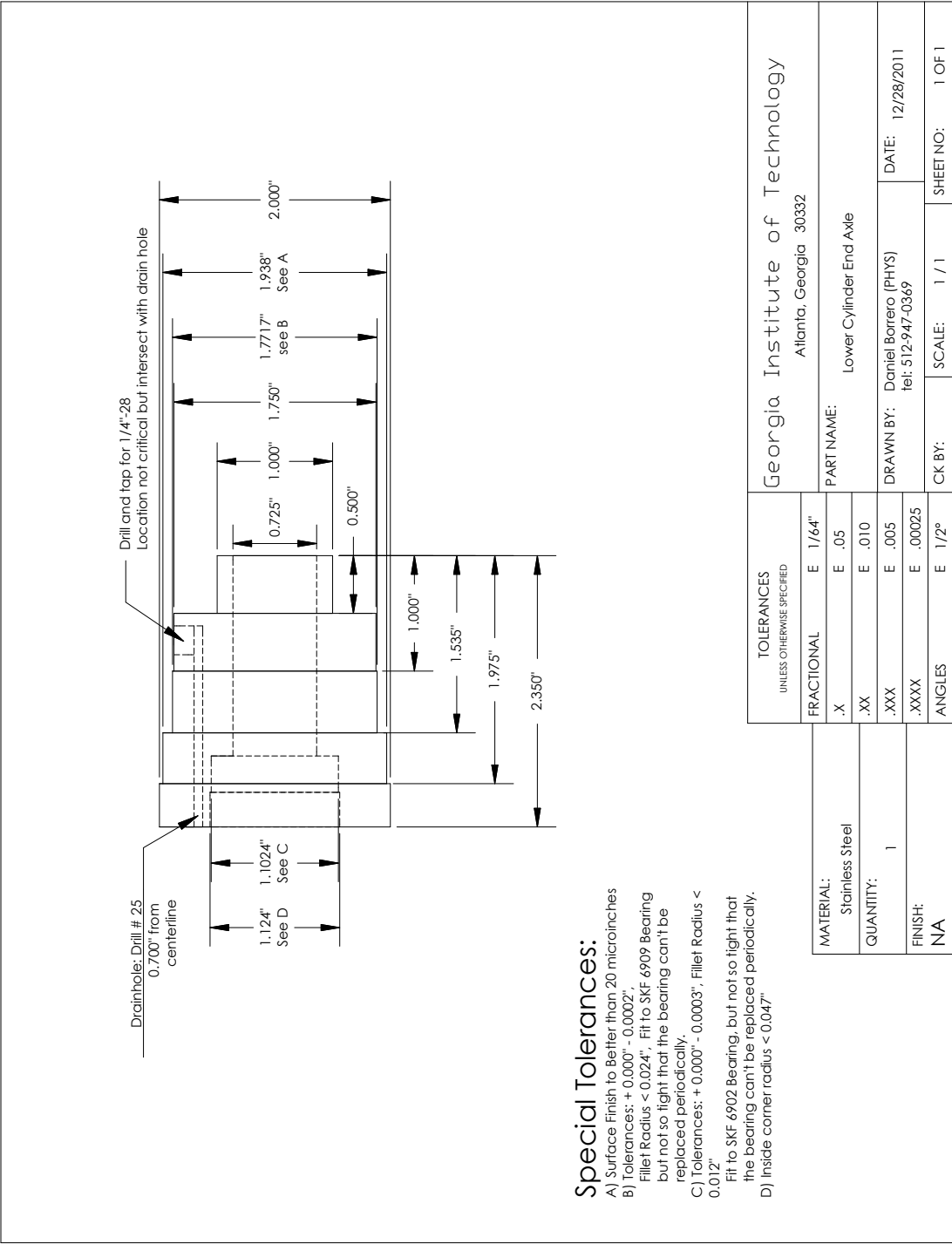
Figure C.14: Mechanical Drawing for New Outer Cylinder Bottom Axle.
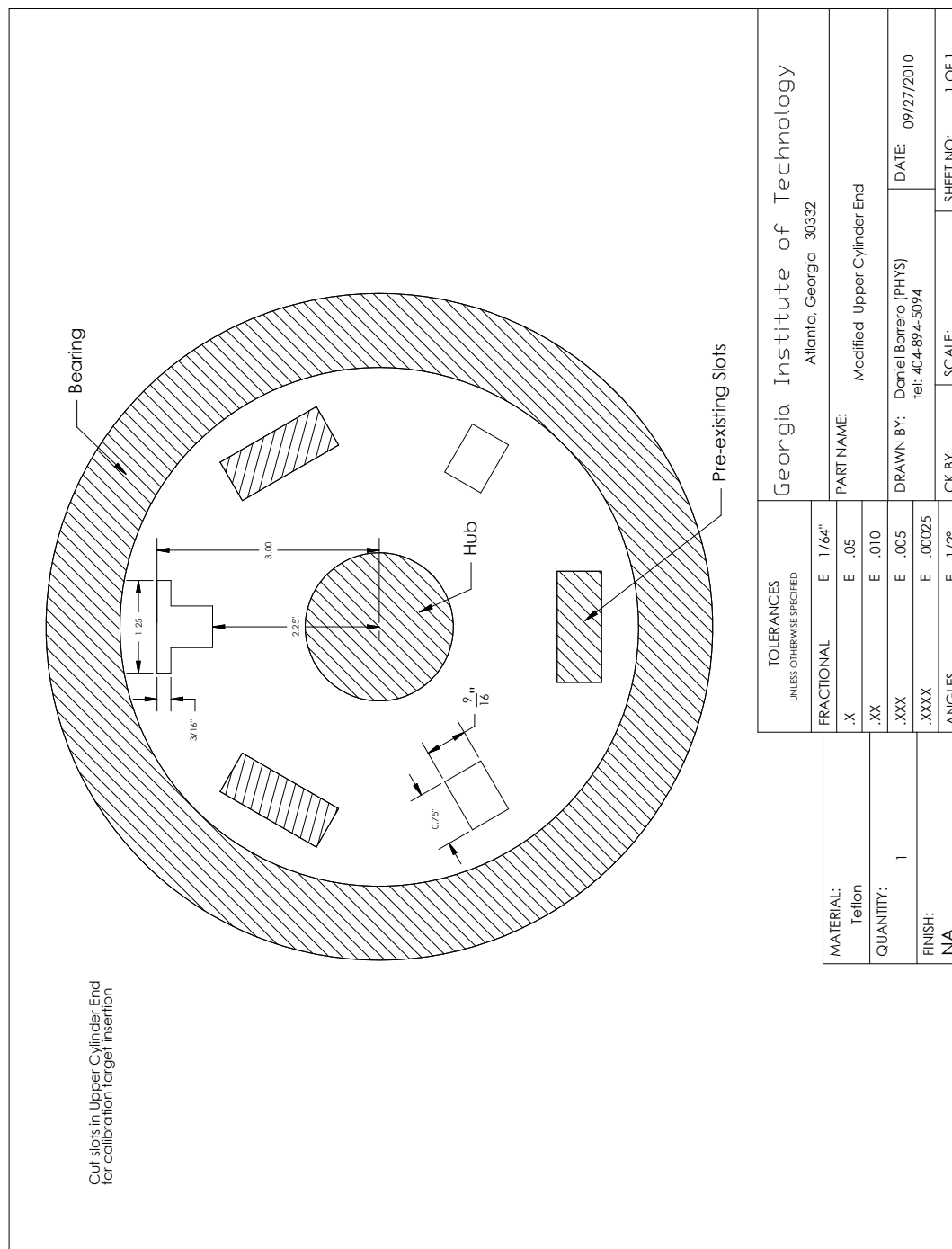
Figure C.15: Mechanical Drawing for Outer Cylinder Upper End Modifications. A t-shaped slot was machined into the upper end of the outer cylinder to translate a planar calibration target through the volume. Two additional slots were cut to balance the apparatus.
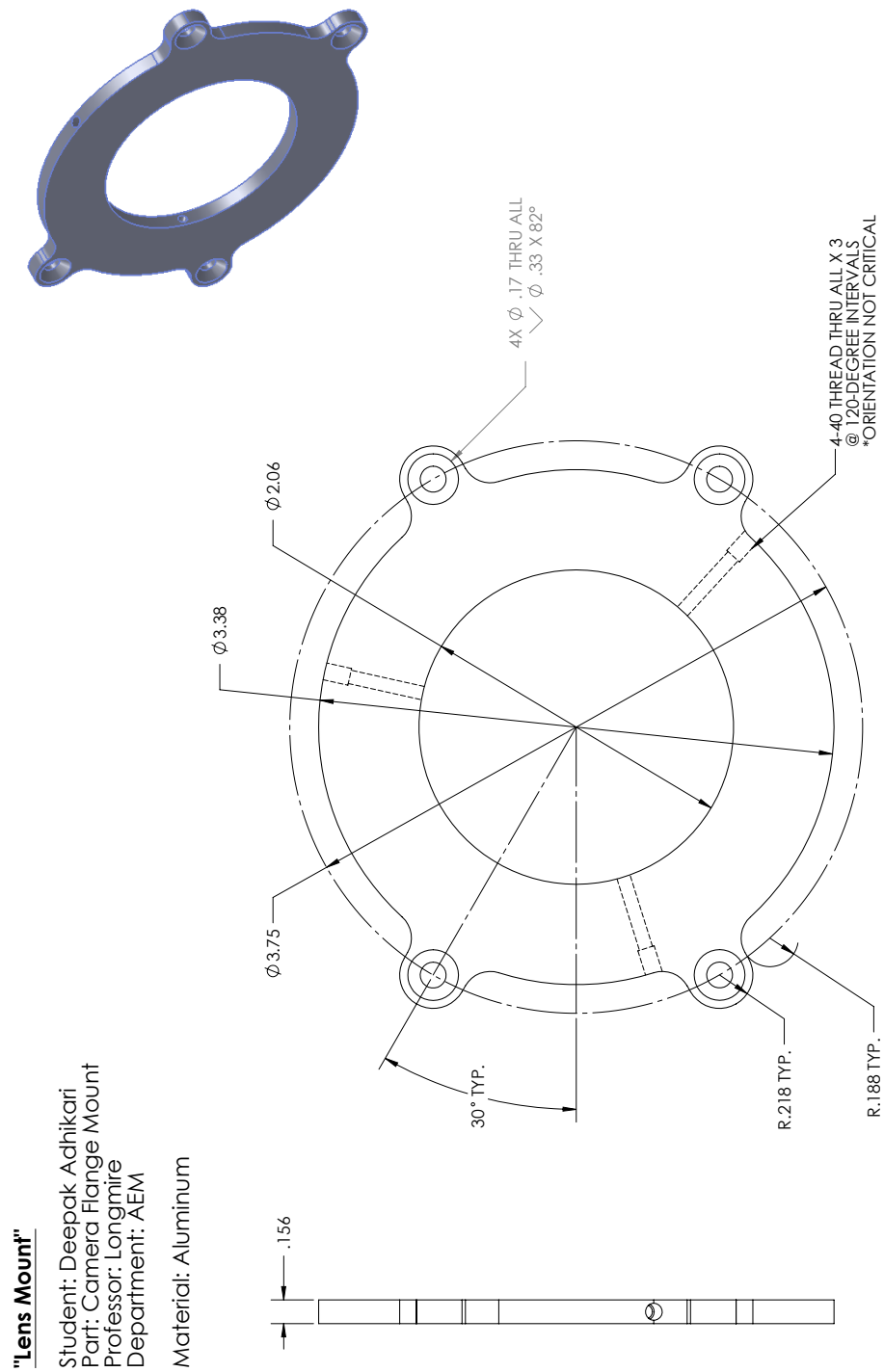
Figure C.16: Flange for attaching LaVision v1 Scheimpflung mount to Vision Research Phantom v210 Camera. Original design by Deepak Adhikari from Prof. Ellen Longmire's group at the University of Minnesota (now a postdoctoral fellow in Prof. Don Webster's group in the School of Civil and Environmental Engineering at Georgia Tech).

APPENDIX D

CAD DRAWINGS FOR INNER CYLINDER WITH JETS

This appendix contains CAD drawings for the parts that make up the inner cylinder used in the experiments of Chapters 4 and 6. It features a series of 84 ports in an axial line that can be used to inject or remove fluid to perturb the flow. Unused ports can be plugged from inside with #3-56 cap screws. It is recommended to use stainless steel screws (316 if using NH_4SCN solution for refractive index-matching) to avoid corrosion problems. Unused ports can be smoothed over by filling them with softened bees' wax. The bees' wax can be made darker by mixing it with black shoe polish. Precision ruby orifice assemblies that screw into #3-56 threads of the ports are available from Bird Precision (Waltham, Massachusetts) in a variety of sizes. Three sets of four orifices (part no. RB-82453) were purchased with $0.030''$, $0.015''$, and $0.0075''$ diameters.
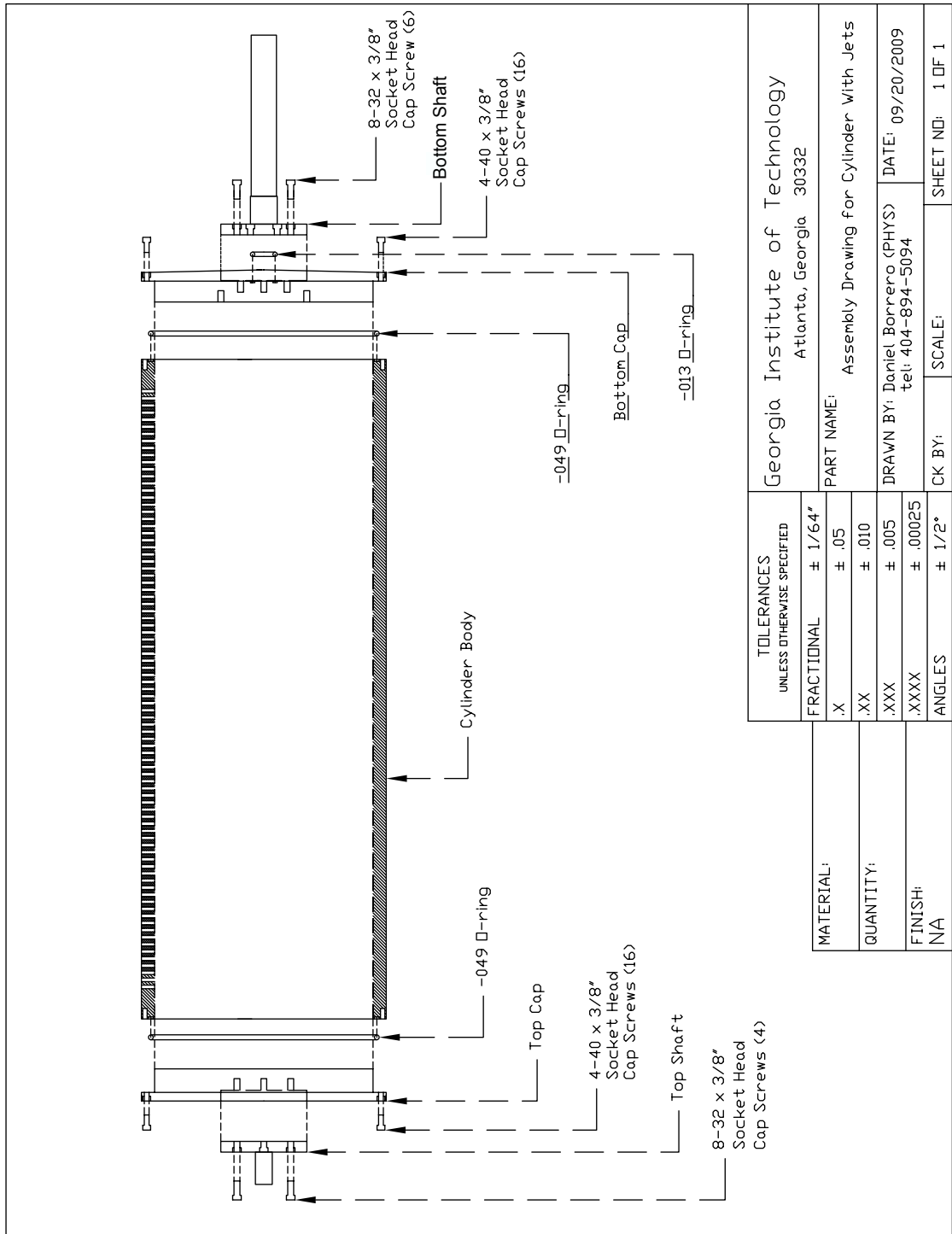
Figure D.1: Assembly of Cylinder with Jets with $r_i = 7.239$ cm. Detailed part drawings are given in Figures D.2-D.7.
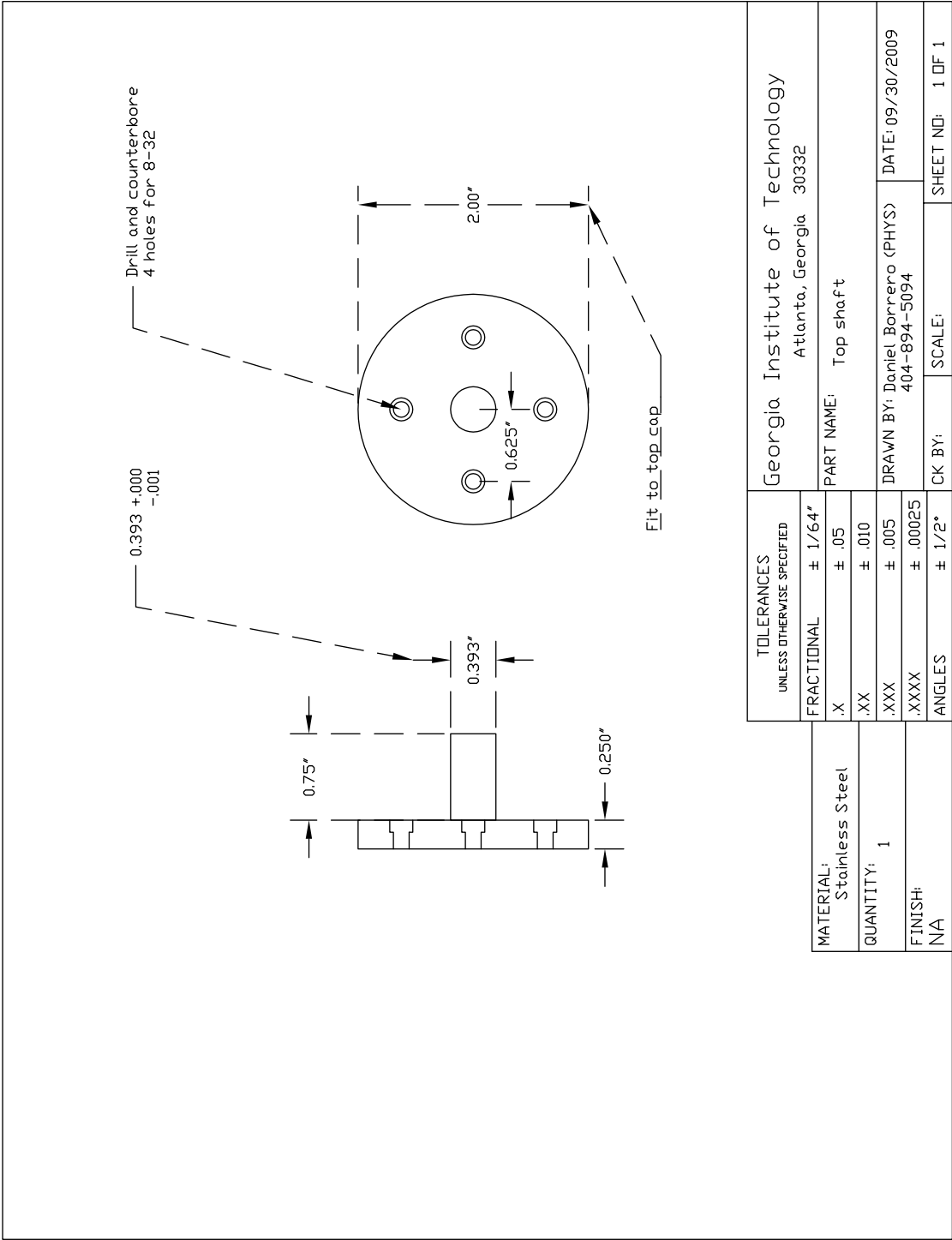
Figure D.2: Top Shaft for Cylinder with Jets.
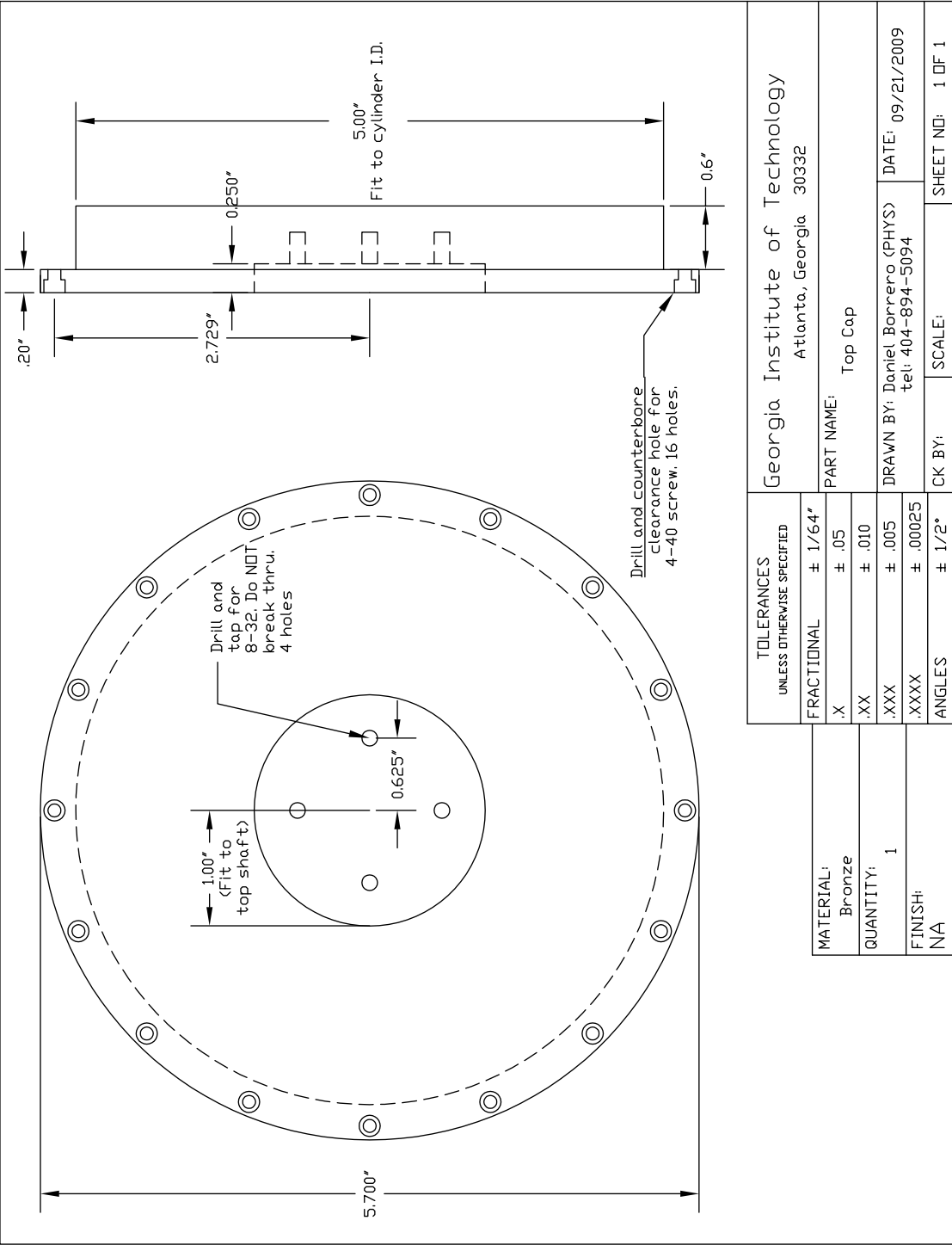
Figure D.3: Bottom Cap for Cylinder with Jets.
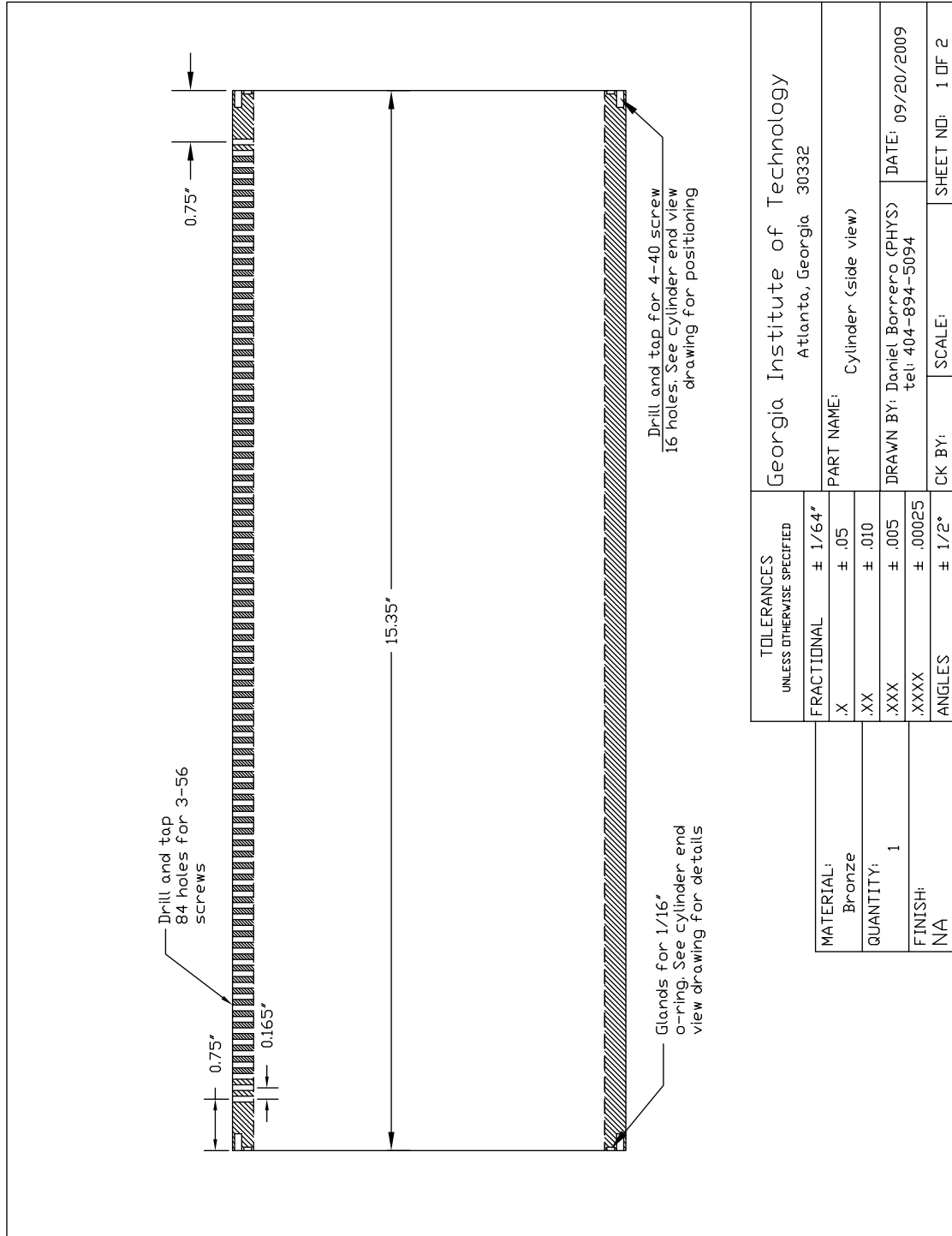
Figure D.4: Side View of Cylinder Body. The cylinder body has a line of 84 ports along an axial line that can be fitted with miniature barbed fittings for $1/16''$ tubing to inject fluid.
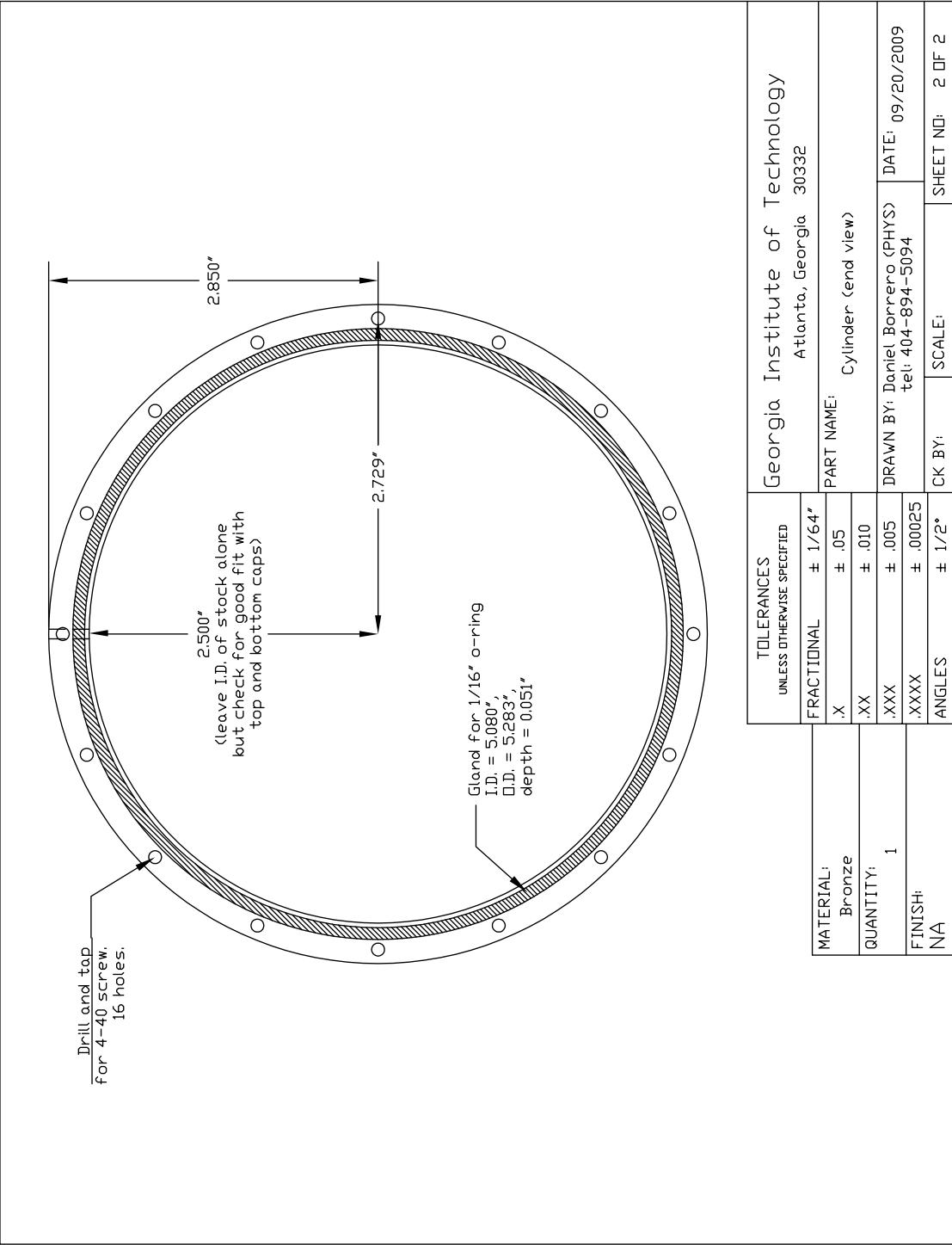
Figure D.5: End View of Cylinder Body.
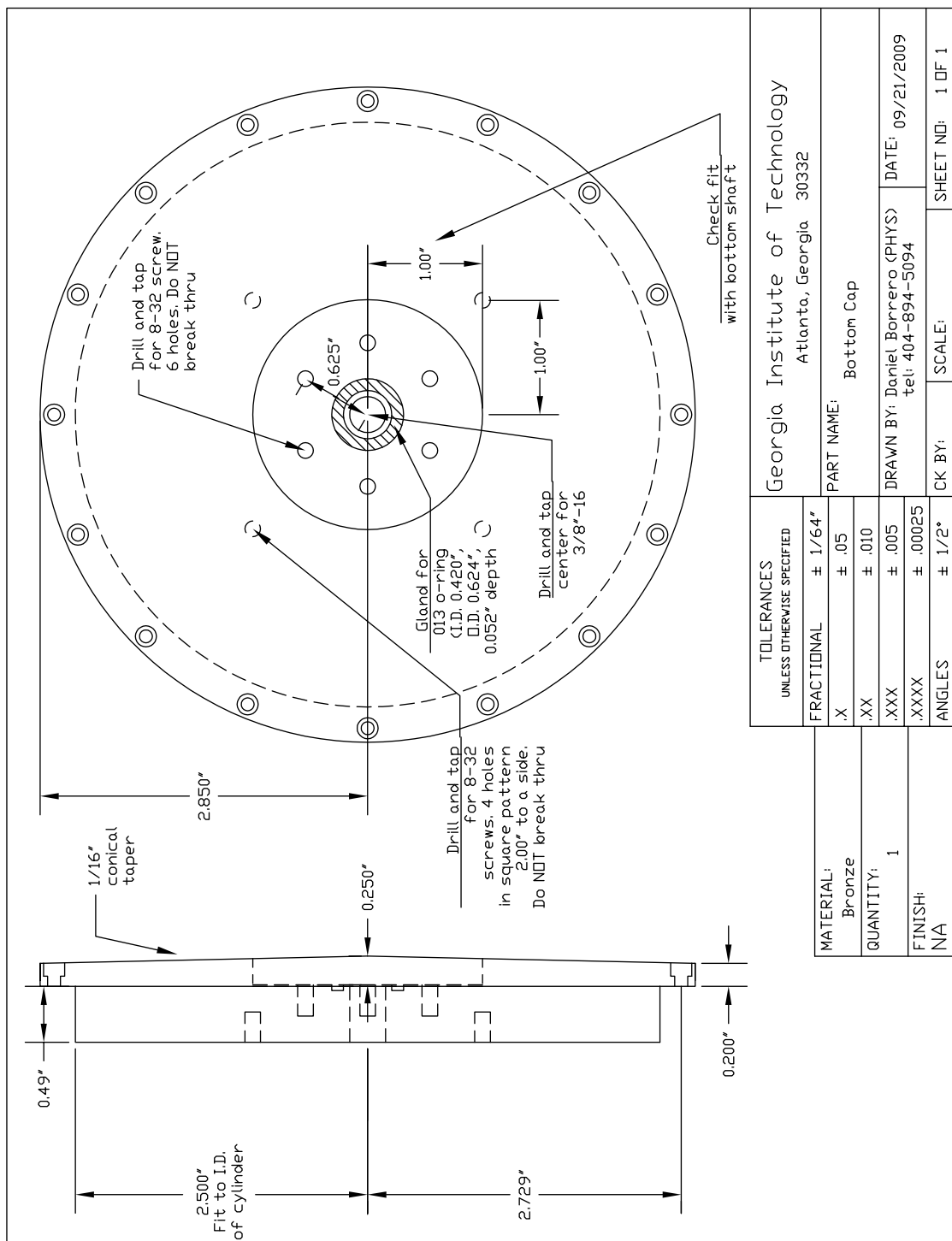
Figure D.6: Bottom Cap for Cylinder with Jets.
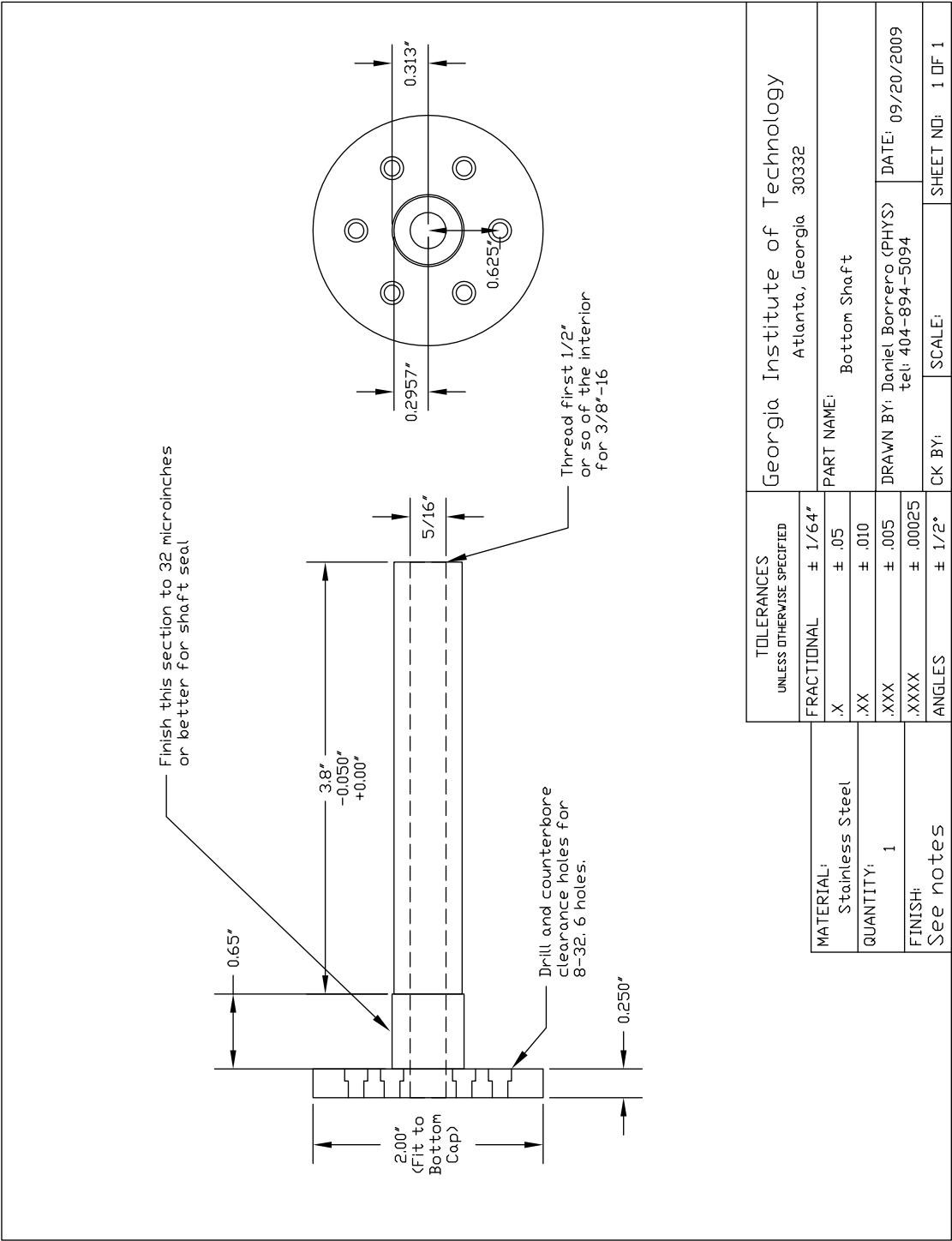
Figure D.7: Bottom Shaft for Cylinder with Jets. The shaft is hollowed out as a feedthrough for the jets.

APPENDIX E

MECHANICAL DRAWINGS FOR 3-D CALIBRATION TARGET FOR TOMOGRAPHIC PIV

By machining the calibration target into the movable end ring, the calibration procedure is greatly accelerated since the target can be positioned quickly and repeatably. It also guarantees that the axial coordinate and the Y coordinate of the reconstructed volume are aligned. In theory, the larger the separation between the calibration planes and the greater the number of calibration marks, the better the overall calibration. However, several design constraints exist in practice:

- The calibration marks on the back plane must be visible from cameras pointing at the target at an angle.

- DaVis's calibration software searches for marks on the back plane in the middle of the square formed by four adjacent marks on the front plane. The spacing between the calibration marks must be large enough so that as the cameras are angled away from normal, the dots on the back plane do not drift outside of this square by perspective effects.

- The spacing must be small enough so that at least 7 points are visible in each direction for each plane.

The dimensions of the calibrations target were designed based on these considerations and are similar to the now-discontinued Type 2.5 three-dimensional calibration target from LaVision. This design provides significantly more calibration marks than necessary for the typical measurement volumes used here, so future designs might use fewer marks with a larger separation between planes, or even a third calibration plane.

211
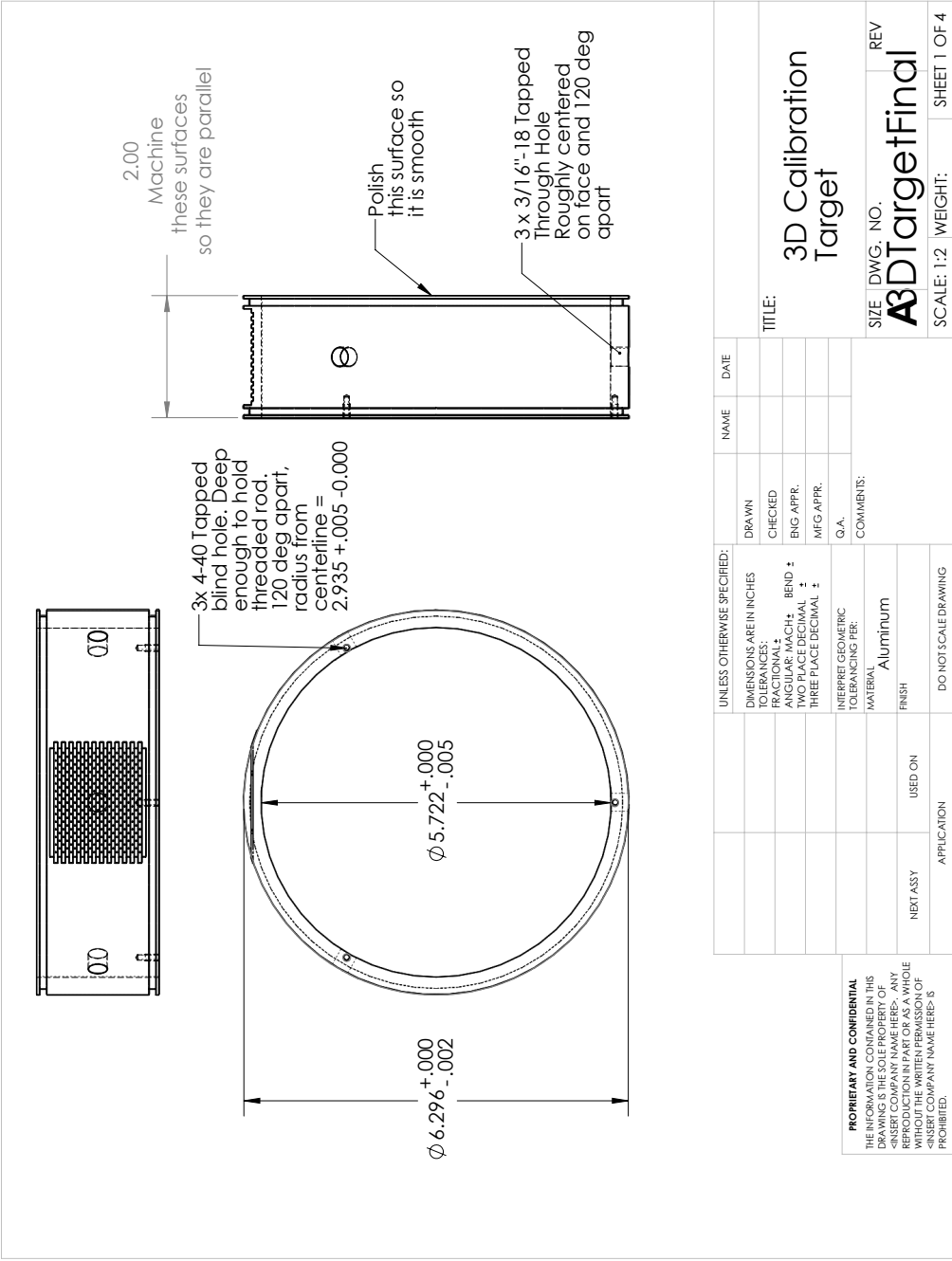
Figure E.1: Mechanical Drawing for 3-D Calibration Target. Additional details are provided in Figures E.4-E.3.
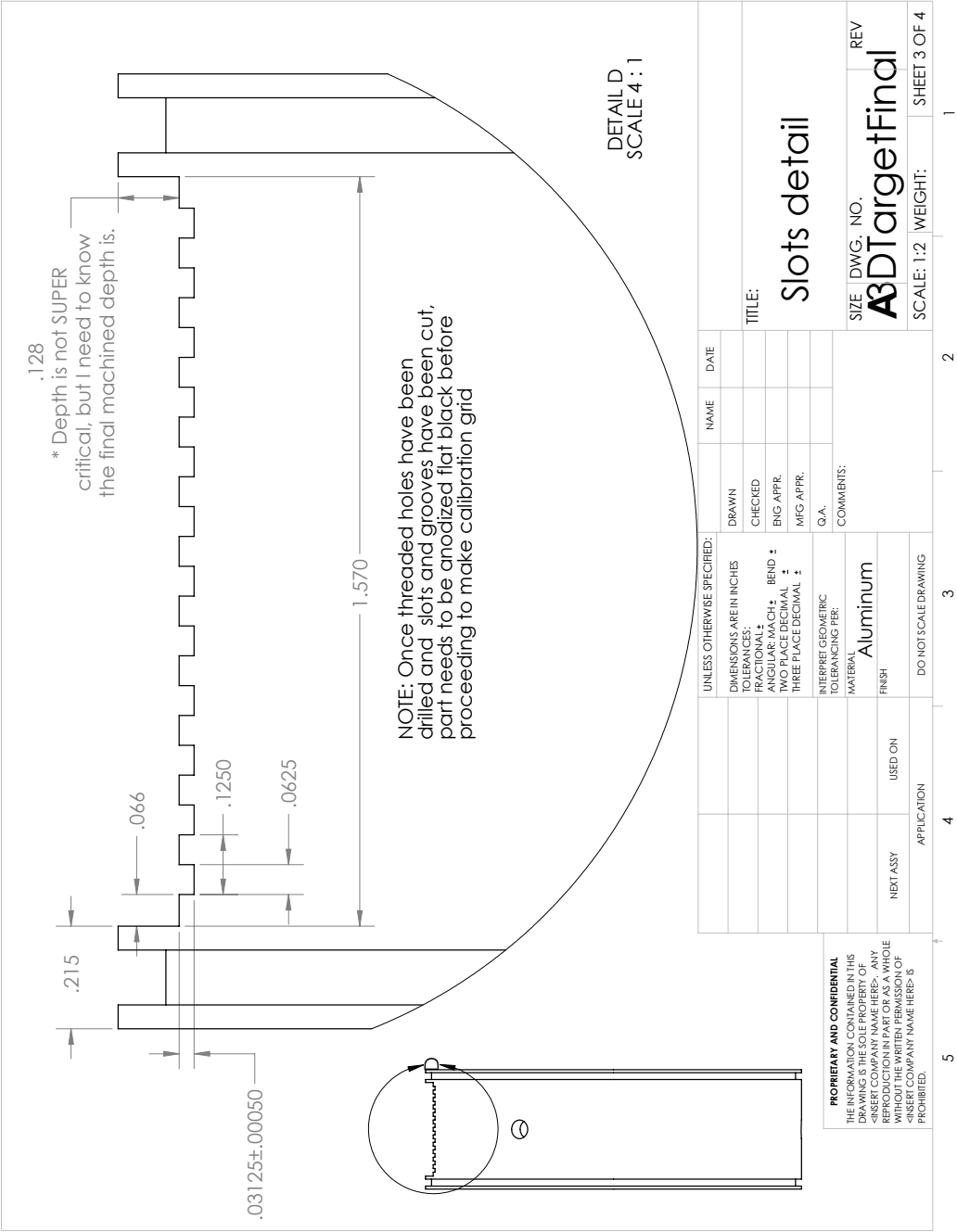
Figure E.2: Detailed Drawing for 3-D Calibration Target Recessed Calibration Plane.
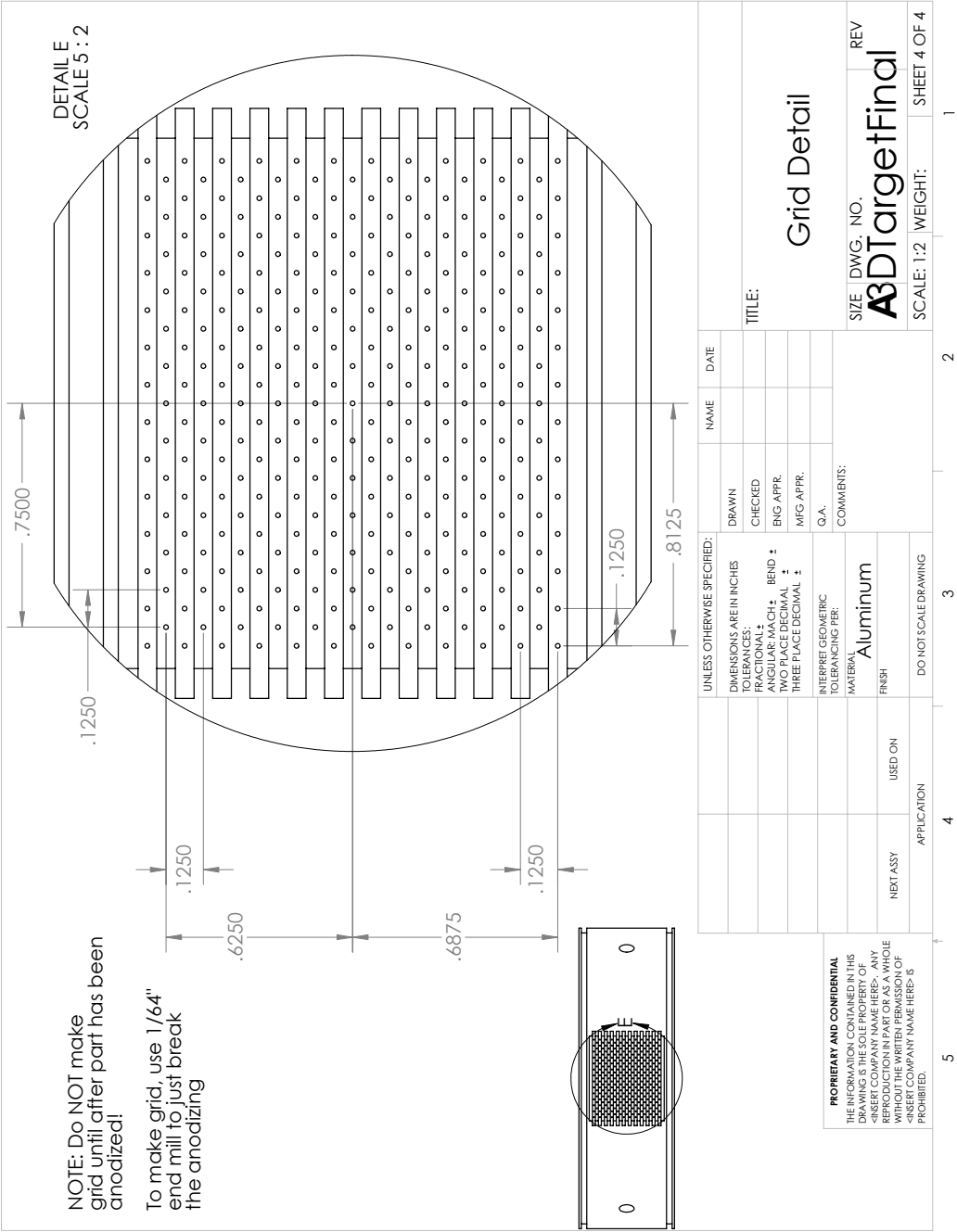
Figure E.3: Detailed Drawing for 3-D Calibration Target Mark Pattern.

214

Figure E.4: Detailed Drawing for 3-D Target O-ring Grooves.
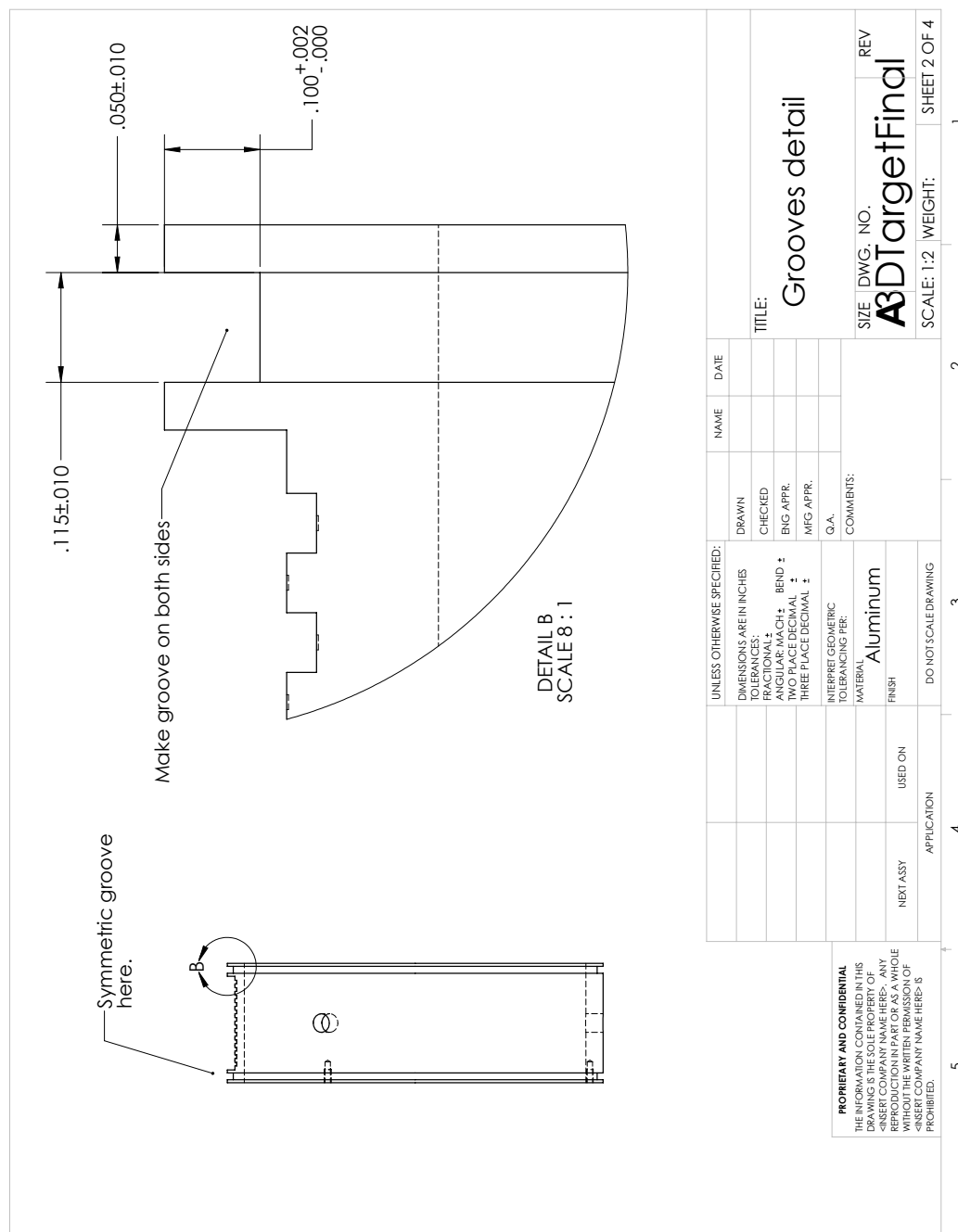
APPENDIX F

DISTRIBUTED PROCESSING CLUSTER

Tomographic PIV can generate huge amounts of data and can require significant computational resources to process. However, because many of the required operations are carried out on a single frame or pair of frames at a time and are independent of the computations that need to be carried out on all the other frames, the process is trivially parallelizable. In order to exploit this, a computer cluster was assembled to distribute the computational load. This consisted of sixteen[1] Lenovo ThinkCentre MT-M-6138-CTO desktop computers with Intel Core 2 Quad processors (running at 2.66 GHz) and 8 GB of memory. The computers were obtained from the School of Physics's Information Technology (IT) department after they were retired from the School's teaching laboratories. They were networked together using a Netgear Prosafe 16 Port Gigabit Switch (model no. GS116) and CAT 6 Ethernet cable and a stand-alone local area network (LAN) was implemented using the 64-bit version of Microsoft's Windows 7 operating system. Windows 7 was chosen over other operating systems because LaVision updates the Windows version of their DaVis software more frequently than those for other operating systems. Because of the novelty of tomographic PIV, algorithms are constantly being improved so being able to use the most up-to-date software took precedence over creating a more general purpose distributed computing environment as would be possible under Linux.

LaVision implements distributed processing via their Distributed Computing in DaVis package. This provides several different options for distributed computing, of which the Master/Slave model was chosen. In this model, a single computer, called the Master DaVis, farms out individual computations to all the other computers, called Remote Workers, and gathers the results. This model was chosen because it has the advantage that it only requires a DaVis license and dongle for the Master DaVis. The Remote Workers do not require a

---

[1]Recently expanded to 30.

216

license but are limited to executing jobs assigned to them by the Master DaVis. They cannot initiate any jobs of their own or display any data. For more details on distributed processing in DaVis, see LaVision Distributed Computing manual [320].

REFERENCES

[1] T. Kreilos, B. Eckhardt, and T. M. Schneider, "Increasing lifetimes and the growing saddles of shear flow turbulence," *Phys. Rev. Lett.*, vol. 112, p. 044503, 2014.

[2] G. Taylor, "Stability of a viscous liquid contained between two rotating cylinders," *Phil. Trans. R. Soc. A*, vol. 223, pp. 289–343, 1923.

[3] S. Chandrasekhar, *Hydrodynamic and Hydromagnetic Stability*. Oxford, UK: Oxford University Press, 1961.

[4] P. Drazin and W. Reid, *Hydrodynamic Stability*. Cambridge, UK: Cambridge University Press, 1981.

[5] E. Koschmieder, *Bénard Cells and Taylor Vortices*. Cambridge, UK: Cambridge University Press, 1993.

[6] M. Cross and P. Hohenberg, "Pattern formation outside of equilibrium," *Rev. Mod. Phys.*, vol. 65, p. 851, 1993.

[7] H. Kurtuldu, *New Methods of Characterizing Spatio-temporal patterns in Laboratory Experiments*. PhD thesis, Georgia Institute of Technology, 2010.

[8] T. Mullin and R. Kerswell, eds., *IUTAM Symposium on Laminar-Turbulent Transition and Finite Amplitude Solutions*, vol. 77 of *Fluid Mechanics and Its Applications*. Dordrecht, The Netherlands: Springer, 2005.

[9] B. Eckhardt, "Turbulence transition in pipe flow: Some open questions," *Nonlinearity*, vol. 21, pp. T1–T11, 2008.

[10] B. Eckhardt, H. Faisst, A. Schmiegel, and T. M. Schneider, "Dynamical systems and the transition to turbulence in linearly stable shear flows," *Phil. Trans. R. Soc. A*, vol. 366, pp. 1297–1315, 2008.

[11] P. Manneville, "On the transition to turbulence of wall-bounded flows in general and plane Couette flow in particular," *Eur. J. Mech B: Fluids*, 2014.

[12] B. Dubrulle, O. Dauchot, F. Daviaud, P.-Y. Longaretti, D. Richard, and J.-P. Zahn, "Stability and turbulent transport in Taylor-Couette flow from analysis of experimental data," *Phys. Fluids*, vol. 17, p. 095103, 2005.

[13] C. D. Andereck, S. S. Liu, and H. L. Swinney, "Flow regimes in a circular Couette system with independently rotating cylinders," *J. Fluid Mech.*, vol. 164, pp. 155–183, 1986.

[14] D. Coles, "Transition in circular Couette flow," *J. Fluid Mech.*, vol. 21, no. 3, pp. 385–425, 1965.

[15] A. Prigent, B. Dubrulle, O. Dauchot, and I. Mutabazi, "The Taylor-Couette flow: The hydrodynamic twin of Rayleigh-Bénard convection," in *Dynamics of Spatio-Temporal Cellular Structures* (I. Mutabazi, J. Wesfreid, and E. Guyon, eds.), vol. 207 of *Springer Tracts in Modern Physics*, pp. 227–242, Springer, 2006.

[16] D. Joseph, *Stability of Fluid Motions I*, vol. 27 of *Springer Tracts in Natural Philosophy*. Berlin, Heidelberg, New York: Springer, 1976.

[17] H. Tennekes and J. Lumley, *A First Course in Turbulence*. Cambridge, MA: The MIT Press, 1972.

[18] S. Pope, *Turbulent Flows*. Cambridge, UK: Cambridge University Press, 2000.

[19] E. Hopf, "A mathematical example displaying features of turbulence," *Commun. Appl. Math.*, vol. 1, p. 303, 1948.

[20] P. Cvitanović and B. Eckhardt, "Periodic orbit expansions for classical smooth flows," *J. Phys. A*, vol. 24, p. L237, 1991.

[21] P. Cvitanović, R. Artuso, R. Mainieri, G. Tanner, and G. Vattay, *Chaos: Classical and Quantum*. Copenhagen: Niels Bohr Inst., 2014. Available online: http://www.chaosbook.org.

[22] P. Holmes, J. Lumley, and G. Berkooz, *Turbulence, Coherent Structures, Dynamical Systems, and Symmetry*. New, York, NY: Cambridge University Press, 1996.

[23] T. Bohr, M. Jensen, G. Paladin, and A. Vulpiani, *Dynamical Systems Approach to Turbulence*, vol. 8 of *Cambridge Nonlinear Science Series*. Cambridge, United Kingdom: Cambridge University Press, 1998.

[24] J. Gibson, J. Halcrow, and P. Cvitanović, "Visualizing the geometry of state space in plane Couette flow," *J. Fluid Mech.*, vol. 611, pp. 107–130, 2008.

[25] J. Gibson and P. Cvitanović, "Movies of plane Couette flow." http://www.chaosbook.org/tutorials, 2014.

[26] G. Kawahara, M. Uhlmann, and L. van Veen, "The significance of simple invariant solutions in turbulent flows," *Ann. Rev. Fluid Mech.*, vol. 44, pp. 203–225, 2012.

[27] M. Nagata, "Three-dimensional finite-amplitude solutions in plane Couette floow: bifurcation from infinity," *J. Fluid Mech.*, vol. 217, pp. 519–527, 1990.

[28] R. Clever and F. Busse, "Tertiary and quaternary solutions for plane Couette flow," *J. Fluid Mech.*, vol. 344, pp. 137–153, 1997.

[29] F. Waleffe, "Three-dimensional coherent states in plane Couette flows," *Phys. Rev. Lett.*, vol. 81, p. 4140, 1998.

[30] H. Faisst and B. Eckhardt, "Traveling waves in pipe flow," *Phys. Rev. Lett.*, vol. 91, p. 224502, 2003.

[31] G. Chandler and R. R. Kerswell, "Invariant recurrent solutions embedded in a turbulent two-dimensional Kolmogorov flow," *J. Fluid Mech.*, vol. 722, pp. 554–595, 2013.

[32] D. Lucas and R. R. Kerswell, "Recurrent flow analysis in spatiotemporally chaotic 2-dimensional Kolmogorov flow." http://arxiv.org/abs/1406.1820, 2014.

[33] B. Hof, C. W. H. van Doorne, J. Westerweel, F. T. M. Nieuwstadt, H. Faisst, B. Eckhardt, H. Wedin, R. R. Kerswell, and F. Waleffe, "Experimental observation of nonlinear traveling waves in turbulent pipe flow," *Nature (London)*, vol. 305, pp. 1594–1598, 2004.

[34] A. de Lozar, F. Mellibovsky, M. Avila, and B. Hof, "Edge state in pipe flow experiments," *Phys. Rev. Lett.*, vol. 108, p. 214502, 2012.

[35] R. Tagg, "The Couette-Taylor problem," *Nonlinear Sci. Today*, vol. 4, no. 3, pp. 1–25, 1994.

[36] R. Tagg, "A guide to literature related to the Taylor-Couette problem," in *Ordered and Turbulent Patterns in Taylor-Couette Flow*, pp. 303–354, New York, NY: Plenum Press, 1992.

[37] R. Di Prima and H. L. Swinney, "Instabilities and transition in flow between concentric rotating cylinders," in *Hydrodynamic Instabilities and the Transition to Turbulence*, pp. 139–180, New York, NY: Springer, 1985.

[38] I. Newton, *Philosophiæ Naturalis Principia Mathematica (trans. Andrew Motte)*. New York, NY: Daniel Adee, 1846.

[39] M. Brillouin, *Leçons sur la Viscosité des Liquides et des Gaz*, vol. 1. Paris, France: Gauthier-Villars, 1907.

[40] J. Piau and M. Piau, "Letter to the editor: Comment on origin of concentric cylinder viscometry [J. Rheol. 49, 807818 (2005)]. The relevance of the early days of viscosity, slip at the wall, and stability in concentric cylinder viscometry," *J. Rheol.*, vol. 49, p. 1539, 2005.

[41] G. G. Stokes, "On the theories of the internal friction of fluids in motion and of the equilibrium and motion of elastic solids," in *Mathematical and Physical Papers*, pp. 102–104, Cambridge, UK: Cambridge University Press, 1880.

[42] R. Donnelly, "Taylor-Couette flow: The early days," *Phys. Today*, pp. 32–39, November 1991.

[43] J. Perry, "Liquid friction," *Philos. Mag.*, vol. 35, pp. 441–458, 1893.

[44] P. Dontula, C. W. Macosko, and L. Scriven, "Origins of concentric cylinders viscometry," *J. Rheol.*, vol. 49, pp. 807–818, 2005.

[45] A. Mallock, "Determination of the viscosity of water," *Proc. R. Soc. London*, vol. 45, pp. 126–132, 1888.

[46] D. Coles and C. Van Atta, "Measured distortion of a laminar circular Couette flow by end effects," *J. Fluid Mech.*, vol. 25, pp. 513–521, 1966.

[47] R. Tagg, "Taylor-Couette Reference List." http://clasfaculty.ucdenver.edu/rtagg/tc_refs/taylor_couette.html, 1999.

[48] M. J. Burin, H. Ji, E. Schartman, C. R., P. Heitzenroeder, W. Liu, L. Morris, and S. Raftopolous, "Reduction of Ekman circulation within Taylor-Couette flow," *Exp. Fluids*, vol. 40, pp. 962–966, 2006.

[49] H. Ji, M. Burin, E. Schartman, and J. Goodman, "Hydrodynamic turbulence cannot transport angular momentum effectively in astrophysical disks," *Nature (London)*, vol. 444, pp. 343–346, 2006.

[50] M. Paoletti and D. Lathrop, "Angular momentum transport in turbulent flow between independently rotating cylinders," *Phys. Rev. Lett.*, vol. 106, p. 024501, 2011.

[51] E. Schartman, H. Ji, M. J. Burin, and J. Goodman, "Stability of quasi-Keplerian shear flow in a laboratory experiment," *Astron. Astrophys.*, vol. 543, p. A94, 2012.

[52] M. Burin and C. Czarnocki, "Subcritical transition and spiral turbulence in circular Couette flow," *J. Fluid Mech.*, vol. 79, pp. 106–122, 2012.

[53] M. Avila, "Stability and angular-momentum transport of fluid flows between corotating cylinders," *Phys. Rev. Lett.*, vol. 108, p. 124501, 2012.

[54] K. Avila and B. Hof, "High-precision Taylor-Couette experiment to study subcritical transitions and the role of boundary conditions and size effects," *Rev. Sci. Instrum.*, vol. 84, p. 065106, 2013.

[55] E. Edlund and H. Ji, "Nonlinear stability of laboratory quasi-Keplerian flows," *Phys. Rev. E*, vol. 89, p. 021004, 2014.

[56] A. Mallock, "Experiments on fluid viscosity," *Phil. Trans. R. Soc. A*, vol. 1897, pp. 41–56, 1896.

[57] J. Piau, M. Bremond, J. Couette, and M. Piau, "Maurice Couette, one of the founders of rheology," *Rheol. Acta*, vol. 33, pp. 357–368, 1994.

[58] R. Donnelly, "Evolution of instrumentation for Taylor-Couette flow," in *Ordered and Turbulent Patterns in Taylor-Couette Flow*, pp. 1–27, New York, NY: Plen, 1992.

[59] E. Drew, "A determination of the viscosity of water," *Phys. Rev.*, vol. 12, pp. 114–120, 1901.

[60] L. Gurney, "The viscosity of water at very low rates of shear," *Phys. Rev.*, vol. 26, pp. 98–120, 1908.

[61] L. Rayleigh, "On the dynamics of revolving fluids," *Proc. R. Soc. Lond. A*, vol. 93, pp. 148–154, 1917.

[62] G. Taylor, "Experiments with rotating fluids," *P. Camb. Philos. Soc.*, vol. 20, pp. 326–329, 1921.

[63] J. Lewis, "An experimental study of the motion of a viscous liquid contained between two coaxial cylinders," *Proc. R. Soc. Lond. A*, vol. 117, pp. 388–407, 1928.

[64] G. Taylor, "Distribution of velocity and temperature between concentric rotating cylinders," *Proc. R. Soc. A*, vol. 151, pp. 494–512, 1935.

[65] G. Taylor, "Fluid friction between rotating cylinders I - Torque measurements," *Proc. R. Soc. A*, vol. 157, pp. 546–564, 1936.

[66] A. Prigent, G. Grégoire, H. Chaté, O. Dauchot, and W. van Saarloos, "Long-wavelength modulation of turbulent shear flows," *Physica D*, vol. 174, pp. 100–113, 2003.

[67] F. Daviaud, J. Hegseth, and P. Berg, "Subcritical transition to turbulence in plane Couette flow," *Phys. Rev. Lett.*, vol. 69, pp. 2511–2514, 1992.

[68] G. Taylor, "Fluid friction between rotating cylinders II - Distribution of velocity between concentric cylinders when outer one is rotating and inner one is at rest," *Proc. R. Soc. A*, vol. 157, pp. 565–578, 1936.

[69] Math Geneology Project, "Fritz Wendt." http://genealogy.impa.br/id.php?id=61669, 2014.

[70] F. Wendt, "Turbulente Strömungen zwischen zwei rotierenden konaxialen Zylindern," *Ing.-Arch.*, vol. 4, pp. 577–595, 1933.

[71] W. H. Hager and U. Liiv, "Johann Nikuradse - Hydraulic experimenter," *J. Hydraul. Res.*, vol. 46, pp. 435–444, 2008.

[72] A. Hollis-Hallett, "Experiments with a rotating cylinder viscometer in liquid helium II," *Math. Proc. Cambridge*, vol. 49, pp. 717–727, 1953.

[73] W. Heikkila and A. Hollis-Hallett, "The viscosity of liquid helium II," *Can. J. Phys.*, vol. 33, pp. 420–435, 1955.

[74] C. Barenghi and C. Jones, "The stability of the Couette flow of helium II," *J. Fluid Mech.*, vol. 197, pp. 551–569, 1988.

[75] H. Hall and W. Vinen, "The rotation of liquid helium II. II: The theory of mutual friction in uniformly rotating helium II," *Proc. R. Soc. Lond. A*, vol. 238, pp. 215–234, 1954.

[76] I. Bekharevich and I. Khalatnikov, "Phenomenological derivation of the equations of motion in He II," *Sov. Phys. JETP*, vol. 13, pp. 643–646, 1961.

[77] R. Hills and P. Roberts, "Superfluid mechanics for a high density of vortex lines," *Arch. Rat. Mech. Anal.*, vol. 66, pp. 43–71, 1977.

[78] R. Donnelly, "Experiments on the hydrodynamic stability of helium II between rotating cylinders," *Phys. Rev. Lett.*, vol. 3, pp. 507–508, 1959.

[79] R. Donnelly and M. LaMar, "Flow and stability of helium II between concentric cylinders," *J. Fluid Mech.*, vol. 186, pp. 163–198, 1988.

[80] R. Bagnold, "Experiments on a gravity-free dispersion of large solid spheres in a Newtonian fluid under shear," *Proc. R. Soc. Lond. A*, vol. 225, pp. 49–63, 1954.

[81] M. Hunt, R. Zenit, C. Campbell, and C. Brennen, "Revisiting the 1954 suspension experiments of R.A. Bangold," *J. Fluid Mech.*, vol. 452, pp. 1–24, 2002.

[82] F. Schultz-Grunow and H. Hein, "Beitrag zur Couetteströmung," *Z. Flugwissensch.*, vol. 4, pp. 28–30, 1956.

[83] J. E. Wesfreid, "Scientific biography of Henri Bénard (1874-1939)," in *Dynamics of Spatio-Temporal Cellular Structures* (I. Mutabazi, J. Wesfreid, and E. Guyon, eds.), vol. 207 of *Springer Tracts in Modern Physics*, pp. 9–37, Springer, 2006.

[84] T. Terada and K. Hattori, "Some experiments on motions of fluids. IV. Formation of vortices by rotating disc, sphere, or cylinder," *Rep. Aeron. Res. Inst. (Tokyo)*, vol. 2, pp. 287–326, 1926.

[85] W. Hagerty, *A Study of the Motion of a Viscous Fluid in a Bounded Annulus of Variable Length.* PhD thesis, University of Michigan - Ann Arbor, 1947.

[86] L. Landau, "On the problem of turbulence," *CR Acad. Sci. URSS*, vol. 44, p. 311, 1944.

[87] D. Ruelle and F. Takens, "On the nature of turbulence," *Commun. Math. Phys.*, vol. 20, pp. 167–192, 1971.

[88] D. Ruelle and F. Takens, "Note concerning our paper "On the nature of turbulence"," *Commun. Math. Phys.*, vol. 23, pp. 343–344, 1971.

[89] J.-P. Eckmann, "Roads to turbulence in dissipative dynamical systems," *Rev. Mod. Phys.*, vol. 53, pp. 643–654, 1981.

[90] J. P. Gollub and H. L. Swinney, "Onset of turbulence in a rotating fluid," *Phys. Rev. Lett.*, vol. 35, pp. 927–930, 1975.

[91] L. Tuckerman and D. Barkley, "Patterns and dynamics in transitional plane Couette flow," *Phys. Fluids*, vol. 23, p. 041301, 2011.

[92] C. Van Atta, "Exploratory measurements in spiral turbulence," *J. Fluid Mech.*, vol. 25, no. 3, pp. 495–512, 1966.

[93] D. Coles and C. Van Atta, "Progress report on a digital experiment in spiral turbulence," *AIAA J.*, vol. 4, pp. 1969–1971, 1966.

[94] D. Coles and C. Van Atta, "Digital experiment in spiral turbulence," *Phys. Fluids*, vol. 10, pp. S120–S121, 1967.

[95] J. Serrin, "On the stability of viscous fluid motions," *Arch. Rat. Mech. Anal.*, vol. 3, pp. 1–13, 1959.

[96] D. Joseph and B. Munson, "Global stability of spiral flow," *J. Fluid Mech.*, vol. 43, pp. 545–575, 1970.

[97] D. Joseph and W. Hung, "Contributions to the nonlinear theory of stability of viscous flow in pipes and between rotating cylinders," *Arch. Rat. Mech. Anal.*, vol. 44, pp. 1–22, 1971.

[98] V. Levinski and J. Cohen, "The evolution of a localized vortex disturbance in external shear flows. Part 1. Theoretical considerations and preliminary experimental results," *J. Fluid Mech.*, vol. 289, p. 159, 1995.

[99] E. Malkiel, V. Levinski, and J. Cohen, "The evolution of a localized vortex disturbance in external shear flows. Part 2. Comparison with experiments in rotating shear flows," *J. Fluid Mech.*, vol. 379, pp. 351–380, 1999.

[100] P. Garaud and G. Ogilvie, "A model for the nonlinear dynamics of turbulent shear flows," *J. Fluid Mech.*, vol. 530, pp. 145–176, 2005.

[101] D. Richard, *Instabilités hydrodynamiques dans les écoulements en rotation diffrentielle.* PhD thesis, Université de Paris VII, 2001.

[102] Y. B. Zeldovich, "On the friction of fluids between rotating cylinders," *Proc. R. Soc. Lond. A*, vol. 374, pp. 299–312, 1981.

[103] B. Dubrulle, "Differential rotation as a source of angular momentum transfer in the solar nebula," *Icarus*, vol. 106, pp. 59–76, 1993.

[104] D. Richard and J.-P. Zahn, "Turbulence in differentially rotating flows - what can be learned from the Couette-Taylor experiment," *Astron. Astrophys.*, vol. 347, pp. 734–738, 1999.

[105] N. Tillmark and P. Alfredsson, "Experiments on rotating plane Couette flow," in *Advances in Turbulence VI* (L. Machiels Gavrilakis and P. Monkewitz, eds.), (Dordrecht, The Netherlands), p. 391, Kluwer Academic, 1996.

[106] Y. Yamada and S. Imao, "Flow of a fluid contained between concentric cylinders both rotating," *B. JSME*, vol. 29, pp. 1691–1697, 1986.

[107] J. Hegseth, C. Andereck, F. Hayot, and Y. Pomeau, "Spiral turbulence and phase dynamics," *Phys. Rev. Lett.*, vol. 62, pp. 257–260, 1989.

[108] F. Hayot and Y. Pomeau, "Turbulent domain stabilization in annular flows," *Phys. Rev. E*, vol. 50, pp. 2019–2021, 1994.

[109] H. Litschke and K. G. Roesner, "New experimental methods for turbulent spots and turbulent spirals in the Taylor-Couette flow," *Exp. Fluids*, vol. 24, pp. 201–209, 1998.

[110] C. Hamill, "Turbulent bursting in the Couette-Taylor system," Master's thesis, The University of Texas at Austin, 1995.

[111] P. W. Colovas and C. D. Andereck, "Turbulent bursting and spatiotemporal intermittency in the counterrotating Taylor-Couette system," *Phys. Rev. E*, vol. 55, pp. 2736–2741, 1997.

[112] K. Coughlin and P. Marcus, "Turbulent bursts in Couette-Taylor flow," *Phys. Rev. Lett.*, vol. 77, pp. 2214–2217, 1996.

[113] A. Goharzadeh and I. Mutabazi, "Experimental characterization of intermittency regimes in the Couette-Taylor system," *Eur. Phys. J. B*, vol. 19, pp. 157–162, 2001.

[114] J. Hegseth, "Turbulent spots in plane Couette flow," *Phys. Rev. E*, vol. 54, pp. 4915–4923, 1996.

[115] S. Bottin and H. Chaté, "Statistical analysis of the transition to turbulence in plane Couette flow," *Eur. Phys. J. B*, vol. 6, pp. 143–155, 1998.

[116] A. Prigent, G. Grégoire, H. Chaté, O. Dauchot, and W. van Saarloos, "Large-scale finite-wavelength modulation within turbulent shear flows," *Phys. Rev. Lett.*, vol. 89, p. 014501, 2002.

[117] A. Prigent and O. Dauchot, "Visualization of a Taylor-Couette flow avoiding parasitic reflections," *Phys. Fluids*, vol. 12, pp. 2688–2690, 2000.

[118] H. Faisst and B. Eckhardt, "Transition from the Couette-Taylor system to the planeCouette system," *Phys. Rev. E*, vol. 61, pp. 7227–7230, 2000.

[119] A. Prigent and O. Dauchot, "Transition to versus from turbulence in subcritical Couette flows," in *IUTAM Symposium on Laminar-Turbulent Transition and Finite Amplitude Solutions* (T. Mullin and R. Kerswell, eds.), vol. 77 of *Fluid Mechanics and its Applications*, pp. 195–219, Springer Netherlands, 2005.

[120] D. Barkley and L. Tuckerman, "Computational study of turbulent laminar ppattern in Couette flow," *Phys. Rev. Lett.*, vol. 94, p. 014502, 2005.

[121] D. Barkley and L. Tuckerman, "Mean flow of turbulent-laminar patterns in plane Couette flow," *J. Fluid Mech.*, vol. 579, pp. 109–137, 2007.

[122] A. Meseguer, F. Mellibovsky, M. Avila, and F. Marques, "Instability mechanisms and transition scenarios of spiral turbulence in Taylor-Couette flow," *Phys. Rev. E*, vol. 80, p. 046315, 2009.

[123] S. Dong, "Evidendence for internal structures of spiral turbulence," *Phys. Rev. E*, vol. 80, p. 067301, 2009.

[124] S. Dong and X. Zheng, "Direct numerical simulation of spiral turbulence," *J. Fluid Mech.*, vol. 668, pp. 150–173, 2011.

[125] M. Paoletti, D. van Gils, B. Dubrulle, C. Sun, D. Lohse, and D. Lathrop, "Angular momentum transport and turbulence in laboratory models of Keplerian flows," *Astron. Astrophys.*, vol. 547, p. A64, 2012.

[126] F. Waleffe, "Homotopy of exact coherent structures in plane shear flows," *Phys. Fluids*, vol. 15, pp. 1517–1534, 2003.

[127] A. Meseguer, F. Mellibovsky, M. Avila, and F. Marques, "Families of subcritical spirals in highly counter-rotating Taylor-Couette flow," *Phys. Rev. E*, vol. 79, p. 036309, 2009.

[128] A. Meseguer, F. Mellibovsky, F. Marques, and M. Avila, "Shear instabilities in Taylor-Couette flow," in *Advanced in Turbulence XII* (B. Eckhardt, ed.), vol. 132 of *Springer Proceedings in Physics*, (Berlin-Heidelberg), Springer-Verlag, 2009.

[129] K. Deguchi, A. Meseguer, and F. Mellibovsky, "Subcritical equilibria in Taylor-Couette flow," *Phys. Rev. Lett.*, vol. 112, p. 184502, 2014.

[130] I. Wygnanski and F. Champagne, "On transition in a pipe. Part 1. The origin of puffs and slugs and the flow in a turbulent slug," *J. Fluid Mech.*, vol. 59, pp. 281–335, 1973.

[131] A. Darbyshire and T. Mullin, "Transition to turbulence in constant-mass-flux pipe flow," *J. Fluid Mech.*, vol. 289, pp. 83–114, 1995.

[132] N. Tillmark and P. H. Alfredsson, "Experiments on transition in plane Couette flow," *J. Fluid Mech.*, vol. 235, pp. 89–102, 1992.

[133] M. Nishioka, S. Iida, and Y. Ichikawa, "An experimental investigation of the stability of plane Poiseuille flow," *J. Fluid Mech.*, vol. 72, pp. 731–751, 1975.

[134] D. R. Calrson, S. E. Widnall, and M. F. Peeters, "A flow-visualization study of transition in plane Poiseuille flow," *J. Fluid Mech.*, vol. 121, pp. 487–505, 1982.

[135] F. Alavyoon, D. S. Henningson, and P. H. Alfredsson, "Turbulent spots in plane Poiseuille flow Flow visualization," *Phys. Fluids*, vol. 29, p. 1328, 1986.

[136] H. Emmons, "The laminar-turbulent transition in a boundary layer. Part I," *J. Aeronaut. Sci.*, vol. 18, pp. 490–498, 1951.

[137] I. Wygnanski, S. M., and F. D., "On a turbulent 'spot' in a laminar boundary layer," *J. Fluid Mech.*, vol. 78, pp. 785–819, 1976.

[138] U. Brosa, "Turbulence without strange attractor," *J. Stat. Phys.*, vol. 55, pp. 1303–1312, 1989.

[139] H. Faisst and B. Eckhardt, "Sensitive dependence on initial conditions in transition to turbulence in pipe flow," *J. Fluid Mech.*, vol. 504, pp. 343–352, 2004.

[140] T. M. Schneider and B. Eckhardt, "Lifetime statistics in transitional pipe flow," *Phys. Rev. E*, vol. 78, p. 046310, 2008.

[141] T. Mullin and J. Peixinho, "Transition to turbulence in pipe flow," *J. Low Temp. Phys.*, vol. 145, pp. 75–88, 2006.

[142] J. Peixinho and T. Mullin, "Decay of turbulence in pipe flow," *Phys. Rev. Lett.*, vol. 96, p. 094501, 2006.

[143] B. Hof, J. Westerweel, T. M. Schneider, and B. Eckhardt, "Finite lifetime of turbulence in shear flows," *Nature (London)*, vol. 443, no. 7, pp. 59–62, 2006.

[144] A. P. Willis and R. R. Kerswell, "Critical behavior in the relaminarization of localized turbulence in pipe flow," *Phys. Rev. Lett.*, vol. 98, p. 014501, 2007.

[145] M. Lagha and P. Manneville, "Modeling transitional plane Couette flow," *Eur. Phys. J. B*, vol. 58, pp. 433–447, 2007.

[146] B. Hof, A. de Lozar, D. J. Kuik, and J. Westerweel, "Repeller or attractor? Selecting the dynamical model for the onset of turbulence in pipe flow.," *Phys. Rev. Lett.*, vol. 101, no. 21, p. 214501, 2008.

[147] M. Avila, A. P. Willis, and B. Hof, "On the transient nature of localized pipe flow turbulence," *J. Fluid Mech.*, vol. 646, pp. 127–136, 2010.

[148] E. L. Rempel, G. Lesur, and M. R. E. Proctor, "Supertransient magnetohydrodynamic turbulence in Keplerian shear flows," *Phys. Rev. Lett.*, vol. 105, p. 044501, 2010.

[149] W. Schoepe, "Fluctuations and stability of superfluid turbulence at mK temperatures," *Phys. Rev. Lett.*, vol. 92, p. 095301, 2004.

[150] L. P. Kadanoff and C. Tang, "Escape from strange repellers," *Proc. Nat. Acad. Sci. U.S.A.*, vol. 81, pp. 1276–1279, 1984.

[151] H. Kantz and P. Grassberger, "Repellers, semi-attractors, and long-lived chaotic transients," *Physica D*, vol. 17, pp. 75–86, 1985.

[152] G.-H. Hsu, E. Ott, and C. Grebogi, "Strange saddles and the dimensions of their invariant manifolds," *Phys. Lett. A*, vol. 127, pp. 199–204, 1988.

[153] S. Ross, *A First Course in Probability*. Upper Saddle River, NJ: Prentice Hall, 2002.

[154] C. Grebogi and E. Ott, "Crises, sudden changes in chaotic aattractor, and transient chaos," *Physica D*, vol. 7, pp. 181–200, 1983.

[155] P. Manneville, "Understanding the sub-critical transition to turbulence in wall flows," *Pramana*, vol. 70, no. 6, pp. 1009–1021, 2008.

[156] T. Shinbrot, C. Grebogi, E. Ott, and J. A. Yorke, "Using small perturbations to control chaos," *Nature (London)*, vol. 363, pp. 411–417, 1993.

[157] F. Schultz-Grunow, "Zur Stabilität der Couette-Strömung," *Z. Angew. Math. Mech.*, vol. 39, p. 101110, 1959.

[158] A. Alidai, "Transient turbulence in Taylor-Couette flow," Master's thesis, Delft University of Technology, 2011.

[159] A. Esser and S. Grossmann, "Analytic expression for Taylor-Couette stability boundary," *Phys. Fluids*, vol. 8, no. 7, pp. 1814–1819, 1996.

[160] D. A. Hirst, *The Aspect Ratio Dependence of the Attractor Dimension in Taylor-Couette Flow*. PhD thesis, The University of Texas at Austin, 1987.

[161] Compumotor Division, Parker Hannafin Corporation, 5500 Business Park Drive, Rohnert Park, California 94928, *Compumotor Model 2100 Indexer User Guide*, 1996.

[162] Minco Products, Inc, Fridley, Minnesota, *Report of Calibration for Platinum Resistance Thermometer Model S1059PA5X6 Serial No. 560*, March 1997.

[163] P. Matisse, "Kalliroscopes - History." http://www.paulmatisse.com/history/, 2014.

[164] P.H.R. Matisse, "Graphic Display." U.S. Patent 3 464 132 (A), Sep. 2, 1969.

[165] R. Krishnamurti, "On the transition to turbulent convetion. Part 1. The transition from two- to three-dimensional flow," *J. Fluid Mech.*, vol. 42, pp. 295–307, 1970.

[166] M. Keith, "Ocean-floor convergence: A contrary view of global techtonics," *J. Geol.*, vol. 80, pp. 249–276, 1972.

[167] W. M. Phillips, J. A. Brighton, and W. S. Pierce, "Artificial heart evaluation using flow visualization techniques," *T. Am. Soc. Art. Int. Org.*, vol. 18, pp. 194–199, 1972.

[168] G. Willis, J. Deardorff, and R. Somerville, "Roll-diameter dependence in Rayleigh convection and its effect upon the heat flux," *J. Fluid Mech.*, vol. 54, pp. 351–367, 1972.

[169] M. Sorrentino and S. Mason, "Rheo- and electro-optical behavior of platelets," *J. Colloid Interface Sci.*, vol. 41, pp. 178–181, 1972.

[170] R. Krishnamurti, "Some further studies on the transtion to turbulent convetion," *J. Fluid Mech.*, vol. 60, pp. 285–303, 1973.

[171] F. Busse and C. Carrigan, "Convection induced by centrifugal buoyancy," *J. Fluid Mech.*, vol. 62, pp. 579–592, 1974.

[172] K. B. Katsaros, W. Liu, J. Businger, and J. Tillman, "Heat transport and thermal structure in the interfacial boundary layer measured in an open tank of water in turbulent free convection," *J. Fluid Mech.*, vol. 83, pp. 311–335, 1977.

[173] E. Davis and C. Choi, "Cellular convection with liquid-film flow," *J. Fluid Mech.*, vol. 81, pp. 565–592, 1977.

[174] H. Swinney, P. R. Fenstermacher, and J. Gollup, "Transition to turbulence in a fluid flow," in *Synergetics* (H. Haken, ed.), vol. 2 of *Springer Series in Synergetics*, pp. 60–69, Berlin, Germany: Springer-Verlag, 1977.

[175] H. Swinney and J. P. Gollub, "The transtion to turbulence," *Phys. Today*, pp. 41–49, August 1978.

[176] K. B. Katsaros, "Turbulent free convection in fresh and salt water: Some characteristics revealed by visualization," *J. Phys. Oceanogr.*, vol. 8, pp. 613–626, 1978.

[177] P. Fenstermacher, H. Swinney, and J. P. Gollub, "Dynamical instabilities and the transition to chaotic Taylor vortex flow," *J. Fluid Mech.*, vol. 94, pp. 103–128, 1979.

[178] M. Gorman and H. Swinney, "Visual observation of the second characteristic mode in a quasiperiodic flow," *Phys. Rev. Lett.*, vol. 43, pp. 1871–1875, 1979.

[179] P. Matisse and M. Gorman, "Neutrally buoyant anisotropic particles for flow visualization," *Phys. Fluids*, vol. 27, no. 4, pp. 759–760, 1984.

[180] M. Dominguez-Lerma, G. Ahlers, and D. S. Cannell, "Effects of "Kalliroscope" flow visualization particles on rotating Couette-Taylor flow," *Phys. Fluids*, vol. 28, no. 4, pp. 1204–1206, 1985.

[181] G. Gauthier, P. Gondret, and M. Rabaud, "Motions of anisotropic particles: Application to visualization of three-dimensional flows," *Phys. Fluids*, vol. 10, no. 9, pp. 2147–2154, 1998.

[182] O. Savas, "On flow visualization using reflective flakes," *J. Fluid Mech.*, vol. 152, pp. 235–248, 1985.

[183] N. Abcha, N. Latrache, O. Crumeyrolle, and I. Mutabazi, "Qualitative relation between reflected light intensity by Kalliroscope flakes and velocity field in the Couette-Taylor flow system," *Exp. Fluids*, vol. 45, pp. 85–94, 2008.

[184] S. Goto, S. Kida, and S. Fujiwara, "Flow visualization using reflective flakes," *J. Fluid Mech.*, vol. 683, pp. 417–429, 2011.

[185] S. Thoroddsen and J. Bauer, "Qualitative flow visualization using colored lights and reflective flakes," *Phys. Fluids*, vol. 11, pp. 1702–1704, 1999.

[186] W. L. Barth and C. A. Burns, "Virtual rheoscopic fluids for flow visualization," *IEEE T. Vis. Comput. Gr.*, vol. 13, pp. 1751–1758, 2007.

[187] F. Hecht, P. J. Mucha, and G. Turk, "Virtual rheoscopic fluids," *IEEE T. Vis. Comput. Gr.*, vol. 16, pp. 147–160, 2010.

[188] D. S. Moore and G. P. McCabe, *Introduction to the Practice of Statistics*. New York, New York: W.H. Freeman and Company, 4 ed., 2003.

[189] K. Avila, D. Moxey, A. de Lozar, M. Avila, D. Barkley, and B. Hof, "The onset of turbulence in pipe flow," *Science*, vol. 333, pp. 192–196, 2011.

[190] B. Hof, A. de Lozar, M. Avila, X. Tu, and T. M. Schneider, "Eliminating turbulence in spatially intermittent flows," *Science*, vol. 327, pp. 1491–1494, 2010.

[191] N. Goldenfeld, N. Guttenberg, and G. Gioia, "Extreme fluctuations and the finite lifetime of the turbulent state," *Phys. Rev. E*, vol. 81, p. 035304(R), 2010.

[192] P. Manneville, "Spatiotemporal perspective on the decay of turbulence in wall-bounded flows," *Phys. Rev. E*, vol. 79, p. 025301, 2009.

[193] A. P. Willis and R. R. Kerswell, "Turbulent dynamics of pipe flow captured in a reduced model: puff relaminarization and localized 'edge' states," *J. Fluid Mech.*, vol. 619, pp. 213–233, 2009.

[194] Y. Pomeau, "Front motion, metastability and subcritical bifurcations in hydrodynamics," *Physica D*, vol. 23, pp. 3–11, 1986.

[195] B. Eckhardt and H. Faisst, "Dynamical systems and the transition to turbulence," in *IUTAM Symposium on Laminar-Turbulent Transition and Finite Amplitude Solutions* (T. Mullin and R. Kerswell, eds.), vol. 77 of *Fluid Mechanics and Its Applications*, (Dordrecht, The Netherlands), pp. 35–50, Springer, 2005.

[196] A. de Lozar and B. Hof, "An experimental study of the decay of turbulent puffs in pipe flow," *Phil. Trans. R. Soc. A*, vol. 367, pp. 589–599, 2009.

[197] G. Kreiss, A. Lundbladh, and D. Henningson, "Bounds for threshold aamplitude in subcritical shear flows," *J. Fluid Mech.*, vol. 270, pp. 175–198, 1994.

[198] O. Dauchot and F. Daviaud, "Finite amplitude perturbation and spots growth mechanism in plane Couette flow," *Phys. Fluids*, vol. 7, pp. 335–343, 1995.

[199] S. Chapman, "Subcritical transtion in channel flows," *J. Fluid Mech.*, vol. 451, pp. 35–97, 2002.

[200] B. Hof, A. Juel, and T. Mullin, "Scaling of the turbulence transition threshold in a pipe," *Phys. Rev. Lett.*, vol. 91, p. 244502, 2003.

[201] F. Mellibovsky and A. Meseguer, "The role of streamwise perturbations in pipe flow transition," *Phys. Fluids*, vol. 18, p. 074104, 2006.

[202] F. Mellibovsky and A. Meseguer, "Pipe flow transition threshold following localized impulsive perturbations," *Phys. Fluids*, vol. 19, p. 044102, 2007.

[203] F. Mellibovsky and Mes, "Critical threshold in pipe flow transtion," *Phil. Trans. R. Soc. A*, vol. 367, pp. 545–560, 2009.

[204] J. Peixinho and T. Mullin, "Finite-amplitude thresholds for transition in pipe flow," *J. Fluid Mech.*, vol. 582, pp. 169–178, 2007.

[205] G. Lemoult, J.-L. Aider, and J. E. Wesfreid, "Experimental scaling law for the subcritical transition to turbulence in plane Poiseuille flow," *Phys. Rev. E*, vol. 85, p. 025303(R), 2012.

[206] W. Pfenniger, "Transition in the inlet length of tubes at high Reynolds numbers," in *Boundary Layer and Flow Control* (G. Lachman, ed.), (Oxford, UK), pp. 970–980, Pergamon, 1961.

[207] L. Trefethen, A. Trefethen, S. Reddy, and T. Driscoll, "Hydrodynamic stability without eigenvalues," *Science*, vol. 261, pp. 578–584, 1993.

[208] B. Hof, "Transition to turbulence in pipe flow," in *IUTAM Symposium on Laminar-Turbulent Transition and Finite Amplitude Solutions* (T. Mullin and R. Kerswell, eds.), vol. 77 of *Fluid Mechanics and Its Applications*, (Dordrecht, The Netherlands), pp. 221–231, Springer, 2005.

[209] J. Philip, A. Svizher, and J. Cohen, "Scaling law for a subcritical transition in plane Poiseuille flow," *Phys. Rev. Lett.*, vol. 98, p. 154502, 2007.

[210] G. Ben-Dov and J. Cohen, "Critical Reynolds number for a natural transition to turbulence in pipe flows," *Phys. Rev. Lett.*, vol. 98, p. 064503, 2007.

[211] D. Henningson and G. Kreiss, "Threshold amplitudes in subcritical shear flows," in *IUTAM Symposium on Laminar-Turbulent Transition and Finite Amplitude Solutions* (T. Mullin and R. Kerswell, eds.), vol. 77 of *Fluid Mechanics and Its Applications*, (Dordrecht, The Netherlands), pp. 233–249, Springer, 2005.

[212] S. Grossmann, "The onset of shear flow turbulence," *Rev. Mod. Phys.*, vol. 72, no. 2, pp. 603–618, 2000.

[213] L. Trefethen, S. Chapman, D. Henningson, A. Meseguer, T. Mullin, and F. Nieuwstadt, "Threshold amplitudes for transtion to turbulence in a pipe." http://arxiv.org/abs/arXiv:physics/0007092, 2000.

[214] J. Baggett and L. Trefethen, "Low-dimensional models of subcritical transition to turbulence," *Phys. Fluids*, vol. 9, p. 1043, 1997.

[215] F. Waleffe, "Transition in shear flows: Non-linear normality vs. non-normal linearity," *Phys. Fluids*, vol. 7, p. 3060, 1995.

[216] T. Gebhardt and S. Grossmann, "The Taylor-Couette eigenvalue problem with independently rotating cylinders," *Z. Phys. B: Condens. Matter*, vol. 90, pp. 475–490, 1993.

[217] H. Hristova, S. Roch, P. Schmid, and L. Tuckerman, "Transient growth in Couette-Taylor flow," in *Proceedings of the 12th International Couette-Taylor Workshop* (R. Lueptow, ed.), 2001.

[218] H. Hristova, S. Roch, P. Schmid, and L. Tuckerman, "Transient growth in Taylor-Couette flow," *Phys. Fluids*, vol. 14, pp. 3475–3484, 2002.

[219] S. Maretzke, B. Hof, and M. Avila, "Transient growth in linearly stable Taylor-Couette flows," *J. Fluid Mech.*, vol. 742, pp. 254–290, 2014.

[220] T. M. Schneider, B. Eckhardt, and J. A. Yorke, "Turbulence transition and the edge of chaos in pipe flow," *Phys. Rev. Lett.*, vol. 99, p. 034502, 2007.

[221] D. Viswanath, "Recurrent motions within plane Couette turbulence," *J. Fluid Mech.*, vol. 580, pp. 339–358, 2007.

[222] R. Panton, *Incompressible Flow.* Hoboken, NJ: Wiley, 3 ed., 2005.

[223] J. Peixinho. Private communication, February 2010.

[224] A. Meseguer, "Energy transient growth in the Taylor-Couette problem," *Phys. Fluids*, vol. 14, pp. 1655–1660, 2002.

[225] ANSYS, Inc., 275 Technology Drive, Canonsburg, Pennsylvania, *ANSYS Fluent Theory Guide*, October 2012.

[226] R. Adrian and J. Westerweel, *Particle Image Velocimetry.* Cambridge, UK: Cambridge University Press, 2011.

[227] P. Cvitanović, "Recurrent flows: The clockwork behind turbulence," *J. Fluid Mech.*, vol. 726, pp. 1–4, 2013.

[228] G. Kawahara and S. Kida, "Periodic motion embedded in plane Couette turbulence: regeneration cycle and burst," *J. Fluid Mech.*, vol. 449, pp. 291–300, 2001.

[229] T. Itano and S. Toh, "The dynamics of bursting process in wall turbulence," *J. Phys. Soc. Japan*, vol. 70, pp. 703–716, 2001.

[230] C. Pringle and R. Kerswell, "Asymmetric, helical, and mirror-symmetric traveling waves in pipe flow," *Phys. Rev. Lett.*, vol. 99, p. 074502, 2007.

[231] T. M. Schneider, J. Gibson, and J. Burke, "Snakes and ladders: Localized solutions of plane Couette flow," *Phys. Rev. Lett.*, vol. 104, p. 104501, 2010.

[232] T. Kreilos and B. Eckhardt, "Periodic orbits near onset of chaos in plane Couette flow," *Chaos*, vol. 22, p. 047505, 2012.

[233] R. Kerswell, "Recent progress in understanding the transition to turbulence in a pipe," *Nonlinearity*, vol. 18, pp. 17–44, 2005.

[234] J. J. Halcrow, *Charting the state space of planeCouette flow: Equilibria, relative equilibria, and heteroclinic connections.* PhD thesis, Georgia Institute of Technology, July 2008.

[235] J. Halcrow, J. Gibson, P. Cvitanović, and D. Viswanath, "Heteroclinic connections in plane Couette flow," *J. Fluid Mech.*, vol. 621, pp. 365–376, 2009.

[236] D. Viswanath and P. Cvitanović, "Stable manifolds and the transition to turbulence in pipe flow," *J. Fluid Mech.*, vol. 627, pp. 215–233, 2009.

[237] P. Cvitanović and J. Gibson, "Geometry of the turbulence in wall-bounded shear flows: periodic orbits," *Phys. Scr.*, vol. T142, p. 014007, 2010.

[238] B. Eckhardt, "Turbulence transition in shear flows: Chaos in high-dimensional spaces," *Procedia IUTAM*, vol. 5, pp. 165–168, 2012.

[239] A. Willis, P. Cvitanović, and M. Avila, "Revealing the state space of turbulent pipe flow by symmetry reduction," *J. Fluid Mech.*, vol. 721, pp. 514–540, 2013.

[240] M. Raffel, C. Willert, S. T. Wereley, and J. Kompenhans, *Particle image velocimetry: a practical guide.* New York, NY: Springer, 2nd ed., 2007.

[241] B. Baumert, D. Liepmann, and S. Muller, "Digital particle image velocimetry in flows with nearly closed pathlines: the viscoelastic Taylor-Couette instability.," *J. Non-Newton. Fluid.*, vol. 69, pp. 221–237, 1997.

[242] S. T. Wereley and R. M. Lueptow, "Spatio-temporal character of non-wavy and wavy Taylor-Couette flow," *J. Fluid Mech.*, vol. 364, pp. 59–80, 1998.

[243] S. T. Wereley and R. M. Lueptow, "Velocity field for Taylor-Couette flow with an axial flow," *Phys. Fluids*, vol. 11, pp. 3637–3649, 1999.

[244] S. T. Wereley, A. Akonur, and R. M. Lueptow, "Particle-fluid velocities and fouling in rotating filtration of a suspension," *J. Membr. Sci.*, vol. 209, pp. 469–484, 2002.

[245] B. Judat, A. Racina, and M. Kind, "Macro- and micromixing in a Taylor-Couette reactor with axial flow and their influence on the precipitation of barium sulfate," *Chem. Eng. Technol.*, vol. 27, pp. 287–292, 2004.

[246] M. Smieszek and C. Egbers, "Flow structures and stability in Newtonian and non-Newtonian Taylor-Couette flow," *J. Phys.: Conf. Ser.*, vol. 14, pp. 72–77, 2005.

[247] L. Wang, M. Olsen, and R. Vigil, "Reappearance of azimuthal waves in turbulent Taylor-Couette flow at large aspect ratio," *Chem. Eng. Sci.*, vol. 60, pp. 5555–5568, 2005.

[248] C. Coufort, D. Bouyer, and A. Liné, "Flocculation related to local hydrodynamics in a Taylor-Couette reactor and in a jar," *Chem. Eng. Sci.*, vol. 60, pp. 2179–2192, 2005.

[249] A. Racina and M. Kind, "Specific power input and local micromixing times in turbulent Taylor-Couette flow," *Exp. Fluids*, vol. 41, pp. 513–522, 2006.

[250] R. Deng, D. Arifin, Y. Mak, and C.-H. Wang, "Characterization of Taylor vortex flow in a short liquid column," *AIChE J.*, vol. 55, pp. 3056–3065, 2009.

[251] S.-H. Lee, H.-T. Chung, C.-W. Park, and H.-B. Kim, "Experimental investigation of the effect of axial wall slits on Taylor-Couette flow," *Fluid Dyn. Res.*, vol. 41, p. 045502, 2009.

[252] M. Sathe, S. Deshmukh, J. Joshi, and S. Koganti, "Computational fluid dynamics simulation and experimental investigation: Study of two-phase liquid-liquid flow in a vertical Taylor-Couette contactor," *Ind. Eng. Chem. Res.*, vol. 49, pp. 14–28, 2010.

[253] R. van Hout and J. Katz, "Measurements of mean flow and turbulence characteristics in high-Reynolds number counter-rotating Taylor-Couette flow," *Phys. Fluids*, vol. 23, p. 105102, 2011.

[254] S. Huisman, D. van Gils, S. Grossmann, C. Sun, and D. Lohse, "Ultimate turbulent Taylor-Couette flow," *Phys. Rev. Lett.*, vol. 108, p. 024501, 2012.

[255] S. Grossmann and D. Lohse, "Multiple scaling in the ultimate regime of thermal convection," *Phys. Fluids*, vol. 23, p. 045108, 2011.

[256] A. Akonur and R. M. Lueptow, "Three-dimensional velocity field for wavy Taylor-Couette flow," *Phys. Fluids*, vol. 15, no. 4, pp. 947–960, 2003.

[257] A. Akonur and R. M. Lueptow, "Chaotic mixing and transport in wavy Taylor-Couette flow," *Physica D*, vol. 167, pp. 183–196, 2002.

[258] F. Ravelet, R. Delfos, and J. Westerweel, "Influence of global rotation and reynolds number on the large-scale features of a turbulent Taylor-Couette flow," *Phys. Fluids*, vol. 22, p. 055103, 2010.

[259] M. P. Arroyo and K. D. Hinsch, "Recent developments of PIV towards 3D measurements," in *Particle image velocimetry* (A. Schroeder and C. Willert, eds.), vol. 112 of *Topics in Applied Physics*, pp. 127–154, Berlin, Germany: Springer-Verlag, 2008.

[260] K. D. Hinsch, "Three-dimensional particle velocimetry," *Meas. Sci. Technol.*, vol. 6, pp. 742–753, 1995.

[261] K. D. Hinsch, "Holographic particle image velocimetry," *Meas. Sci. Technol.*, vol. 13, pp. R61–72, 2002.

[262] S. Herrmann and K. D. Hinsch, "Light-in-flight holographic particle image velocimetry," *Meas. Sci. Technol.*, vol. 15, pp. 613–621, 2004.

[263] J. Sheng, E. Malkiel, , and J. Katz, "Digital holographic microscope for measuring three-dimensional particle distributions and motions," *Appl. Opt.*, vol. 45, pp. 3893–3901, 2006.

[264] S. S. Orlov, S. I. Abarzhi, S. B. Oh, G. Barbastathis, and K. R. Sreenivasan, "High-performance holographic technologies for fluid-dynamics experiments," *Phil. Trans. R. Soc. A*, vol. 368, pp. 1705–1737, 2010.

[265] C. Brücker, "3-D scanning PIV applied to an air flow in a motored engine using digital high-speed video," *Meas. Sci. Technol.*, vol. 8, pp. 1480–1492, 1997.

[266] T. Hori and J. Sakakibara, "High-speed scanning stereoscopic PIV for 3D vorticity measurement in liquids," *Meas. Sci. Technol.*, vol. 15, pp. 1067–1078, 2004.

[267] S. Burgmann, C. Brücker, and W. Schroder, "Scanning PIV measurements of a laminar separation bubble," *Exp. Fluids*, vol. 41, pp. 319–326, 2006.

[268] Y. Cheng, M. Torregrosa, A. Villegas, and F. Diez, "Time resolved scanning PIV measurements at fine scales in a turbulent jet," *Int. J. Heat Fluid Flow*, vol. 32, pp. 708–718, 2011.

[269] L. Schaefer, J. Goebbert, M. Klaas, and W. Schroeder, "Comparison of holographic and tomographic particle-image velocimetry turbulent channel flow measurements," in 9th *International Symposium on Particle Image Velocimetry*, (Kobe, Japan), 2011.

[270] F. Scarano, "Tomographic PIV: principles and practice," *Meas. Sci. Technol.*, vol. 24, p. 012001, 2013.

[271] H. Meng, G. Pan, Y. Pu, and S. H. Woodward, "Holographic particle image velocimetry: From film to digital recording," *Meas. Sci. Technol.*, vol. 15, pp. 673–685, 2004.

[272] S. Huisman, D. van Gils, and S. Chao, "Applying laser Doppler anemometry inside a Taylor-Couette geometry using a ray-tracer to correct for curvature effects," *Eur. J. Mech B: Fluids*, vol. 36, pp. 115–119, 2012.

[273] C. Willert and M. Gharib, "Three-dimensional particle imaging using a single camera," *Exp. Fluids*, vol. 12, pp. 353–358, 1992.

[274] F. Pereira, M. Gharib, D. Dabiri, and D. Modarress, "Defocusing digital particle image velocimetry: A 3-component 3-dimensional DPIV measurement technique: Application to bubbly flows," *Exp. Fluids*, vol. 29, pp. S78–S84, 2000.

[275] L. Kajitani and D. Dabir, "A full three-dimensional characterization of defocusing digital particle velocimetry," *Meas. Sci. Technol.*, vol. 16, pp. 790–804, 2005.

[276] E. Castao Graff, F. Pereira, and M. Gharib, "Defocusing digital particle image velocimetry: A volumetric DPIV technique for dual and single phase flows," in *14th International Symposium on Applications of Laser Techniques to Fluid Mechanics*, (Lisbon, Portugal), 2008.

[277] F. Pereira and M. Gharib, "Defocusing digital particle image velocimetry and the three-dimensional characterization of two-phase flows," *Meas. Sci. Technol.*, vol. 13, pp. 683–694, 2002.

[278] P. Russell, "Secret of the Hartmann mask... Revealed!." http://www.iceinspace.com.au/index.php?id=63,187,0,0,1,0, April 2005.

[279] G. E. Elsinga, F. Scarano, B. Wieneke, and B. W. van Oudheusden, "Tomographic particle image velocimetry," *Exp. Fluids*, vol. 41, pp. 933–947, 2006.

[280] H.-G. Maas, A. Gruen, and D. Papantoniou, "Particle tracking velocimetry in three-dimensional flows," *Exp. Fluids*, vol. 15, pp. 133–146, 1993.

[281] G. Herman and A. Lent, "Iterative reconstruction algorithms," *Comput. Biol. Med.*, vol. 6, pp. 273–294, 1976.

[282] S. Tokgoz, G. Elsinga, R. Delfos, and J. Westerweel, "Spatial resolution and dissipation rate estimation in Taylor-Couette flow for tomographic PIV," *Exp. Fluids*, vol. 53, pp. 561–583, 2012.

[283] G. Elsinga, B. W. van Oudheusden, and F. Scarano, "Experimental assessment of tomographic-PIV accuracy," in *13ᵗʰ International Symposium on Applications of Laser Techniques to Fluid Mechanics*, (Lisbon, Portugal), 2006.

[284] A. Schröder, R. Geisler, and D. Michaelis, "Flow structures in a tripped turbulent boundary layer flow: An investigation using time-resolved tomographic PIV," in *7ᵗʰ International Symposium on Particle Image Velocimetry*, 2007.

[285] F. Scarano and C. Poelma, "Three-dimensional vorticity patterns of cylinder wakes," *Exp. Fluids*, vol. 47, pp. 69–83, 2009.

[286] C. Atkinson, S. Coudert, J.-M. Foucaut, M. Stanislas, and J. Soria, "The accuracy of tomographic particle image velocimetry for measurements of a turbulent boundary layer," *Exp. Fluids*, vol. 50, pp. 1031–1056, 2011.

[287] A. Prasad and K. Jensen, "Scheimpflug stereocamera for particle image velocimetry in liquid flows," *Appl. Opt.*, vol. 34, pp. 7092–7099, 1995.

[288] A. Melling, "Tracer particles and seeding for particle image velocimetry," *Meas. Sci. Technol.*, vol. 8, pp. 1406–1416, 1997.

[289] S. Someya, J. Kuwabara, Y. Li, and K. Okamoto, "Experimental investigation of a flow-induced oscillating cylinder with two degrees-of-freedom," *Nucl. Eng. Des.*, vol. 240, p. 40014007, 2010.

[290] S. Prahl, *Rhodamine 6G*. Oregon Medical Laser Center, URL: http://omlc.ogi.edu/spectra/PhotochemCAD/html/083.html, Accessed June 18, 2013.

[291] F. Pedocchi, J. E. Martin, and M. H. García, "Inexpensive fluorescent particles for large-scale experiments using particle image velocimetry," *Exp. Fluids*, vol. 45, p. 183186, 2008.

[292] C. D. Dudgeon, "Polyester resins," in *Composites*, vol. 1 of *Engineered Materials Handbook*, CRC Press, 1987.

[293] G. Duran Group, "Duran precision bore tubing brochure." http://www.duran-group.com/uploads/tx_fedownloads/DURAN_Precision_bore_tubing_E.pdf, 2014.

[294] I. Filmetrics, "Refractive index of BK7, float glass." http://www.filmetrics.com/refractive-index-database/BK7/Float-Glass, 2014.

[295] S. Khodier, "Refractive index of standard oils as a function of wavelewave and temperature," *Opt. Laser Technol.*, vol. 34, pp. 125–128, 2002.

[296] H. G. Hooper, "Experimental studies of the hemodynamics in abdominal aortic aneurysms," Master's thesis, University of Idaho, 1992.

[297] R. Budwig, D. Elger, H. Hooper, and J. Slippy, "Steady flow in abdominal aortic aneurysm models," *Trans. ASME, J. Biomech. Eng.*, vol. 115, pp. 418–423, 1993.

[298] C. Egelhoff, R. Budwig, D. Elger, T. Khraishi, and K. Johansen, "Model studies of the flow in abdominal aortic aneurysms during resting and exercise conditions," *J. Biomech.*, vol. 32, pp. 1319–1329, 1999.

[299] B. Bailey and M. Yoda, "An aqueous low-viscosity density- and refractive index-matched suspension system," *Exp. Fluids*, vol. 35, p. 13, 2003.

[300] V. A. Patil and J. A. Liburdy, "Flow characterization using PIV measurements in a low aspect ratio randomly packed porous bed," *Exp. Fluids*, vol. 54, p. 1497, 2013.

[301] R. Budwig, "Refractive index matching methods for liquid flow investigations," *Exp. Fluids*, vol. 17, pp. 350–355, 1994.

[302] R. Donnelly, "Fluid dynamics," in *American Institute of Physics 50th Anniversary Physics Vade Mecum* (H. Anderson, ed.), ch. Fluid dynamics, American Institute of Physics, 1991.

[303] T. L. Narrow, "Flow visualization within a seven-rod micro-bundle," Master's thesis, School of Mechanical Engineering, Georgia Institute of Technology, 1998.

[304] D. Michaelis, M. Novara, F. Scarano, and B. Wieneke, "Comparison of volume reconstruction techniques at different particle densities," in *15th International Symposium on Applications of Laser Techniques to Fluid Mechanics*, (Lisbon, Portugal), 2010.

[305] A. Prasad, "Stereoscopic particle image velocimetry," *Exp. F*, vol. 29, pp. 103–116, 2000.

[306] S. Soloff, R. Adrian, and Z. Liu, "Distortion compensation for genegeneral stereoscopic particle image velocimetry," *Meas. Sci. Technol.*, vol. 8, pp. 1441–1454, 1997.

[307] B. Wieneke, "Volume self-calibration for 3D particle image velocimetry," *Exp. Fluids*, vol. 49, pp. 549–556, 2008.

[308] LaVision GmbH, Anna-Vandenhoeck-Ring 19, D-37081 Göttingen, Germany, *FlowMaster Tomographic PIV User's Guide*, January 2012.

[309] C. H. Atkinson and J. Soria, "Algebraic reconstruction techniques for tomographic particle image velocimetry," in *16th Australasian Fluid Mechanics Conference*, (Gold Coast, Australia), 2007.

[310] N. A. Worth and T. B. Nickels, "Acceleration of tomo-PIV by estimating the initial volume intensity distribution," *Exp. Fluids*, vol. 45, pp. 847–856, 2008.

[311] C. Atkinson and J. Soria, "An efficient simultaneous reconstruction technique for tomographic particle image velocimetry," *Exp. Fluids*, vol. 47, pp. 553–568, 2009.

[312] H.-G. Maas, P. Westfeld, T. Putze, N. Bøtkjær, J. Kitzhofer, and C. Brücker, "Photogrammetric techniques in multi-camera tomographic PIV," in *8th International Symposium on Particle Image Velocimetry*, (Melbourne, Australia), 2009.

[313] C. Atkinson, N. Buchmann, M. Stanislas, and J. Soria, "Adaptive MLOS-SMART improved accuracy tomographic PIV," in *15th International Symposium on Applications of Laser Techniques to Fluid Mechanics*, (Lisbon, Portugal), 2010.

[314] M. Novara, K. J. Batenburg, and F. Scarano, "Motion tracking-enhanced MART for tomographic PIV," *Meas. Sci. Technol.*, vol. 21, p. 035401, 2010.

[315] D. Michaelis. Product Manager for Volumetric Flow Measurement, LaVision GmbH, Private communication, June 2013.

[316] F. Scarano, "Iterative image deformation methods in PIV," *Meas. Sci. Technol.*, vol. 13, pp. R1–R19, 2002.

[317] J. Hunt, A. Wray, and P. Moin, "Eddies, streams, and convergence zones in turbulent flows," in *Proceedings of the CTR Summer Program*, (Stanford, CA), pp. 193–208, Center for Turbulence Research, Stanford University, 1988.

[318] G. Taylor, "The spectrum of turbulence," *Proc. R. Soc. London Ser. A*, vol. 164, p. 476, 1938.

[319] Hewlett-Packard Company, Palo Alto, California, *HP 34401A Multimeter User's Guide*, 1996.

[320] LaVision GmbH, Anna-Vandenhoeck-Ring 19, D-37081 Göttingen, Germany, *Distributed Computing in DaVis*, January 2012.

VITA

Daniel Borrero Echeverry was born in Bogotá, Colombia on June 6th, 1981. He spent his formative years running around barefoot, building sweet jumps for his go-kart, and blowing stuff up on his family's farm. In his spare time, Daniel attended Colegio Nueva Granada, where he got really into metal and acquired a distaste for shaving. Daniel graduated CNG in 2000. After a brief stint in the Colombian military, where he was stationed with the 13th Military Police Batallion and sucked down enough tear gas to make a small mouse explode, Daniel enrolled at the University of Texas at Austin. While at UT, Daniel worked in the laboratory of Dan Heinzen, where he was part of a team attemping to make precision measurements of the electric dipole moment of the electron. Daniel received a B.S. in Physics from UT in 2005 and joined the doctoral program in the School of Physics at the Georgia Institute of Technology that fall.

At Georgia Tech, Daniel joined the research group of Mike Schatz, where he first cut his chops working on an optically-actuated microfluidic device with Vivek Sharma. Daniel received his M.S. in Physics in 2006. Sometime around 2007, Mike got the turbulence bug and drove to the University of Colorado-Denver, where he picked up a Taylor-Couette apparatus that had been dutifully stored for 20 years by Prof. Randy Tagg. Daniel immediately became fascinated with the system and has been working on it ever since. During his time at Georgia Tech, Daniel also found an unexpected soft spot for teaching, which he was able to explore through Mike's various educational outreach programs. His teaching earned him several teaching awards, including the 2011 CETL/BP Outstanding Graduate Teaching Assistant Award, Georgia Tech's only institute-wide award for teaching assistants. While in the School of Physics, Daniel was lucky to have the opportunity to work with Predrag Cvitanović on symmetry reduction schmes for high-dimensional dynamical systems and with Kurt Wiesenfeld on synchronization of coupled nonlinear oscillators. Eventually, it became apparent to Daniel that grad student emeritus is not a thing, so he wrote up his dissertation, receiving a Ph.D. in Physics from Georgia Tech in 2014.